Charge Transport Layers and Passivation for Improved Efficiency and Stability of N-I-P Perovskite Solar Cells

Suer Zhou

St Anne's College

A thesis submitted for the degree of

Doctor of Philosophy

at the University of Oxford

Hilary Term 2023

Declaration

This thesis is entirely a result of my own work except where otherwise indicated.
I declare that no part of this work has been submitted for a degree or any other qualifications at this or any other university.
Suer Zhou, April 2023.

Abstract

Perovskite solar cells have become a promising photovoltaic technology for harvesting energy from the sun. However, despite their low-cost processing and high performance, a few issues remain for their wider application. One of the main concerns is their stability. Commercializable solar photovoltaic technologies must remain stable under constant illumination and high-temperature not only for a few days as they would be tested in a lab, but for several years. In particular, low-cost, dopant-free, and stable hole-transporting materials need to be found to replace Spiro-OMeTAD, due to its instability issues. Furthermore, better passivation strategies need to be discovered and employed.

The primary aim of this project was to look for alternative charge-transfer materials to replace those typically used in a regular architecture solar cell device, and to make the perovskite absorber material more stable by additive engineering. To achieve this, various hole-conducting materials and passivation molecules were tested, and those which improved the film quality were further characterized and tested in devices for their performance and stability. The lessons learned from these studies led to the fabrication of a very stable solar cell architecture.

Chapter 4 focuses on a pair of alternative hole-conductors that are dopant-free and low in cost. They were found to perform just as well as spiro-OMeTAD whilst being more stable. **Chapter 5** discusses an often-overlooked additive approach of applying aromatic amines to passivate the perovskite absorber. Our average benzylamine-modified perovskite devices maintained 80% of their initial efficiency over 2,400 hours in 65°C 1 sun aging test. Meanwhile, the average control devices without additives degraded to 45% of their initial efficiency. **Chapter 6** investigates the potential of applying a fullerene-based self-assembling monolayer to stabilize the electron-transporting layer/perovskite interface. However, the results of the fullerene self-assembling monolayer-modified interface were less stable. Despite that, the rea-

sons for their instability were investigated and a future research direction is proposed to improve them.

The novel charge-transporting materials and bulk/interface modifications studied in this thesis are promising solutions for stabilizing the regular architecture of perovskite solar cells. Moreover, the investigation into why certain passivation methods work and others fail can help us design and select better materials and passivation methods for more durable solar cells.

Acknowledgements

First and foremost, I want to thank Prof. Henry Snaith for taking me in and advising me. So many opportunities have been opened up to me since I joined the group. I also want to thank Prof. Andrew Watt from the Oxford Department of Materials for initially accepting me into his group. Thanks also to our group academic administrator, Clare Moloney, for helping me at various times. Next, I want to thank Ashley Marshall and Kelly Schutt who have provided me with so much help and guidance both in getting my projects started and throughout the rest of my PhD. I am really indebted to them. I would like to thank Olivia Ashton for teaching me nanocrystals synthesis at the beginning of my Ph.D. I want to thank Ashley Marshall, Micheal Farrar, Nakita Noel, and Daniel Worthing for reading my thesis and giving me feedback. They have directly contributed to the improvement of this thesis.

In our group, I would like to thank Joel Smith and James Drysdale (Jake) who have been working on the benzylamine project with me and provided invaluable advice and assistance. Thanks to Akash Dasgupta who did PL imaging for various projects in this work. Thanks also to Pietro Caprioglio, for showing me how to do QFLS analysis, and to Nobuya Sakai, Bernard Wenger, and Manuel Kober-Czerny, for their help and advice on photoluminescence measurements. Thanks to Benjamin Gallant (Benny), who did the NMR spectroscopy analysis for the benzylamine project, and to Philippe Holzhey, for doing the cost analysis in the carbazole HTM project and giving me various suggestions during my Ph.D. Thanks also to Seongrok Seo, Philippe Holzhey, and Benny, who helped me work on optimizing n-i-p device performance. I would also like to thank Jae Lee from Prof. Laura Hertz's group, who worked on the C_{60}-PA SAMs with me and spent several days measuring THz spectroscopy.

I also want to thank my collaborators in Prof. Tadas Maulinauskas and Vytautas Getautis' group for synthesizing and characterizing the carbazole-based enamine hole transporting materials, particularly Maryte Daskevicieneb and Matas Steponaitis, who

are my co-authors on the paper. I want to thank Prof. David Ginger's group, particularly Yangwei Shi and Margherita Taddei, for working on the benzylamine project with me. My thanks also go to Prof. Seth Marder's group, in particular, Raghunath Dasari (Reddy) for synthesizing the C_{60}-PA SAM, and Junxiang for synthesizing BnFAI. Without their contribution, my research could not be completed.

I want to thank the Rank Prize fund which supported me financially during the COVID pandemic lockdown.

I would also like to thank my entire group which provided me with both career and research advice throughout my 4-year journey, as well as interesting conversations, discussions, and activities to help me stay motivated.

I want to thank the great friends I have made at Oxford. In particular, I want to thank Virginia, who has always supported me through academic and personal difficulties. She has given me invaluable suggestions throughout my Ph.D. I want to thank Varnika, my friend previously in Prof. Andrew Watt's lab, who has given me great support.

Last but not least, I want to thank my family and Dan. Without their unconditional support, I would not have been able to get this far with my Ph.D. I owe them a great deal in life.

Contents

List of Publications

1. Zhou, S., Daskeviciene, M., Steponaitis, M., Bubniene, G., Jankauskas, V., Schutt, K., ... & Snaith, H. J. (2022). "Low-Cost Dopant-Free Carbazole Enamine Hole-Transporting Materials for Thermally Stable Perovskite Solar Cells". *Solar RRL*,.6(1), 2100984.

2. Taddei, M., Smith, J. A., Gallant, B. M., Zhou, S., Westbrook, R. J., Shi, Y., ... & Ginger, D. S. (2022). "Ethylenediamine Addition Improves Performance and Suppresses Phase Instabilities in Mixed-Halide Perovskites". *ACS Energy Letters*,.7(12), 4265-4273.

3. Dasgupta, A., Mahesh, S., Caprioglio, P., Lin, Y. H., Zaininger, K.A., Oliver, R.D., Holzhey, P., Zhou, S., McCarthy, M.M., Smith, J.A. ... & Snaith, H. J. (2022). "Visualizing macroscopic inhomogeneities in perovskite solar cells". *ACS Energy Letters*,.7(7), 2311-2322.

4. Sturdza, B. K., Lauritzen, A. E., Zhou, S., Bennett, A. J., Form, J., Christoforo, M. G., ... & Nicholas, R. J. (2022). "Improving the performance of fully scalable, flexible transparent conductive films made from carbon nanotubes and ethylene-vinyl acetate". *Energy Reports*, 8(S11).

5. Duijnstee, E. A., Gallant, B. M., Holzhey, P., Kubicki, D. J., Collavini, S., Sturdza, B. K., Sansom, H.C., Smith, J., Gutmann, M.J., Saha, S. and Gedda, M.,... Zhou, S.,... & Snaith, H. J. (2023). "Understanding the degradation of methylenediammonium and its role in phase-stabilizing formamidinium lead triiodide". *Journal of the American Chemical Society*, 145(18), 10275-10284.

6. Wang, W-T., Holzhey, P., Zhang, Q., Zhou, S., Duijnstee, E. A., Rietwyk, K.J.,

Acknowledgements

Chiang, C-H, Zhang.Y., Bach, U., Wu, C-G., Snaith. H.J., Feng, S-P. (2023). "Water and heat-activated dynamically evolving passivation for perovskite photovoltaics". Submitted to *Nature*, under review.

List of Abbreviations

AFM atomic force microscopy

EQE external quantum efficiency

ETL electron-transporting layer

FA formamidinium

FF fill factor

FTO fluorine-doped tin oxide

HTM hole-transporting material

J_{sc} short-circuit current

KPFM Kelvin probe force microscopy

Li-TFSI lithium bis-(trifluoromethanesulfonyl)imide

MA methylammonium

MPP maximium power point

NMR nuclear magnetic resonance

η_{MPP} maximium power point tracked efficiency

OPV organic photovoltaic

$PC_{60}BM$ Phenyl-C61-butyric acid methyl ester

List of abbreviations

PCE power conversion efficiency

PL photoluminescence

PLQY photoluminescence quantum yield

PMMA poly(methyl methacrylate)

Poly-TPD poly(N,N'-bis-4-butylphenyl-N,N'-bisphenyl)benzidine

PSC perovskite solar cell

PTAA Poly[bis(4-phenyl)(2,4,6-trimethylphenyl)amine]

PV photovoltaics

QFLS quasi-Fermi level splitting

SAM self-assembling monolayer

SEM scanning electron microscopy

Spiro-OMeTAD 2,2',7,7'-tetrakis(N,N'-di-p-methoxyphenylamine)-9,9'-spirobifluorene

SSPL steady-state photoluminescence

tBP 4-tert-Butylpyridine

TRPL time-resolved photoluminescence

V_{oc} open circuit voltage

XPS x-ray photoelectron spectroscopy

XRD x-ray diffrection

List of Figures

CHAPTER 1

Introduction

1.1 Motivation for Solar Cells

Historically, before the European Industrial Revolution, fossil fuels played less of a part in human activities. Among the three major fossil fuel resources, coal, oil, and natural gas, coal has been used for heating since prehistoric times, as it was discovered that coal could burn longer than wood. Archaeologists have found that the Romans used coal in Britain between 40 and 50 AD [1, 2]. The first time that coal was used on an industrial scale was in the eleventh century in China [3]. The Chinese also drilled wells to reach natural gas reservoirs as early as 500 B.C.[4]. A few hundred years later, they used bamboo pipes to carry natural gas to heat up people's houses [5, 6]. They also appear to be the first to drill oil around 200 B.C.[7]. Oil used to be a by-product of salt wells, and it was not widely used until recently. It was during the Industrial Revolution (1750-1870s) that the use of fossil fuels expanded widely, rising up to over 120,000 terawatt-hours globally by 2021 [8] (Figure 1.1). Following James Watt's development of the steam engine, the use of coal dramatically increased. The

burning of fossil fuels emits carbon dioxide (CO_2), which is a greenhouse gas that enters the atmosphere and traps heat. This in turn warms up our atmosphere which is the main cause of global warming.

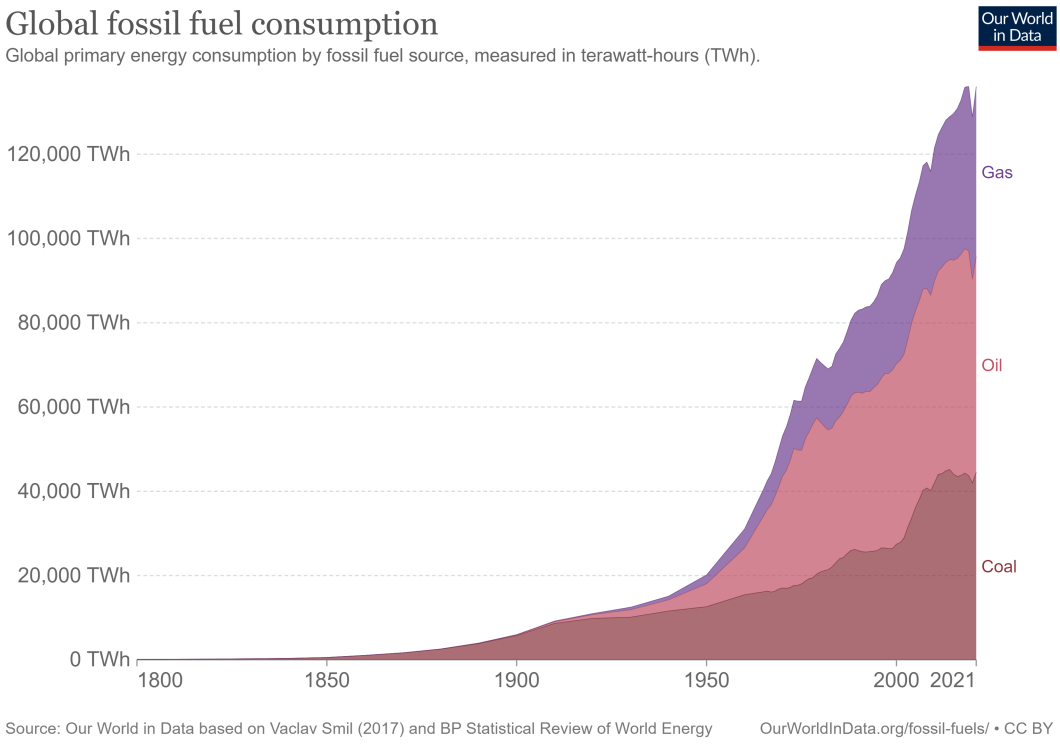

Figure 1.1: Global primary energy consumption by fossil fuel source, measured in terawatt-hours (TWh). Reproduced from reference [8].

Today, the world is hungrier for fuel than ever. The result of excessive usage of fossil fuels became apparent to climate scientists in the mid-1980s [9]. The concern was raised in international political forums in the early 1990s when global warming was recognized as a threat to our planet [10]. The Intergovernmental Panel on Climate Change (IPCC) issued its First Assessment Report in 1990, pushing a strategy to reduce fossil fuel consumption [11]. However, the use of fossil fuels keeps on rising sharply. At the 2009 Copenhagen Climate Summit, major governments in the world proposed a list of goals for cutting carbon emissions by 2020, which mostly ended in failure. In the Paris Summit in 2015, the central objective was to limit the long-term rise in temperature (by 2100) to "well below 2 °C above pre-industrial levels". By

November 2022, the world was already 1.2 °C hotter than the pre-industrial average temperature, and rising (See Figure 1.2).

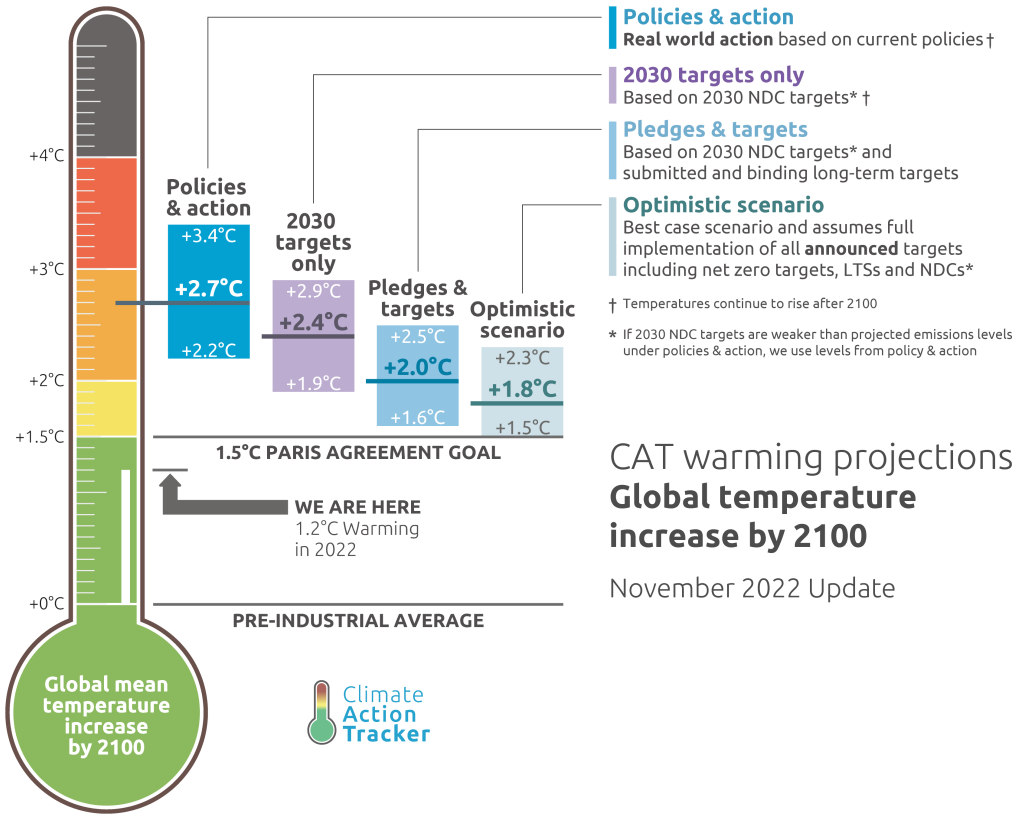

Figure 1.2: The climate action tracker thermometer. The temperatures on the CAT thermometer are 'median' warming estimates in 2100. This means that there is a 50% chance that the calculated temperature would be exceeded if the given emissions pathway is followed. Reproduced from ref. [12].

Limiting global warming requires a transition from non-renewable, fossil fuel energy to renewable energy, such as wind energy, tidal energy, and solar energy. Solar power is particularly promising. The Cambridge physicist, David MacKay, has estimated that the amount of solar energy that reaches the earth every 40 minutes is enough to satisfy the entire world's energy needs for a year. The claim of course refers to an oversimplified and idealized situation, since it is impossible to cover the entire surface of the earth in solar panels and solar panels do not convert 100% of the energy they receive. Nevertheless, it does show that there is a huge source of energy that we have

not made the most of. As the cost of utility-scale solar photovoltaics (PVs) becomes cheaper, solar energy has become more competitive with fossil fuel energy such as oil and gas (see Figure 1.3). As of September 2022, solar PVs accounted for 3.6% of global electricity generation [13]. However, to achieve the ambitious goal of net zero emissions by 2050, we need an annual generation growth of 25%. To achieve this, we need better policies that foster renewable energy growth, we need the private sector to invest more in renewable energy, and we need cheaper and higher power conversion efficiency solar cells.

The global solar PV market was estimated at 85 billion USD in 2021 and is projected to exceed 369 billion USD by 2030 [14]. In the PV market, crystalline silicon solar cells make up 86% of the market share, while thin film solar cells (GaAs, CIGS, etc.) make up 14% [14]. Silicon PVs also have the longest lifetimes, which makes the initial investment worthwhile. There are solar cells installed in the 1970s that are still in operation today [15]. While the fabrication of silicon solar cells is already competitively cheap, it has other challenges. The production of silicon solar cells requires a temperature of over 1,420°C to melt silicon. Crystalline Si (c-Si) has fewer grain boundaries and recombination centers and gives high performance ($\sim$26.1%) [16]. However, c-Si is much more difficult to grow; a single-crystal Si seed is required to extract molten Si to grow a single-crystal boule. While polycrystalline Si is easier to fabricate and widely commercialized, it is also lower in performance (15$\sim$20%) [17]. At the moment, fossil fuels such as coal and oil are still needed for the manufacturing of silicon PVs. However, some of the next generation 'thin film' solar cells are cheaper to fabricate and use less material, so could potentially be produced with a smaller energy budget. A typical crystalline (c-Si) wafer is about 200 μm thick, while thin film solar cells are only several nanometers to tens of micrometers thick.

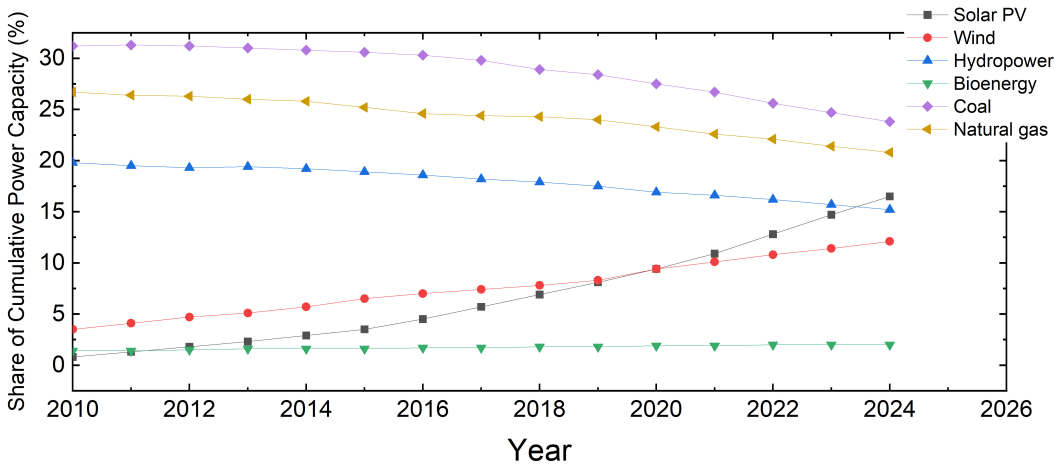

Figure 1.3: Projected share of cumulative power capacity by technology, 2010-2024. Reproduced from reference [13]. This is a work derived by me from IEA material and I am solely liable and responsible for this derived work. The derived work is not endorsed by the IEA in any manner.

While second-generation thin-film PV technologies have advantages compared to traditional Si PV, they have their challenges too. Gallium arsenide (or other III-V) solar cells have higher efficiency than Si solar cells, but they still require strict growth and processing conditions such as molecular beam epitaxy and chemical vapor deposition, which is still expensive and not scalable. Therefore, they could be used in applications where cost is not an important consideration compared to efficiency and reliability, such as in aerospace projects. Copper indium gallium selenide (CIGS) solar cells have high efficiencies of up to 23.4% (2018-12) and can be made on flexible substrates for portable devices. However, CIGS solar cells consist of a toxic CdS layer. Other chemicals used to produce CIGS cells like thiourea and H_2Se are also toxic and require proper disposal and waste treatment [18]. While many elements used in CIGS cells are earth-abundant, indium is scarce and researchers are currently searching for an alternative.

Third-generation organic photovoltaics (OPV) and perovskite photovoltaics (PPV) have recently gained more attention as competitors in the PV market. OPVs can provide electricity at a low cost. They are lightweight and roll-to-roll processable. They do not contain toxic heavy metals which can have an environmental impact. However, they are lower in efficiency (highest 18.2% in 2020-11 [16, 19]), and their long-term

stability (predicted ∼10 years unencapsulated [20]) needs to be improved to compete with silicon PV. Research on PPV has increased substantially over the past decade and their efficiencies are rivaling of c-Si and GaAs. They can be solution-processed or vapor-deposited, which makes them scalable and can be fabricated on flexible substrates. The main concern regarding PPVs is the toxicity of the lead they contain. Alternative perovskite materials such as tin-based perovskite, and $CuAgBiI_5$, $Cs_2AgBiBr_6$ have been investigated to overcome this issue. Another problem with lead halide perovskite is its long-term stability. Currently, PPVs have an estimated lifetime of ∼a year [21] whereas Si PVs have a lifetime of over 25 years [22].

CHAPTER 2

Theory and Background

2.1 Light from the Sun

When sunlight passes through the atmosphere, many processes can attenuate the light intensity. For example, the ozone layer can scatter ultraviolet radiation, and water and carbon dioxide can absorb infrared radiation. Air mass is used to quantify the amount of sunlight reaching different parts of the earth. It is defined as the direct path length the light takes to reach the earth's atmosphere, expressed as a ratio relative to the path length vertically upwards. The air mass (AM) coefficient is used to characterize the performance of solar cells under standardized conditions. The standard spectrum reaching the earth's surface is AM 1.5G (G stands for globally), which is normalized to give 1 kW/m^2 or 100 mW/cm^2 (spectrum shown in Figure 2.1). The sun's intensity outside of the earth's atmosphere is called AM 0 because the light does not pass through the earth's atmosphere [23]. For all terrestrial solar cell applications, as in this thesis, we use AM 1.5G to characterize our solar cells' efficiencies.

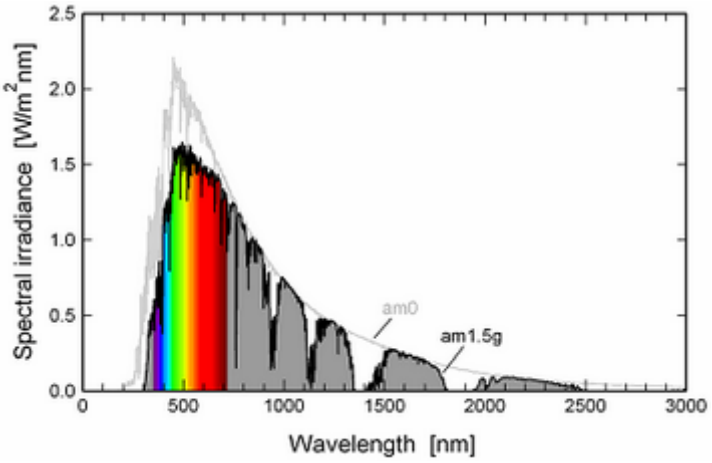

Figure 2.1: Spectral irradiance of the AM 1.5G spectrum. Reproduced from reference [24].

2.2 Semiconductor Materials

Solar cells use semiconductor materials as light absorbers. Semiconductor materials often have some long-range periodicity. In a crystalline solid, there is some basic structure that is repeated throughout the solid so that the crystal appears to be the same at one point as it does at another point. This periodicity is given by a symmetric array of points called a lattice. Atoms or a group of atoms can be added to lattice points to create a basis. The basis is then repeated to get a crystal.

Electrons in a material are not free to exist in any state. In crystalline materials with a repeating lattice structure, the energy and momenta of electrons are restricted. This restriction can be understood in two ways: through the interaction of electron orbitals in the compounds, which limits the available states, or by considering the wavefunctions of free electrons interacting with the periodic Coulomb potential created by the nuclei at lattice sites. As a result, specific combinations of energy and momenta are permitted for the electrons. Moreover, at energies where the wave function of the electron would form standing waves with respect to the lattice, there is destructive interference with the wave function of the electron. This phenomenon creates a forbidden gap, known as the band gap (E_g), within the energy-momenta space of permissible states (see Figure 2.2).

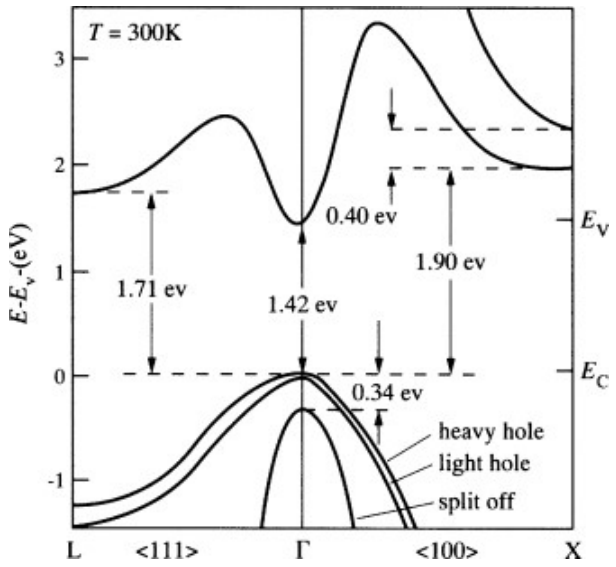

Figure 2.2: Conduction and valence band energies of GaAs as a function of wave vector. The values noted on the diagram are those appropriate for room temperature. Reproduced with permission from Journal of Applied Physics [25].

When a large number of atoms combine to form a crystal, the atomic orbitals of their outermost shell electrons interact to form continuums which consist of closely spaced orbitals. These continuums are called bands. The range of highest energies that the electrons can have but still be bound to specific lattice sites is the valence band E_v and the range of lowest energies that the electrons have to become free charge carriers is the conduction band E_c. In between E_v and E_c is the E_g. The band gap energy is the lowest required amount of energy to promote the electron from the valence band to the conduction band. An electron can obtain energy either from a photon or phonon and get excited from the valence band to the conduction band, leaving behind a "hole", an absence of an electron; these electrons and holes can then participate in conduction. For an intrinsic semiconductor, in the middle of the band gap, halfway between the valence band and the conduction band, lies the Fermi level (or chemical potential), $E_f = E_{gap}/2$. At 0 K, the electrons have no kinetic energy and occupy the lowest available energy levels. The Fermi energy is the highest energy an electron can fill up to at temperature 0 K. At any temperature above 0 K, some electrons have enough energy to occupy states above the Fermi energy, as shown in

Figure 2.3. At any given temperature, the Fermi level is the energy level at which it has 50% probability of occupancy at any given time.

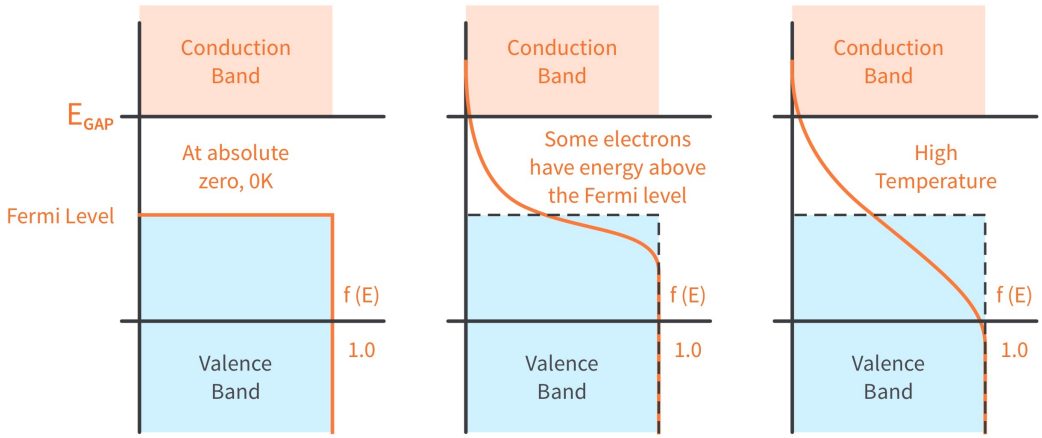

Figure 2.3: Semiconductor Fermi level band diagram under 0 K, a low temperature and a high temperature. Reproduced from reference [26].

Semiconductors can either be direct E_g or indirect E_g. For a direct E_g semiconductor, the E_c and the E_v occur at the same momentum in the momentum space. Whereas, for an indirect E_g semiconductor, the E_c and the E_v occur at different momentums. Thus, for an indirect E_g semiconductor, an energy transition and a momentum transition are needed for an electron to move from band to band.

2.2.1 Intrinsic Semiconductor and Doping

At absolute zero, 0 K, no electrons in the valence band can be excited to the conduction band. However, as the temperature increases above absolute zero, some electrons gain enough thermal energy to populate the conduction band, while leaving behind holes. In the process, the material becomes more conductive. At 300 K, around the temperature that solar cells are measured, in silicon there are about 9.65×10^9 cm^{-3} charge carriers [27], which are called intrinsic charge carriers. For intrinsic semiconductors, the Fermi level lies in the middle of the E_g.

The charge carrier concentration can also be increased by doping. Doping a group IV material (for example Si) with a group III material (eg. boron) causes

the crystal lattice to be deficient in one valence electron (leaving an extra hole) and doping the group IV material with a group V material (eg. phosphorus) gives the lattice an extra electron. The extra electrons and holes can increase the charge carrier density for conduction, and they are called extrinsic carriers. An excess electron-doped semiconductor is an n-type semiconductor and its Fermi level (E_{Fn}) lies closer to the conduction band. An excess hole-doped semiconductor is a p-type semiconductor and its Fermi level (E_{Fp}) lies closer to the conduction band. In the case of an n-type semiconductor, the majority charge carriers are electrons, and the minority charge carriers are holes, and vice versa with p-type semiconductors.

2.2.2 Charge Carrier Generation

When light passes through a semiconductor material, depending on its energy, three things can happen. (1) When the photon energy, $h\nu$, is greater than the bandgap, E_g, the photon can get absorbed by the material, promoting an electron to the conduction band, and excess energy greater than the E_g is subsequently lost due to thermalization. (2) When the photon energy is equal to the E_g energy, there is just enough energy for the photon to be absorbed by the semiconductor. (3) When the photon energy is less than the E_g, the light passes through the material as if it is transparent. For the solar spectrum, there is an ideal E_g that is not too wide, where most wavelengths of light pass through it, nor is it too narrow, where some of the energy from higher energy photons is lost to phonon scattering. For example, metal-halide perovskite is a material with tunable E_g. Thus, it is possible to adjust its composition such that it maximizes the energy absorbed.

In a p-type semiconductor, the light incident on it generates electron-hole pairs, the minority carriers (in this case electrons) instantly recombine with an overwhelmingly large number of majority carriers (holes), whereas, the hole is in excess and free to move around. Most of the electron-hole pairs are generated near the surface of

the absorber material, as the absorption (and therefore light intensity in the material) varies with depth according to the equation

$$I(x) = I_0 exp(-\alpha x) \tag{2.1}$$

Where I is the light intensity at a certain depth (x), I_0 with a unit of [cm^{-2}] is the intensity of incident light, and α is the absorption coefficient. The photon current (per unit of time) is therefore:

$$j(x) = j_0 exp(-\alpha x) \tag{2.2}$$

The absorption coefficient, α varies with the light frequency, $\alpha(\hbar\nu)$ with a unit of [cm^{-1}].

The charge generation rate, G with a unit of [cm^{-3} s^{-1}], is related to Equation 2.2.

$$G(x) = \int \alpha(\hbar\nu, x) dj(\hbar\nu, x) \tag{2.3}$$

The integral should be extended to the absorbed photon energies that result in free carrier generation (pg. 89 [28]).

2.2.3 Charge Carrier Recombination

The charge carrier recombination process is the opposite to charge carrier generation. The electron in the conduction band is in a meta-stable state and ultimately releases its energy and combines with a hole in the valence band, annihilating the pair. When the electron-hole pair recombines, they give off either light or heat. There are three kinds of recombination that can happen in a solar cell: radiative recombination, non-radiative recombination, and Auger recombination. (1) Radiative recombination is also called band-to-band recombination. During this process, the electrons in the conduction band recombine with holes in the valence band and release energy in the

form of a photon with energy equal to the E_g energy. (2) The non-radiative recombination or trap-assisted recombination/Shockley-Read-Hall recombination process consists of two stages. First, an electron in the conduction band is captured by a trap state or defect level inside the bandgap. Second, if a hole moves to the same trap state from the valence band before the trapped electron is re-thermalized into the conduction band, then the electron will recombine with the hole. In this case, because neither the electron nor the hole gives off energy as wide as the bandgap, it is likely to give off energy in the form of heat rather than light. If the charge carrier (electron/hole) is trapped close to the conduction band/valence band edge (shallow trap states), it is more likely that it will be re-thermalized to the conduction/valence band. However, if the defect level is deep in the middle of the bandgap, then it is less likely that the trapped charges will re-thermalize to the conduction/valence bands. For example, most of the trap states in perovskite materials are shallow, so the material is considered defect tolerant. (3) Auger recombination involves three charge carriers. When an electron recombines with a hole, the energy is given to a third electron in the conduction band, this electron then thermalizes back to the conduction band. The process applies less to perovskite material under 1 sun intensity of light (100 mW/cm^2). It applies to semiconductors with high injection rates and high carrier concentrations, such as heavily doped silicon under high-intensity illumination.

Surface/interface, and grain boundary recombination are particularly relevant and important for perovskite solar cells and in general, all solar cells. Because perovskite is a polycrystalline material, there are disruptions to the periodicity of the crystal lattice which create dangling bonds and adsorb impurities at the surface and grain boundary. These defects often called surface states act as traps and recombination centers. These surface states can have a continuous distribution within the bandgap and when they trap electrons and holes, they can be recombination centers. Therefore, passivating these surfaces and grain boundaries becomes crucial for enhancing the performance and stability of solar cells.

2.2.4 Charge Carrier Lifetime, Mobility, and Diffusion Length

Charge carrier transport is important for photovoltaic devices because in order to extract current out of the device, the charge carriers must be able to reach the contacts before they recombine. There are certain parameters that are important to measure for charge carrier transport in semiconducting materials. The charge carrier diffusion length, L, is the average distance that charge carriers travel before they recombine. The average amount of time that the charge carriers stay in the excited states before they recombine is called the carrier lifetime, τ. The minority carrier lifetime decreases with doping since there is faster recombination of minority carriers with majority carriers when the material has a high doping density. The lifetime also generally decreases as the material is doped more heavily because the lattice mismatch of the introduced material can cause more strain and recombination centers. If the material is more crystalline, there are fewer recombination centers and if the material is polycrystalline or amorphous, there are more recombination centers. The mobility (μ) relates to how easy it is for charge carriers to move across a material under the influence of an electric field. For a highly doped material, the μ also drops because electrons are strongly scattered by the long-range Coulomb field of the charged dopant [29, 30]. The diffusivity, D, is the rate of diffusion, a measure of the rate at which the charge carriers can spread. The Einstein relation relates mobility to diffusivity.

$$D = \mu k_B T \tag{2.4}$$

Where D is the diffusivity, k_B is Boltzmann's constant, and T is the absolute temperature in Kelvin. The charge carrier diffusion length, L, is given by

$$L = \sqrt{D\tau} \tag{2.5}$$

Thus, at a given temperature, the longer the carriers travel before it recombine, and the higher the charge carrier mobility, the longer the charge carrier diffusion length.

2.2.5 Charge Transport

Since light is mainly absorbed near the surface of the material, charge carriers are generated close to the surface. The generated electron-hole pair randomly move inside the material and eventually recombines. The charge carriers move for a certain mean free path before colliding with the lattice and scattering off in a different direction. The generated charge carriers will redistribute from a high concentration gradient to a low concentration gradient until they are evenly distributed. Carrier movement due to a concentration gradient is called diffusion. The electron current contribution from charge carrier diffusion, $J_{n,diff}$, is given by

$$J_{n,diff}(x) = qD_n \frac{dn(x)}{dx} \tag{2.6}$$

And likewise, the diffusion current from holes, $J_{p,diff}$, is

$$J_{p,diff}(x) = -qD_p \frac{dp(x)}{dx} \tag{2.7}$$

Where q is the elemental electron charge, D_n and D_p are the diffusion coefficients for the electron and holes and n is the electron concentration and p is the hole concentration. There is a negative sign for $J_{p,diff}$ since an electron carries a negative charge -q.

Aside from charge carrier diffusion, the current density can also arise in the presence of an electric field. Electrons carrying a negative charge move opposite to the direction of the electric field and holes move in the direction of the electric field. Thus, a net current flows in the direction of the electric field. The drift equation is given by

$$J_x(x) = q(n\mu_n + p\mu_p)E_x \tag{2.8}$$

Where J_x is the current density in the x direction, q is the electron charge, μ_n and μ_p are the electron and hole mobilities, respectively, n and p are the electron and hole concentrations, and E_x is the electric field in the x-direction.

2.3 Semiconductor Heterojunctions

2.3.1 p-n Junctions

When a p-type material is layered with an n-type material, since the electrons are higher in concentration in the n-type material and the holes are higher in concentration in the p-type material, the electrons will diffuse into the p-type material due to the concentration gradient and vice versa. When electrons diffuse away from the n-region, they leave behind positive ions and when holes diffuse away from the p-region, they leave behind negative ions. This creates an electric field from the positive to the negative ions, forming a space-charge depletion region. The voltage generated in this region is called the built-in voltage (V_{bi}). Due to the electric field, most of the electrons stay inside the n-type region and the holes stay inside the p-type region, but there is always a small number of minority carriers that are within a diffusion length of the depletion region that will get swept across the depletion region into the majority carrier material. The depletion region presents a low resistance path to minority carriers and high resistance to the majority carriers due to the electric field.

Without an electrical bias, this process reaches equilibrium, and the net current flow is zero. However, with an electrical bias, the space-charge region will expand or shrink. Under forward bias, electrons and holes flow towards the p-n junction where they recombine and the depletion region is reduced, increasing the probability of minority carriers being swept across the depletion region; under reverse bias, electrons, and holes move away from the junction and the depletion region is expanded, reducing

the probability of minority carriers being swept across the depletion region. In other words, under forward bias, the applied voltage is subtracted from the V_{bi} and the charge extraction barrier is lower; under reverse bias, the applied voltage is added to the V_{bi} and the charge extraction barrier is higher. The built-in voltage is given by

$$V_{bi} = (E_g - E_{Fp} - E_{Fn})/q \tag{2.9}$$

Illumination reduces the built-in voltage by generating an electric field that opposes the V_{bi}. Under illumination, excess electrons and holes are generated in the n and p regions, respectively. Since the voltage is reduced over the depletion region, the energetic barrier to the (majority carrier) diffusion current is lowered.

2.3.2 p-i-n and n-i-p Junctions

P-i-n and n-i-p junctions have an extra intrinsic (i) layer sandwiched between the n-type region and the p-type region. For MHP solar cells, the n-i-p device architecture is normally referred to as the regular architecture and p-i-n is the inverted architecture. The difference is that light is incident on opposite sides of the device stack. Junctions with an intrinsic layer are preferred when carriers are unlikely to be generated in the n and p-type regions, but are only advantageous in materials with a long charge carrier diffusion length (such as perovskite materials) since the charge carriers have to diffuse through the thick intrinsic region. This architecture effectively separates the charge generation and collection processes. Rather than having a thin depletion region, the electric field extends across the entire intrinsic region. Charge carriers are generated in the intrinsic region rather than the p- or n-regions. The exciton (bound state of an electron-hole pair) is separated by the electric field across the intrinsic region and collected by the n- and p-type regions. The electron transport layer (n-layer) presents a low-resistance path for electrons and a high-resistance for holes and vice versa. In the p-i-n/n-i-p configuration, since there are no majority or minority carriers in the intrinsic region, there is no diffusion current, and the drift current dominates.

In the n-type material, the E_{Fn} is closer to the conduction band, whereas, in the p-type material, the E_{Fp} is closer to the valence band. In the intrinsic layer, E_{Fi} is at the intrinsic level in the middle. However, at equilibrium in the dark, the Fermi level must be aligned throughout the heterojunction (Figure 2.4). Therefore, this creates a "step-like structure" among the p-i-n conduction bands and among the p-i-n valence bands. The V_{bi} is extended across the entire intrinsic region and the electric field is constant throughout the intrinsic region.

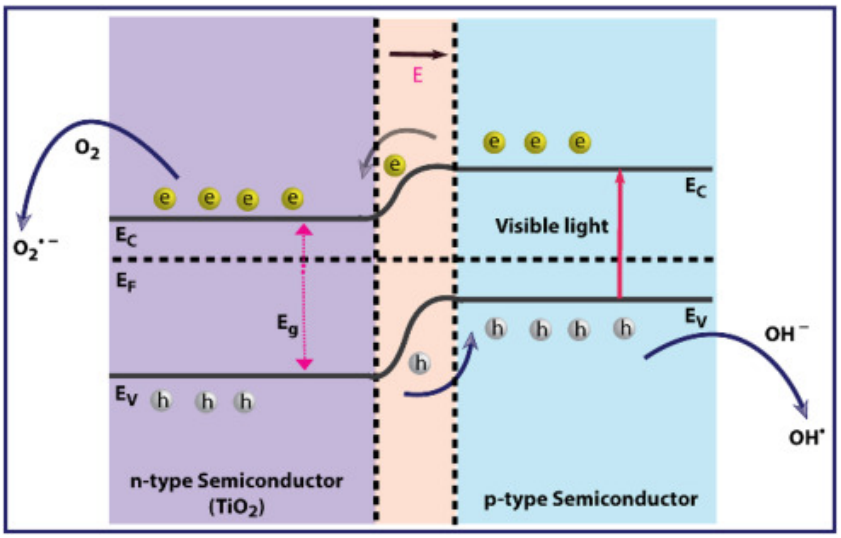

Figure 2.4: Schematic band alignment of type-II semiconductor heterojunction showing charge separation at the interface. Illustration of band bending in order for the E_F to stay flat under equilibrium. The example given is a plasmonic metal and semiconductor nanoparticle decorated TiO_2-based photocatalysts. Reproduced from ref.[31] with permission.

2.3.3 Photovoltaic Action

When light is absorbed by the intrinsic layer material, an electron-hole pair is generated. The electron-hole pair is separated by the electric field across the intrinsic region and can only survive for an amount of time equal to the charge carrier lifetime (τ). If the electrons and holes are not collected by an external circuit within this lifetime, then the charge carriers will recombine and the current/ power from them will be lost. The charge carriers that make it to the electrode and are successfully extracted will contribute to the measured current. In that case, the holes flow to

the p-contact, whereas, the electrons flow through the external circuit and recombine with the holes at the p-contact. The effect of light is to "shift" the dark J-V curve from the first quadrant downward to the fourth quadrant (Figure 2.5), effectively increasing the negative current and generating energy. Illuminating the cells adds the illuminated current onto the dark current, following the diode equation:

$$I = I_0[exp(\frac{qV}{nkT}) - 1] - I_L \tag{2.10}$$

Where I_L is the current generated under illumination and n is the ideality factor. The ideality factor can range from 1 to 2. An ideality factor close to 1 shows mostly bimolecular recombination or trap-assisted recombination in the bulk material, whereas, an ideality factor greater than 1 can happen under Auger recombination (n=2/3) or trap-assisted recombination under high-intensity illumination. The effect of the ideality factor greater than 1 is to reduce the fill factor.

The short-circuit current density (J_{sc}) is the photogenerated current density when no voltage is applied and the Fermi level is constant at the junction. It is the J-V curve interception with the y-axis. The open-circuit voltage (V_{oc}) is the voltage at which the applied voltage cancels out the V_{bi}. It is the J-V curve interception with the x-axis (see Figure 2.5). When the applied voltage keeps on increasing towards V_{oc}, the light-generated current exactly balances the forward bias diffusion current and there is no net current flow.

The fill factor (FF) is defined by the power at the maximum power point, P_{Max}, over $V_{oc} \cdot J_{sc}$

$$FF = \frac{V_{MPP} \cdot J_{MPP}}{V_{oc} \cdot J_{sc}} \tag{2.11}$$

Where V_{MPP} and J_{MPP} are the voltage and current density under maximum power point conditions. It is the largest "rectangle" that can be fit under the J-V curve (see Figure 2.5).

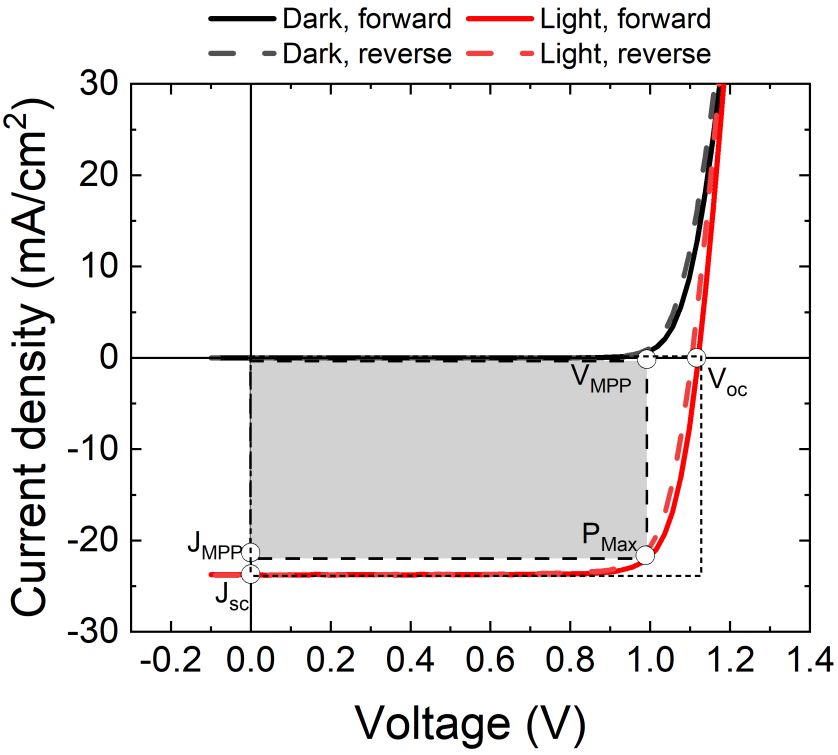

Figure 2.5: Example solar cell J-V curve (from a real device) with properties highlighted.

$$P_{Max} = FF \cdot V_{oc} \cdot J_{sc} \tag{2.12}$$

The power conversion efficiency (η_{MPP}) is the fraction of incident energy (P_{in}) converted to power (P_{Max}). It is given by

$$\eta_{MPP} = \frac{FF \cdot V_{oc} \cdot J_{sc}}{P_{in}} \tag{2.13}$$

The presence of series resistance (R_s) and shunt resistance (R_{sh}) have the effect of lowering the η_{MPP} by reducing the J_{MPP} and V_{MPP}.

For a given semiconductor with bandgap, E_g, the Shockley-Queisser limit gives the theoretical maximum solar energy conversion efficiency for that E_g. The calculation assumes that all photons with energy above E_g are absorbed and all charge carriers are collected [32]. In reality, not all photons with energy above E_g are absorbed, as some are reflected or transmitted (due to the film being too thin). Not all charge carriers

are collected, as some recombine before they are collected. The external quantum efficiency (EQE) is the ratio of the number of charge carriers collected by the solar cell to the number of incident photons at a certain wavelength. Likewise, internal quantum efficiency (IQE) is the ratio of the number of charge carriers generated to the number of photons absorbed.

2.3.4 Multi-junction Solar Cells

Even in an idealized situation, the η_{MPP} is limited by the Shockley-Queisser limit. Moreover, a solar cell with a certain E_g always has some losses because for a low E_g semiconductor, high energy photons would thermalize to the E_c edge, "wasting" energy, and a high E_g semiconductor would not be able to absorb lower energy photons. Hence, a multi-junction solar cell, called a tandem solar cell, can be fabricated to increase the absorption from the solar spectrum. The advantage of having a tandem solar cell is that sub-cells with different E_g can be optimized to absorb a different spectrum of light and then combined to maximize the overall efficiency. The idea is that light is incident on the higher E_g semiconductor first and the sub-cell would absorb the higher energy portion of the solar spectrum. Then the longer wavelength light would pass through a lower E_g semiconductor and the sub-cell would absorb the remaining lower energy light, as shown in Figure 2.6 (a) and (b).

There are mainly two designs for tandem solar cells: two-terminal (2-T) and four-terminal (4-T), as shown in Figure 2.6 (c). In a 2-T tandem solar cell, the sub-cells are connected monolithically by a recombination layer, and a second sub-cell is fabricated on top of the first sub-cell. In a 4-T tandem solar cell, the sub-cells are connected separately through an external circuit so the sub-cells are fabricated on separate substrates and operate independently. The sub-cells are only physically stacked on top of one another. The 2-T configuration has only two contacts and one needs to be semi-transparent. Since the two sub-cells are electrically connected, it requires current-matching of the top and bottom sub-cells. In comparison, since the

4-T tandem solar cell requires four contacts, of which three must be semi-transparent, there are more optical losses due to parasitic absorption of semi-transparent layers.

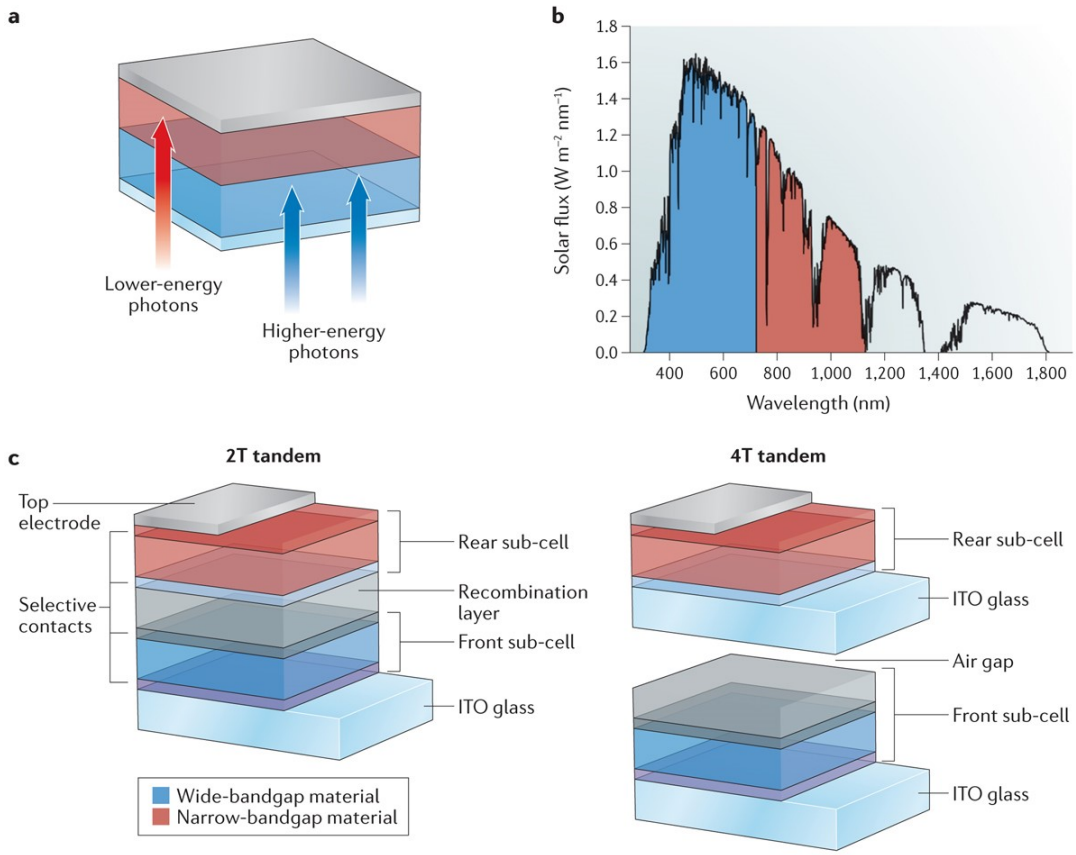

Figure 2.6: (a) Tandem solar cell concept, where higher-energy photons are absorbed from the wider-bandgap semiconductor (in blue) and lower-energy photons can be absorbed by the narrower-bandgap semiconductor (in red). (b) Solar irradiance spectrum showing the spectral regions over which the two semiconductors could absorb. (c) Diagram of the architecture of two-terminal (2-T) and four-terminal (4-T) tandem solar cells. (a) and (b) are reproduced from reference [33], Nat Rev Chem. (c) is reproduced from reference [34], AAAS.

2.4 Metal Halide Perovskite Solar Cells

Metal halide perovskite solar cells (PSCs) are a class of emerging thin-film solar cells. The efficiencies of PSCs have increased from 3.8% [35] when they were first made in 2009 to a record 25.7% by 2022 [16], making their efficiency competitive with silicon PV technology. PSCs also have the advantage of potentially lowering the fabrication cost compared to other PV technologies, as the entire device stack can

be blade-coated [36, 37], slot-die coated [38, 39], or evaporated [40, 41], requiring relatively low temperatures. It is compatible with large-scale roll-to-roll processing. Additionally, metal halide perovskite has a tunable E_g and the E_g can be easily tuned by changing the composition. This allows them to be integrated into perovskite/perovskite, perovskite/silicon, perovskite/organic, or perovskite/CIGS tandem solar cells to overcome the single junction limit. However, the main challenge for the commercialization of metal halide PSCs is their stability and large-scale uniformity. When the device area increases, it is more likely to get more pinholes and defects, increasing the likelihood of shunts and reduced V_{oc}. A typical silicon solar cell can last up to 20 years without much efficiency lost, whereas perovskite solar cells are less environmentally inert and some of the most stable ones are only stable up to 10,000 hours ($>$400 days) [42] when well encapsulated. In this thesis, I attempt to address some issues relating to metal halide PSC stability.

2.4.1 Architecture

Most metal halide PSCs are fabricated as an intrinsic region (i) with p- and n-type extraction layers. The photo-absorption happens in the intrinsic region rather than the doped p and n regions. The p-i-n architecture is better for long wavelength absorption since the perovskite layer can be made several hundreds of nanometers thick, increasing the quantum efficiency (QE). Long-wavelength light just above the E_g has a higher chance of being absorbed and generates electron-hole pairs deep into the perovskite layer. Owing to long charge carrier lifetimes and diffusion lengths (up to $\sim$1 µm) of perovskites [43], most charge carriers can reach the charge extraction layers before recombining. The p- and n-type layers are only responsible for extracting holes and electrons, respectively.

2.4.2 Working Principle

When light is illuminated on a PSC, the perovskite absorbs the frequencies of light with photon energies equal to or greater than its E_g, and the absorbed energy generates an exciton (a bound electron-hole pair). The exciton dissociates into an electron and hole by the electric field in the intrinsic region. The electrons in the E_c of the perovskite get injected into the E_c of the electron-transporting layer (ETL) and then transported through the layer to reach the fluorine-doped tin oxide (FTO) or indium tin oxide (ITO) substrate. On the other hand, holes in the E_v of the perovskite get injected into the E_v of the HTL and transported through the layer to the metal contact. The electrons flow through the external circuit to the counter electrode (cathode) where it recombines with the holes.

2.4.3 n-i-p vs p-i-n Perovskite Solar Cells

Most metal halide perovskite solar cells have either the regular architecture, negative-intrinsic-positive (n-i-p) (planar or mesoporous) or inverted architecture, positive-intrinsic-negative (p-i-n) (planar or mesoporous) (Figure 2.7). For an n-i-p device, the light is incident through the ETL, whereas, in a p-i-n device, the light is incident through the hole-transporting layer (HTL). As mentioned previously, metal halide perovskite is an ambipolar material that has a high absorption coefficient and long carrier-diffusion lengths. Thus, the transport layers are solely used to conduct electrons and holes that are extracted from the perovskite layer. In the early days when solid-state perovskite solar cells just emerged, they had the mesoporous n-i-p structure with TiO_2 as the mesoporous scaffold (Figure 2.7 a). This architecture was borrowed from the dye-sensitized solar cells (DSSCs) structure before the perovskite material was known to have a long enough diffusion length for charge carriers to reach the contacts; therefore, a mesoporous metal-oxide and perovskite blend was used to increase the ETL/perovskite contact area and reduce the distance that charge carriers

have to travel to reach the contacts. Later studies with an insulating mesoporous Al_2O_3 [44, 45] (Figure 2.7 b) and planar heterojunction PSC architectures showed that electrons and holes can be transferred within the perovskite film itself and semiconducting scaffolds are unnecessary [46]. More recently, the planar architecture has been used more frequently, especially as SnO_2 (used in the planar architecture) was found to be a more UV-stable material than TiO_2 (used in the mesoscopic architecture). In fact, the latest record PSC of efficiency 25.7% was a planar n-i-p device. For planar solar cells, there are also the n-i-p (Figure 2.7 c) and p-i-n (Figure 2.7 d) architectures. The two architectures apply different materials as the electron and hole selective layers due to different energy level alignments and practical processing readability considerations. Some of the reasons why the architecture cannot just be flipped are because of the processing temperatures limitations (eg. metal oxides cannot be processed on top of a perovskite because they require high temperature) and the transparency of the materials (whichever faces the light needs to be transparent, while whichever is on top can be absorbing). In a typical planar n-i-p PSC, FTO or ITO is used as the substrate. TiO_2 or SnO_2 is used as the ETL due to both their n-type transporting property and their resistance to perovskite solvents. Above the ETL is the perovskite layer. On top of the perovskite layer is the HTL. Common HTL materials used for n-i-p are 2,2',7,7'-tetrakis[N,N-di(4-methoxyphenyl)amino]-9,9'-spirobifluorene (Spiro-OMeTAD), Poly(3-hexylthiophene) (P3HT), and poly[bis(4-phenyl)(2,4,6-trimethylphenyl)amine] (PTAA) due to their suitable band-energy alignment and solvent orthogonality with the perovskite solvents. The top electrodes are usually metals such as Au, Ag, or Cu. MoO_x/Al was also reported to enhance stability [47].

On the other hand, for a p-i-n device, FTO or ITO are also used as the substrate. An inorganic HTL material used is NiO_x and common organic materials used are polymers such as PTAA, Poly[N,N' -bis(4-butylphenyl)-N,N' -bis(phenyl)-benzidine] (Poly-TPD), and poly (3,4-ethylenedioxythiophene) polystyrene sulfonate (PEDOT:PSS). Polymer materials are used as the bottom HTL because they are

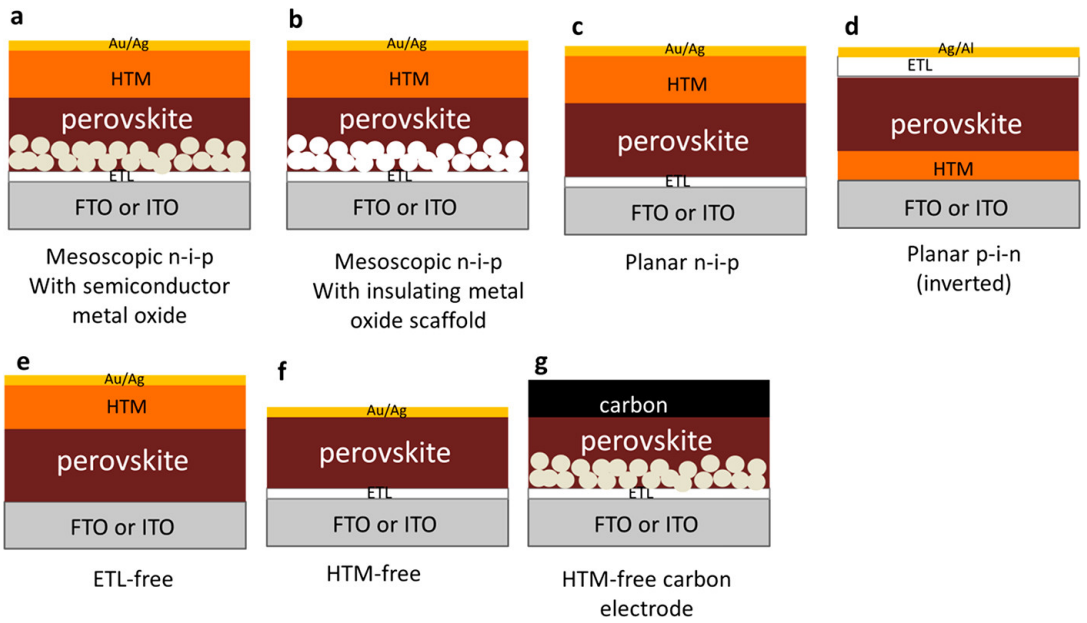

Figure 2.7: Variety of device architectures for perovskite solar cells. Reproduced with permission from reference [46].

more perovskite-solvent resistant than small organic molecular HTLs. Common ETL materials used are fullerene derivatives such as $PC_{61}BM$ and C_{60}, mainly due to their solvent orthogonality to perovskite, high electron affinity, and high electron mobility [48]. Electrode materials used are similar to that of n-i-p, Au, Ag, and Cu, but often to achieve more stable devices, Cr/Au electrodes or sputtered zinc-doped indium oxide (IZO) or ITO can be used.

2.4.4 Surface and Interface Recombination

Most of the charge carriers are generated close to the surface as the penetration depth of perovskite materials is typically 20 nm$\sim$200 nm for UV-vis light ($\lambda = 100 \sim 800$ nm). Moreover, the absorber material surface has more defects than the bulk since there is a disruption to the crystal lattice, high doping in the HTL/ETL, and dangling bonds that either act as traps or recombination centers. Thus, most of the non-radiative recombination losses of perovskite solar cells come from interfacial or surface recombination [49, 50]. The quantum efficiency at short wavelengths ($<$350 nm) is very low due to the high front surface recombination rate and the QE is also low

at long infrared wavelengths due to back surface recombination. Charge carriers generated near the surface will quickly recombine. Moreover, the high-defect density and charge-trapping at the interface make the surface chemically reactive and initiates degradation. Therefore, finding suitable interfacial passivation is becoming crucial for further improving the efficiency and stability of PCSs.

2.5 Perovskite Material as a Photo-absorber

2.5.1 Perovskite Structure

Unlike most solar cell materials such as silicon and III-V's, the perovskite structure is not covalent but ionic. The typical perovskite structure is given by the formula ABX_3, where A is a cation, such as formamidinium ($HC(NH_2)^{2+}$), methylammonium ($CH_3NH_3^+$), and Cs^+. The B site is a metal which has 6-side coordination with anions (such as Pb^{2+}, Sn^{2+}, Ge^{2+}, Bi^{2+}). The X can be a halide or other anion that fits into the octahedral lattice. The superior optical properties of perovskite arise from its direct bandgap, high optical absorption coefficient ($\sim 10^5$ cm^{-1}) [51], and long diffusion lengths ($\sim$1 µm) [43, 52]. These properties originate from direct bandgap p-p transition enabled by the Pb lone-pair s orbitals, perovskite symmetry, and strong antibonding coupling between Pb lone-pairs and I p orbitals [53]. The valence bands of lead halide perovskite are mainly halogen p orbitals mixing with a small component of Pb s states. The conduction bands are mainly derived from unoccupied Pb p orbitals [46, 53] (see Figure 2.8).

The bands of MHP are preferable to both Si and GaAs because it is a more efficient transition (see figure 2.9). Si has an indirect bandgap, so it requires the assistance of an optical phonon for the energy transition. GaAs has a direct bandgap but its valence band arises from the p orbital of As and the conduction band from the s orbitals of Ga and As, and since there is less overlap between an s-p orbital compared to a p-p orbital, there is less coupling and it is more dispersive. The p-p

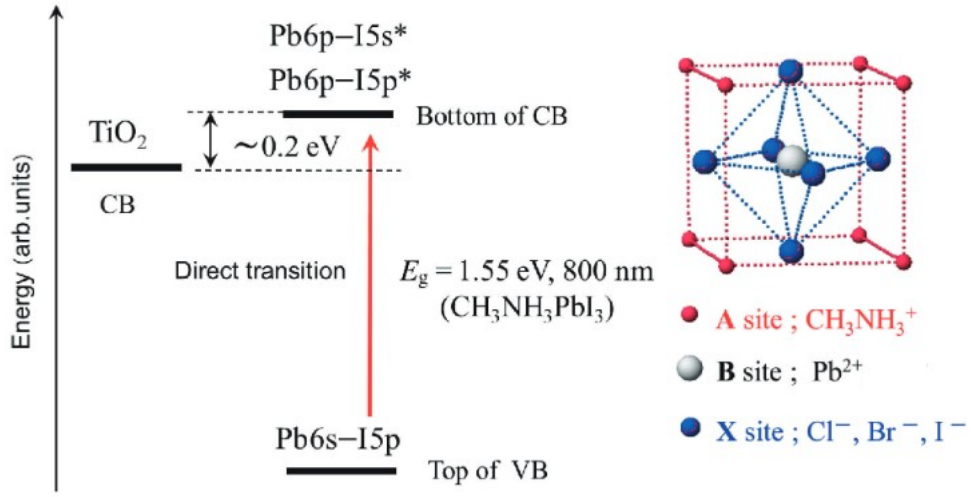

Figure 2.8: Band energy levels and structure of $CH_3NH_3PbI_3$. Reproduced with permission from reference [44]

transition can only arise from elements that have lone pair s electrons. MHP is ideal because it has the advantages of both p-p transition and a direct bandgap. Therefore, the Pb lone-pair s orbitals and high symmetry give rise to a high optical absorption coefficient [53]. Due to the low loss in energy transition, lead halide perovskite has higher theoretical V_{oc} and PCE compared to conventional semiconductors like Si and GaAs. In lead halide perovskite, the effective mass of holes is smaller than that of electrons, which is different from p-s semiconductors. As a result, the transfer of electrons and holes is well-balanced.

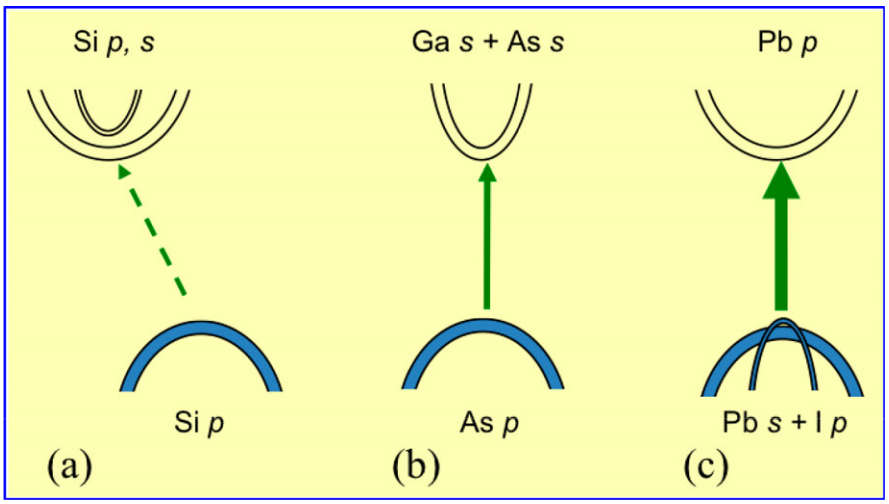

Figure 2.9: Schematic optical absorption of (a) Si, (b) GaAs, and (c) $CH_3NH_3PbI_3$ perovskite. Reproduced with permission from reference [53].

2.5.2 Defect Tolerance

Many defects can exist in crystalline materials. Defects can be categorized by their dimensionality. Point defects include vacancies, interstitials, substitutions, Frenkel, and Schottky defects. Vacancies occur when a normally occupied atomic site is missing an atom. Unfortunately, it is not possible to eliminate vacancy defects in crystalline materials, because according to thermodynamics, the presence of vacancies increases entropy in the crystalline material. Interstitials, on the other hand, arise when extra atoms are crowded into small void spaces that are not normally occupied. In substitutional defects, atoms or ions are replaced by impurity species. Frenkel defects happen when an atom leaves its place in the lattice and becomes an interstitial, meanwhile, leaving a vacancy behind. Schottky defects forms when a pair of oppositely charged ions leave their lattice sites and create oppositely charged vacancies. Line defects are one-dimensional imperfections that occur along a line in the crystal lattice. The most common type is dislocation, including edge dislocation, resulting from an extra half-plane of atoms inserted into the lattice structure, and screw dislocation, when there is a shear distortion along a plane in the lattice. Two-dimensional defects include grain boundary defects and surface defects. Grain boundary defects occur between two

grains with likely the same chemical composition and crystal structure but with different crystallographic orientations. Surface defects occur at the boundaries between the crystal and a foreign material or external environment. They can influence surface energy and reactivity. Lastly, volume defects involve three-dimensional irregularities within the bulk of the crystal, including voids and cracks.

These defects can influence the ionic conductivity of a solid. In crystalline solids, defects provide pathways for ion migration. Vacancies create vacant sites that the ions can occupy, therefore, facilitating their movement. On the other hand, interstitials can obstruct ion movement by creating barriers or distortions in the lattice, thereby reducing ionic conductivity. Substitutional defects involve impurity ions that can lead to enhanced ionic conductivity if they have higher mobility compared to the host ions. For example, it can occur when impurity ions are smaller in size, allowing for easier ion movement. Grain boundary defects can create additional pathways for ion transport, increasing ion conductivity, but there can also be grain boundary defects that hinder ion movement. For example, ions can be trapped at the grain boundaries, inhibiting their diffusion [54]. Overall, defects have a significant effect on the ionic conductivity of crystalline solids, thus, controlling defect formation becomes crucial for reducing nonradiative recombination and limiting ion migration in perovskite solar cells.

Due to their soft ionic nature, lead halide perovskites are more defect-tolerant. Their defect states are either shallow near the band edge or reside within the bands and are therefore benign. Instead of causing electron-hole recombination, these trap states will only temporarily trap charge carriers. The defect states with low formation energy, such as I vacancy or Pb dangling bond, have shallow defect states close to the E_c minimum and E_v maximum. Whereas, deep defect states that can form come from Pb-p, Pb-p or I-p, I-p wrong bonding or I_{Pb}, I_{MA}, Pb_i, and Pb_I, which have high formation energies [53].

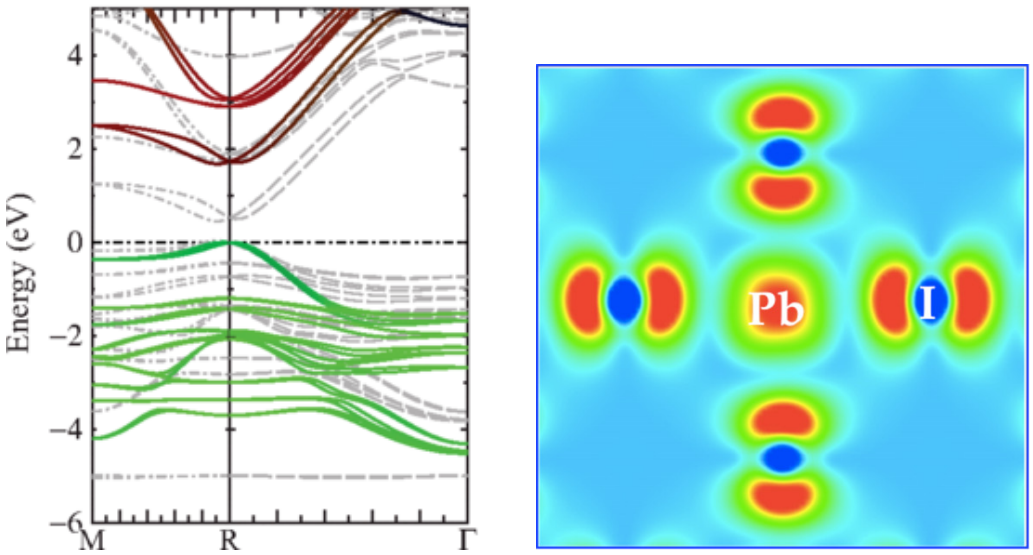

(a) (b)

Figure 2.10: (a) Quasiparticle Self-consistent GW (QSGW) Electronic structure of $CH_3NH_3PbI_3$. Zero denotes the valence band maximum. Bands are colored according to their orbital character: green depicts I 5p, red depicts Pb 6p, and blue depicts Pb 6s. Points denoted M and R are zone-boundary points close to $(\frac{1}{2},\frac{1}{2},0)$ and $(\frac{1}{2},\frac{1}{2},\frac{1}{2})$, respectively. Reproduced with permission from reference [55]. (b) PbI_2 bonding. Reprinted (adapted) with permission from [53]. Copyright 2015 American Chemical Society.

2.5.3 Bandgap Tunability

One advantage of lead halide perovskite over other conventional PV absorber materials is their E_g tunability. By changing the A-site, B-site cations, or anion X, the E_g can be adjusted in a wide range, from the narrowest Sn-based perovskite of 1.22 eV [56] to wide-bandgap Cs and Br-rich perovskites of over 2.00 eV [57]. The bandgap tunability allows easy integration of PSCs into tandem solar cells. As mentioned previously, the perovskite $E_{c,min}$ and $E_{v,max}$ are mainly determined by the Pb and I orbitals [53]. The Pb-I octahedral framework, therefore, determines the E_g. The organic cation sitting in the middle of the cage provides charge compensation. However, the cation still influences the E_g by causing lattice contraction/expansion or tilting of the BX_3 octahedra [58]. For example, small cations like Cs^+ causes the lattice to contract, which pulls the Pb-I bonds closer together and thus increases the E_g, whereas large cations like FA^+ cause lattice expansion and reduces the E_g. Similarly, changing the

halide from I^- to Br^- increases the E_g due to the smaller ionic radii of Br^- compared to I^-.

Substituting some Pb with Sn first narrows the E_g reaching a minimum at ∼40∼60% Sn and then increases the E_g again when Sn content is further increased up to 100% Sn [59]. This is called the "bandgap bowing" effect which defies Vergard's law. The E_g is determined by

$$E_g(x) = (1-x)E_g(x=0) + xE_g(x=1) - bx(1-x) \tag{2.14}$$

Where b is the bowing parameter which describes how strong the band bowing is. The reason for this bandgap bowing is still under debate. One hypothesis is that the band structure of Sn is similar to that of Pb. However, ab initio calculations at DFT, hybrid DFT and QSGW [60] have shown that the $E_{v,max}$ and $E_{c,min}$ energy levels for Sn are shallower than that of Pb. Thus, in the mixed Pb-Sn system, the $E_{c,min}$ would consist of Pb-I orbitals, and the $E_{v,max}$ would consist of Sn-I orbitals, which narrows the E_g and gives rise to a bowing parameter of 1.08.

Since Pb-based perovskite can only give bandgaps as low as 1.48 eV, which is slightly higher than the Schockley-Queisser ideal E_g of ∼1.34 eV [61], alloying Pb with Sn can help achieve a lower bandgap that is closer to the ideal E_g.

Different E_g solar cells can be put together to make either two-terminal monolithic solar cells or four-terminal tandem solar cells. Each bandgap can then absorb a different range of the solar spectrum and be added together so that it is no longer bound to the theoretical Schockey-Queisser limit of 33%. By exploiting the bandgap tunability of perovskite material, monolithic perovskite/silicon tandem solar cells have achieved a record efficiency of 32.5% [16] and all-perovskite tandem solar cells achieved a record of 27% by December 2022 [62].

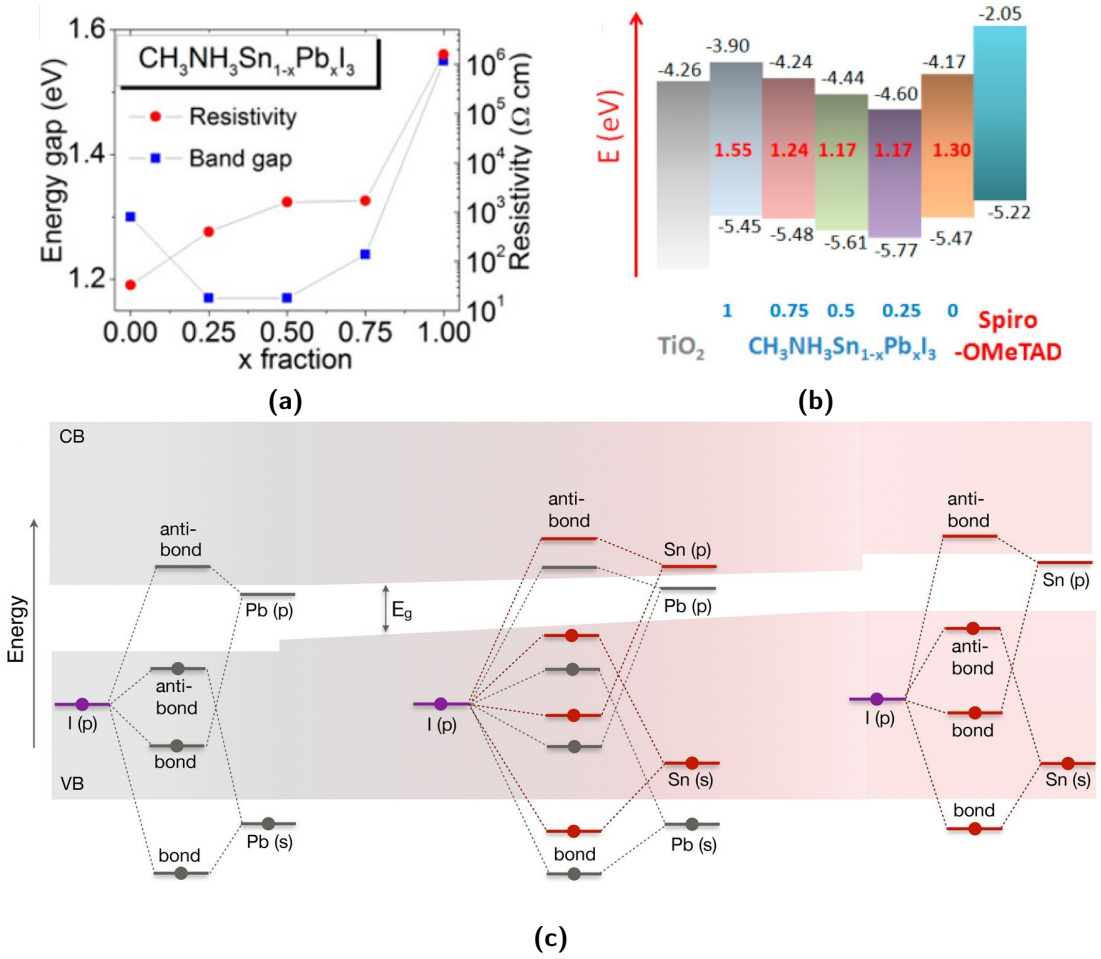

Figure 2.11: Anomalous bandgap behavior (bowing effect) of Pb-Sn mixed perovskites as seen by (a) plot of energy gap vs. fraction of Pb, (b) schematic diagram showing the E_c and E_v levels and corresponding bandgap values. a) and b) reprinted (adapted) with permission from [59]. Copyright 2014 American Chemical Society. (c) Schematic summarizing the origin of the band gap bowing in MA(Pb1–xSnx)I_3. Shaded regions represent the valence and conduction bands with thick lines showing the molecular orbital picture of the formation of electronic bands in the alloy. Reprinted (adapted) with permission from [60]. Copyright 2018 American Chemical Society.

2.6 Stability of Planar n-i-p PSCs

2.6.1 Material Instability

As mentioned previously, PSCs in general are less stable than other PV technologies. Planar n-i-p devices especially have worse stability compared to their p-i-n counterparts. This can be due to many reasons. The n-type layer in the regular architecture (usually metal-oxide) could be less stable than the organic n-type materials used in

p-i-n (C_{60}, $PC_{61}BM$, etc.). Originally, compact TiO_2 and mesoporous TiO_2 were used as the ETL for n-i-p. However, TiO_2 was found to be unstable under UV light illumination [63]. An alternative ETL material is ZnO. It has an appropriate energetic alignment, high electron mobility, and high transmittance in the visible light range. However, perovskite processed on the ZnO surface is found to be thermally unstable [64]. The thermal instability stems from the basic nature of ZnO and an acid-base reaction can happen once the perovskite is in contact with the ZnO [65, 66]. SnO_2 was introduced as an ETL to improve the UV and thermal stability.

Aside from the ETL, the top HTL used is also considered unstable. The commonly used HTL in n-i-p devices with the best performance is a small organic hole transport material, 2,2',7,7'-tetrakis(N, N-di-p-methoxyphenylamine)-9,9'-spirobifluorene (Spiro-OMeTAD). Spiro-OMeTAD has a low glass-transition temperature (T_g) of 125°C [67]. Long-term operation under temperature close to its T_g can degrade the material. Moreover, iodine migration was found to cause doping in the HTL which creates trap states in the HTL and interface [68]. The deeper highest unoccupied molecular orbital (HOMO) level HTLs are more resistant to iodine doping [69]. Spiro-OMeTAD, however, has a relatively shallow HOMO level of 5.20 eV compared to other HTMs such as PTAA (5.40 eV). Pristine Spiro-OMeTAD also has poor conductivity and doping, or pre-oxidizing is necessary for it to work as an HTL. The common dopants added to Spiro-OMeTAD are lithium bis(trifluoromethanesulfonyl)imide (Li-TFSI), 4-tert-butyl pyridine (tBP), and Tris [4-(tert-butyl)-2-(1H-pyrazol-1-yl)pyridine] cobalt(II) bis(trifluoromethanesulfonimide) (Co(III)-TFSI or FK209). Li-TFSI was found to cause instability due to its hygroscopic nature [70] and Li-ion migration [71]. tBP was also believed to de-dope Spiro-OMeTAD and erode the perovskite surface [72, 73, 74]. Hence, finding stable alternative HTL and ETL materials that do not require doping (or contain stable dopants) becomes important for enhancing the stability of n-i-p PSCs.

2.6.2 Mechanical Instability

In addition to the thermal and light stability of the ETL, the residual strain that comes from processing "soft" perovskite on a "hard" metal oxide surface under high temperature induces strain that has to be relaxed in the perovskite grains when it cools down [75]. This is due to the thermal expansion coefficient (TEC) mismatch of the two materials [76, 77]. Residual strain can induce degradation through delamination of the perovskite grain from the substrate, creating cracks and voids [78, 79].

Fabricating perovskite films on substrates with different thermal expansion coefficients can either induce or relax the strain in the perovskite lattice [75]. If perovskite is fabricated on a material with a higher TEC, then when the stack cools down after annealing, the substrate will induce compressive strain to the perovskite lattice; if the perovskite is fabricated on a material with a lower TEC, then when the stack cools down, the substrate will induce tensile strain to the perovskite lattice [80]. Studies have shown that while tensile stress causes cracks and delamination which accelerates perovskite degradation, compressive stress suppresses cracks and delamination, improving the perovskite stability [78, 81, 82].

In comparison, for a p-i-n device, the first layer processed on the substrate is usually a polymer material, which has a larger TEC than perovskite, whereas, a metal oxide has a lower TEC than perovskite [80]. Therefore, when perovskite films are processed on substrates at an elevated temperature, there is a residual compressive strain for p-i-n devices, whereas, there is a residual tensile strain for n-i-p devices. As a result, the tensile strain in n-i-p devices accelerates their degradation, and n-i-p devices aged under light and elevated temperatures without any ETL/perovskite interlayer modification often show voids, cracks, and delamination [83, 84, 85].

2.6.3 Ion Migration

Metal halide perovskites are often susceptible to ion migration. In particular, I^-, Br^-, and Cl^- species can diffuse and form vacancies over time. Iodide reacts to form iodine and can leave the perovskite in the form of iodine vapor. Ion migration is especially pronounced under illumination. For mixed-halide wide-bandgap perovskite, photoinduced halide segregation is observed to occur on the order of seconds to minutes.

The typical PSC metal contacts such as gold can migrate through the HTL into the perovskite layer at temperatures as low as 70°C [86]. Following gold migration, the degradation products of perovskite which formed iodine/iodide species will react with gold to form AuI_2 and AuI_3 [87]. Gold can further react with other halide species to form $AuCl_3$, $AuBr_3$ and AuI [88]. Other more reactive metal contacts such as Ag can accelerate the degradation of the perovskite and form PbO, PbI_2, and AgI [89].

Aside from materials and mechanical concerns, one reason for the worse stability of n-i-p solar cells under open-circuit conditions might be that there is inherently a difference in the architecture. While n-i-p devices are illuminated from the n-type charge selective contact, the p-i-n devices are illuminated from the p-type contact. For n-i-p, this biases the direction of I^- ion migration towards the top hole-transporting layer where it can escape as I_2 [90, 91, 92, 93]. Whereas, it is speculated that for a p-i-n under open circuit conditions, iodine cannot escape so readily as the p side is the substrate side. This is hypothesized because from our group's experience, an n-i-p device with stable charge-selective contacts degrades at a similar rate as a p-i-n device under dark, elevated temperature (85°C) conditions. However, under illumination at open circuit conditions, where ion migration is accelerated [94, 95], our n-i-p devices degrade faster than p-i-n devices.

2.7 The Role of Additional Amine in Perovskite

Amine additives or surface modification have long been used to improve the grain size and crystallinity of perovskite [96, 97]. Sometimes, it is used to create surface 2D phases to passivate the surface and grain boundaries [98]. Other times, they are used as ligands to "anchor" on the grain boundaries and increase the (001) orientation [99]. Amines can potentially play many roles in perovskite, including N-alkylation with other organic perovskite cations, such as formamidinium (FA^+) and methylammonium (MA^+). For example, in solution, methylamine generated from deprotonated methylammonium iodide reacts with formamidinium to form N-methyl FAI and N,N'-dimethyl FAI within 24 hours [100, 101]. On a perovskite film, Jiang et al. used 3-(aminomethyl)pyridine (3-APy) as a perovskite surface treatment and found that 3-APy reacts with FA to form N-(3-methylpyridine)formamidinium ($MPyFA^+$) passivating the surface [102]. The result is the formation of ammonia and a new amine which can further react with another acidic alkylammonium.

Aside from alkylation, the presence of Pb^{2+} complicates the matter, as Pb^{2+} is a soft Lewis acid that can react with the basic amine. Amine can assist in dissolving PbI_2 as it is more strongly coordinated to Pb than other common perovskite solvents such as dimethylformamide (DMF) and dimethyl sulfoxide (DMSO). As a result, an alkylammonium salt and Pb-alkylamide (Pb(II)-NHR) can form after solution aging [103]. These roles that amines play not only affect the precursor solution, but also may affect the crystallization process to obtain the final polycrystalline metal halide perovskite film. The new organic species formed in the solution can either co-crystallize in the precursor phase and then subsequently be lost (such as methylamine), or stay in secondary phases that are retained in the end material (such as benzylamine or ethylenediamine). In chapter 5, I will discuss this in more detail in the case of using benzylamine as a bulk passivation.

2.8 The Structure of This Thesis

In this thesis, I will attempt to address some of the long-term stability issues, particularly in regular n-i-p architecture devices.

Following the general introduction given in this and the preceding chapter, in **Chapter 3**, I will give a summary of the experimental methods used in the projects to follow.

In **Chapter 4**, I will introduce a pair of new carbazole-based enamine hole-transporting materials (HTMs). These small organic molecular HTMs have high mobility and conductivity even without dopants, which makes them cheap and easy to process. Additionally, they have enhanced stability compared to a more established material, Spiro-OMeTAD. The syntheses of these materials are also facile and require inexpensive materials, reducing the cost by ten-fold compared to Spiro-OMeTAD.

In **Chapter 5**, I will discuss modifying the perovskite absorber layer with amine passivation to improve performance and stability. In particular, I will look into a wide-bandgap (1.68 eV) methylammonium-free perovskite for stable integration into silicon/perovskite tandem solar cells. In this chapter, the detailed mechanism of how the amine additive reacts with the perovskite cation to form new products and phases in-situ will be investigated. This understanding is generalizable to other types of monoamine passivation.

In **Chapter 6**, I will move on to present a new n-type self-assembling monolayer, C_{60}-phosphonic acid (C_{60}-PA) SAM, as a surface modifier to the ETL. C_{60}-PA passivated the SnO_2 surface and improved the voltage and efficiency of n-i-p solar cells. C_{60}-PA can also slightly improve the charge-transfer efficiency. The solar cell hysteresis was also reduced by applying this surface modification. Although the performance of the device is improved with the C_{60}-PA modification, the stability is worsened. I will delve into why the interface is less stable. Lastly, I will present the stability result of the most stable n-i-p architecture I have thus far.

In **Chapter 7**, I will summarize the findings of my research. Future research directions will be proposed to better understand the origin of the instability of perovskite solar cells and improve them for commercial applications.

CHAPTER 3

Experimental Methods

3.1 Synthesis of Materials

3.1.1 Syntheses of MeO5PECz and MeO4PEBCz

The syntheses of MeO5PECz and MeO4PEBCz are reported in reference [104]. Briefly, MeO5PECz and MeO4PEBCz are synthesized through the reflux and re-crystallization methods.

N3, N3, N6, N6, 9-pentakis [2,2-bis (-methoxyphenyl) ethenyl] -9H-carbazole-3, 6- diamine (MeO5PECz): a mixture of 9H-carbazole-3,6-diamine (0.5 g, 2.5 mmol), 2,2-bis(4-methoxyphenyl)acetaldehyde (4.06 g, 15.8 mmol) and camphor-10-sulfonic acid (β) (0.59 g, 2.5 mmol) were dissolved in THF (10 ml + volume of the Dean-Stark trap ml), 3Å molecular sieves were added to absorb water. The mixture was heated under an argon atmosphere for 8 hours at reflux. Afterwards, the reaction mixture was cooled to room temperature and poured into 200 ml of ethanol. The precipitate was filtered and washed with 200 ml of ethanol and then

crystalized from acetone, resulting in yellow crystals of MeO5PECz (m.p. 187-189°C). Yield: 2.05 g (58 %).

N3, N3, N6, N6, 9-tetrakis[2,2-bis(-methoxyphenyl)ethenyl]-9-butyl-9H-carbazole-3,6-diamine (MeO4PEBCz): a mixture of 9-Butyl-9H-carbazole-3,6-diamine (1 g, 3.9 mmol), 2,2-bis (4-methoxyphenyl) acetaldehyde (5.0 g, 19.7 mmol) and camphor-10-sulfonic acid (β) (0.9 g, 3.9 mmol) were dissolved in toluene (10 ml + volume of the Dean-Stark trap ml). The mixture was heated for 1 hour at reflux. Afterwards, the reaction mixture was cooled to room temperature and extracted with ethyl acetate. The organic layer was dried over anhydrous Na_2SO_4, filtered, and then the solvent was removed. The crude product was washed with hot ethanol giving green crystals, which were then recrystallized from a mixture of THF and ethanol (1:1), resulting in yellowish crystals of MeO4PEBCz (247-249°C). Yield: 2.31 g (49 %).

3.1.2 Synthesis of C60-Phosphonic Acid Self-Assembling Monolayer

The synthesis of C_{60}-phosphonic acid SAM is reported elsewhere in reference [105].

3.2 Device Fabrication

3.2.1 Materials

Tin(II) chloride dihydrate (99.995%), urea (≥98%), hydrochloric acid (37%), thioglycolic acid (≥99%), potassium chloride (KCl), n-octylammnonium bromide, n-hexylammonium bromide and phenethylammonium iodide (PEAI) were purchased from Sigma-Aldrich. Ultrapure water was purchased from Cambridge Bioscience. Formamidinium iodide (FAI) (99.999%) and methylammonium chloride (MACl) were purchased from Dyenamo. Methylammonium bromide (MABr) was purchased from

Xi'an Polymer Light Technology Corp. Lead(II) iodide (PbI_2) (99.999%) and cesium iodide (CsI) (>99.999%) were purchased from Alfa Aesar. Lead(II) bromide ($PbBr_2$) (>98.0%) was purchased from TCI. 4-methoxy-phenethylammonium iodide (MeO-PEAI) was purchased from GreatCell Solar Materials. 2,2',7,7'-tetrakis(N,N'-di-p-methoxyphenylamine)-9,9'-spirobifluorene (Spiro-OMeTAD) (>99.5%) was obtained from Luminescence Technology Corp. Poly[N,N' -bis(4-butylphenyl)-N,N' -bis(phenyl)-benzidine] (Poly-TPD) was purchased from Luminescence Technology Corp. Poly[bis(4-phenyl)(2,4,6-trimethylphenyl)amine] (PTAA) (Mn = ∼17,500 g/-mol) was purchased from Flexink. $PC_{61}BM$ (99.5%) was purchased from Solenne. Bathocuproine ($C_{26}H_{20}N_2$ > 98%) was purchased from TCI Chemicals. Lithium bis-(trifluoromethanesulfonyl)imide (Li-TFSI, >99%), 4-tert-butylpyridine (tBP, 98%), Isopropanol (IPA, 99.5%), N, N-dimethylformamide (DMF, anhydrous 99.8%), dimethyl sulfoxide (anhydrous DMSO, >99.9%), anisole (anhydrous, 99.7%), chlorobenzene (CB, 99.8%), acetonitrile (ACN, anhydrous 99.8%), Al_2O_3 nanoparticles (20 wt.% in isopropanol) were purchased from Sigma-Aldrich. Chemicals were used as received without further purification. Gold pellets and chromium bars for evaporation were purchased from Kurt J. Lesker.

3.2.2 n-i-p Device Fabrication

Substrate Cleaning

Pre-etched FTO substrates (Pilkington Tec 7) were cleaned by subsequently sonicating in Decon 90 solution (1% vol. in D.I. water), D.I. water, acetone, and isopropanol for 10 min each. Then they were dried in a stream of nitrogen gas and UV-ozone cleaned for 15 minutes.

SnO_2 Chemical Bath Deposition

17.4 mg/mL tin(II) chloride dihydrate was dissolved in isopropanol and spin-coated onto the FTO substrates at 3,000 rpm for 25 seconds under an ambient atmosphere.

Subsequently, they were dried on a hotplate at 100°C for 10 minutes. Then the hotplate temperature was increased to 180°C and the substrates were annealed for 1 hour and then they were cooled to room temperature. A chemical bath solution containing 200 mL D.I. water, 2.5 g urea, 50 µL thioglycolic acid, 2.5 mL hydrochloric acid, and 540 mg tin(II) chloride dihydrate was stirred until fully dissolved. The substrates were then laid inside a Pyrex glass dish with the FTO side face up. The chemical bath solution was added to the glass dish and closed with a glass lid. The container was left in a 90°C oven for 3∼4 hours for the chemical bath deposition. Afterward, the substrates were taken out and subsequently sonicated in D.I. water and isopropanol for 5 minutes each and dried with a nitrogen gun. Then the substrates were annealed again at 180°C for 1 hour.

PCBM Passivation of SnO_2

Before PCBM deposition, the substrates were UV-ozone cleaned again for 15 minutes. The substrates were transferred into a nitrogen-filled glovebox. A 5 mg/mL PCBM in chlorobenzene solution was spincoated on the substrates at 5,000 rpm for 30 seconds. Then the substrates were annealed at 100°C for 10 minutes.

KCl Passivation of SnO_2

20 mM KCl in D.I. water was spincoated onto the SnO_2 substrate at 3,000 rpm for 30 s (2000 rpm/s ramp speed). Then the substrates were annealed at 100°C for 10 min. The substrates were UV-ozone cleaned for another 15 min before the perovskite film deposition.

$FAPbI_3$ (with MACl and $MAPbBr_3$) Deposition

1.5 M $FAPbI_3$ (99%) with 35% excess MACl and 1% $MAPbBr_3$ additive was used as the absorber material and prepared in a nitrogen-purged glovebox. 255.4 mg of FAI, 35.4 mg of MACl, 1.7 mg of MABr, 684.6 mg PbI_2, and 5.5 mg of $PbBr_2$ were dissolved in 1 mL of 4:1 DMF:DMSO. The solution was stirred on the hotplate at room temperature for 1 h. The solution was passed through a 0.45 µm polytetrafluoroethylene (PTFE) syringe filter before use. Inside a compressed dry air-purged drybox, 100 µL of precursor solution was drop-casted on the substrate and spun at 6,000 rpm for

30 s (3000 rpm/s ramp speed). 300 µL of anisole was dropped onto the substrate 10 s into the spinning program. The perovskite films were then annealed at 150°C for 15 min.

$FA_{0.83}Cs_{0.17}Pb(I_{0.9}Br_{0.1})_3$ Deposition

1.45 M $FA_{0.83}Cs_{0.17}Pb(I_{0.9}Br_{0.1})_3$ precursor solution was made by dissolving 64.0 mg CsI, 79.8 mg $PbBr_2$, 207.0 mg FAI, and 568.2 mg PbI_2 into 1 mL of a DMF:DMSO solvent mixture (4:1 volume ratio). The precursor solution was stirred on a hotplate at room temperature for 1 hour in a nitrogen-purged glovebox before use. The solution was passed through a 0.45 µm PTFE filter and transferred to a compressed dry air-purged drybox at around 10% relative humidity for perovskite deposition. Then 35 µL of the precursor solution was spread on an FTO/SnO_2 substrate using a pipette tip and then spun at 6,000 rpm for 35 s (with a ramp speed of 2000 rpm/s). 100 µL anisole was dropped at the center of the substrate 10 s before the end of spinning. The film was annealed on a hotplate at 100°C for 45 min.

$FA_{0.75}Cs_{0.25}Pb(I_{0.8}Br_{0.2})_3$ (1% access PbI_2) Deposition

A 1.2 M perovskite precursor solution was made by dissolving 154.8 mg FAI, 77.9 mg CsI, 132.1 mg $PbBr_2$, and 391.1 mg PbI_2 in 1 mL 7:3 ratio of DMF:DMSO. The perovskite precursor solution was dropped dynamically onto the substrate spinning at 1,000 rpm for 10 seconds with 200 rpm/s acceleration and then 5,000 rpm for 45 seconds with 800 rpm/s acceleration. The antisolvent (1:1 diethyl ether: ethyl acetate) was dropped onto the substrates 15 seconds before the end of the program. Then the substrates were annealed at 100°C for 45 minutes.

PEAI Passivation on Perovskite

For perovskite layer passivation, 5 mM phenethylammonium iodide (PEAI) was dissolved in isopropanol and spin-coated onto the perovskite layer. The PEAI solution was dynamically dropped onto the substrate spinning at 3,000 rpm for 30 s without annealing.

MeO-PEAI Passivation on Perovskite

4-methoxy-phenethylammonium iodide (MeO-PEAI) was dissolved in isopropanol to

make a 16 mM solution. The solution was dropped onto the substrate at 5,000rpm (2,500 rpm/s ramp) for 30 s. Then the substrate was annealed at 100°C for 5 minutes.

Spiro-OMeTAD

85 mg/ml Spiro-OMeTAD was dissolved in chlorobenzene. 33 µL of tert-butyl pyridine (tBP) is added to every 1 mL of the Spiro-OMeTAD solution first. A 517 mg/ml Li-TFSI stock solution in acetonitrile is made separately. Then 20 µL of the Li-TFSI solution is added to every 1 mL of Spiro-OMeTAD solution. The Spiro-OMeTAD solution is dynamically dropped onto the substrate spinning at 2,500 rpm (2,500 rpm/s ramp) for 30 seconds.

MeO5PECz

MeO5PECz solution was prepared by dissolving 25 mg MeO5PECz in 1 mL anhydrous chlorobenzene along with 20 µL Li-TFSI solution (concentration: 64.6 mg/mL in acetonitrile) to achieve 25 mol% Li-TFSI with respect to MeO5PECz (Mw=1388.67 g/mL). 33 µL tBP was added to the solution. The solution was stirred and heated at ∼60°C overnight until it had completely dissolved. Then the solution was passed through a 0.22 µL PTFE filter. 50 µL of MeO5PECz solution was dynamically deposited onto the substrates at 2,500 rpm for 30 s. The dopant-free MeO5PECz solution and the tBP dopant-only solution were prepared in a similar way.

MeO4PEBCz

MeO4PEBCz solution was prepared by dissolving 25 mg MeO4PEBCz in 1 mL anhydrous chlorobenzene along with 20 µL Li-TFSI solution (concentration: 74.4 mg/mL in acetonitrile) to achieve 25 mol% Li-TFSI with respect to MeO4PEBCz (Mw=1206.49 g/mol). 33 µL tBP was added to the solution. The solution was stirred and heated at ∼60°C overnight until it had completely dissolved. Then the solution was passed through a 0.22 µL PTFE filter. 50 µL of MeO4PEBCz solution was dynamically deposited onto the samples at 2,500 rpm for 30 sec. The dopant-free MeO4PEBCz solution and the tBP dopant-only solution were prepared in a similar way.

PTAA

The PTAA solution was prepared by dissolving it in toluene at 20 mg/mL. 10μL/mL tBP was added to the solution. Then 5 μL/mL Li-TFSI solution (520 mg/mL in acetonitrile) was added. The solution was stirred on the hotplate overnight until it was fully dissolved. The solution was filtered with a 0.22 μm PTFE filter before spin-coating. 200 μL solution was dropped onto the substrate and then spun at 6,000 rpm for 20 sec (3,000 rpm/sec acceleration). No annealing was necessary.

Metal Electrodes

For the top metal contact, the evaporation chamber was pumped down until the pressure reaches $<$5X10^{-6} Torrs. Then 80 nm of Au was evaporated at the rate of 0.1 Å/s for the first 10 Å and then the evaporation rate was gradually increased to 0.7 Å/s for the rest. For Cr/Au evaporation, first 3.5 nm Cr was evaporated at the rate of 0.1 Å/s then the same Au program was subsequently used to evaporate 80 nm of Au.

C_{60}-PA Deposition

C_{60}-phosphonic acid SAM was dissolved in DMSO at a concentration of 1 mM (0.932 mg/mL). Due to the low solubility of the SAM, the vial was first stirred at 70°C for 3 days and then sonicated at 40°C for 3 hours. The solution was passed through a 0.22 µm PTFE filter right before use. The SAM solution was dropped onto the substrate and spun at 3,500 rpm for 1 minute and then annealed at 100°C for 10 minutes. Afterward, any excess unbound SAMs were rinsed away with pure DMSO solvent using the same spin-coating program and dried again at 100°C for 10 minutes.

C_{60}-CA Deposition

C_{60}-carboxylic acid SAM was dissolved in a 1:1 v:v cosolvent of tetrahydrofuran: chlorobenzene (THF:CB) at a concentration of 1 mM. The solution was passed through a 0.22 µm PTFE filter right before use. The SAM solution was dropped onto the substrate and spun at 3,500 rpm for 1 minute and then annealed at 100°C for 10 minutes. Afterward, any excess unbound SAMs were rinsed away with pure THF:CB solvent using the same spin-coating program and dried again at 100°C for 10 minutes.

3.2.3 p-i-n Device Fabrication

For the p-i-n device fabrication, Pilkington Tec 15 FTO was used. Following the same substrate cleaning procedure in the n-i-p device, the rest of the p-i-n stack is fabricated as follows:

Poly-TPD

The hole-transporting layer is poly (N,N'-bis-4-butylphenyl-N,N'-bisphenyl) benzidine (poly-TPD). Poly-TPD was dissolved in toluene at a concentration of 1.2 mg/ml and heated at 70°C and stirred overnight. Then the solution was filtered with a 0.22 µm PTFE filter. Poly-TPD was dropped onto the substrate spinning at 2,000 rpm (2,000 rpm/s ramp) for 20 s. Then the substrate was annealed at 130°C for 10 minutes.

Al_2O_3 nanoparticles

Al_2O_3 nanoparticles were used to improve adhesion of the perovskite on Poly-TPD. A dispersion of Al_2O_3 nanoparticles (20 wt.% in IPA) was diluted with IPA at a 1:150 ratio. Then the colloidal dispersion was dropped onto the substrate and spun at 5,000 rpm (5,000 rpm/s ramp) for 20 s. The substrate was subsequently annealed at 100°C for 2 minutes.

Perovskite

The $FA_{0.75}Cs_{0.25}Pb(I_{0.8}Br_{0.2})_3$ (1% access PbI_2) perovskite layer was deposited the same way as in the n-i-p recipe.

Electron-transporting layer, PCBM

Phenyl-C61-butyric acid methyl ester (PCBM) was dissolved in 3:1 by volume chlorobenzene (CB): dichlorobenzene (DCB) at a concentration of 20 mg/ml. The solution was dropped onto the substrate spinning at 2,000 rpm (2,000 rpm/s ramp) for 30 s. Then the film was annealed at 100°C for 4 minutes.

Hole blocking layer, BCP

Bathocuproine (BCP) was dissolved in IPA at a concentration of 0.5 mg/ml. The solution was dropped onto the substrate spinning at 5,000 rpm (2,000 rpm/s ramp) for 20 s. Then the films were annealed at 100°C for 1 minute.

Metal Electrodes

For the top metal contact, the evaporation chamber was pumped down until the pressure reaches $<5X10^{-6}$ Torrs. Then 80 nm of Au was evaporated at the rate of 0.1 Å/s for the first 10 Å and then the evaporation rate was gradually increased to 0.7 Å/s for the rest. For Cr/Au evaporation, first 3.5 nm Cr was evaporated at the rate of 0.1 Å/s then the same Au program was subsequently used to evaporate 80 nm of Au.

3.3 Materials Characterization

3.3.1 Solution NMR

The nuclear magnetic resonance (NMR) experiments (including ^{1}H, ^{13}C, COSY, and HSQC) were conducted using a two-channel Bruker Avance III HD Nanobay 400 MHz instrument running TOPSPIN 3 equipped with a 5 mm z-gradient broadband/fluorine observation probe. Deuterated DMSO was used as the solvent for this experiment.

3.3.2 UV-vis Absorption Measurement

Absorption spectra were measured in dilute solutions and on glass substrates using a UV/Vis-NIR spectrophotometer, Lambda 35 (Perkin-Elmer).

3.3.3 Steady-state and Time-resolved Photoluminescence

Steady-state and time-resolved PL measurements were acquired using a time-correlated single-photon counting (TCSPC) setup (FluoTime 300, PicoQuant GmbH). Film samples were photoexcited using either a 510 nm/405 nm/630 nm laser head (LDH-P-C-510/LDH-P-C-405/LDH-P-635, Pico Quant GmbH) pulsed at a frequency of 5 kHz$\sim$1 MHz, with a pulse duration of 128 ps$\sim$4 ns and fluence of 30 nJ/cm^2. The PL was collected using a high-resolution monochromator and hybrid photomultiplier

detector assembly (PMA Hybrid 40, PicoQuant GmbH) with a detection wavelength set to the peak PL emission wavelength from the sample.

3.3.4 Photoluminescence Quantum Yield (PLQY)

PLQY (or PLQE) values were determined following the method of De Mello et al.[106] using a 532 nm or 410 nm continuous wave laser excitation source (Roithner, RLTMLL-532 2 W) to illuminate a sample in an integrating sphere (Newport, 70682NS), and the laser scatter and PL were collected using a fiber-coupled spectrometer (Ocean Optics MayaPro). The beam intensity was modified using neutral density filters. To obtain PLQY values that correlate with a device operating under 1 sun illumination for a particular wavelength laser, an optical density filter was used to adjust the laser output to the equivalent of AM 1.5G for each perovskite bandgap. See Figure 3 from Kirchartz et al. [107]. Reproduced in Figure 3.1.

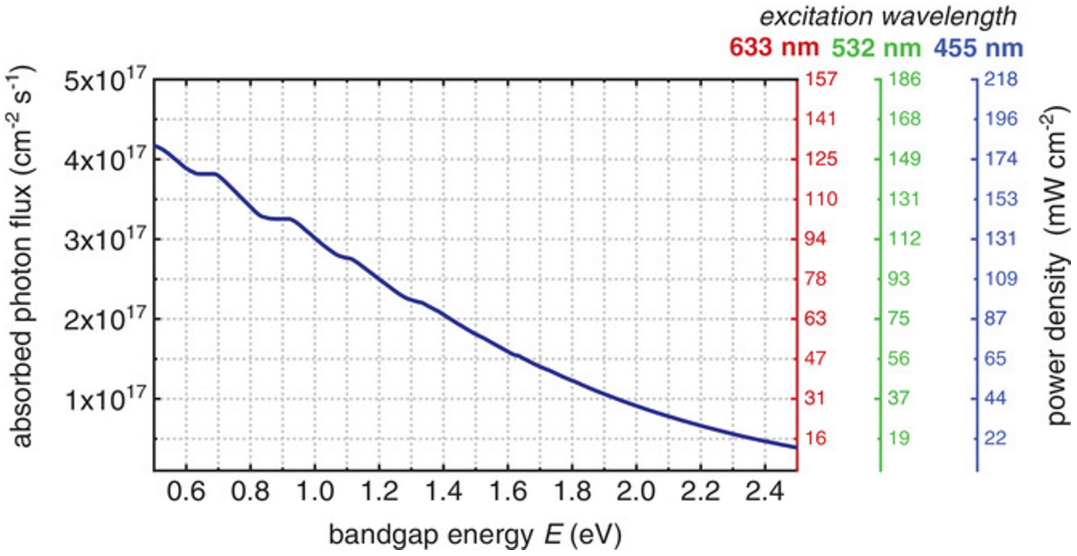

Figure 3.1: AM1.5G equivalent steady-state absorbed photon flux for different bandgap energies, assuming a step-function-like absorptivity where all the photons with energy above the bandgap are absorbed. The power density required to achieve such photon flux values for different excitation wavelengths is stated on the right axis. Reproduced from reference [107].

3.3.5 Ionization potential measurement (I_p)

For the carbazole hole-transporting materials (HTMs), the ionization potential (I_p) of each enamine compound was measured by electron photoemission in air (the error of this method is evaluated as ± 0.03 eV). The samples were prepared by dissolution in THF and the solutions were coated on Al plates pre-coated with a methyl methacrylate and methacrylic acid copolymer adhesive layer (∼0.5 mm). The thickness of the transporting material layer was 0.5 $\sim$ 1 mm. The organic materials investigated are stable enough in oxygen that the measurements may be carried out in ambient conditions. The samples were illuminated with monochromatic light from a quartz monochromator fitted with a deuterium lamp. The power of the incident light beam was $(2 \sim 5) \times 10^{-8}$ W. A negative voltage (-330 V) was supplied to the sample substrate. The counter electrode with a 4.5 mm $\times$ 15 mm slit for illumination was placed 8 mm from the sample surface. The counter electrode was connected to the input of the BK2–16 type electrometer, working in the open input regime, for the photocurrent measurement. The $10^{-15} \sim 10^{-12}$ A photocurrent (I) flowed in the circuit under illumination. The value of I is strongly dependent on the incident-light photon energy (hν). The dependence $I^{0.5}$ on incident-light quanta energy hν was plotted from the experiment results. Usually, the dependence of I on the incident light quantum energy is described well by the linear relationship $I^{0.5} = f(h\nu)$ near the threshold. The linear part of this dependence was extrapolated to the hν axis and the I_p value was determined as the photon energy at the interception point.

3.3.6 Charge carrier mobility measurements (μ)

The samples for the charge carrier mobility measurements were prepared by spin-coating solutions of the synthesized compounds in THF onto polystyrene films with a conductive Al layer. The layer thickness was in the range 5∼10 μm. The charge drift mobility was measured by Xerographic time of flight (XTOF). An electric field

was created by positive corona charging. The charge carriers were generated at the layer surface by illumination with pulses of a nitrogen laser (pulse duration = 2 ns, λ = 337 nm). The layer surface potential decrease as a result of pulse illumination was up to 1∼5% of the initial potential before illumination. The capacitance probe that was connected to the wide-frequency band electrometer measured the speed of the surface potential decrease (dU/dt). The transit time (t_t) was determined by the kink on the curve of the dU/dt transient on a linear or double logarithmic scale. The drift mobility was calculated by the formula $\mu = d^2/U_0 t_t$ (d is the layer thickness, U_0 is the surface potential at the moment of illumination).

3.3.7 Contact Angle Measurement

The contact angles of the HTM films were measured using a video-based optical contact angle measuring device (Ossila Contact Angle Goniometer) and analyzed using the Ossila Contact Angle 3.0.9.1 software. All measurements were performed in ambient atmosphere and at room temperature.

3.3.8 Kelvin Probe Force Microscopy (KPFM)

$FAPbI_3$ (with MACl and $MAPbBr_3$) perovskite films used for KPFM experiments (in Chapter 6) were made using a precursor solution that is diluted down 10 × to achieve a thin perovskite film of around 50∼60 nm. All other processing procedures were the same as in the aforementioned device processing procedure, except the stack was processed only up to the perovskite layer.

Work function measurements were collected with the Kelvin Probe system SKP5050 in air. The probe tip was first calibrated by a standard Highly Ordered Pyrolytic Graphite (HOPG) sample for a reference work function.

3.3.9 X-ray Photoelectron Spectroscopy (XPS)

The samples made for XPS experiments were made following the procedure in the experimental methods. For this experiment, SnO_2 and SnO_2/C_{60}-PA films were made on TEC 7 FTO substrates.

XPS was measured with a Thermo Scientific Kα X-ray photoelectron spectrometer. The samples were measured using a monochromated Al Kα X-ray source. The measurements were made at room temperature and at a takeoff angle of 90°. The core level spectra were recorded using a pass energy of 20 eV (with a resolution of approximately 0.4 eV) from an analysis area of 400 μm $\times$ 400 μm. The spectrometer work function and binding energy scale were calibrated using the Fermi edge and 3d peak recorded from a polycrystalline silver sample prior to the experiments. Fittings that were done to extract relative stoichiometry from the XPS data were carried out using the Avantage XPS software suite.

3.3.10 Optical-pump-terahertz-probe (OPTP) Measurement

The half-stack samples for this characterization were made on quartz substrates. Subsequently, the ETL and $FAPbI_3$ perovskite layers were fabricated following the same procedure as reported in the experimental methods. Afterward, a PMMA layer was processed on top of the perovskite film to encapsulate it. 20 mg/mL PMMA layer was spin-coated on top of the half-stack at a spin speed of 2,000 rpm (2,000 rpm/s ramp rate) for 20 s.

Optical-pump Terahertz-probe (OPTP) setup (described in more detail in reference [108, 109]) was measured using a Spectra Physics Mai Tai-Empower-Spitfire Pro Ti:Sapphire regenerative amplifier. The amplifier generates an ultra-fast laser with 35 fs pulse duration, 800 nm center wavelength, and 5 kHz repetition rate. 400 nm optical pump excitation wavelength was achieved by frequency doubling the fundamental laser output through a BBO crystal. THz probe pulses were generated

by a spintronic emitter consisting of quartz/2 nm Tungsten/1.8 nm $Co_{40}Fe_{40}Be_{20}$/2 nm Platinum. The samples were stored in an evacuated chamber at a pressure of less than 10^{-1} mbar and were excited with the pump and probed with the THz pulse shortly after. The pump and THz pulses were chopped with optical choppers with frequencies of 1.25 and 2.5 kHz respectively to obtain the THz transmission change ΔT. The diameters (FWHM) of the pump and probe beam at the sample positions were measured as 4.4 mm and 0.7 mm respectively. The power of pump pulses was tuned by an ND filter wheel. The THz transmission from samples was detected by electro-optic sampling in a (110)-ZnTe crystal (1 mm thickness) with a spatially and temporally overlapping 800 nm gate pulse. The THz transmission was measured at the peak of the THz pulse for different delays of the pump beam, mapping the THz transmission as a function of time after photoexcitation. The OPTP decay traces with different delays were measured for 4 fluences (in the range of 4.2 $\mu J \cdot cm^2 \sim 54.6$ $\mu J \cdot cm^2$) on the quartz side for each sample. The identical experimental procedure was repeated after each aging time.

3.3.11 X-Ray Diffraction (XRD)

XRD patterns were collected using a Panalytical X'Pert Pro X-ray diffractometer with a Cu Kα source (λ=1.54 Å).

3.3.12 Scanning Electron Microscopy (SEM)

Cross-sectional SEM and surface SEM images were collected using an FEI Quanta 600 scanning electron microscope at 5 kV acceleration voltage and a spot size of 3.0.

3.4 Photovoltaic Device Characterization

3.4.1 Current Density-Voltage (J-V) Measurements

The photovoltaic devices were characterized in ambient conditions with the room temperature around 20∼25°C and 25% relative humidity under AM 1.5G simulated sunlight generated by a class AAA WaveLabs Sinus-220 solar simulator, using a Keithley 2400 source meter. The intensity of the solar simulator was set to produce 100 mW/cm^2 equivalent irradiance using a certified KG3-filtered Si reference photodiode (Fraunhofer ISE). The voltage was swept at a rate of 0.61 V/s first from forward bias to reverse bias followed by a reverse sweep in the opposite scan direction. The minimum voltage was -0.2 V and the maximum voltage was 1.2 V. On each substrate, there were three devices with an area 0.25 cm^2 and one larger device with an area of 1.00 cm^2. The areas were defined using black anodized aluminum shadow masks in direct contact with the glass side of the substrates within enclosed sample holders.

3.4.2 External Quantum Efficiency (EQE) Measurements

External quantum efficiency was acquired with a custom build Fourier transform photocurrent spectrometer utilizing a Bruker Vertex 80v Fourier Transform Interferometer. Devices were calibrated to a Newport-calibrated silicon reference solar cell with known external quantum efficiency and illuminated with an AM1.5 filtered solar simulator. Device were masked with the same metal aperture masks as in the J-V measurements, with active areas 0.25 cm^2 and 1 cm^2.

3.5 Device Stability Measurements

3.5.1 65°C and 85°C AM 1.5 Light-soaking Box

The 65°C and 85°C light aging tests were done on encapsulated devices in an ambient atmosphere, either 65°C or 85°C, full spectrum pulsed light ATLAS SUNTEST XLS+ aging box. The (1,700 W) xenon lamp is pulsed at 100 Hz and averaged off to 1 sun intensity.

3.5.2 85°C N_2 Aging Box

The 85°C thermal aging test was done on unencapsulated devices in a dark nitrogen atmosphere. Devices were put inside a home-built oven with temperature control set to 85°C ($\pm$3°C) and removed periodically to measure device performance under ambient conditions.

3.6 Data Analysis

3.6.1 Quasi-Fermi Level Splitting (QFLS)

The quasi-Fermi level splitting (QFLS) analysis was done using methods previously reported by Caprioglio et al. [49, 110].

3.6.2 Time-resolved Photoluminescence (TRPL) Fitting

The time-resolved PL decays were fitted to a stretched exponential function

$$f(t) = Aexp(-\frac{t}{\tau})^{\beta} \tag{3.1}$$

in which β is the stretching parameter. 0<β<1 indicates how much the curve deviates from a mono-exponential decay of β=1. The mean lifetime of the photogenerated charges ⟨τ⟩ is given by

$$< \tau >= \int_0^\infty dt\ exp(-(\frac{t}{\tau})^\beta) = \frac{\tau}{\beta}\Gamma(\frac{1}{\beta}) \tag{3.2}$$

where Γ is the gamma function. The fitting method is detailed in this paper published by Habisreutinger et al. [111].

CHAPTER 4

Low-cost dopant-free carbazole enamine hole-transporting materials for thermally stable perovskite solar cells

The research in this chapter is based on the following publication:

Suer Zhou, Maryte Daskeviciene, Matas Steponaitis, Giedre Bubniene, Vygintas Jankauskas, Kelly Schutt, Philippe Holzhey, Ashley R. Marshall, Pietro Caprioglio, Grey Christoforo, James M. Ball, Tadas Malinauskas, Vytautas Getautis, Henry J. Snaith. (2022), "Low-Cost Dopant-Free Carbazole Enamine Hole-Transporting Materials for Thermally Stable Perovskite Solar Cells". Sol. RRL, 6: 2100984.

DOI: 10.1002/solr.202100984

Direct link: https://onlinelibrary.wiley.com/doi/full/10.1002/solr.202100984

 The structure and content of this article are modified to fit the format of this thesis. Where

data was collected and analyzed by co-authors, this is indicated in the relevant figure caption. Unless otherwise stated, all other data were collected and analyzed by me.

4.1 Introduction

Perovskite solar cells (PSCs) have dramatically risen in performance in the past decade owing to the considerable changes to their device architecture, the composition of perovskite, processing methodologies, and electron extraction layers since the early reports. However, the hole-conductor, 2,2´,7,7´-tetrakis(N,N-di-p-methoxyphenylamine)-9-9´-spirobifluorene (Spiro-OMeTAD), along with a "cocktail" of ionic and basic additives, remains essentially unaltered in the highest efficiency perovskite cells. [112, 113, 114] This extraction layer was first employed in the first solid-state perovskite cells reported in 2012, and originated in solid-state dye-sensitized solar cells from 1998 [115].

Despite the promises of this technology, PSCs can degrade due to a variety of reasons [116, 117, 118] and moisture is one of the key culprits [119]. The best-performing perovskite materials are usually comprised of a mixture of multiple small organic and inorganic mono-cations, lead(II) cations, and halide anions [120]. When such perovskites interact with water, they can form an intermediate hydrated structure, followed by degradation to lead halide, which leads to a large drop in power conversion efficiency (PCE) [121, 122, 123]. One of the possible pathways for moisture to reach the perovskite layer is through the hygroscopic dopants (ionic and basic additives) used to induce chemical oxidation that improves conductivity and photoelectric properties of the hole-transporting materials (HTMs) [124]. For example, one commonly used dopant, bis(trifluoromethane)sulfonimide lithium salt (Li-TFSI), is hygroscopic [125]. Doping increases the conductivity of commonly-used HTMs by increasing the hole density, since conductivity is proportional to the product of the hole density and mobility [126, 127, 128]. However, it is preferable to improve the inherent mobility of the HTMs because doping can lead to additional instabilities.

Different doping strategies can be applied to boost the performance of the HTM, such as oxidation in air, the addition of chemical oxidization agents (such as cobalt-based metal complexes) [129], direct addition of pre-synthesized HTM^+ bis (trifluoromethane) sulfonimide $(TFSI)^-$ and the use of chemical adducts [130, 131, 132]. For instance, the most widely used hole-transporting material for devices in the n-i-p configuration is Spiro-OMeTAD, which has low conductivity in its pure form. It is commonly doped with Li-TFSI, 4-tert-butyl pyridine (tBP), and cobalt-based metal complexes (for example tris(2-(1H-pyrazol-1-yl)-4-tert-butylpyridine)cobalt(III) tri[bis(trifluoromethane)sulfonimide]) (FK209) [129]. If Li-TFSI is used without the cobalt salt, the oxidation process depends on prolonged ambient oxygen exposure and therefore suffers from poor control over doping levels [133]. FK209 partially oxidizes Spiro-OMeTAD by reducing Co(III) to Co(II), thus initially increasing the HTM conductivity. To further oxidize Spiro-OMeTAD, air oxidation with Li-TFSI is still needed to deliver the most efficient solar cells [125, 134, 135]. The addition of lithium ions can contaminate other parts of the device, potentially lowering the PCE over time through processes such as lithium-ion migration causing increased hysteresis [136, 137].

The presence of tBP was also shown to reduce the glass-transition temperature of Spiro-OMeTAD to below 100°C [138]. Adding tBP along with Li-TFSI further causes morphological transformations at the perovskite/Spiro-OMeTAD interface at elevated temperatures ($>$85 °C) [139, 140]. Therefore, it is desirable to avoid chemical oxidation and additives for better device stability, thus making "dopant-free" HTMs very attractive alternatives. There are two main types of dopant-free HTMs for the common (n-i-p) device architecture: polymers and small molecules. Without additives, polymers tend to demonstrate better device PCEs, possibly due to the ability to coat thinner uniform films, in comparison to their small-molecule counterparts. However, they suffer from drawbacks such as purity, batch-to-batch reproducibility [141], and higher synthetic costs [142]. On the other hand, the PCEs of small-molecule, additive-free HTMs are typically around 15%, with very few examples over

18% [143, 144, 145]. Nevertheless, the synthesis of these small molecules, p-type semiconductors is reproducible; they can be purified in many different ways and, similarly to dopant-free polymers, increase the long-term stability of devices [142].

In this study, we describe the synthesis and application of new carbazole-based enamines as HTMs, specifically, N3, N3, N6, N6, 9-pentakis [2,2-bis (-methoxyphenyl) ethenyl]-9H-carbazole-3, 6-diamine (MeO5PECz) and N3, N3, N6, N6, 9-tetrakis[2,2-bis(-methoxyphenyl)ethenyl]-9-butyl-9H-carbazole-3,6-diamine (MeO4PEBCz) (Figure 4.1). These materials are the product of a simple synthesis that avoids expensive organometallic catalysts or costly purification techniques, resulting in significantly reduced costs. Furthermore, no chemical oxidation or dopants are required to reach high PCEs, making these materials attractive alternatives for applications in PSCs.

4.2 Synthesis

The syntheses of enamines MeO5PECz and MeO4PEBCz from commercially available carbazole diamines are shown in Figure 4.1. See details of the ^{1}H NMR spectra of these materials in Appendix A.

The carbazole diamine precursors are dissolved in THF (for MeO5PECz) or toluene (for MeO4PEBCz) and heated at reflux with acid catalysts. Then they were cooled to room temperature and purified via recrystallization.

Carbazole derivatives MeO5PECz and MeO4PEBCz have been obtained without the use of expensive palladium-catalyzed cross-coupling in a simple, acid-catalyzed condensation reaction between carbazole diamines and bis (4-methoxyphenyl) - acetaldehyde (Figure 4.1). MeO5PECz and MeO4PEBCz were purified by recrystallization, without column chromatography or sublimation. Recently, Chang et al [146] found that Spiro-OMeTAD would be the highest single contributor to cost, by a significant margin, if employed in perovskite solar cells and perovskite/silicon tandems.

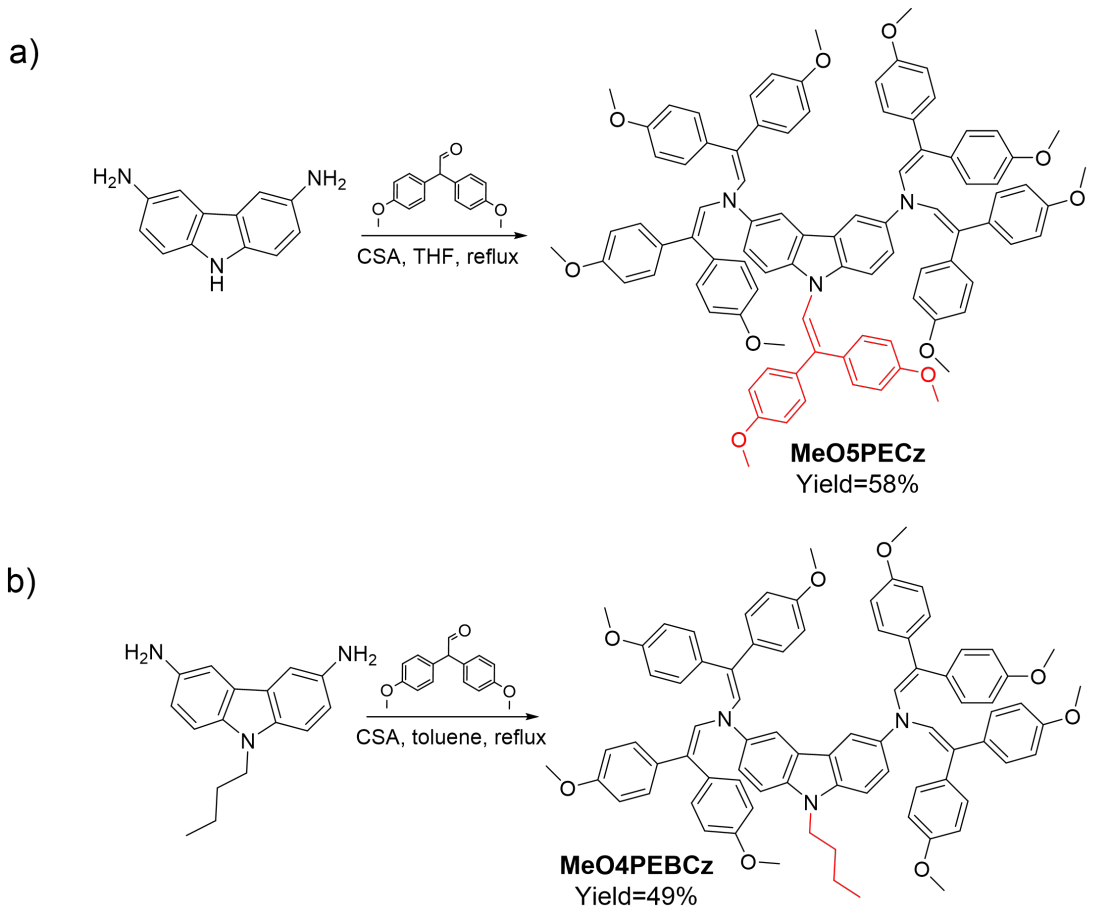

Figure 4.1: a) Synthesis of carbazole enamines MeO5PECz and b) MeO4PEBCz. Reproduced from reference [104]. The syntheses were done by Dr. Maryte Daskeviciene and Dr. Giedre Bubniene, Kaunas University of Technology, Lithuania.

It is possible to lower the manufacturing cost of the HTM by around one order of magnitude from 92 USD/g for Spiro-OMeTAD [146] to 10.33 USD/g for MeO4PEBCz and 7.83 USD/g for MeO5PECz (based on calculations done in Appendix B).

4.3 Optoelectronic Characterizations

Optical properties, such as absorption spectrum, and electrical properties, such as ionization potential (I_p) and mobility are essential parameters for assessing the success of an HTM in optoelectronic devices. UV-vis absorption was performed on thin films of the HTMs on glass substrates (Figure 4.2). The π–π* transition of MeO4PEBCz can be seen at 353 nm and of MeO5PECz at 358 nm. The π–π* transitions peaks of

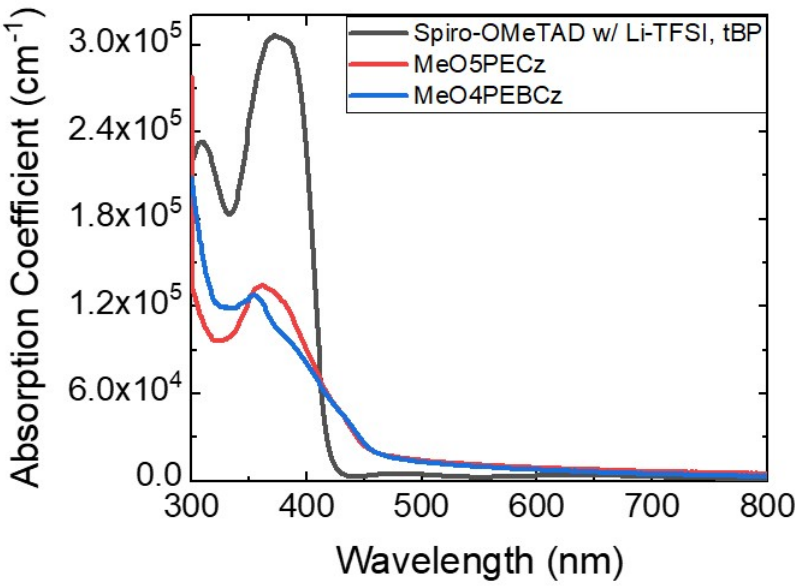

Figure 4.2: UV-vis absorption spectra of carbazole derivatives MeO5PECz, MeO4PEBCz, and Spiro-OMeTAD thin films on glass.

both carbazole HTMs are at slightly shorter wavelengths than that of Spiro-OMeTAD (peak at 385 nm [147]) and weaker absorption in the visible range (380∼700 nm). The π–π* transition is indicative of an electron transfer from the bonding π state to its antibonding π* state. In other words, it is the charge transition from its highest occupied molecular orbital (HOMO) level to the lowest unoccupied molecular orbital (LUMO) level.

Photoemission spectroscopy in air was used to measure the ionization potential (I_p) of the carbazole derivatives in the solid-state (the error is estimated to be ±0.03 eV) (Figure 4.3a; Figure 4.3b). All materials have similar I_p of near 5.00 eV (Table 4.1); interestingly, the additional electron donating bis(4-methoxyphenyl)ethenyl moiety in MeO5PECz increases the Ip slightly compared with MeO4PEBCz. Steric hindrance, resulting from five bis(4-methoxyphenyl)ethenyl fragments connected to the carbazole core, could be the main factor behind the small differences in I_p, since it influences the electronic coupling between the peripheral phenyl units and the carbazole core. In this case, the one additional bis(4-methoxyphenyl)ethenyl group in MeO5PECz increases the steric hindrance around the carbazole core, thus forcing

other phenylethenyl fragments to adopt a less planar configuration, mitigating the electron donor impact of the substituents.

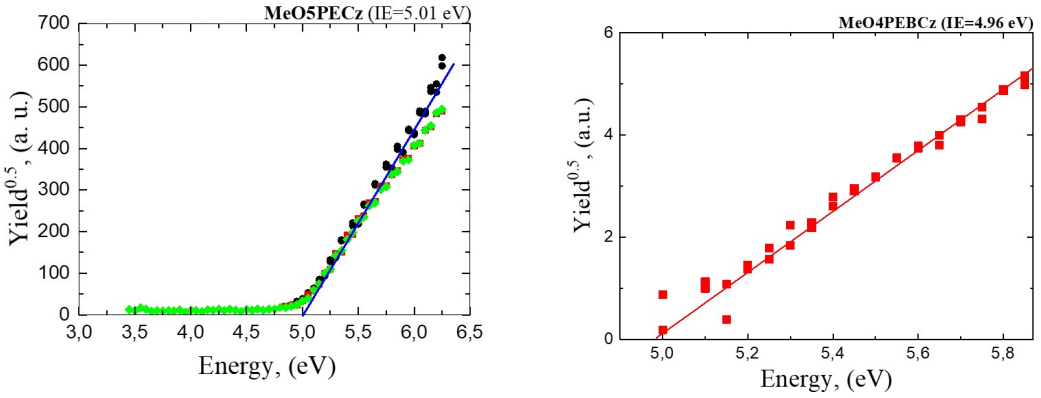

(a) **(b)**

Figure 4.3: (a) I_p measurements of MeO5PECz (b) I_p measurement of MeO4PEBCz. The I_p are measured and analyzed by Dr.Egidijus Kamarauskas, Kaunas University of Technology, Lithuania.

Table 4.1: Photophysical properties of the synthesized materials and Spiro-OMeTAD for comparison.

Compound	I_p, eV (a)	$\mu_0, cm^2V^{-1}s^{-1}$ (b)	$\mu, cm^2V^{-1}s^{-1}$ (c)	α (d)
MeO5PECz	5.01	3.7×10^{-5}	7.8×10^{-4}	0.0038
MeO4PEBCz	4.96	1.2×10^{-4}	1.1×10^{-3}	0.0027
Spiro-OMeTAD [130]	5.00	4.1×10^{-5}	5×10^{-4}	0.0031

(a) Ionization potential was measured on films by photoemission spectroscopy in air; (b) Hole mobility value at zero field strength; (c) Hole mobility value at the electric field strength of 6.4×10^5 V·cm^{-1}; (d) Poole–Frenkel parameter. The I_p are measured and analyzed by Dr. Egidijus Kamarauskas. The Xerographic time-of-flight mobilities were measured and analyzed by Dr. Vygintas Jankauskas, Vilnius University, Lithuania.

The xerographic time-of-flight (XTOF) method (Figure 4.4) was used to estimate the drift carrier mobility of the investigated pristine materials. MeO4PEBCz displayed slightly higher mobility of 1.1×10^{-3} cm^{2}V^{-1}s^{-1} versus 7.8×10^{-4} cm^{2}V^{-1}s^{-1} for MeO5PECz under an electric field (Table 4.1). Despite many similarities between the molecules, the difference in drift carrier mobility could be explained by the closer packing of MeO4PEBCz and consequentially smaller charge hopping distance. This correlates well with the I_p results, since the additional electron donating bis(4-methoxyphenyl)ethenyl moiety in MeO5PECz increases steric hindrance

in the molecule and π–π stacking distances, reducing the charge carrier mobility [148, 149, 150, 151, 152, 153].

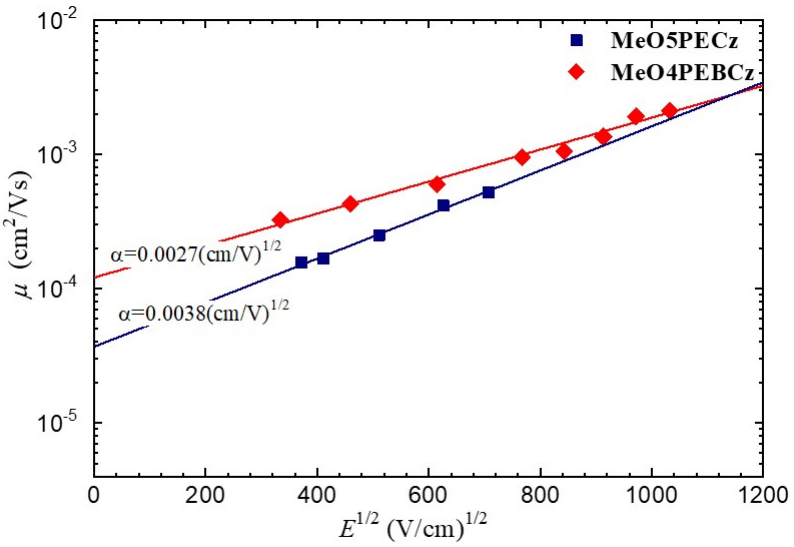

Figure 4.4: Drift carrier mobility of the tested MeO5PECz and MeO4PEBCz. The Xerographic time-of-flight mobilities were measured and analyzed by Dr. Vygintas Jankauskas, Vilnius University, Lithuania.

Four-point probe conductivity measurements were carried out on MeO5PECz, MeO4PEBCz, and Spiro-OMeTAD films with various doping concentrations of Li-TFSI on glass. When undoped, MeO5PECz has around a factor of 10 higher conductivity and MeO4PEBCz has around a factor of 100 higher conductivity compared to pristine Spiro-OMeTAD (Figure 4.5). For MeO4PEBCz, this is in part due to mobility that is three times higher, but for both MeO4PEBCz and MeO5PECz, the higher conductivities are mostly attributed to their higher intrinsic carrier density compared to pristine Spiro-OMeTAD, since conductivity is proportional to both mobility and carrier density. Furthermore, while the conductivity of Spiro-OMeTAD increases significantly (approximately three orders of magnitude) with the addition of Li-TFSI, the conductivities of the carbazole-based enamines improve more moderately (approximately two orders of magnitude) up to 250 mol% Li-TFSI. Typically, 50 mol% Li-TFSI is added to Spiro-OMeTAD in devices [154, 155]. At the highest doping

concentrations, MeO4PEBCz is still an order of magnitude more conductive than Spiro-OMeTAD.

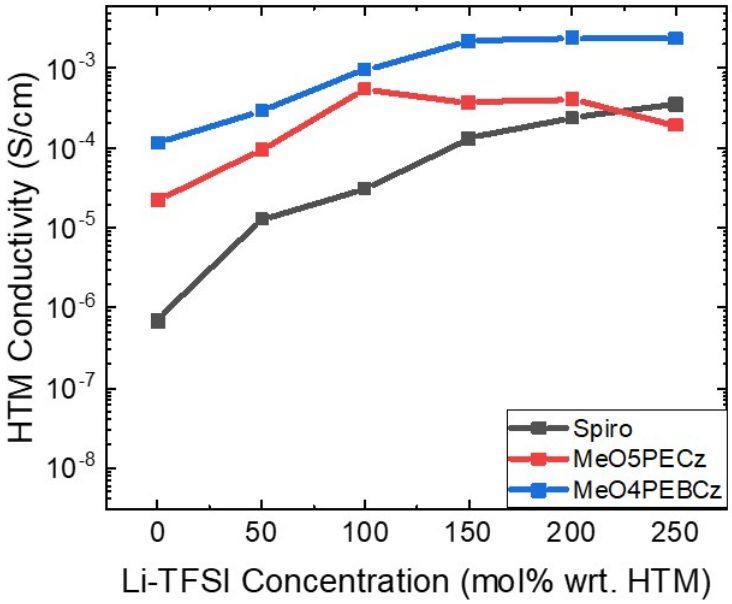

Figure 4.5: The conductivity of Spiro-OMeTAD, MeO5PECz, and MeO4PEBCz variation with Li-TFSI doping concentration (after having been left in an air-filled dry box for 24 hours), were measured with a 4-point probe.

4.4 Thermal and Moisture Stability

The thermal stability of the HTMs was determined using thermogravimetric analysis (TGA), the results are shown in Figure 4.6 and Table 4.2. The materials demonstrated 5% weight loss just slightly below 400°C, showing that they are sufficiently thermally stable for application in PSCs. Furthermore, the rapid weight loss seen in Figure 4.6 just above 450°C suggests that the investigated materials can readily sublime and demonstrate the potential for vacuum deposition.

Under working conditions, PSCs can reach temperatures well above 65°C; [156] therefore, HTMs must have glass transition temperatures (T_g) above 65°C. The T_g of the enamines was measured using differential scanning calorimetry (DSC) and the results show that both MeO5PECz and MeO4PEBCz have acceptable T_g's of 152°C and 140°C, respectively (Table 4.2). The difference in T_g becomes clearer when we look

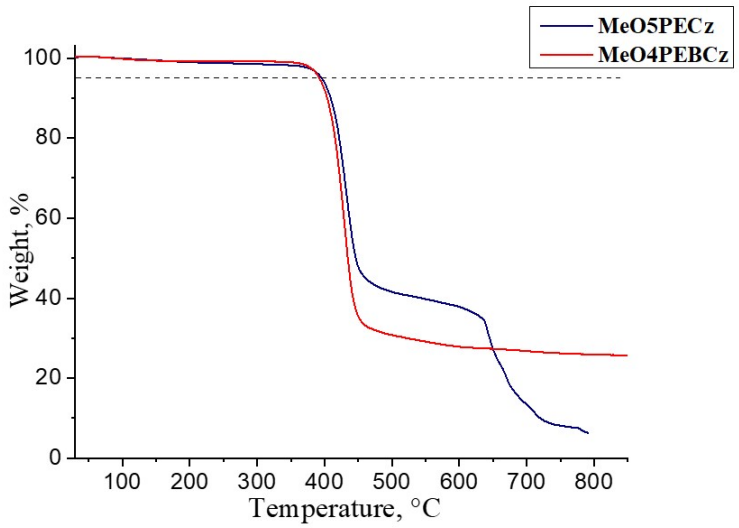

Figure 4.6: TGA heating curves of MeO5PECz and MeO4PEBCz. Measurements were done by Maryte Daskeviciene and Matas Steponaitis, Kaunas University of Technology, Lithuania.

Table 4.2: Thermal characteristics of the carbazole enamine HTMs and Spiro-OMeTAD for comparison.

Compound	T_g, °C (a)	T_m, °C (b)	T_{cr}, °C (c)	$T_{5\%}$,°C (d)
MeO5PECz	152	204	–	395
MeO4PEBCz	140	260	214	392
Spiro-OMeTAD	126	245	–	449

(a) Determined by DSC: scan rate = 10 °C min^{-1}, N_2 atmosphere; second run; (b) Determined by DSC: scan rate = 10 °C min^{-1}, N_2 atmosphere; first run; (c) Determined by DSC: scan rate = 10 °C min^{-1}, N_2 atmosphere; (d) 5% weight loss determined by TGA: heating rate = 10 °C min^{-1}, N_2 atmosphere. Measurements were done by Dr. Matas Steponaitis, Kaunas University of Technology, Lithuania.

at the structure of the HTMs. Both organic semiconductors are carbazole derivatives, however, MeO5PECz has an additional bis(4-methoxyphenyl)ethenyl fragment at the 9-position of the carbazole moiety, while MeO4PEBCz has an aliphatic butyl chain instead, which reduces the bulkiness of the molecule thus lowering the T_g [157]. Furthermore, both materials are partially crystalline with melting temperatures of 204°C for MeO5PECz and 261°C for MeO4PEBCz (Figure 4.7). Interestingly, during the second heating of MeO5PECz, no crystallization takes place, which is important for the formation of good quality thin films, since spontaneous and uncontrollable crystallization causes charge trapping and layer separation which result in a drop in device

efficiency [158]. Although MeO4PEBCz starts to crystallize during the first and second heating, it also possesses relatively high T_g which should lower the probability of the crystallization occurring in a working device quite significantly.

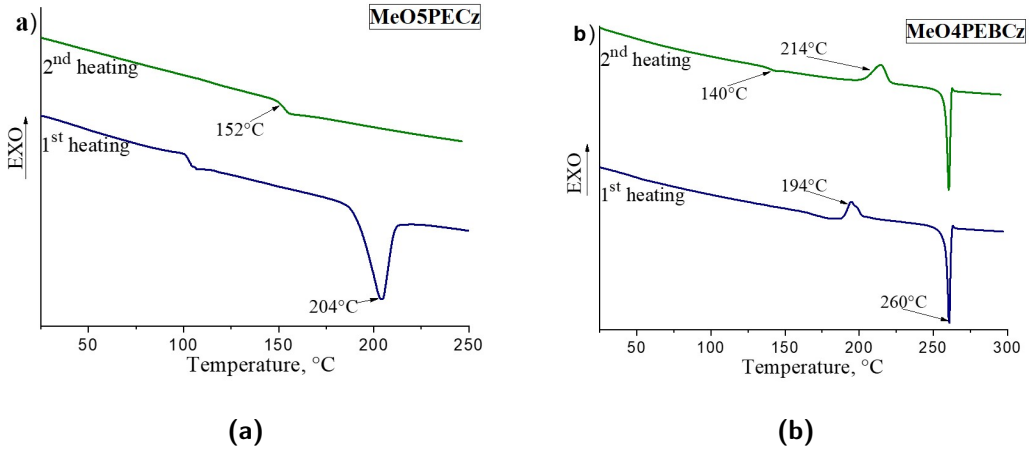

Figure 4.7: DSC heating curves of (a) MeO5PECz and (b) MeO4PEBCz (heating and cooling rate 10 K·min^{-1}). Measurements were done by Dr. Matas Steponaitis.

The water contact angles were measured for Spiro-OMeTAD with Li-TFSI and the carbazole-based enamine HTMs without Li-TFSI (as shown in Figure 4.8). Without the hygroscopic Li-TFSI dopant, the water contact angles of the carbazole HTMs are both higher than that of Spiro-OMeTAD, which suggests that the carbazole HTMs can effectively reduce moisture ingress to the perovskite layer when coated on top without dopant.

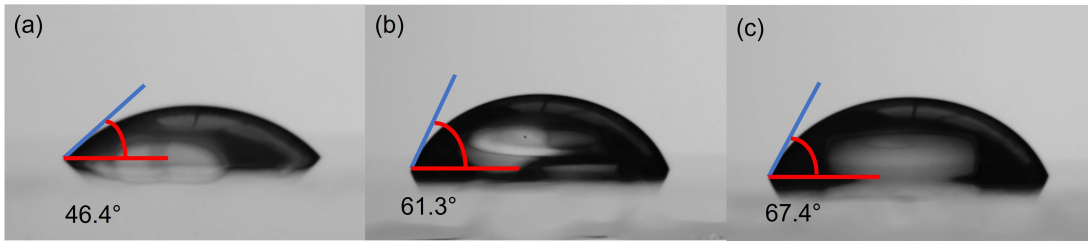

Figure 4.8: Water contact angle of films (a) Spiro-OMeTAD doped with Li-TFSI and tBP (b) MeO5PECz doped with tBP (c) MeO4PEBCz doped with tBP

4.5 Interfacial Properties

To probe the quality of the interface between the HTMs and the perovskite absorber layers, we performed absolute photoluminescence (PL) measurements. We determined the external PL quantum yield (PLQY) on "half-devices" made with the structure: glass/perovskite/HTM and compared them to films of perovskite on glass (Table 4.3 and Figure 4.9). The samples were illuminated with a 532 nm wavelength laser under 1 sun equivalent intensity for the perovskite bandgap (59.28 mW/cm^2 for a 1.6 eV E_g perovskite). The perovskite absorber material was $FA_{0.83}Cs_{0.17}Pb(I_{0.9}Br_{0.1})_3$ with a bandgap of $\sim$1.6 eV. Compared to the perovskite films deposited on glass, we observe a reduction in absolute PLQY for all films coated with the charge-extraction layers denoting the presence of non-radiative recombination at the transport layer interfaces. Perovskite films coated with the undoped enamine HTMs have the highest PLQY of all the HTM-coated samples, while perovskite films coated with the doped enamines show higher PLQY as compared to the doped Spiro-OMeTAD. Notably, the perovskite films coated with the undoped MeO5PECz show very little quenching of the PLQY.

From these PLQY measurements, it is estimated that the quasi-Fermi-level-splitting (QFLS) in the perovskite layer following the method outlined in reference [159] which is equivalent to the maximum open-circuit voltage (V_{oc}) which could be generated by the perovskite/HTM heterojunction. Specifically, we found the Spiro-OMeTAD interface, either doped or undoped, to be the one characterized by the largest amount of recombination losses, limiting the QFLS to $\sim$1.15 eV for the doped case. Remarkably, when the Spiro-OMeTAD is replaced with enamine HTMs, the losses at the HTL interface are significantly reduced, achieving a QFLS as high as 1.24 eV. To examine the ETL/perovskite heterojunction, we also fabricated and measured the PLQY of a sample: FTO/SnO_2/perovskite and calculated the QFLS. In Figure 4.9, the SnO_2 interface shows significant recombination losses, limiting the QFLS to $\sim$1.17 eV. These results highlight how both the electron transport layer (ETL) and hole transport layer

(HTL) interfaces limit the V_{oc} of n-i-p devices, with the conventional materials SnO_2 and Spiro-OMeTAD. Since the V_{oc} of a full device stack is limited by its weakest interface, the QFLS results (enamine HTMs $>$ FTO/SnO_2 $>$ Spiro-OMeTAD) indicate that Spiro-OMeTAD is limiting V_{oc}, but when using enamine HTMs, FTO/SnO_2 becomes the limiting interface.

Across all three of the HTMs, the PLQYs of the perovskite/HTM films consistently drop when Li-TFSI is added to the HTMs (Table 4.3 and Figure 4.9b). Contrary to what is often interpreted as more efficient carrier extraction [159, 160, 161], under open-circuit conditions, a higher degree of PL quenching implies increased non-radiative recombination [126, 162]. Since our half-devices are not connected to an external circuit, they are operating similarly to a device at open-circuit conditions and the charge carriers only recombine through internal pathways. Since adding Li-TFSI increases the PL quenching, it suggests that adding Li-TFSI increases the rate of non-radiative recombination relative to the rate of radiative recombination, which will negatively impact open-circuit voltage. Li-TFSI has poor solubility directly in chlorobenzene, so it is normally dissolved in acetonitrile before adding it to the Spiro-OMeTAD/chlorobenzene solution. Previous reports have shown that both acetonitrile and tBP can dissolve PbI_2 and damage the perovskite surface, which may cause an increased level of defects [101, 163, 164, 165]. On the other hand, tBP has been shown to interact with the perovskite surface favorably, by passivating defects or inducing p-type surface doping [166]. We hypothesize that without the addition of Li-TFSI, there are fewer traps at the perovskite/HTM interface which gives better perovskite/HTM interfacial properties.

Time-resolved photoluminescence (TRPL) decays were measured via time-correlated single-photon counting (TCSPC) on the same films used for the PLQY measurements, the results of which we show in Figure 4.10. Fitting the decays using a stretched-exponential curve (details in chapter 3 section 6.2), we determine a mean carrier lifetime ($<\tau>$) of the PL decay of 308.4 ns for the neat perovskite film coated on glass, 40.2 ns for perovskite films coated with neat Spiro-OMeTAD, compared to

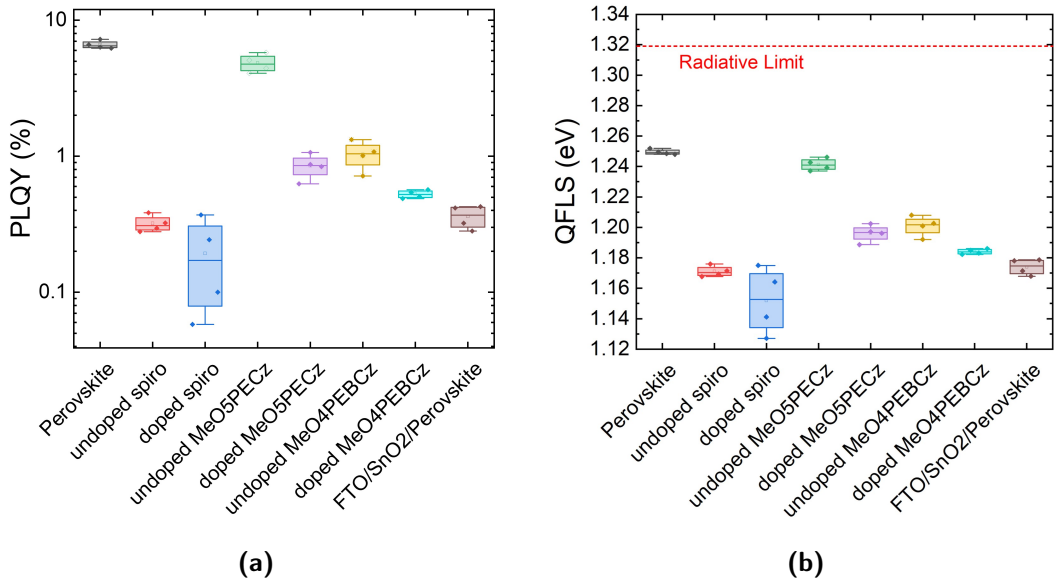

Figure 4.9: a) PLQY of half stacks on glass with the middle line denoting the median value and the boxes showing 25% $\sim$ 75% range of the data points with the raw data plotted as circles. b) Box plot for the corresponding QFLS calculated using the PLQY.

Table 4.3: Photoluminescence properties and estimated quasi-Fermi level splitting (QFLS) of $FA_{0.83}Cs_{0.17}Pb(I_{0.9}Br_{0.1})_3$ perovskite thin-films coated on glass substrates and coated with different HTMs, with and without Li-TFSI doping.

HTM	PLQY(%)	QFLS (eV)
Perovskite	6.6±0.5	1.249±0.002
Perovskite/Spiro (neat)	0.32±0.05	1.171±0.004
Perovskite/Spiro (50%mol Li-TFSI, tBP)	0.2±0.1	1.15±0.02
Perovskite/MeO5PECz (neat)	4.8±0.8	1.241±0.004
Perovskite/MeO5PECz (25%mol Li-TFSI, tBP)	0.9±0.2	1.196±0.006
Perovskite/MeO4PEBCz (neat)	1.0±0.3	1.201±0.006
Perovskite/MeO4PEBCz (25% mol Li-TFSI, tBP)	0.53±0.04	1.184±0.002
FTO/SnO2/Perovskite	0.36±0.07	1.174±0.005

All samples were illuminated from the glass side similar to in devices. The data reported in the table were averaged across four PLQY measurements for each condition. The errors given for the PLQY are the statistical error of the measurements, and those for the QFLS are the propagated errors from the PLQY. For the PLQY measurements and subsequent QFLS calculations, the excitation was measured using a 532 nm laser, with an absorbed photon fluence approximately matching AM 1.5 100 mW/cm^{-2} irradiance. The dopant concentration in each type of HTM is optimized for the best device performance.

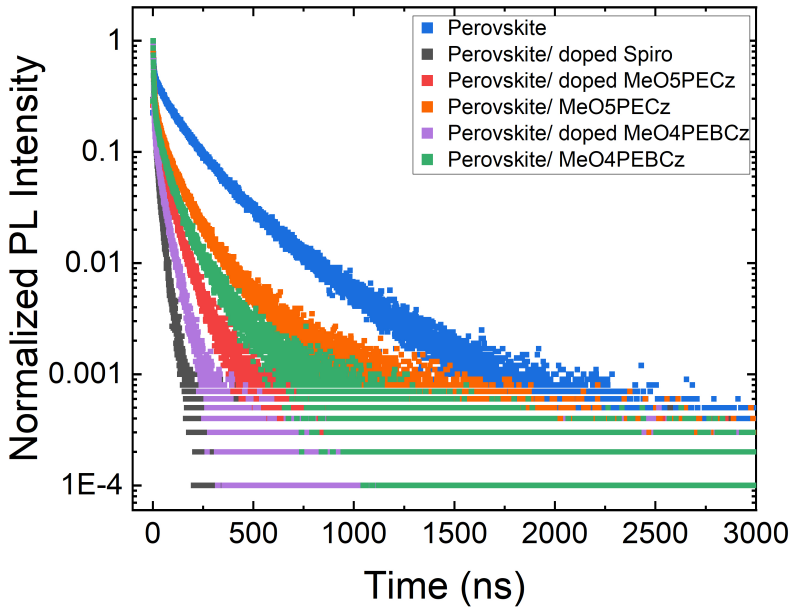

Figure 4.10: Time-resolved photoluminescence measurements of perovskite films on glass (pristine), perovskite coated with Spiro-OMeTAD doped with both tBP and Li-TFSI, and perovskite with the new enamine hole-transporting materials with and without both Li-TFSI and tBP dopants. Measured with 510 nm excitation, fluence 221.1 nJ·cm^{-2}

160.3 ns and 52.0 ns for neat MeO5PECz and MeO4PEBCz films, respectively (Table 4.4). This varies consistently with the PLQY trends (Figure 4.9a), indicating for the new enamine-based HTMs, there is less non-radiative recombination introduced at the perovskite/HTM interfaces, in contrast to the perovskite/Spiro-OMeTAD heterojunction.

Table 4.4: TRPL curve fitted parameters according to equation 3.1 and equation 3.2.

Compound	$\tau(ns)$	β	Lifetime (ns)
Perovskite	244.4	0.70	308.4
Perovskite/Spiro (neat)	34.6	0.77	40.2
Perovskite/Spiro (50%mol Li-TFSI, tBP)	6.7	0.74	8.1
Perovskite/MeO5PECz (neat)	126.2	0.70	160.3
Perovskite/MeO5PECz (25%mol Li-TFSI, tBP)	37.0	0.67	48.9
Perovskite/MeO4PEBCz (neat)	41.0	0.70	52.0
Perovskite/MeO4PEBCz (25% mol Li-TFSI, tBP)	28.2	0.68	36.9
FTO/SnO2/Perovskite	60.8	0.62	87.3

The excitation wavelength for the TRPL was 510 nm, illuminated from the glass side, excited at 300 MHz frequency.

4.6 Device Performancec

We fabricated n-i-p perovskite solar cells with the architecture FTO/ SnO_2/ $FA_{0.83}Cs_{0.17}Pb(I_{0.9}Br_{0.1})_3$ / HTM/ Au (Figure 4.11). Upon investigating doping Li-TFSI and tBP into the new carbazole enamine HTMs, we optimized the doping concentrations for each HTM layer. Champion devices made with MeO5PECz achieved a maximum power point tracked efficiency (η_{mpp}) of 17.4% when doped with 33 µL/mL tBP and 25 mol% Li-TFSI with respect to MeO5PECz (Figure 4.12b). Similarly, MeO4PEBCz achieved a η_{mpp} of 16.7% at the same mol% dopant concentrations (Figure 4.12a).

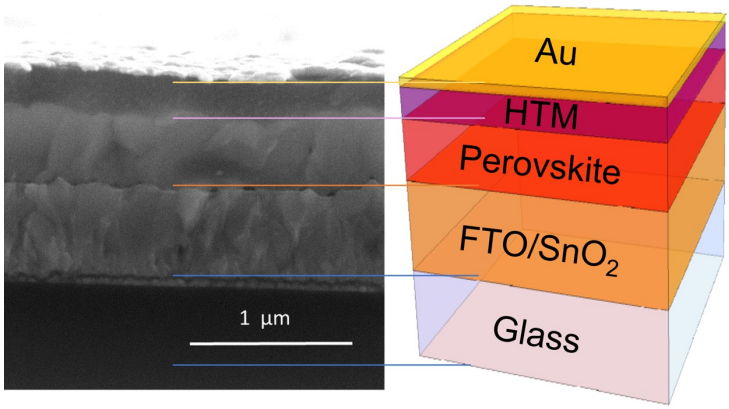

Figure 4.11: Cross-sectional SEM image of a MeO5PECz device and schematic illustration of the device stack.

Due to their high hole mobilities, MeO5PECz and MeO4PEBCz were further tested as dopant-free HTMs (Figures 4.13a, 4.13b). The MeO5PECz and MeO4PEBCz layers are 55 nm and 45 nm, respectively, according to thin film profilometry. In Table 4.5 we report the parameters of the devices with the HTMs without dopants, with only tBP, and with both tBP and Li-TFSI. J-V scans and maximum power point tracked efficiency (η_{mpp}) plots show that the devices made with undoped MeO4PEBCz and MeO5PECz have performances similar to that of devices employing doped Spiro-OMeTAD. Without any Li-TFSI or tBP doping, MeO4PEBCz achieved a η_{mpp} of 15.9% while MeO5PECz devices achieved a η_{mpp} of 16.1%, as compared to 17.4% with doped Spiro-OMeTAD. Notably, there are quite significant hystereses among all

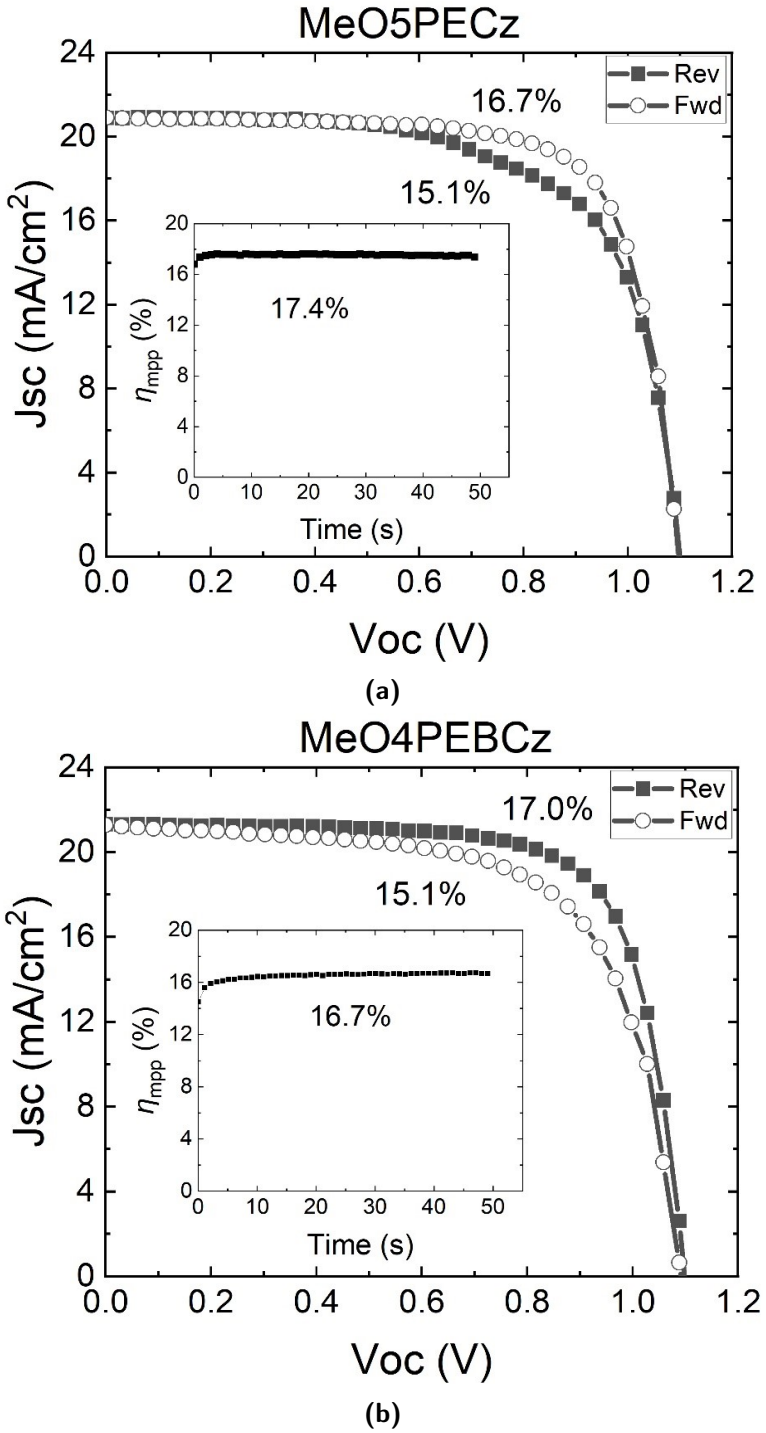

Figure 4.12: (a) J-V scan of MeO5PECz device. MeO5PECz was doped with both Li-TFSI and tBP (b) J-V scans of MeO4PEBCz device. MeO4PEBCz was doped with both Li-TFSI and tBP. The insets show their maximum power point tracked efficiencies for 50 seconds.

three devices made with different HTMs. This is partly due to the fast voltage sweep speed (0.61 V/s) we used in our solar cell measurements since we focus on the stabilized max power point tracking for our analysis. On the other hand, high hysteresis is common in n-i-p devices and is often attributed to the lower charge carrier mobility of the ETL, SnO_2, compared to the HTL [167, 168, 169]. Charges accumulate at the SnO_2/perovskite interface, causing increased hysteresis. Since hysteresis is highly scan-rate dependent, we analyze our devices based on the stabilized maximum power point efficiency instead of each forward/reverse scan efficiency.

The external quantum efficiency (EQE) spectra are also similar for devices made

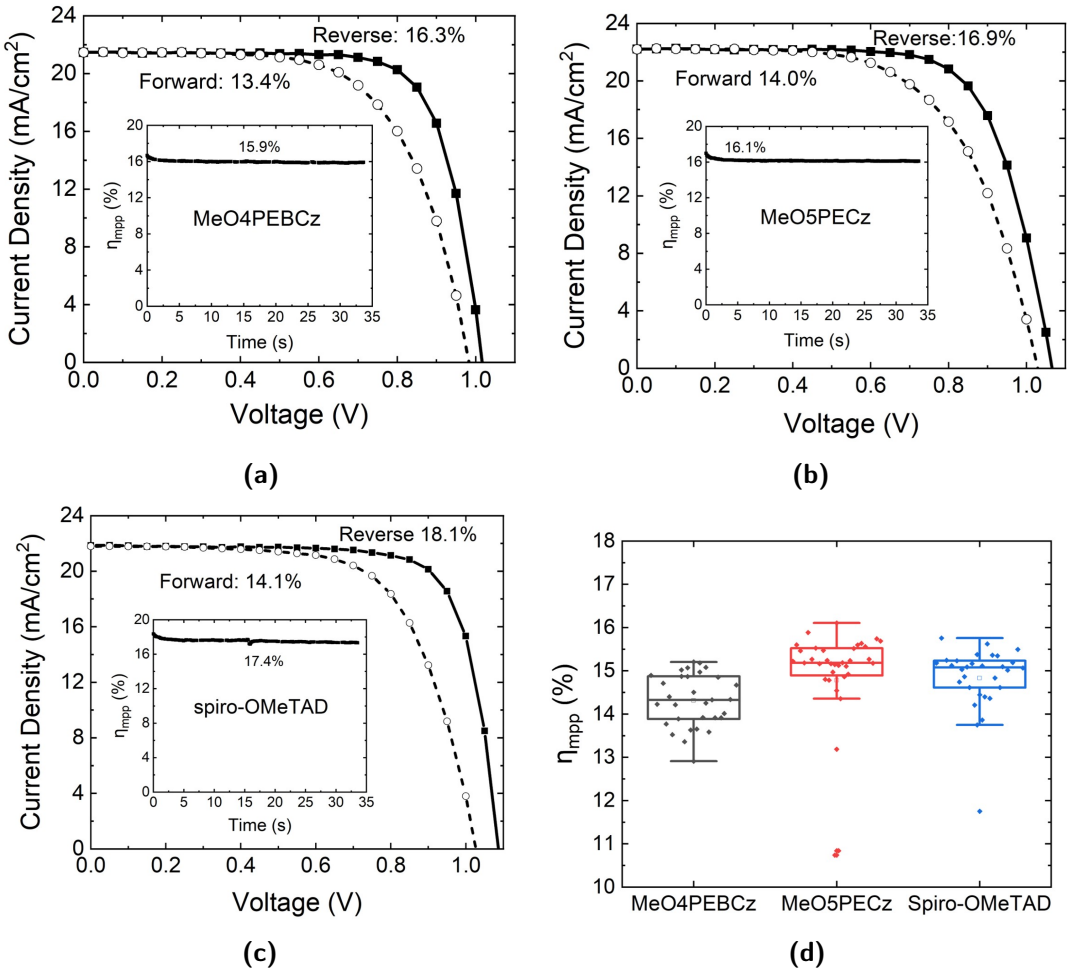

Figure 4.13: (a) Undoped MeO4PEBCz (b) undoped MeO5PECz (c) Spiro-OMeTAD (doped with Li-TFSI and tBP) as HTMs with their corresponding maximum power point tracked efficiency (η_{mpp}) shown in the insets. (d) Statistics of the η_{mpp} for all devices. Spiro-OMeTAD was doped with tBP and Li-TFSI. MeO5PECz and MeO4PEBCz were undoped.

Table 4.5: J_{sc}, V_{oc}, FF, PCE (reverse scans) of champion devices and average performance ± standard deviation (both forward and reverse scans) of a batch of devices fabricated with different HTMs, with or without dopants.

	J_{sc} (mA/cm^2)		V_{oc} (V)		FF (%)		PCE (%)	
	Best	Average	Best	Average	Best	Average	Best	Average
Undoped MeO4PEBCz	21.9	21.6±0.2	1.02	1.00±0.04	74	65±7	16.4	14.1±1.5
MeO4PEBCz , tBP	21.0	21.0±0.4	1.12	1.04±0.06	72	64±8	16.9	14.5±1.4
MeO4PEBCz, tBP, Li-TFSI	21.3	20.7±0.5	1.09	1.09±0.02	74	68±6	17.0	15.2±1.4
Undoped MeO5PECz	22.2	21.6±0.4	1.06	1.03±0.05	72	63±9	16.9	14.3±1.6
MeO5PECz, tBP	20.9	20.3±0.6	1.09	1.05±0.05	73	67±5	16.5	14.4±1.4
MeO5PECz, tBP, Li-TFSI	20.9	20.4±0.5	1.12	1.10±0.03	74	67±7	17.6	15.0±1.6
Undoped spiro-OMeTAD	21.8	21.7±0.2	1.05	1.01±0.08	66	53±7	15.1	11.6±1.9
Spiro-OMeTAD, tBP, Li-TFSI	21.9	20.5±0.6	1.09	1.01±0.06	76	67±8	18.1	14.6±2.1

with the three different HTMs (Figure 4.15). Notably, there are some differences between the Spiro-OMeTAD device and the carbazole HTM devices in the EQE spectra, likely to originate from the difference in the HTM layer thicknesses and coherent interference from the incident and light reflected from the rear Au electrode.

Based on the EQE and PLQY measurements for the full devices made with doped Spiro-OMeTAD, undoped MeO5PECz, and MeO4PEBCz, we can perform QFLS analysis on these full devices stacks and compare with the measured V_{oc} to assess the V_{oc} loss in each case (Figure 4.17).

The approach used follows that reported by Rau et al. [110]. Briefly, the black body photon flux is

$$\phi_{BB} = \frac{1}{4\pi^2\hbar^3c^2}\frac{E^2}{exp(\frac{E}{k_BT}) - 1} \tag{4.1}$$

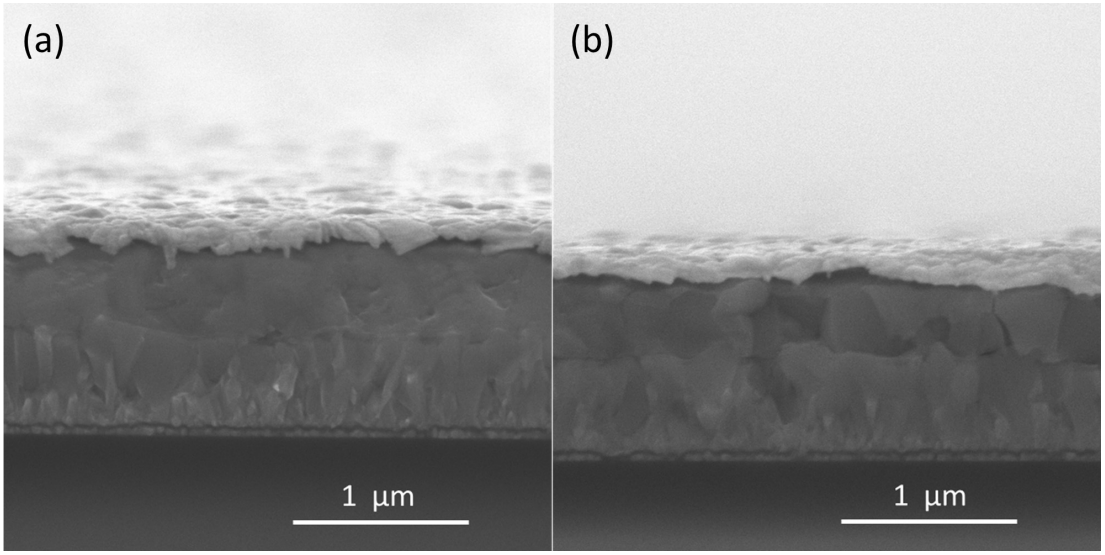

Figure 4.14: Cross-sectional SEM image of devices with (a) undoped MeO5PECz and (b) undoped MeO4PEBCz as HTMs.

Where $\hbar$ is the reduced Planks constant, k_B is the Boltzmann constant and T is the temperature. Assuming that the perovskite solar cell is at 300 K in thermal equilibrium with its environment, the dark radiative recombination current is

$$J_{0,em} = q \int EQE_{pv}(E)\phi_{BB}(E)dE = J_{0,rad} \tag{4.2}$$

With EQE_{PV} the photovoltaic external quantum efficiency of the perovskite solar cell and $J_{em,0}$ the current giving rise to emission, which also defines the dark radiative recombination current at V=0. From that, the radiative limit of the QFLS ($QFLS_{rad}$) at EQE_{EL}=1 can be calculated with the following equation

$$QFLS_{rad} = \frac{k_B T}{q} \ln \frac{J_G}{J_{0,rad}} \cdot 1 \tag{4.3}$$

Where J_G is the generation current under illumination, in this case, approximated to the short circuit current J_{sc}. We calculated the radiative V_{oc} of our perovskite absorber by using equation 4.3.

$$V_{oc,rad} = \frac{k_B T}{q} \ln \frac{J_{sc}}{J_{0,rad}} = 1.320V \tag{4.4}$$

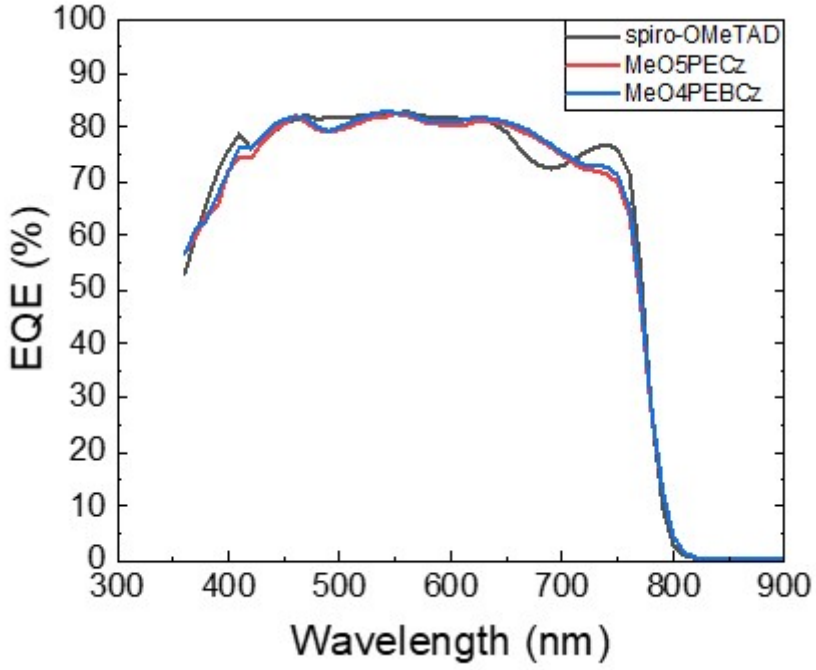

Figure 4.15: External quantum efficiency of devices with Spiro-OMeTAD (doped with tBP and Li-TFSI), undoped MeO5PECz and undoped MeO4PEBCz as HTMs.

$$\begin{aligned} QFLS &= k_B T \cdot \ln\left(\frac{J_{rad}}{J_{0,rad}}\right) \\ &= k_B T \cdot \ln\left(PLQY \frac{J_G}{J_{0,rad}}\right) \\ &= QFLS_{rad} + k_B T \cdot \ln\left(PLQY\right) \end{aligned} \tag{4.5}$$

From the QFLS analysis on the half-stacks, we find similar values for the devices fabricated regardless of HTM. As such, this finding highlights that, in a full device, even if the carbazole HTMs improve the perovskite/HTL interfaces, the detrimental SnO_2 interface dominates the V_{OC} losses and the QFLS in a working device. Therefore, as a future study, the ETL/perovskite interface should be concomitantly improved to fully benefit from the HTL optimizations that we report here.

Comparing the QFLS calculated for the full devices to the measured V_{oc} reveals a further loss in the complete devices. In all cases, the measured V_{oc} is lower than

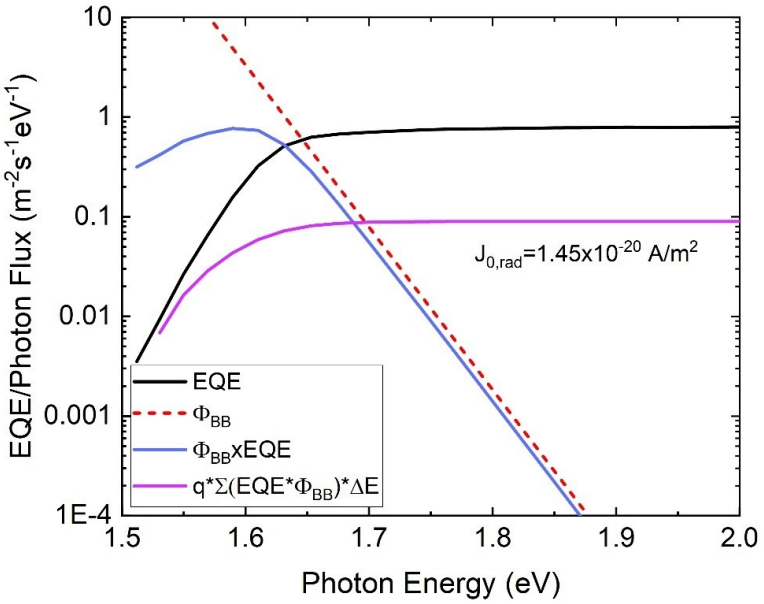

Figure 4.16: EQE_{PV} onset (black line) convoluted with the black-body (Φ_{BB}) radiation of the surroundings at 300 K (red dotted line). The perovskite emission spectra resulting from the convolution are plotted in blue. The emission spectra are integrated over the photon energy and multiplied by the elementary charge q in order to calculate the dark radiative current $J_{0,rad}$, plotted in purple.

the estimated QFLS of the device stack, and this difference is more severe for the cells employing the undoped enamine-based HTMs than those employing the doped Spiro-OMeTAD. The difference between the QFLS of the full device stack and the V_{oc} could be explained by either an energetic misalignment between the perovskite and the charge transport layers or the imperfect selectivity of the charge extraction layers [49, 50]. From the device results shown in Table 4.5 and Figure 4.17, devices without Li-TFSI and tBP dopants in the HTM have higher V_{oc} losses, which contradicts the QFLS results in Figure 4.9. However, if the ETL/perovskite interface is the dominant recombination channel, the improvements in the HTM will be obscured in the full devices [50]. Furthermore, there could be additional interactions between the dopants added to the HTM and the ETL/perovskite interface, especially under bias where lithium ions can readily diffuse to and alter the ETL/perovskite interface [136, 170]. Further studies are required to understand the potential interactions between the dopants and the ETL/perovskite interface. That said, looking at the

histogram (Figure 4.18), while the statistical V_{oc} of MeO4PEBCz is similar to that of Spiro-OMeTAD, the overall V_{oc} of MeO5PECz is slightly higher than the other two.

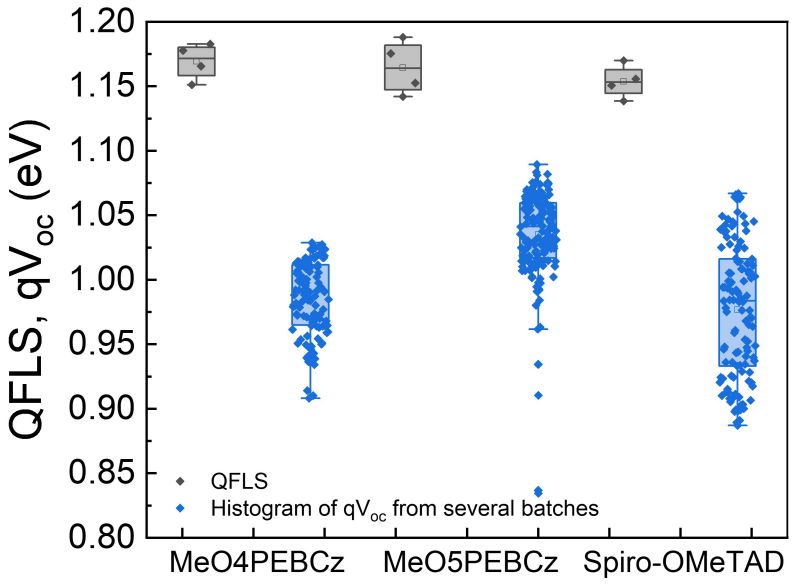

Figure 4.17: Calculated quasi-Fermi level splitting (QFLS) of champion full device stacks with the different HTMs (undoped MeO4PEBCz, undoped MeO5PECz, and doped Spiro-OMeTAD, with metallic electrodes) and measured steady-state open-circuit voltage (V_{oc}) of the same perovskite solar cells. We note that the QFLS analysis in Figure 4.9 was performed on bi-layer films.

According to the device statistics (Figure 4.19), while doping MeO5PECz seems to improve the η_{mpp} of the device, doping MeO4PEBCz does not improve the device efficiency to the same extent. We hypothesize that the higher conductivity of the undoped MeO4PEBCz accounts for the high device performance and removes the need for oxidative p-doping. Spiro-OMeTAD and MeO5PECz device efficiencies are improved by approximately 3% (absolute η_{mpp}, Figure 4.19) at an optimum concentration of 50 mol% Li-TFSI for Spiro-OMeTAD and 25 mol% Li-TFSI for MeO5PECz and 33 µL/mL tBP. In contrast, the performance of MeO4PEBCz devices is not affected by similar doping (25 mol% Li-TFSI and 33 µL/mL tBP). In fact, higher doping concentration reduces the η_{mpp} of the cells employing MeO4PEBCz. This discrepancy in the effectiveness of doping can be explained by the fact that pristine Spiro-OMeTAD has much lower mobility and conductivity than the carbazole-based enamines, and hence requires p-doping to have a suitably low series resistance for

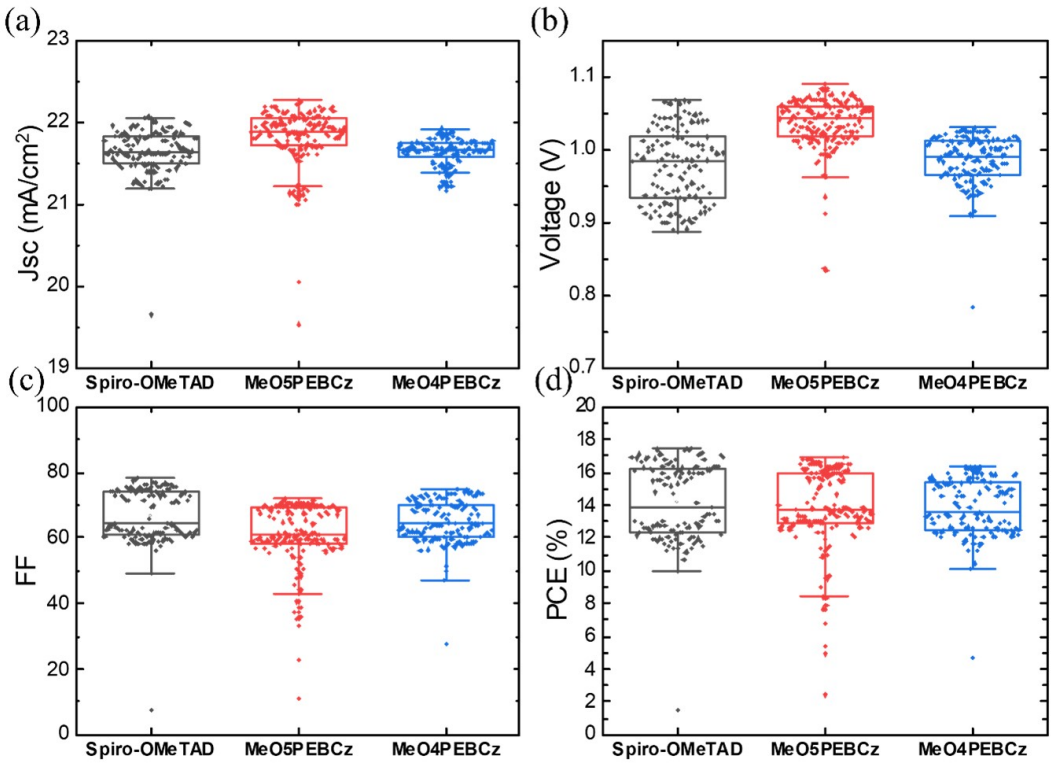

Figure 4.18: Box plots of the device (a) short-circuit current, (b) open-circuit voltage, (c) fill factor, and (d) power conversion efficiencies. Spiro-OMeTAD was doped with both tBP and Li-TFSI, while the carbazole-based HTMs were dopant-free.

the conduction of holes out of the solar cell. Besides the intrinsic properties of the HTM, another effect that could explain why the PCEs of devices employing Spiro-OMeTAD increase significantly upon doping, is that the optimized Spiro-OMeTAD layer (200 nm) is thicker than the undoped carbazole-based enamine layers (45∼55 nm). Predictably, doping is more necessary for thicker transport layers because the resistance through the layer will increase linearly with increasing thickness, causing a fill factor drop in devices [126]. The series resistance could be reduced by decreasing the Spiro-OMeTAD layer thickness, but at a cost of introducing pinholes and lowering shunt resistance, since this material is not effective at forming continuous films when the thickness is decreased. Hence, the ability to form a continuous film in a thin layer is another important property of these carbazole-based enamines HTMs.

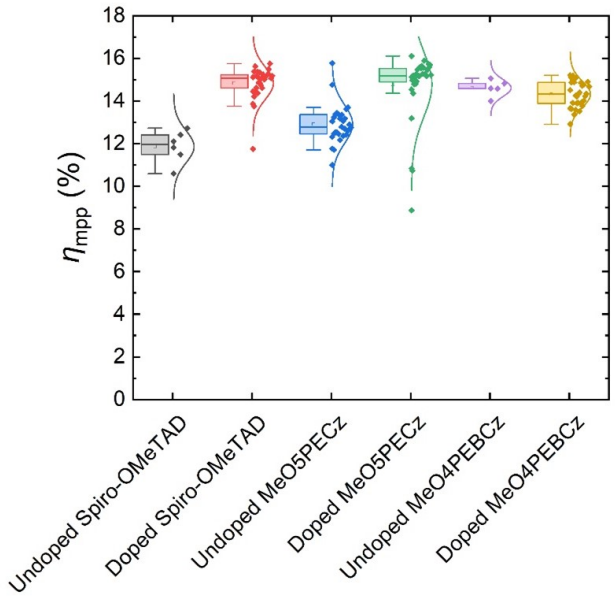

Figure 4.19: Maximum power point tracked efficiencies (η_{mpp}) (for 33 seconds) comparison between undoped HTMs and their corresponding counterparts doped with both Li-TFSI and tBP. Spiro-OMeTAD was doped with 50 mol% Li-TFSI and 33 µL/mL tBP. Both MeO5PECz and MeO4PEBCz were doped with 25 mol% Li-TFSI and 33 µL/mL tBP which were optimized for best device performances.

4.7 Device Stability

Since these new HTMs perform well without dopants and have higher glass-transition temperatures (T_g) than Spiro-OMeTAD, we carried out stability studies on complete solar cells. The n-i-p device stack (shown in Figure 4.11) was modified for better stability by introducing a phenyl-C61-butyric acid methyl ester (PCBM) interlayer between the SnO_2 and the perovskite absorber layer: glass/FTO/SnO_2/PCBM/ $FA_{0.83}Cs_{0.17}Pb(I_{0.9}Br_{0.1})$ /HTM/Au. Upon the addition of a PCBM layer, there is no significant difference in the device performance aside from a slight enhancement in the V_{oc}. Devices with three different HTMs: Spiro-OMeTAD doped with Li-TFSI and tBP, undoped MeO5PECz, and undoped MeO4PEBCz were aged at 85°C in a nitrogen atmosphere (Figure 4.20a). While devices employing Spiro-OMeTAD showed fast degradation within the first 24 hours, the devices employing the two new carbazole-based enamines exhibited a striking contrast – they improved in efficiency over the

first 100 hours and maintained > 80 % of their peak performance after 1,000 hours. Thermal degradation of Spiro-OMeTAD devices has been reported in the literature and has been shown to be caused by the formation of voids at the Spiro-OMeTAD/ perovskite interface [139, 140, 165], post-iodine doping of Spiro-OMeTAD from the perovskite film during aging [171], tBP reacting with Spiro-OMeTAD forming new pyridinated species [172, 173], and Spiro-OMeTAD recrystallizing at 85°C due to its low glass transition temperature [158, 174, 175].

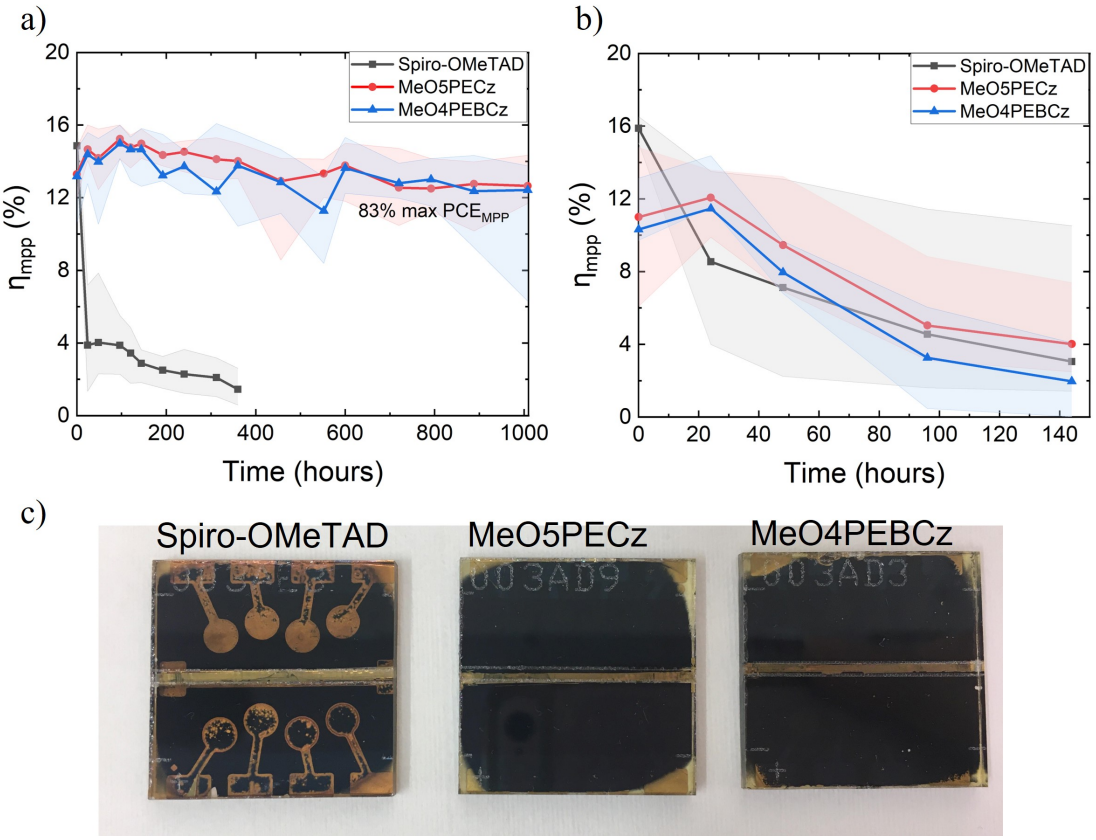

Figure 4.20: (a) 85°C dark aging under a nitrogen atmosphere, removed occasionally and tested at room temperature in air, with max power point tracked efficiency shown, averaged over 18 devices. (b) Efficiency as a function of time for encapsulated perovskite cells aged under AM 1.5 full spectrum sunlight (xenon lamp Suntest aging box) at 85°C. (c) Photograph of (unencapsulated) devices after 7 days of ambient LED light aging (with 60 mW/cm^{-2} intensity under 40°C).

There have been many tests and exemplifications of good stability of perovskite solar cells, in both the p-i-n and n-i-p configuration, stressed under simulated sunlight

at normal operating temperatures [176, 53]. However, the combination of temperature and light is particularly stressful for perovskite solar cells. Although there have been very encouraging results for ambient 65°C and 85°C full-spectrum light soaking for p-i-n cells [177, 178], there have been few reports of stress tests of n-i-p cells under combined (heat and light) stress conditions. There are some reports of n-i-p device stability with SnO_2 under combined light and 65°C in a nitrogen atmosphere [179] or 55°C ambient light stability test [180]. Here we assess the stability of our n-i-p perovskite solar cells comprising the three different HTMs, encapsulated and subject to full-spectrum 1 sun irradiance at 85°C ($\pm$3°C) in ambient conditions; the results of which we show in Figure 4.20b. Unfortunately, all the devices degraded rapidly under the combination of thermal and light stress, however, the degradation trends are somewhat different. The devices made with the new carbazole-based HTMs improved in the initial 24 hours of aging and then gradually degraded, whereas Spiro-OMeTAD-based devices degraded rapidly from the beginning. These results are consistent with the thermally driven degradation due to the Spiro-OMeTAD HTM likely dominating the first 24 hours of aging, but a further degradation mechanism takes over when devices are stressed for longer times under light at elevated temperatures. We postulate that reactions and degradations at the perovskite/n-type layer heterojunction are driving this degradation under light and temperature.

In order to probe the influence of the atmosphere (humidity and oxygen) upon the illuminated cells, we subject complete non-encapsulated devices to LED white light illumination with close to 0.6 sun equivalent irradiance, in air at 40°C, under open-circuit conditions. In Figure 4.20c we show photographs taken at the end of 7 days of aging under the LED light. After stressing, the gold contacts on top of the Spiro-OMeTAD devices have become visible from the glass side, whereas the devices employing MeO5PECz and MeO4PEBCz remain opaque, since the perovskite beneath the new HTMs remains black. This indicates that some form of electrochemical or galvanostatic degradation is taking place within the devices employing Li-TFSI and

tBP doped Spiro-OMeTAD, possibly driven by the migration of water and/or lithium ions into the active layer of the device [47].

These results illustrate that although we have now achieved thermally stable n-i-p cells with the new HTMs and improved stability under light soaking in ambient conditions, the issue of good stability under combined light and elevated temperature remains unsolved. We hypothesize that further improvements to the n-type ETL/perovskite heterojunction and the electrodes are now required, in order to deliver competitively stable n-i-p perovskite solar cells.

4.8 Conclusion

We have presented the synthesis of two novel carbazole-based enamines HTMs. The new HTMs can be obtained in a simple synthesis procedure from commercially available materials and without the use of expensive palladium-catalyzed cross-coupling reactions. Moreover, none of the investigated compounds required column chromatography or any other expensive purification techniques, making them more than tenfold cheaper at research volumes than Spiro-OMeTAD. Both new carbazole-based enamine materials are thermally stable, have high T_g, suitable energy levels and bandgap, and relatively high charge carrier mobilities (up to 1.1×10^{-3} $cm^2V^{-1}s^{-1}$), negating the need for dopant additives in the solar cells.

We demonstrated devices made with MeO5PECz and MeO4PEBCz that can reach $>$16% PCEs without adding Li-TFSI or tBP into the HTM solutions. Through QFLS analysis, we have revealed that significant further improvements in both V_{oc} and efficiency will be possible by focusing future efforts upon improving the ETL/perovskite interface in conjunction with employing the new HTMs reported here. Leaving out Li-TFSI and tBP additives improves the device's moisture and thermal stability, since no hygroscopic additives are present, and no volatile dopants can escape under elevated temperature nor react with the perovskite. The low synthetic cost and less material required in the optimized devices make the new HTMs significantly more

economically viable to integrate into perovskite solar cell devices and tandem modules. Furthermore, the simplicity of synthesis and high operational stability of devices may make these HTMs the new standard HTMs for perovskite PV research going forward.

CHAPTER 5

Benzylamine Passivation of Wide-bandgap Perovskites

5.1 Introduction

The tuneable bandgap (E_g) of metal halide perovskite (MHP) provides an opportunity for integration alongside silicon solar cell technology to fabricate perovskite/silicon tandem photovoltaics capable of yielding PCEs of over 33% [16]. To maximize performance, a two-terminal perovskite/silicon tandem cell requires a top cell with $1.65 < E_g < 1.70$ eV [181]. Typically, mixed-cation mixed-halide perovskites have been employed as the photoabsorber in such top cells. However, many challenges remain for perovskite to be integrated with silicon. For example, their typical lifetime is not commensurate with that of silicon. Particularly, the wide-bandgap mixed-halide perovskite on top of the silicon suffers from a range of degradation mechanisms, many of which are exacerbated by compositional inhomogeneity in the as-fabricated materials [182, 183]. In-operando ion migration, including halide segregation, leads to

reduced photocurrent over time [184]. Furthermore, degradation to photo-inactive non-perovskite phases can reduce photoabsorption and prevent charge carrier extraction leading to reduced photocurrent and device fill factor (FF) [185]. Having established high-performance PSCs of appropriate E_g, much current research effort is dedicated to reducing trap states and suppressing sources of instability in PSCs.

Amines have long been employed as additives to passivate defects in perovskites to improve their photoluminescence and stability. Zheng et.al [96] found that via ligand anchoring, amines can alter the perovskite growth, exhibiting stronger orientation and lower trap density. Feng et al. [186] investigated the defect passivation efficacy of different alkylamine chain lengths and found that amines can anchor on the surface of perovskite grains. Not only can alkylamine additives promote more oriented perovskite growth, but also increases the grain size and the hydrophobicity of the perovskite. Amines can interact with the perovskite precursor solutions in several ways. They can coordinate with Pb and assist in the dissolution of PbI_2/$PbBr_2$ [187]. Kerner et al. [103] found that the acid-base reaction between PbI_2 and alkylamines slowly forms (alkylamido)lead species and alkylammonium halides. Amines can also proton-exchange with acidic species such as ammoniums and amidiniums. Recently, we have shown that a similar reaction occurs between ethylenediamine and formamidinium in perovskite precursor solutions to form imidazolinium achieving more homogeneous mixed-halide perovskite films and enhanced device performance for a 1.69 eV bandgap perovskite [188]. The new organic species formed in the solution can either co-crystallize in the precursor phase and then subsequently be lost, or in secondary phases that are retained in the final material. These amine interactions in the precursor solution will affect the crystallization process, ultimately influencing the composition, morphology, and heterogeneity of the polycrystalline MHP film.

While the effects of adding linear alkylamines into the perovskite precursor solutions have been more extensively studied, there are fewer reports investigating the effects of amines incorporating aryl or heteroaryl groups. There have been reports of their use as surface passivation agents. For example, Jiang et al. used

3-(aminomethyl)pyridine (3-APy) as a perovskite surface treatment and found that 3-APy reacts with FA via a similar addition-elimination reaction to form N-(3- methylpyridine) formamidinium ($MPyFA^+$) which can passivate surface defects [189]. Through this passivation method, they achieved a record 25.35% stabilized power output p-i-n solar cell and impressive stability [189]. Herein, we report using benzylamine (BnAm) as an additive to improve the structural and optoelectronic properties of perovskite materials with a range of bandgaps relevant to Si/perovskite tandem photovoltaics. The use of BnAm as an additive in the perovskite precursor significantly reduces non-radiative recombination, supresses halide segregation, and enhances the long-term stability of wide bandgap perovskite films. Halide segregation of wide-bandgap perovskite is also suppressed. X-ray diffraction (XRD) and nuclear magnetic resonance (NMR) were used to elucidate the mechanism underlying the enhanced properties.

5.2 Reaction of Benzylamine with Formamidinium in Precursor Solution

To investigate the occurrence and rate of any chemical reactions between formamidinium (FA^+) and BnAm when the latter is added to perovskite precursor solutions, we carried out a range of nuclear magnetic resonance (NMR) spectroscopy experiments. Figure 5.3a shows a ^1H NMR spectrum carried out on a solution of formamidinium iodide (FAI) in deuterated dimethyl sulfoxide (DMSO-d6) with 5 mol% BnAm added. By comparison with similar spectra of FAI, BnAm, and benzylammonium iodide (BnAI) alone (Figure 5.4), it is evident that none of the 5 mol% BnAm added is found in solution, nor is it simply protonated. Instead, a mixture of FAI and a new benzyl-containing organic is detected. The new species shows a singlet with chemical shift (δ) at 7.99 ppm, close to the methine environment of FA^+ (7.86 ppm). Correspondingly, ^{13}C NMR of the same solution (Figure 5.3b) shows a new signal at 154.7 ppm, suggesting the presence of a new non-FA^+ methine environment. Heteronuclear single quantum correlation (HSQC) spectroscopy, which shows

cross-peaks between ^{1}H and ^{13}C nuclei that are directly bonded, confirms that the two new signals described correspond to bonded nuclei (Figure 5.3c). Moreover, the HSQC spectrum highlights the correlation between new signals at 44.9 and 4.48 ppm in the ^{13}C and ^{1}H spectra respectively and also shows that the broad singlet at 4.52 ppm is not bonded to any ^{13}C environment (but to a nitrogen). Taken together, we interpret these data as indicating the formation of N-benzyl formamidinium ($BnFA^{+}$) by nucleophilic attack of BnAm on FA^{+}, which is present in 20-fold excess in this solution stoichiometry, with subsequent elimination of ammonia. We show this reaction scheme in Figure 5.3d, and account for it mechanistically in Figure 5.1. Notably and in spite of the nomenclature we have employed, unlike in FA^{+} where the 3-centre, 2-electron conjugated amidinium system deshields all NH environments equally, in $BnFA^{+}$, we are able to resolve independent amine (4.52 ppm) and iminium (7.99 ppm) environments in the cation. The presence of both a Lewis basic amine moiety and a positively charged iminium is expected to have direct implications on the nature of coordination between $BnFA^{+}$ and other species in perovskite precursor solutions.

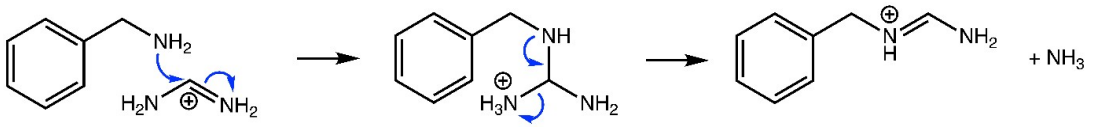

Figure 5.1: Mechanistic justification for the formation of N-benzyl formamidinium ($BnFA^{+}$). Nucleophillic addition of BnAm to FA^{+}, along with acidic H^{+} transfer, is followed by the elimination of ammonia, which is entropically favorable. This figure was made by Benjamin Gallant.

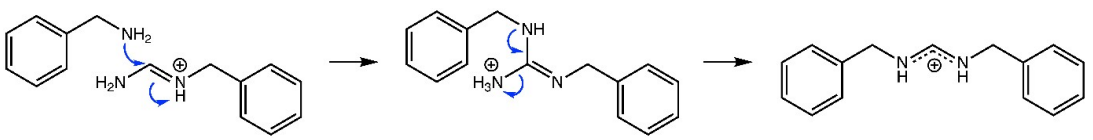

Figure 5.2: Mechanistic justification for formation of N,N'-dibenzyl formamidinium ($2BnFA^{+}$). Nucleophillic addition of BnAm to $BnFA^{+}$, along with acidic H^{+} transfer, is followed by the elimination of ammonia. Release of ammonia is entropically favorable, while reformation of the three centre-two electron conjugated amidinium system is enthalpically favored. However, this process becomes increasingly unlikely with increasing FA^{+}:BnAm stoichiometry; excess FA^{+} leads to the rapid reaction of almost all BnAm with FA^{+}, leaving little or none to react with the forming $BnFA^{+}$. The NMR analysis was done by Benjamin Gallant.

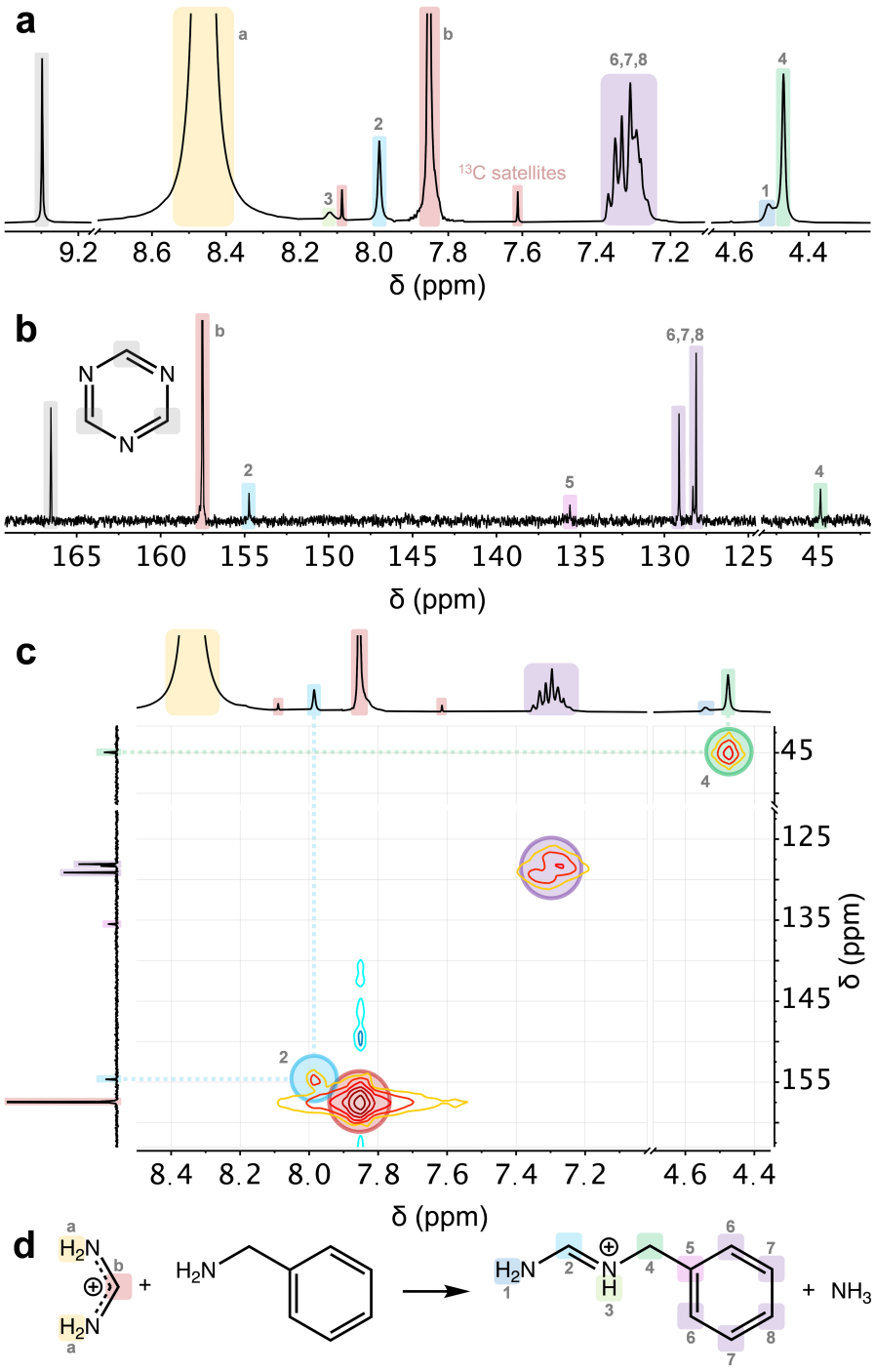

Figure 5.3: (a) ^{1}H NMR of BnAm and FAI in d6-DMSO. (b) ^{13}C NMR of BnAm and FAI in d6-DMSO. (c) HSQC of the solution. (d) Schematic of reaction between FAI and BnAm.The NMR analysis was done by Benjamin Gallant.

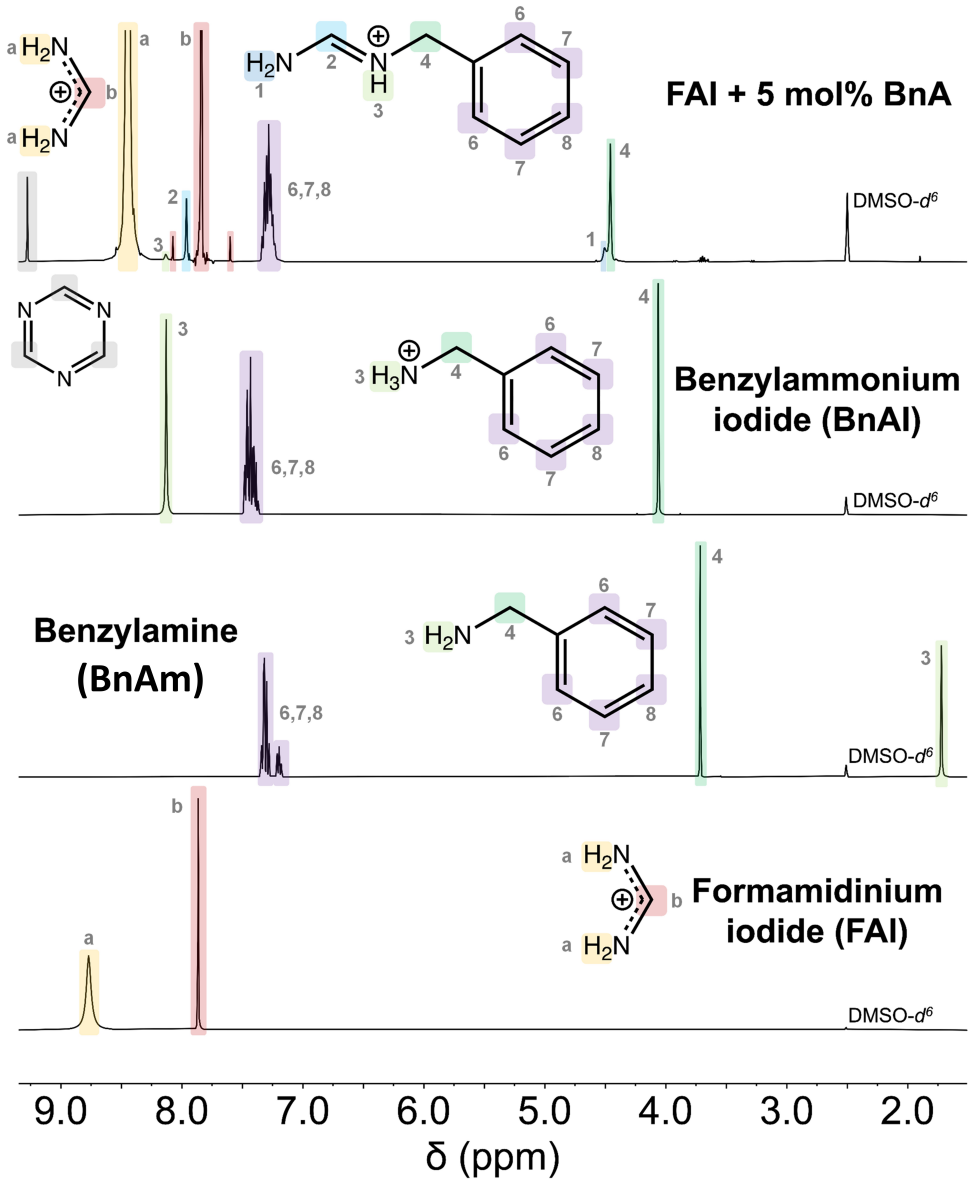

Figure 5.4: Liquid-state ^{1}H nuclear magnetic resonance (NMR) spectra of (bottom to top) formamidinium iodide (FAI), benzylamine (BnAm), benzylammonium iodide and a mixture of 5:75 BnAm:FA^{+} all dissolved in DMSO-d6 at equivalent concentrations. Although the presence of coordinating halides in solution can shift signals in liquid NMR, if concentrations of all species are kept equivalent we expect these effects to be consistent, particularly for ^{1}H in apolar C-H bonds. As such, that signals in the FAI + 5 mol% BnAm sample do not align with those in either BnAm or BnAl demonstrates that these species are not present in this solution. The NMR analysis was done by Benjamin Gallant.

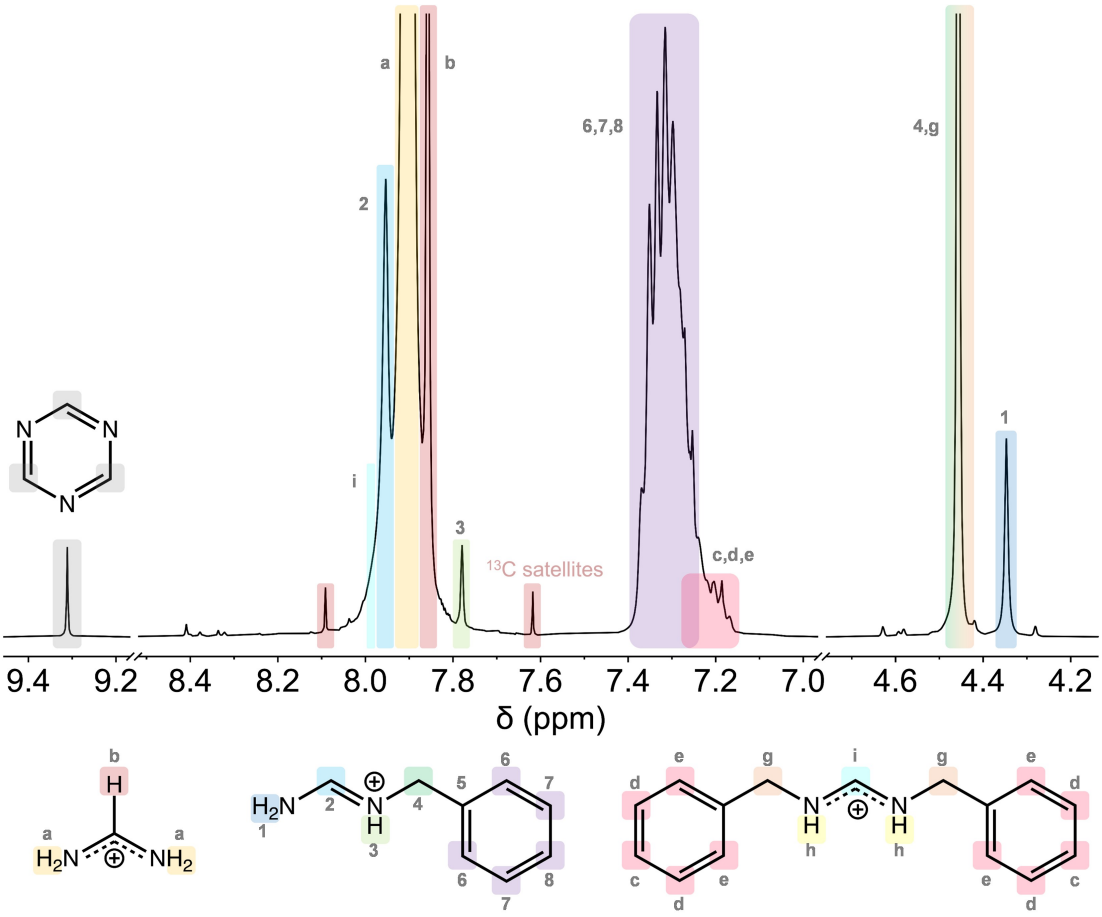

Figure 5.5: Liquid-state ^{1}H NMR spectrum of a solution of FAI + 20 mol% BnAm in DMSO-d6. Formation of $BnFA^{+}$ via the mechanism set out in 5.1 is apparent. However, an additional set of signals is observed, which correspond to the formation of $2BnFA^{+}$, as set out in Figure 5.2. The NMR analysis was done by Benjamin Gallant.

The BnAm is reacted to near completion, as the hydrogen signal from the amine is gone (Figure 5.4). By comparing the ^{1}H NMR spectrum of FAI+5 mol%BnAm with BnAI, it is clear that benzylammonium is not formed from this reaction either.

The use of higher BnAm stoichiometries leads to more complex precursor solution chemistry. For <5 mol% BnAm the substantial excess of FA^{+} in the solution ensures that the only product formed in detectable quantities is $BnFA^{+}$. However, as we show in Figure 5.2, when 20 mol% BnAm is added N,N'-dibenzyl formamidinium ($2BnFA^{+}$) is formed via condensation of a second BnAm molecule with $BnFA^{+}$ in solution.

5.3 BnAm Bulk Additive Thin Film Phase and Morphology

To investigate the effects of the $BnFA^+$ additive on perovskite films, wide-bandgap perovskite films were prepared with a solution composition $FA_{0.75}Cs_{0.25}$ $Pb(I_{0.8}Br_{0.2})_3$ along with a range of BnAm additive concentrations from 0∼5 mol%.

Time-of-flight secondary-ion spectroscopy (Tof-SIMS) data were acquired on a 0.6 mol% BnAm additive perovskite film to determine how $BnFA^+$ is distributed within it (Figure 5.6). Since Tof-SIMS uses sputtered ions to characterize the chemical nature of the material, the first data points in Tof-SIMS can vary significantly. This is because the cations under analysis are not yet destroyed and the surface chemical environment can be different from the bulk so the first points are not fully reliable. As time passes, the sputtering ion beam reaches deeper into the thin film. At around 40 s, the sputtering ion beam reaches the glass substrate. According to the depth profile, the $BnFA^+$ fragment is mostly distributed around the bottom surface (perhaps also the top surface) of the film.

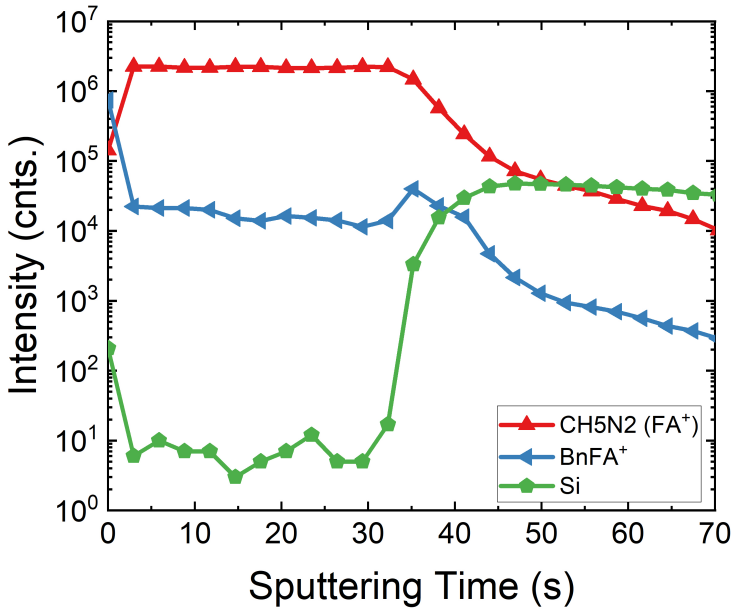

Figure 5.6: Tof-SIMS molecular distribution of perovskite film with 0.6 mol% of Bza additive. The Tof-SIMS was done by Yangwei Shi and Jian Wang, University of Washington, Seattle.

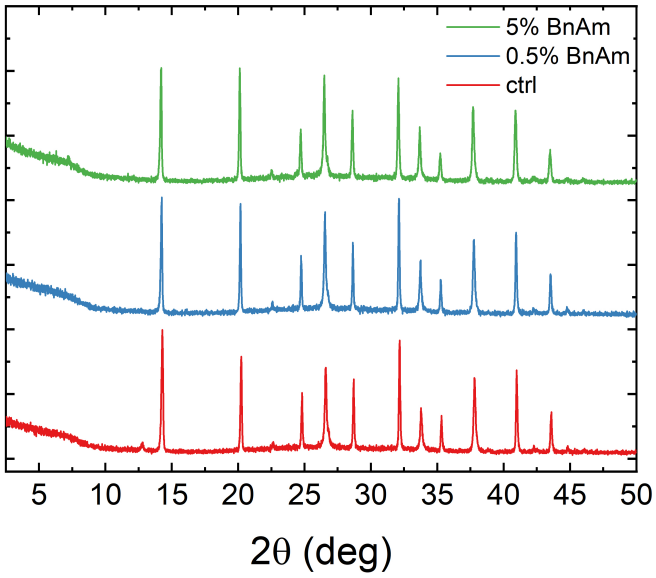

Figure 5.7: XRD of $FA_{0.75}Cs_{0.25}Pb(I_{0.8}Br_{0.2})_3$ perovskite films with different amounts of BnAm additive. The perovskite films were made on FTO substrates.

X-ray diffraction (XRD) was initially acquired from these thin films. As the amount of BnAm increases, a peak at 12.6° corresponding to PbI_2 in the 0 mol% control film disappears, while a new peak around 7.0° starts forming. BnAm consumes excess PbI_2 first and then the 3D perovskite to form a quasi-2D perovskite (Figure 5.7).

The quasi-2D phase large cation formed in the >5 mol% BnAm film likely only involve FA^+ and not Cs^+, so the BnAm was added directly into pure $FAPbI_3$ to confirm the phases present that only consists of $BnFA^+$. To exaggerate the quasi-2D phase and mimic the surface quasi-2D seen in the surface treatment case, larger amounts (20% and 50%) of BnAm are added into a pure $FAPbI_3$ perovskite (Figure 5.8a). Indeed, the peaks that appear at 20% BnAm in $FAPbI_3$ are the same in the FACs-based perovskite. Interestingly, in the 20% and 50% BnAm-$FAPbI_3$ films, the lower dimensional peaks seen in the 3 vol% and 5 vol% surface treatment case can be reproduced (see Figure 5.9).

While in the 20% BnAm case, extra lower dimensional diffraction peaks start forming, this does not happen with the 20% benzylammonium halide counterparts (see Figure 5.8b). In the case of high amounts of BnAI, BnABr, and BnACl additives,

the peaks are still the same as the pure $FAPbI_3$, which suggests that BnAX additive does not consume the 3D perovskite to form secondary phases. Amines are good solvents for perovskite, and amine coordination to PbI_2 is preferred to even strong perovskite solvents like DMSO. This is also evident in the top-view scanning electron microscopy (SEM) images in Figure 5.10. The excess BnAm added reacts with PbI_2 and consumes it. Hence, we hypothesize that while BnAm passivates the perovskite by reacting with the organic cation and dissolve excess PbI_2 to form 2D phases, the benzylammonium halides do not assist in dissolving PbI_2, but instead passivates through filling in cation and anion vacancies by coordinating with Pb^{2+}.

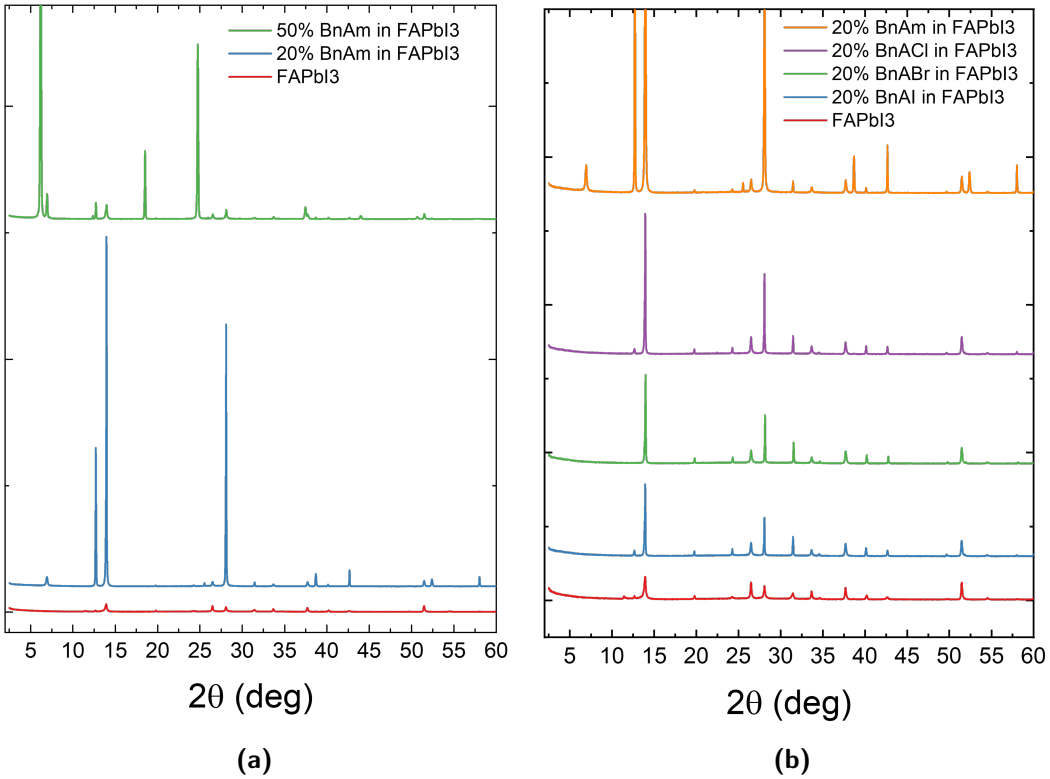

Figure 5.8: (a) XRD of $FAPbI_3$ films with 20 mol% and 50 mol% BnAm addition (b) $FAPbI_3$ film with 20 mol% of different benzylammonium halides (BnAX).

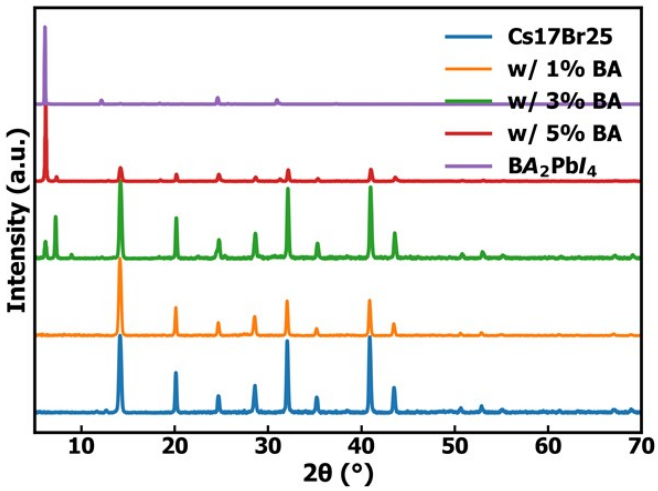

Figure 5.9: XRD patterns of $FA_{0.75}Cs_{0.25}Pb\ (I_{0.8}Br_{0.2})_3$ perovskite films with 1 vol%, 3 vol%, and 5 vol% BnAm surface treatment. This XRD experiment was done by Yangwei Shi from the University of Washington, Seattle, US.

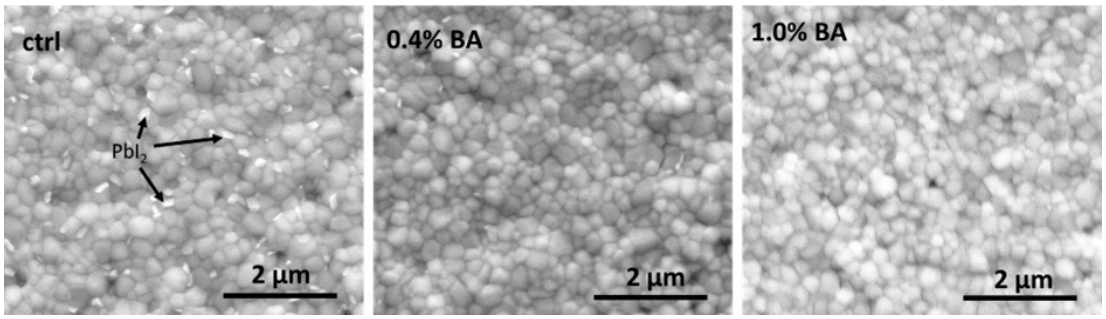

Figure 5.10: Different mol% of BnAm additive in 1.68eV $FA_{0.75}Cs_{0.25}Pb(I_{0.9}Br_{0.1})_3$ perovskite. 1% PbI_2 excess in all of the films.

5.4 Optoelectronic Properties of the Thin Films

To see if the $BnFA^+$ has a passivation effect on the surface and grain boundaries of the perovskite, optoelectronic characterizations were done on the thin films. The photoluminescence quantum yield (PLQY) were measured for these films under a 532 nm laser of 1 sun intensity (53.83 mW/cm^2 for this 1.68 eV E_g perovskite). According to Figure 5.11, the PLQY is optimized when 0.3 mol% is added to the perovskite. Notably, the PL peak position is also slightly red-shifted a few nanometers when BnAm is added (Figure 5.12a). However, the absorption onsets (Figure 5.12b) of the perovskite films with different amounts of BnAm are all identical. This phenomenon is likely due to charge carriers generated in the higher bandgap phase transporting to the lower bandgap phase and then emitting because PL is more sensitive to changes in material composition compared to UV-vis. The apparent peak shift of the PL could also be due to high-energy photo re-emission by a higher bandgap and re-absorption by a lower bandgap. This effect is most prominent when the BnAm additive amount is increased to 5%. It appears that there is a main peak in the original peak position of 740 nm and an extra "shoulder". Since there is a large overlap between the PL and the absorption spectrum (a small Stokes shift), it is possible that there is a small amount of photon recycling, which has a positive effect on the perovskite films [190].

2D spatial mapping (Figure 5.13a and 5.13b) also shows a slight enhancement in the intensity and homogeneity of the QFLS with 0.1 mol% and 0.3 mol% of BnAm additive. However, too much $\sim$1.0 mol% of BnAm actually quenches the QFLS.

Consistent with the surface treatment, the absorbance of the films slightly dropped when a large amount of BnAm (5 mol%) is added, which suggests that some of the black 3D perovskite is etched thinner and/or converted into a less absorbing quasi-2D/2D perovskite.

The PLQY spectrum was recorded over time under a high spectral irradiance of 1,300 mw/cm^2, 532 nm laser to probe accelerated halide segregation in this 1.68 eV mixed halide perovskite. A PLQY spectrum was taken every 30 seconds for both the

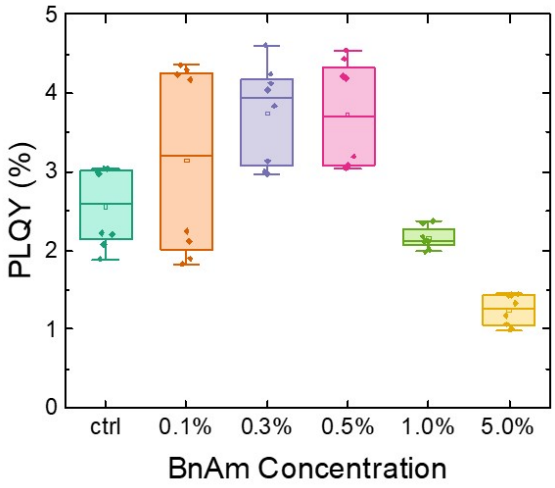

Figure 5.11: Photoluminescence quantum yield (PLQY) of $FA_{0.75}Cs_{0.25}Pb(I_{0.8}Br_{0.2})_3$ with 0.1 mol%∼5.0 mol% BnAm additive measured with a 532 nm laser at 100 mW/cm^2 (AM 1.5) intensity. Four points were measured on each film.

control perovskite sample and the 0.3 mol% BnAm additive sample on glass. As can be seen from the 3D color maps (Figure 5.14a and 5.14b), within the first 30 seconds, the control samples has already dropped to a lower intensity, whereas, the 0.3 mol% BnAm additive perovskite has a much more gradual drop in intensity. In fact, it has not dropped to the same intensity after 6 minutes of high-intensity laser exposure. From the 2D absolute PL spectra (Figure 5.14c and 5.14d), it is also apparent that the control sample's peak position has already red-shifted several nanometers, indicating halide-segregation and charge carrier funneling to a lower, iodide-rich perovskite E_g; whereas, the PL peak position of BnAm additive perovskite still has not dropped to the same position after 6 minutes. It is speculated that the bulky $BnFA^+$ cation which likely gets excluded to the grain boundary, can retard the rate of I^-, Br^- migration, which ultimately slows down halide segregation. As a result, it may be promising to use BnAm to improve the wide-bandgap perovskite stability under light.

Time-resolved photoluminescence (TRPL) was done on the thin films and fitted with a stretched-exponential decay curve, according to Equation 5.1 and 5.2. The 405 nm laser source probes close to the surface. According to the TRPL fitting results, the average lifetime, τ, between the front and back illumination was calculated. The

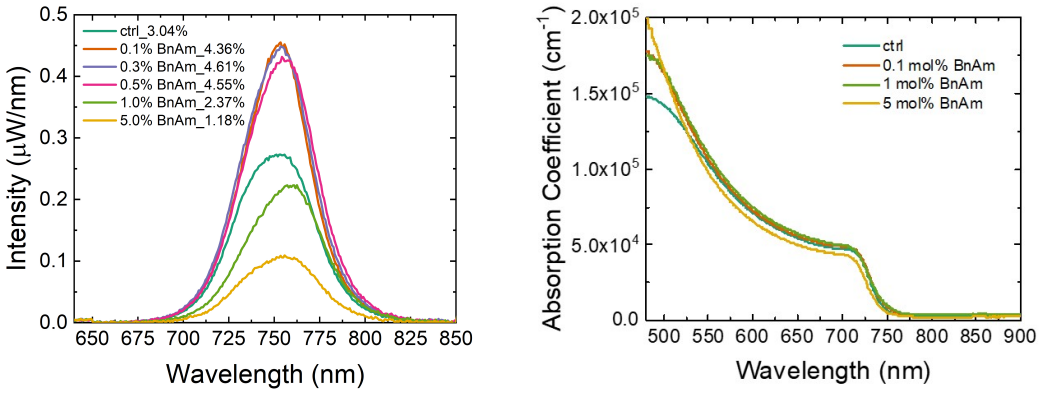

(a) **(b)**

Figure 5.12: (a) Photoluminescence quantum yield (PLQY) spectra with their best PLQY listed. (b) UV-vis absorption spectra of $FA_{0.75}Cs_{0.25}Pb(I_{0.8}Br_{0.2})_3$ with BnAm additiveUV-vis absorption spectra of $FA_{0.75}Cs_{0.25}Pb(I_{0.8}Br_{0.2})_3$ with 0.1 mol%∼5.0 mol% BnAm additive. Corrected with transmission/reflection mode measurements.

average lifetime increased from 0∼0.3 mol% BnAm and starts dropping again at 0.5 mol%. While the control sample has an average lifetime of 305.8 ns, the 0.3 mol% BnAm sample has an enhanced lifetime of 333.0 ns. The β however, consistently decreases as more BnAm is added, from β=0.78 at 0 mol% to β=0.65 at 0.3 mol%, which suggests that the compositional homogeneity is dropping and there could be mixed $BnFA^+$-rich phases at the surface and grain boundaries.

$$y = a\exp(-\frac{t}{\tau_c})^{\beta} \tag{5.1}$$

$$\tau_{avg} = \frac{\tau_c}{\beta}\Gamma(\frac{1}{\beta}) \tag{5.2}$$

The beta value is $0< \beta <1$ and it indicates the heterogeneity of carrier lifetimes distribution. When beta is closer to 0, there is a more heterogenous distribution, whereas, when it is close to 1, the material has a more homogenous distribution.

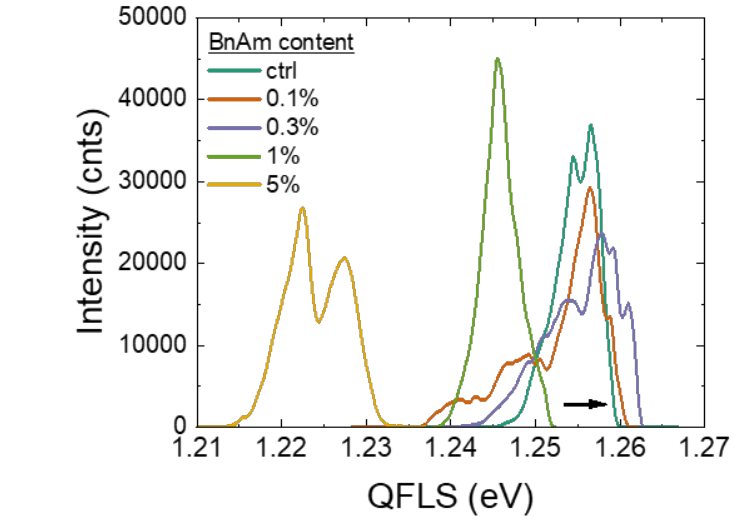

(a)

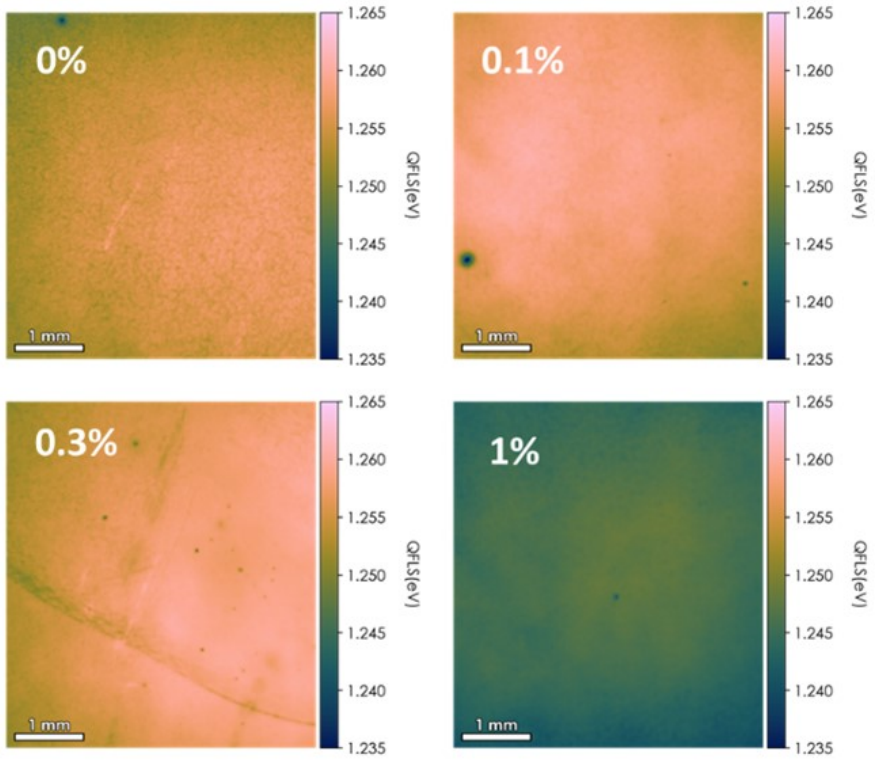

(b)

Figure 5.13: (a) QFLS of each sample calculated by measuring PLQY of four points from photoluminescence imaging. (b) Spatially-resolved QFLS for perovskite films with the first four BnAm concentrations in (a). The PL imaging and analysis were done by Akash Dasgupta, University of Oxford.

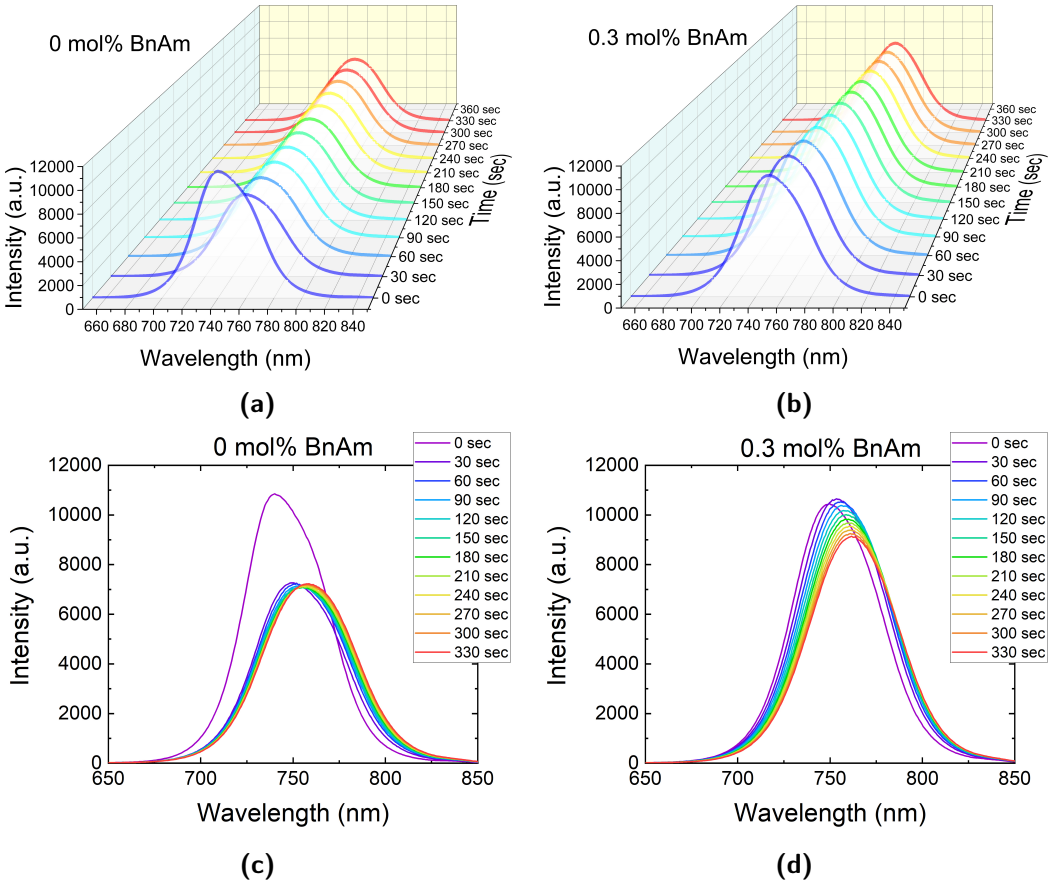

Figure 5.14: Time-dependent photoluminescence color map of (a) pristine $FA_{0.75}Cs_{0.25}Pb(I_{0.8}Br_{0.2})_3$ perovskite and (b) perovskite with 0.3 mol% BnAm additive in it. (c) The 2D PL spectra of the reference sample over time. (d) The 2D PL spectra of perovskite with 0.3 mol% BnAm additive over time. All samples were measured with a 532 nm laser under 1,300 mW/cm^2 intensity.

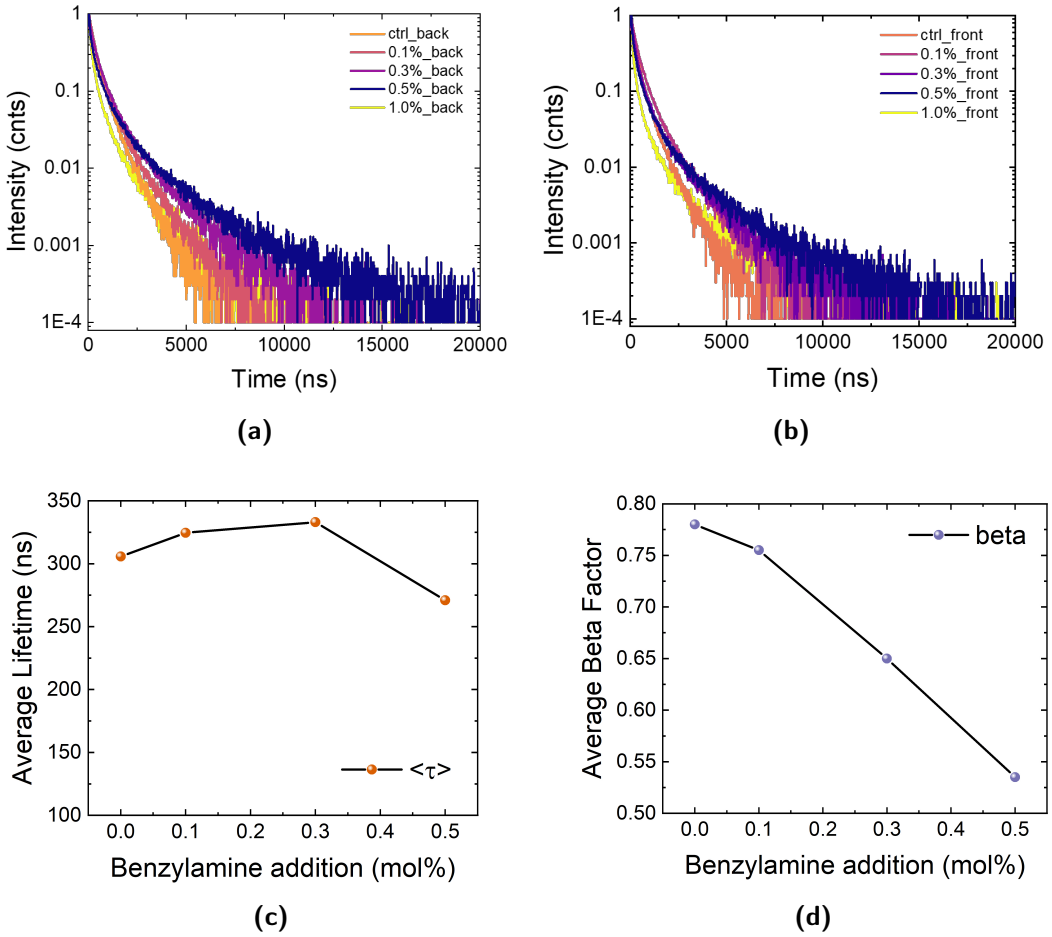

Figure 5.15: Time-resolved photoluminescence of 0.1 mol%∼0.5 mol% BnAm additive in $FA_{0.75}Cs_{0.25}Pb(I_{0.8}Br_{0.2})_3$ perovskite (a) back (b) front. Measured with a 405 nm laser, 5 kHz pulse frequency with a fluence of 242.1 nJ·cm^{-2}. The data were fitted with a stretched-exponential decay fitting. (c) The average charge-carrier lifetime variation with BnAm concentration. (d) The beta factor variation with BnAm concentration.

Table 5.1: TRPL curve fitted parameters according to equation 3.1 and equation 3.2.

Compound	Front	Front	Back	Back	Average	Average
BnAm Concentration	τ (ns)	β	τ (ns)	β	τ (ns)	β
0 mol%	328.3	0.78	283.3	0.78	305.8	0.78
0.1 mol%	283.4	0.78	365.8	0.73	324.6	0.76
0.3 mol%	388.9	0.65	277.1	0.65	333.0	0.65
0.5 mol%	298.5	0.52	243.5	0.55	271.0	0.54
1.0 mol%	125.3	0.57	125.2	0.57	125.2	0.57
5.0 mol%	158.7	0.63	111.8	0.67	135.3	0.65

TRPL spectra were measured with a 405 nm laser, 5 kHz pulse frequency, and 10% excitation attenuation. The data is fitted with a stretched-exponential decay fitting to obtain the average lifetime τ and homogeneity factor β.

5.5 BnAm Additive in Medium and Wide-bandgap MA-free Perovskite Solar Cells

Following the enhancement of the perovskite film quality, we fabricate both negative-intrinsic-positive (n-i-p) and positive-intrinsic-negative (p-i-n) perovskite solar cells (PSCs) with 0 mol%∼1 mol% BnAm additive (the optimum concentration range in thin films) to investigate if the increase in PLQY translates to an increase in open-circuit voltage (V_{oc}) of the device.

For the n-i-p device, the architecture is FTO/SnO_2/PCBM/Perovskite/spiro-OMeTAD/Au with a perovskite absorber of $FA_{0.75}Cs_{0.25}Pb(I_{0.8}Br_{0.2})_3$. Figure 5.16a shows the schematic of the device structure. With BnAm additive, the V_{oc} slightly increases which is consistent with the improvement in PL (Figure 5.17a). The statistical fill factor and short-circuit current density (J_{sc}) are also slightly improved with 0.3 mol% BnAm addition (Figure 5.17b and 5.17c), which contributes to the increase in maximum power point tracked efficiency (η_{MPP}).

From the EQE spectrum (Figure 5.18), the 0.3 mol% BnAm additive perovskite device has a slight "bump" around 700 nm, which corroborates our hypothesis of BnAm additive perovskite films exhibiting a reabsorption effect, increasing the EQE at longer wavelengths. Taking the derivative of the EQE (dEQE/dE), we find that

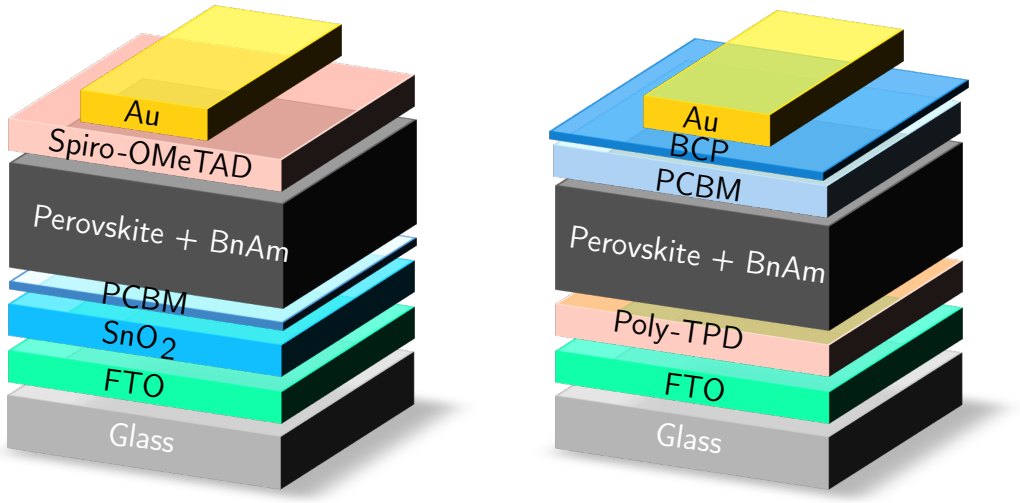

(a) n-i-p device structure.

(b) p-i-n device structure.

Figure 5.16: Schematic illustration of the two device architectures used for this study.

although the PL peak position slightly red-shifts when BnAm is added, the bandgap is maintained at 1.68 eV (Figure 5.19).

Benzylamine was also added to a medium bandgap 1.55 eV $FA_{0.8}Cs_{0.2}PbI_3$ in varying concentrations (Figure 5.20). Devices with the p-i-n configuration FTO/Poly-TPD/perovskite/PCBM/BCP/Au were made (Figure 5.16b). In this case, the BnAm concentration was optimized at 0.2 mol%, reaching a champion reverse scan PCE of 18.82% compared to the control devices at 16.55% (Figure 5.21a). After maximum power point (MPP) tracking for 30 seconds, the devices with 0.2 mol% BnAm were stabilized at η_{MPP} of 17.35%, whereas the control devices were stabilized at 16.07%. Further, EQE measurements reveal that the slight improvement of the J_{sc} stems from the increase in EQE in the visible spectrum 400∼700 nm compared to the control devices (Figure 5.21b).

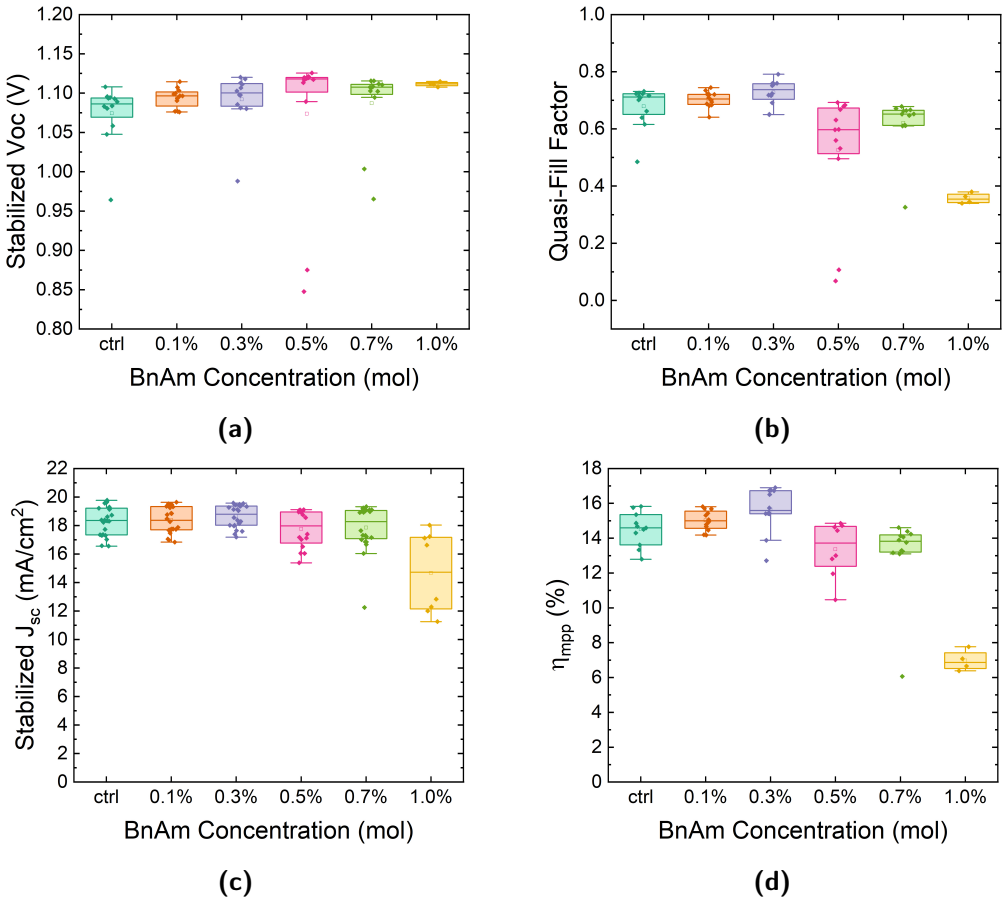

Figure 5.17: n-i-p $FA_{0.75}Cs_{0.25}Pb(I_{0.8}Br_{0.2})_3$ PSC device parameters statistics (a) stabilized V_{oc} (b) quasi-fill factor (c) stabilized J_{sc} (d) maximum power point tracked efficiency (η_{MPP}).

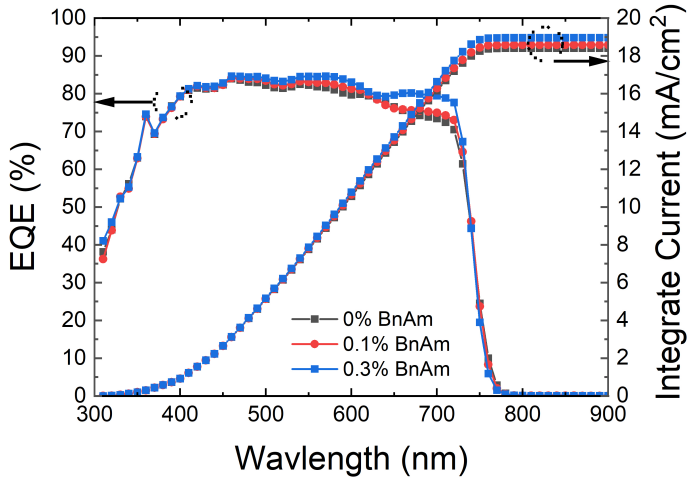

Figure 5.18: EQE spectrum and integrated current density of n-i-p $FA_{0.75}Cs_{0.25}Pb(I_{0.8}Br_{0.2})_3$ devices with 0-0.3 mol% BnAm additive in the perovskite.

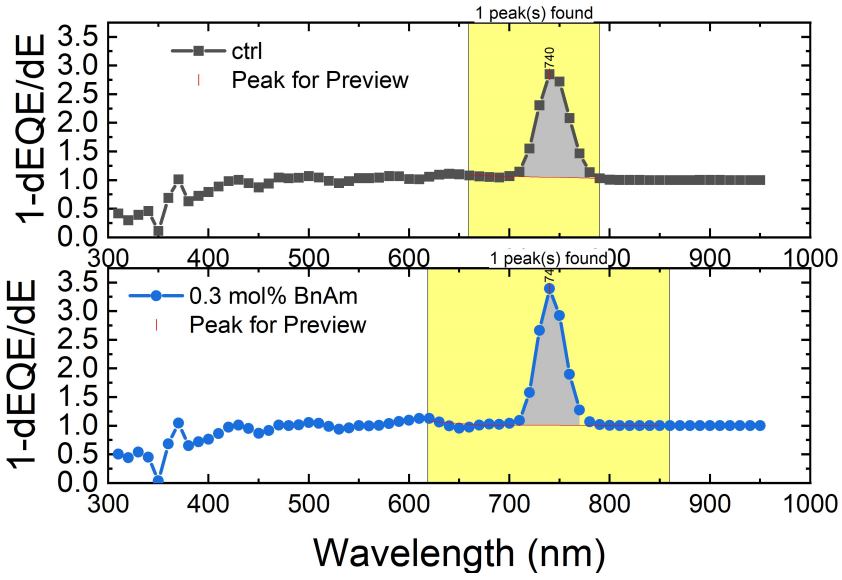

Figure 5.19: The photovoltaic bandgap of a device with (a) pristine wide-E_g perovskite (b) wide-E_g perovskite with 0.3 mol% BnAm. Found by taking the first derivative of their device EQE spectra.

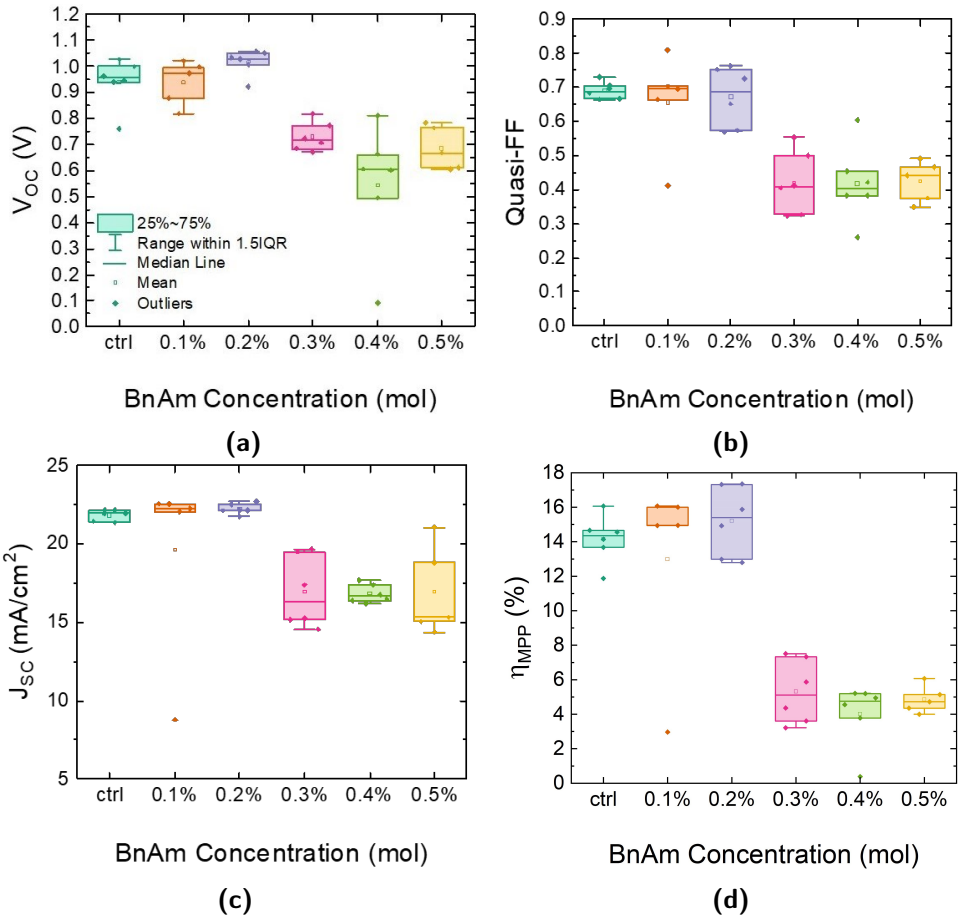

Figure 5.20: 1.55 eV $FA_{0.8}Cs_{0.2}PbI_3$ p-i-n device parameters statistics (a) stabilized V_{oc} (b) quasi-fill factor (c) stabilized J_{sc} (d) maximum power point tracked efficiency (η_{MPP}). 1.55 eV medium bandgap p-i-n devices were made by James Drysdale, University of Oxford.

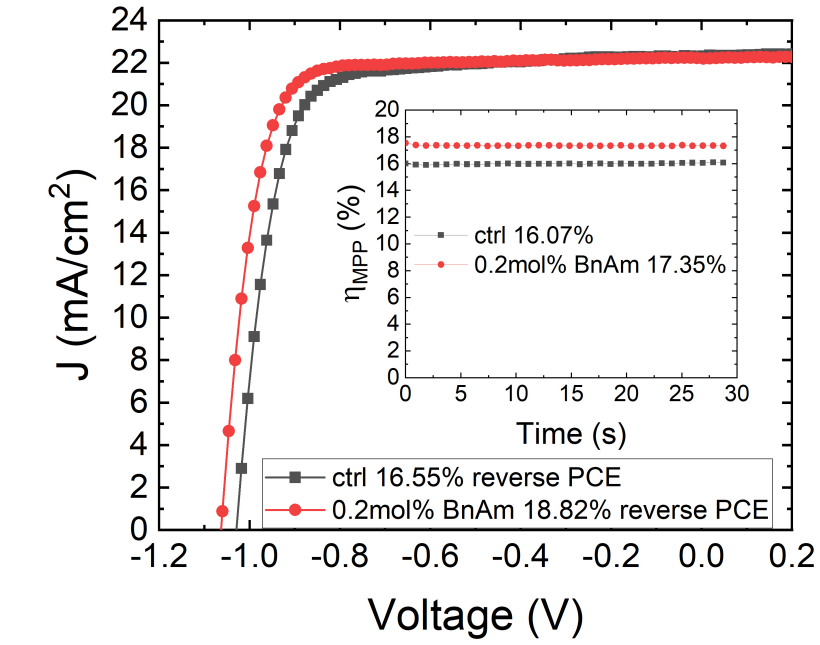

(a)

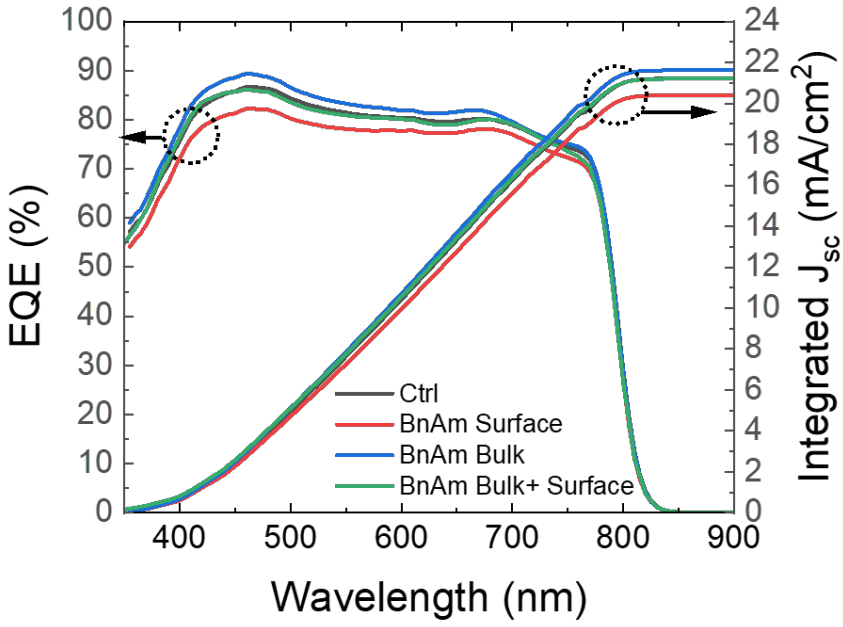

(b)

Figure 5.21: (a) J-V curves of champion $FA_{0.8}Cs_{0.2}PbI_3$ p-i-n solar cells with 0.2 mol% BnAm addition and without BnAm addition. 1.55 eV medium bandgap p-i-n devices were made and measured by James Drysdale. (b) EQE and integrated current density for p-i-n devices with $FA_{0.8}Cs_{0.2}PbI_3$ as the absorber. "BnAm surface" is with 25 mM BnAm (in chlorobenzene) concentration surface treatment, BnAm bulk is with 0.2 mol% BnAm additive. BnAm Bulk+ Surface is perovskite with 0.2 mol% BnAm additive and 25 mM BnAm surface treatment. The EQE was measured by James Drysdale.

5.6 Device Stability with BnAm

Since p-i-n structure devices have been shown to have better stability, this architecture was selected for the accelerated stress test of BnAm-added perovskite. Two MA-free perovskites, medium bandgap, $FA_{0.8}Cs_{0.2}PbI_3$, and wide bandgap, $FA_{0.75}Cs_{0.25}Pb(I_{0.8}Br_{0.2})_3$, were chosen to make devices with the architecture, FTO/Poly-TPD/perovskite/PCBM/BCP/Cr/Au (Figure 5.16b).

An initial stress test of MPP tracking for 1 hour was done on the 1.55 eV $FA_{0.8}Cs_{0.2}PbI_3$ p-i-n, as shown in Figure 5.22. Both devices show an initial increase in MPP after which they stabilize; however, we note that the BnAm-treated perovskite device has a higher initial performance which was maintained over the testing time. After one hour, the control device stabilized to 16.8% PCE, whereas, the BnAm bulk additive device stabilized at 18.6%.

For the medium and wide bandgap MA-free perovskite, control devices with no BnAm additive, devices with the optimum concentration of bulk additive (0.2∼0.3 mol%), and devices with the optimum surface treatment concentration (25 mM) were made and stressed under a 65°C, AM 1.5 light aging box.

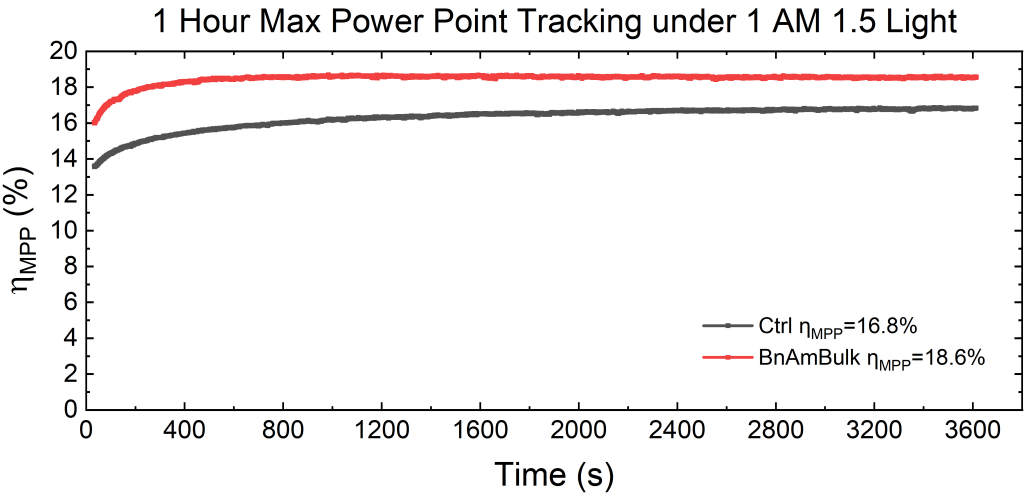

Figure 5.22: Maximum power point tracking (η_{MPP}) of p-i-n devices with the architecture, FTO/Poly-TPD/$FA_{0.8}Cs_{0.2}PbI_3$/PCBM/BCP/Cr/Au (encapsulated) under AM 1.5 intensity. BnAm bulk is with 0.2 mol% additive.

The medium bandgap perovskite devices were unencapsulated to show accelerated aging and the effects of moisture (Figure 5.23). While the control devices and the devices with the best surface treatment degraded rapidly, the BnAm additive devices were more stable and maintained a T_{80} (the time it takes for a device to degrade to 80% of its initial efficiency) of 108 hours.

The wide-bandgap perovskite solar cells were encapsulated and aged under the same condition (Figure 5.24). After the initial burn-in, the BnAm devices gradually increase in efficiency again, while the BnAm surface treatment and control films stay at low η_{MPP} values. The device aging results show that the in-situ formed $BnFA^+$ can passivate the perovskite surface and grain boundary, achieving a remarkable T_{80} stability of 2,460 hours.

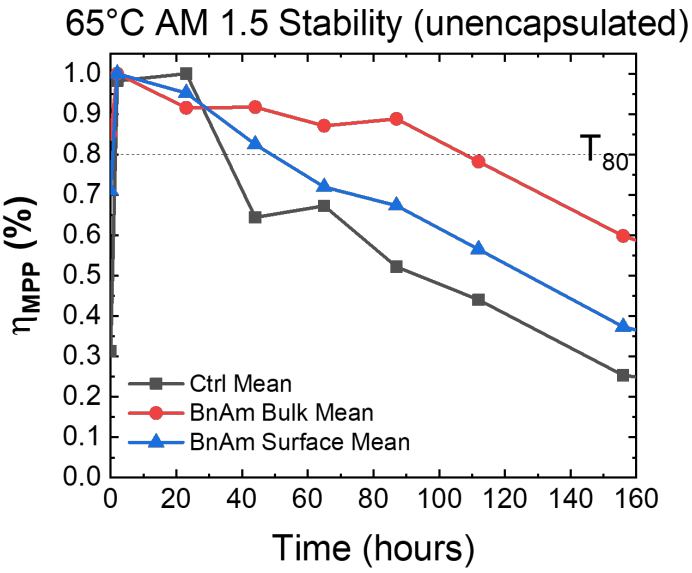

Figure 5.23: 65°C AM 1.5 intensity aging of p-i-n devices with the architecture, FTO/Poly-TPD/$FA_{0.8}Cs_{0.2}PbI_3$/PCBM/BCP/Cr/Au (unencapsulated). BnAm bulk is with 0.2 mol% additive and BnAm surface is with 25 mM of surface passivation. Each data point is the average η_{MPP} of 5 devices for each condition. Devices were aged under open-circuit voltage conditions and taken out of the aging box regularly for testing. This stability test is done by James Drysdale.

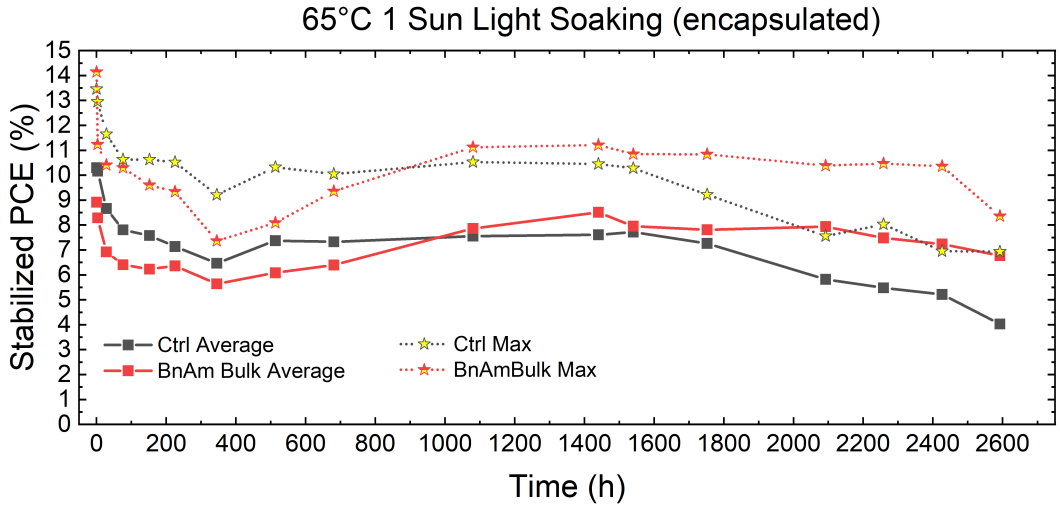

Figure 5.24: 65°C AM 1.5 intensity aging p-i-n devices with the architecture, FTO/Poly-TPD/$FA_{0.75}Cs_{0.25}Pb(I_{0.8}Br_{0.2})_3$/PCBM/BCP/Cr/Au (encapsulated). BnAm bulk is with 0.3 mol% additive and BnAm surface is with 25 mM of surface passivation. Each data point is the average η_{MPP} of 6 devices for each condition.

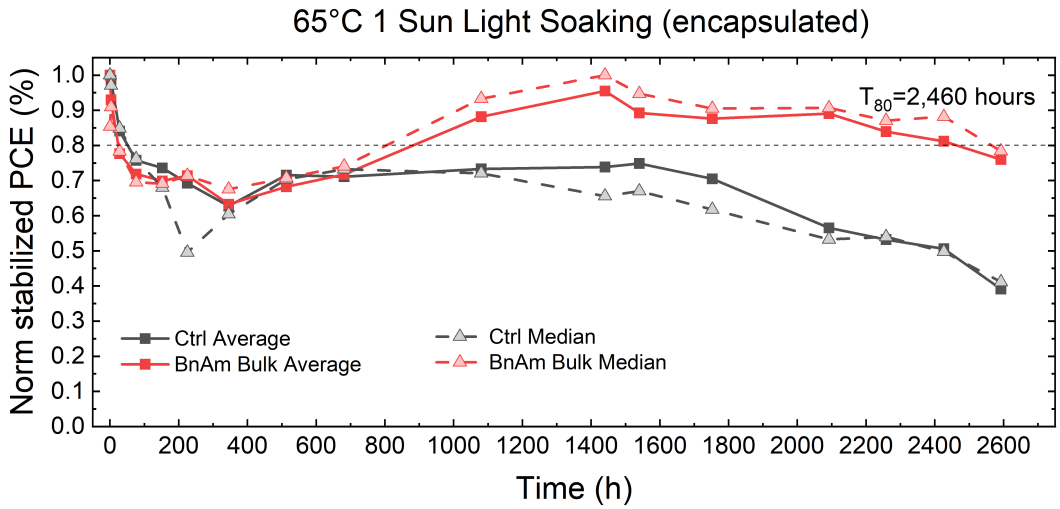

Figure 5.25: Normalized medium and average η_{MPP} of BnAm additive devices and control devices to show T_{80}.

5.7 Conclusion

In this study, we investigated the multitude of effects of adding BnAm into lead-halide perovskite precursor solutions. BnAm reacts with FA^+ to produce $BnFA^+$ and NH_3 and this produces secondary phases seen in the XRD. Meanwhile, the BnAX counterparts do not react with the FA^+ cation and do not produce new phases. The incorporation of $BnFA^+$ into the perovskite grains improves the photoluminescence and charge carrier lifetime, which demonstrates reduced non-radiative recombination. Additionally, the rate of halide segregation under strong irradiance is also slowed down by adding a small amount of BnAm. The enhancement in optoelectronic properties of the perovskite film also translates into an increase in device parameters and performances. Furthermore, $BnFA^+$ helped protect the perovskite from moisture, light, and heat-induced degradation by passivating the surface and grain boundaries and slowing down halide segregation, ultimately improving the device stability. The approach of adding an aryl-containing amine demonstrates an under-explored way of passivating perovskite defects while improving the perovskite stability.

CHAPTER 6

C_{60}-Phosphonic Acid Self-assembling Monolayer-passivated Tin(IV) Oxide for Efficient Solar Cells

6.1 Introduction

In typical planar negative-intrinsic-positive (n-i-p) perovskite solar cells (PSCs), interfaces are often the dominant recombination pathways [191, 50]. In particular, the SnO_2/perovskite interface can introduce non-radiative recombination losses due to the undercoordinated Sn/oxygen vacancies creating trap states [112, 189, 192, 193]. Furthermore, surface hydroxyl groups were shown to cause increased hysteresis and degradation in devices [171]. Hence, passivating the SnO_2 surface becomes crucial for further improving the performance and stability of PSCs. Furthermore, SnO_2 is known to have a lower mobility than the top hole-transporting material (HTM) (often Spiro-OMeTAD), thereby limiting the electron-transport efficiency in a device [168, 194].

To overcome these issues, we look into applying an organic self-assembling monolayer to improve charge extraction while passivating the SnO_2 surface. Fullerene derivatives are good n-type transport layers with defect passivation effects [195, 196]. Fullerenes such as C_{60} and $PC_{60}BM$ (PCBM) are commonly used on top of the perovskite in p-i-n devices. There have been reports of using them as surface passivation for the SnO_2 in n-i-p devices [197, 198, 199]. Mainly, the open-circuit voltage (V_{oc}) is improved by passivating surface defects that likely originate from under-coordinated SnO_x, and the hysteresis is reduced from enhanced charge extraction [197]. By adding anchoring functional groups to the C_{60}, we can create a C_{60}-SAM that will bind to the substrate surface and achieve a thin uniform monolayer for charge-extraction at this interface.

C_{60} SAMs have been commonly used to modify metal-oxide ETLs. Wojciechowski et al. reported enhanced V_{oc} and fill factor by modifying their TiO_2 layer with C_{60}-carboxylic acid (C_{60}-CA) SAM, which is now commercially available. Changing the functional group of the C_{60}-SAM to -$PO(OH)_2$ can potentially improve binding at the surface and passivate more defect sites [200]. The binding mode of -COOH and -$PO(OH)_2$ to the surface hydroxide group is somewhat different. While -COOH can bind to the surface through hydrogen bonding to bridging oxygen and hydrogen bonding to bridging carboxylic oxygen (Figure 6.1b), -$PO(OH)_2$ can bind to the surface through covalent bonding (P-O-M) which is a far stronger bond (Figure 6.1b) and for every -$PO(OH)_2$ up to two under-coordinated Sn/oxygen vacancy sites can be passivated [201]. Furthermore, while PCBM passivation on SnO_2 forms a physisorbed layer, C_{60}-SAMs can form a chemisorbed layer, chemically bonded to the substrate which improves electron injection and reduces non-radiative recombination [202, 203]. Recently, You *et al.* have reported using a 4-(1',5'-dihydro-1'-methyl-2'H-[5,6] fullereno-C60-I_h-[1,9-c]pyrrol-2'-yl) phenylphosphonic acid (C_{60}-PA)/perovskite blend in which the C_{60}-PA molecules get excluded to the grain boundaries (GB) of the perovskite and passivates the GB to improve moisture stability and prevent ion migration [204]. Herein, we use a C_{60}-PA modified SnO_2 layer to improve the

ETL/perovskite interface charge extraction efficiency and passivate SnO_2 surface defects (shown in Figure 6.1b). The solar cells with SAMs treatment show reduced hysteresis and higher fill-factor and V_{oc}. As a result, the maximum power point tracked efficiency (η_{MPP}) was improved from 18.9% to 20.0%.

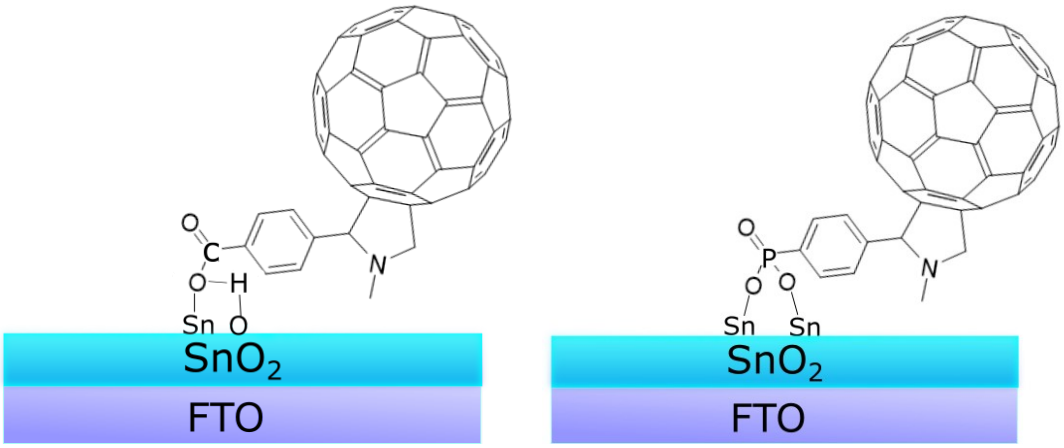

Figure 6.1: (a) Schematic of C_{60}-CA binding to the SnO_2 surface. (b) Schematic of C_{60}-PA binding to the SnO_2 surface. Schematics not drawn to scale.

6.2 Physical Properties

Since n-type SAMs are coated at the perovskite/SnO_2 interface, the SAM needs to be designed such that their absorption does not interfere with the main perovskite absorption spectrum. The SAM exhibits an absorption peak of around 326.1 nm (Figure 6.2). Although the material is weakly absorbing in the UV-visible region, it has little parasitic absorption as the n-type layer, since the deposited SAM is extremely thin. In fact, no difference is detectable from the UV-vis when the SAM is spincoated on a glass substrate compared to pristine glass.

Contact angle measurements were performed on SAMs deposited on fluorine-doped tin oxide (FTO) substrates to assess the surface energy modification and predict the wettability of the perovskite solution (Figure 6.3). For reference, the contact angle of water on FTO directly after UV-ozone is roughly 15° (Figure 6.3 a). The

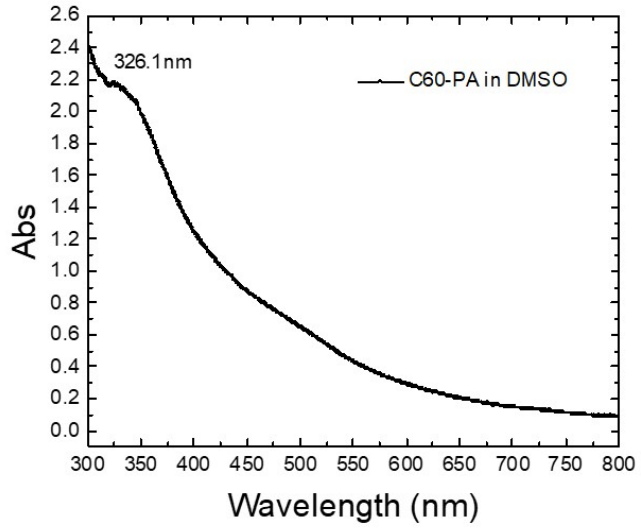

Figure 6.2: C60-PA absorption spectrum in solution, diluted down to 0.2mM.

water contact angle of C_{60}-CA SAM modified FTO increased drastically to 95°. This increase in hydrophobicity makes it more difficult to deposit the perovskite precursor solution on top. In comparison, the contact angle of C_{60}-PA modified FTO is around 37°, which indicates the presence of C_{60}-PA on the substrate whilst not causing a significant increase in hydrophobicity. As a result, we expect the perovskite grown on top to have similar morphology to that of perovskite on SnO_2.

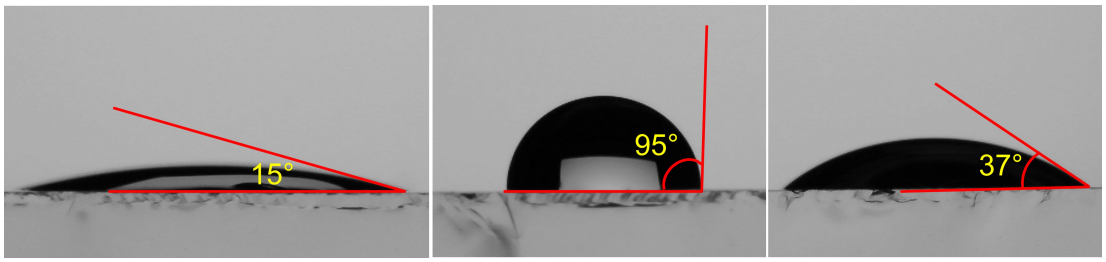

Figure 6.3: Contact angle measurement of water on (a) FTO. (b) C60-CA modified FTO 95° and (c) C60-PA modified FTO 37°

XPS analysis was done on C_{60}-PA modified SAM compared to pristine SnO_2. Although the phosphorous content was below detection limits, the C_{60}-PA modified substrate has a much higher carbon content compared to the control sample, which likely indicates the carbon-rich fullerene-SAM attachment to the substrate (coupled with the reduction in average Sn 3d signal). Part of the carbon content may be

attributed to hydrocarbon contamination, but this is not expected to affect the SAM formation as hydrocarbons do not have a high affinity for the SnO_2 surface [205]. Furthermore, the reduction in the O 1s signal is more compared to the SnO_2 only sample, which could indicate a drop in surface hydroxyl states [206].

Table 6.1: Average XPS intensity ± standard deviation. The analysis is done by Alexandra Ramadan

Elements	C 1s	O 1s	N 1s	Sn 3d
SnO_2	15.37 ± 0.53	61.60 ± 0.98	2.06 ± 0.60	20.58 ± 0.31
SnO_2/C_{60}-PA	42.82 ± 1.62	40.13 ± 4.32	0.86 ± 0.02	16.20 ± 3.33

6.3 Perovskite Grown on C_{60}-PA-modified Tin(IV) Oxide

To investigate if the C_{60}-PA SAM causes any morphological changes, scanning electron microscopy (SEM) images and X-ray diffraction (XRD) patterns were taken for the perovskite grown on FTO/SnO_2 and FTO/SnO_2/C_{60}-PA. As seen from the top view SEM (Figure 6.4), there is little difference in apparent grain size compared to the SnO_2/perovskite samples. They display similar morphologies but perovskite grown on FTO/SnO_2/C_{60}-PA was slightly more compact and has fewer pinholes. From the XRD pattern (Figure 6.5), the α-$FAPbI_3$ (100) peaks were stronger for $FAPbI_3$ (with MACl and $MAPbBr_3$) grown on both SnO_2 and SnO_2/C_{60}-PA, indicating a more oriented crystal growth of perovskite. Although we observe a difference in surface energy, as evidenced by our contact angle measurements, between the SnO_2 control and C_{60}-PA modified substrates there appears to be a negligible difference in the resultant XRD patterns. This indicates that the C_{60}-PA modification on SnO_2 does not alter the resulting perovskite orientation or crystal structure.

To further investigate how the C_{60}-PA modification can change the work function of the perovskite near the ETL/perovskite interface, Kelvin probe force microscopy (KPFM) measurements were conducted on "half stack devices" consisting of only ETL/perovskite bilayers. The perovskite layer was made extremely thin 50∼60 nm

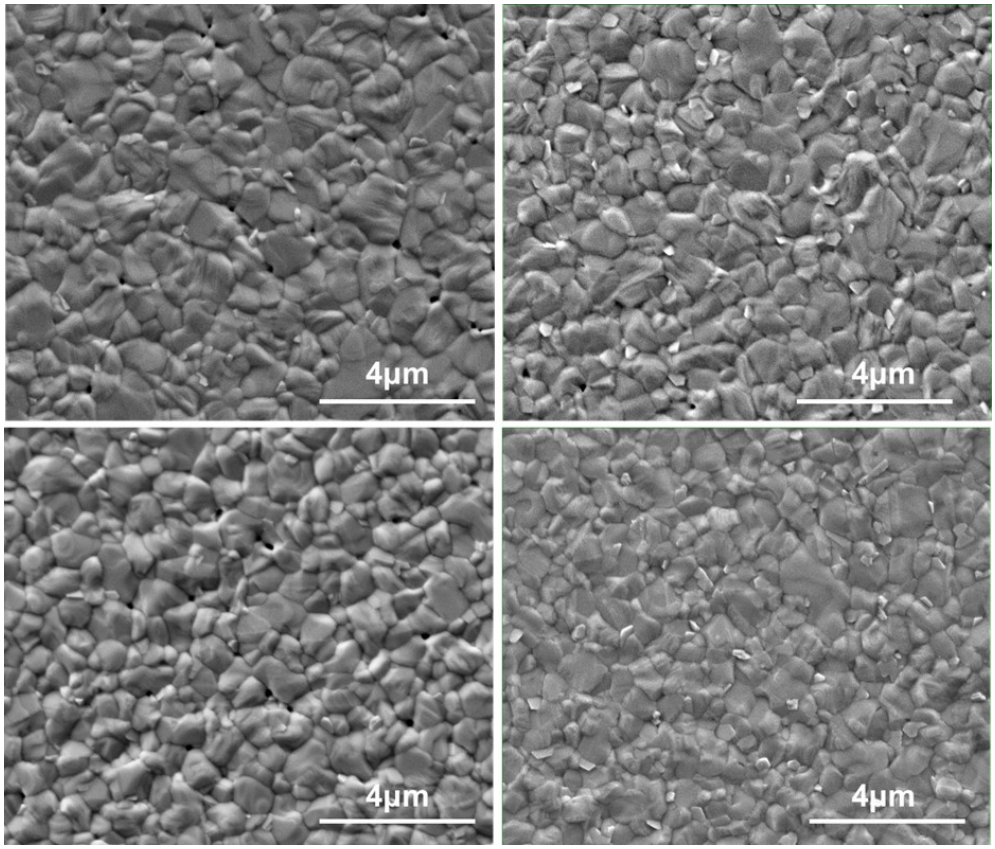

Figure 6.4: Top-view scanning electron microscopy (SEM) images of $FAPbI_3$ processed on (a) FTO (b) FTO/SnO_2 (c) FTO/C_{60}-PA (d) FTO/SnO_2/C_{60}-PA

(see details of fabrication in the experimental methods in chapter 3 section 3.3.8) to probe the energetic effects that the underlying interface has on the thin perovskite. According to the results in Figure 6.6, the C_{60}-PA SAM has very little effect on the FTO/SnO_2 layer, and they both show an n-type work function (WF) of around 4.64 eV. The C_{60}-CA SAM, however, has a slightly deeper work function of 4.71 eV in comparison.

Considering that the aforementioned characterizations show little change in the perovskite bulk, we analyzed the ETL/perovskite interface further. Steady-state photoluminescence (SSPL) was carried out on bilayer films of ETL/perovskite (Figure 6.7). Under open-circuit voltage (V_{oc}) conditions (when the stack is not connected to the external circuit), the electrons and holes must all recombine eventually through internal pathways. Therefore, a higher PL intensity indicates more radiative recom-

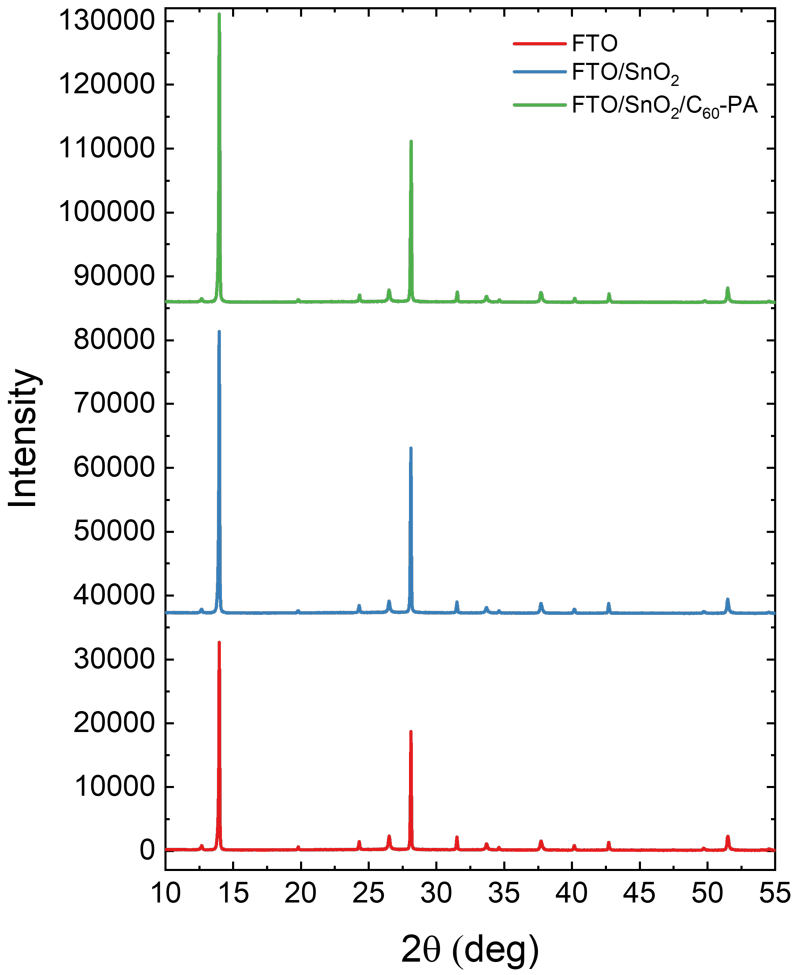

Figure 6.5: X-ray diffraction (XRD) patterns of $FAPbI_3$ with MACl on top of the three different substrates.

bination compared to non-radiative recombination. The increase in SSPL intensity of perovskite films on C_{60}-PA SAM suggests that there is less non-radiative loss at this interface with the perovskite as compared to the unmodified SnO_2 which should result in a greater degree of quasi-Fermi level splitting (QFLS).

To see if there was any improvement in charge carrier lifetimes, time-correlated single photon counting (TCSPC) was performed on "half-stacks" samples with or without C_{60}-PA modification. Stretched exponential decay fitting was applied to extract their charge carrier lifetime, τ, and β. (Figure 6.8). The β exponent is in the range of $0 < \beta < 1$, and it indicates the heterogeneity of the material. A β value closer to 0 indicates a heterogeneous distribution of emissive states and a β value closer to

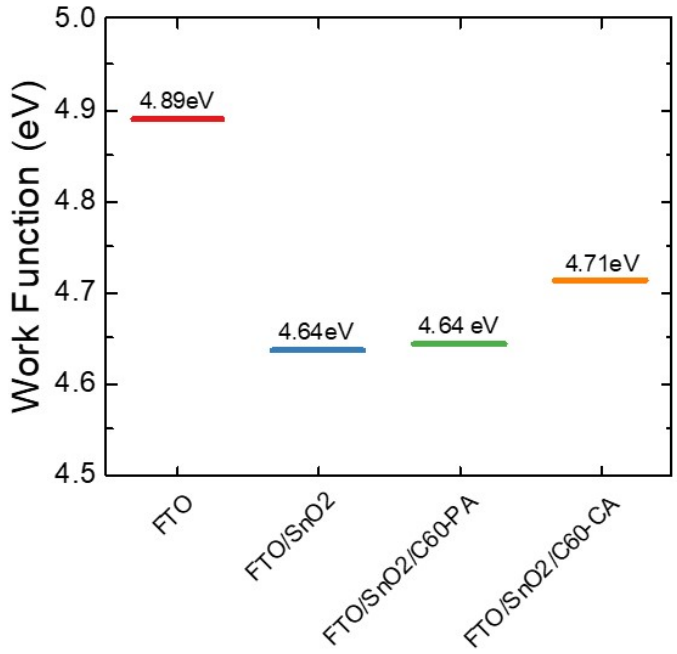

Figure 6.6: Work function of 50 nm $FAPbI_3$ on different n-type substrates, determined by Kelvin probe force microscopy.

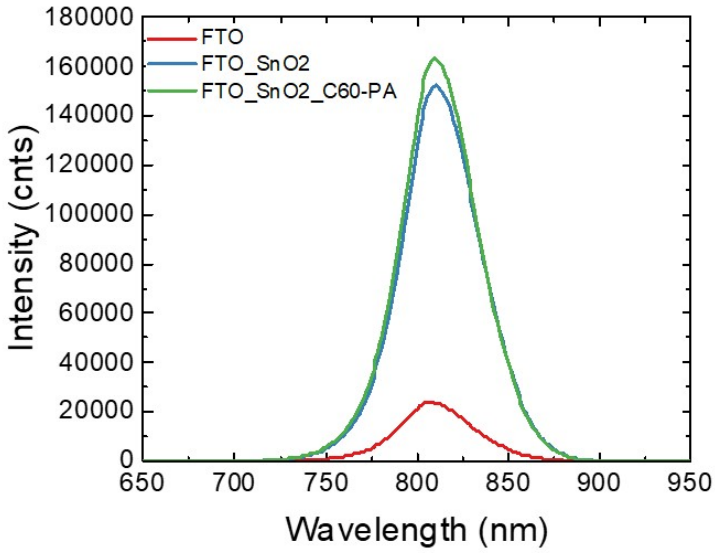

Figure 6.7: Steady-state photoluminescence of perovskite processed on three different FTO-modified substrates.

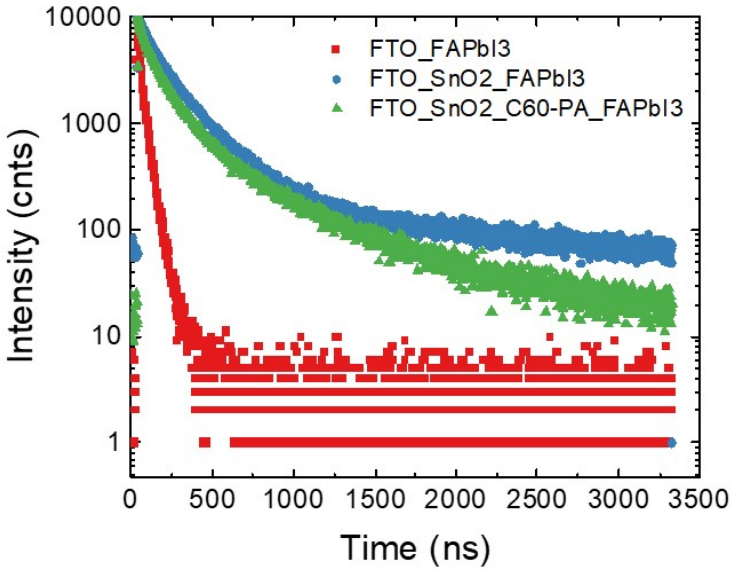

Figure 6.8: Time-resolved photoluminescence of perovskite processed on three different substrates, ETL/perovskite half stack. Excitation frequency 300 kHz, 635 nm laser, with a fluence of 217.2 $nJ{\cdot}cm^{-2}$, measured from the substrate side.

1 indicates a more homogeneous distribution of emissive states [188, 207]. Table 6.2 summarizes the τ and β values for all three bilayer stacks. According to the TCSPC analysis, perovskites fabricated on FTO/SnO_2/C_{60}-PA substrates have the longest charge carrier lifetimes and fewer traps.

Table 6.2: Charge carrier lifetime and β factor of ETL/perovskite bilayer stack determined by stretched exponential decay fitting.

Bilayer Stack	τ (ns)	β
FTO/$FAPbI_3$	22.89	0.69
FTO/SnO2/$FAPbI_3$	189.21	0.82
FTO/SnO2/C60-PA/$FAPbI_3$	139.12	0.71

Intensity-dependent photoluminescence (PL) was measured on these half stacks in an integrating sphere. Under the same fluence, the PLQY of perovskite on FTO/SnO_2/C_{60}-PA is shifted to a higher intensity compared to that of perovskite on FTO/SnO_2 and FTO substrates (Figure 6.9a). Thus, it is expected that the perovskite coated on FTO/SnO_2/C_{60}-PA would have the highest percentage of radiative recombination compared to perovskite on FTO or SnO_2. Therefore, we expect the

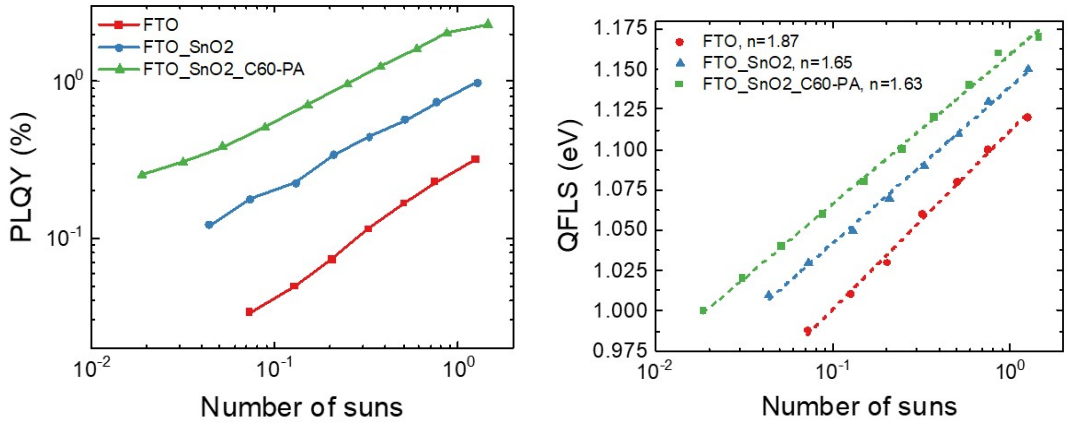

Figure 6.9: (a) Intensity-dependent PLQY of half stacks. (b) Quasi-Fermi level splitting (QFLS) calculated from the Intensity-dependent PLQY.

least amount of interfacial loss from the C_{60}-PA passivated sample and the highest QFLS.

QLFS is then fitted to determine how close their corresponding devices would follow the ideal diode equation (Equation 6.1).

$$I = I_L - I_0[\exp \frac{qV}{nkT} - 1] \tag{6.1}$$

Where n is the ideality factor. An ideality factor close to n=1 generally indicates biomolecular radiative recombination of free charges, whereas, an ideality factor close to n=2 suggests more first-order nonradiative recombination. Under this picture, the ETL stack with FTO/SnO_2/C_{60}-PA gives the device the highest QFLS and would behave closer to an ideal diode (Figure 6.9b).

To investigate whether the extra layer of C_{60}-PA would affect the mobility of charge carriers at the ETL/$FAPbI_3$ interface, Terahertz (THz) spectroscopy was done on "half-stacks" shown in Figure 6.10. The samples were illuminated from the quartz side. From the THz spectroscopy, we extract the mobility (μ) according to Equation 6.2.

$$\phi\mu = -\epsilon_0 c(n_A + n_B) \cdot \frac{A_{eff} hc}{Ee\lambda(1 - R_{pump}(\lambda))(1 - T_{pump}(\lambda))} \cdot (\frac{\Delta T}{T}) \tag{6.2}$$

Where A_{eff} is the effective overlap area of the optical pump and THz probe beams, ϵ_0 is the dielectric permittivity, c is the speed of light, n_A and n_B are the refractive indices of the two media on either side of the film, E is the energy contained in an optical excitation pulse of wavelength λ, R_{pump} and T_{pump} are the sample reflectance and transmittance at the pump wavelength, and ϕ is the branching ratio of photons-to-free-charges. ΔT is the photoinduced change in the transmitted THz electric field.

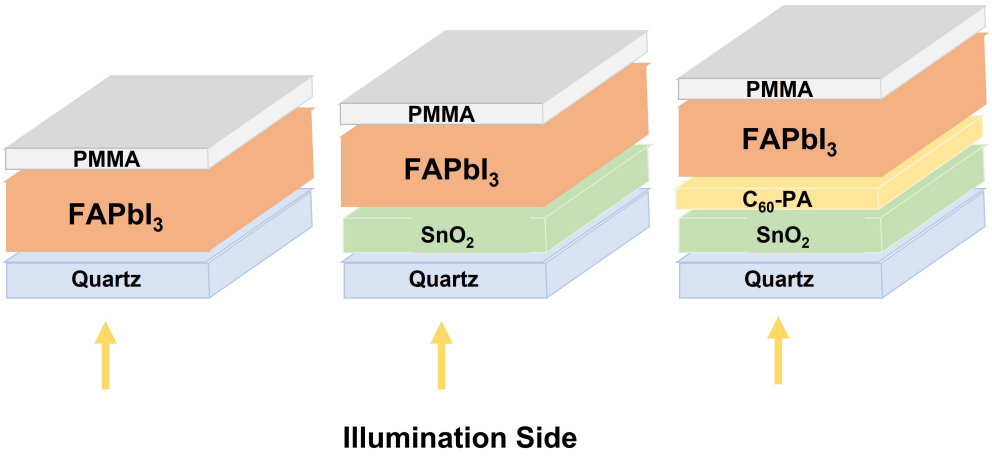

Figure 6.10: Schematic of half-stack devices made with different ETL modifications.

By comparing the mobilities among the three samples, perovskite, SnO_2/perovskite, and SnO_2/C_{60}-PA/perovskite (Figure 6.11), we found no significant differences in their initial mobilities.

A 65°C AM 1.5 light stability test was conducted on these samples and their time-resolved terahertz spectroscopy (TRTS) measurements were taken throughout time. According to Figure 6.12, the mobilities of all of the samples drop as they age, but the drop in mobility is the slowest for $FAPbI_3$, followed by SnO_2/$FAPbI_3$ and SnO_2/$FAPbI_3$/C_{60}-PA. The result suggests that the degradation at the ETL/perovskite interface is accelerated with each layer of SnO_2 and C_{60}-PA added.

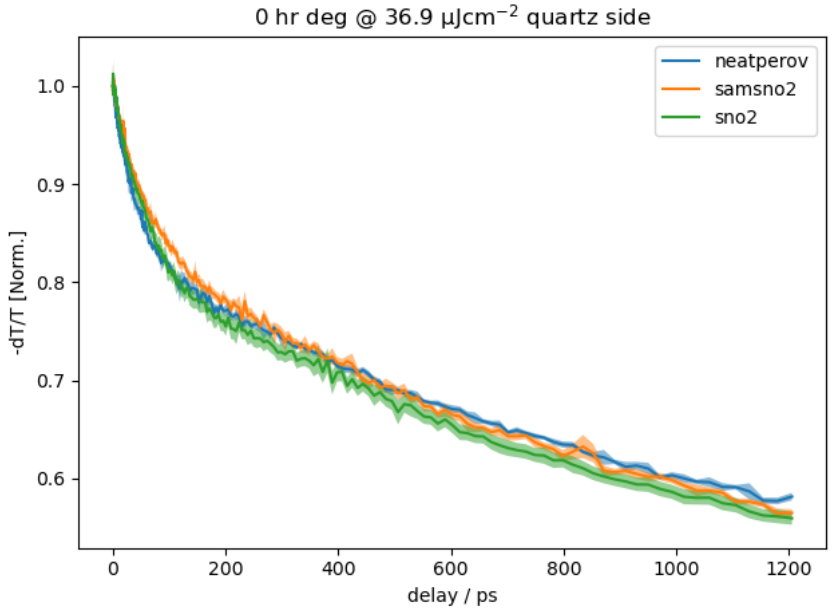

Figure 6.11: Time-resolved THz spectroscopy (TRTS) (400 nm optical pump) of $FAPbI_3$ perovskite on three different substrates: quartz, quartz/SnO_2, and quartz/SnO_2/C_{60}-PA. The measurements were performed and data were plotted by Jae Lee, University of Oxford.

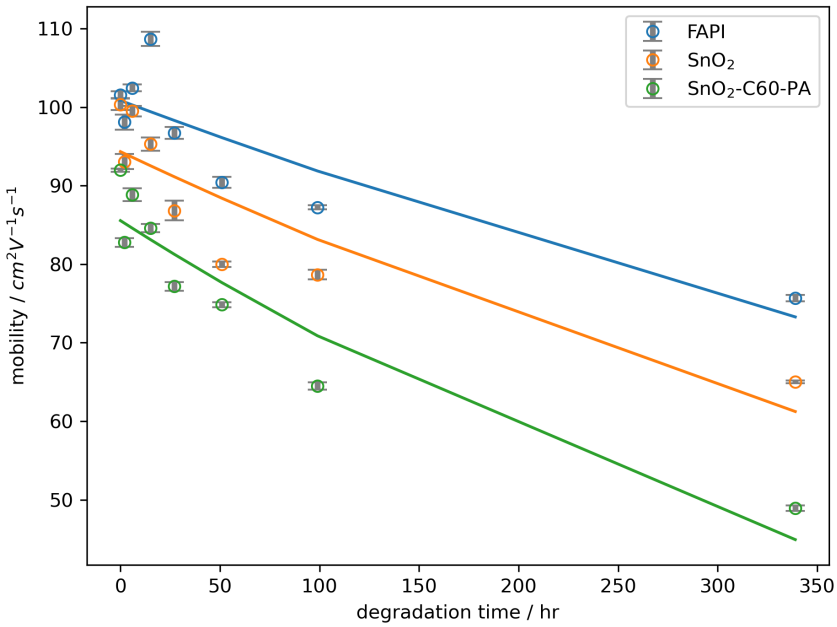

Figure 6.12: THz mobilities of "half-stack" samples aged under 65°C AM 1.5 light over time. The analysis was carried out and the plot was made by Jae Lee, University of Oxford.

6.4 n-i-p Perovskite Solar Cells with C_{60}-PA SAM

To see if the improvement in PLQY would translate to improvements in V_{oc}, negative-intrinsic-positive (n-i-p) perovskite solar cells were made on different n-type layer substrates: directly on FTO, FTO/C_{60}-PA, FTO/SnO_2/C_{60}-PA, or FTO/SnO_2/C_{60}-CA (Figure 6.13). The open-circuit voltage (V_{oc}) of devices on FTO (0.61±0.09 V std. dev) was significantly improved by adding a C_{60}-PA layer on top of the FTO (0.80±0.05 V) and also improved by adding a SnO_2 electron extraction layer (1.01±0.11 V). The combination of C_{60}-PA on top of the SnO_2 gives the best voltage of 1.03±0.09V. From the J_{sc} of devices on FTO compared to FTO/ C_{60}-PA, it is evident that C_{60}-PA enhances electron extraction as the current density was improved by nearly 1 mA/cm^2. Similarly, comparing the J_{sc} of FTO/SnO_2 with that of FTO/SnO_2/ C_{60}-PA (Figure 6.13b), the current density was on average improved by 0.23 mA/cm^2 after adding a C_{60}-PA SAM. With C_{60}-PA-modified SnO_2, the forward J-V scan fill-factor (FF) was slightly enhanced, resulting in reduced hysteresis which is also evident by comparing the J-V scans in Figure 6.14b. As a result of these improvements to the photovoltaic parameters, the average maximum power point tracked efficiency (η_{max}) was improved from 17.5±2.6% for FTO/SnO_2 to 19.3±0.5% for FTO/SnO_2/C_{60}-PA. The champion device η_{max} was improved from 18.9% for SnO_2 to 20.0% for SnO_2/C_{60}-PA. All parameters are listed in Table 6.3.

Table 6.3: The statistical parameters of n-i-p devices made with the different ETL modifications ± standard deviation.

Device ETL	V_{oc} (V)	J_{sc} (mA/cm^2)	$FF_{forward}$	$FF_{reverse}$	η_{MPP} (%)
FTO/SnO_2	1.01 ± 0.11	23.26 ± 0.39	0.70 ± 0.03	0.80 ± 0.02	17.5 ± 2.6
FTO/SnO_2/C_{60}-CA	0.96 ± 0.15	23.31 ± 0.54	0.66 ± 0.10	0.70 ± 0.12	16.3 ± 4.2
FTO/SnO_2/C_{60}-PA	1.03 ± 0.09	23.49 ± 0.28	0.74 ± 0.05	0.79 ± 0.02	19.3 ± 0.5
FTO	0.61 ±0.09	22.80 ± 0.14	0.41 ± 0.04	0.67 ± 0.04	7.8 ± 3.9
FTO/C_{60}-CA	0.72 ± 0.07	23.32 ± 0.34	0.47 ± 0.03	0.65 ± 0.08	9.9 ± 1.8
FTO/C_{60}-PA	0.80 ± 0.05	23.74 ± 0.14	0.51 ± 0.02	0.69±0.03	13.5 ± 2.2

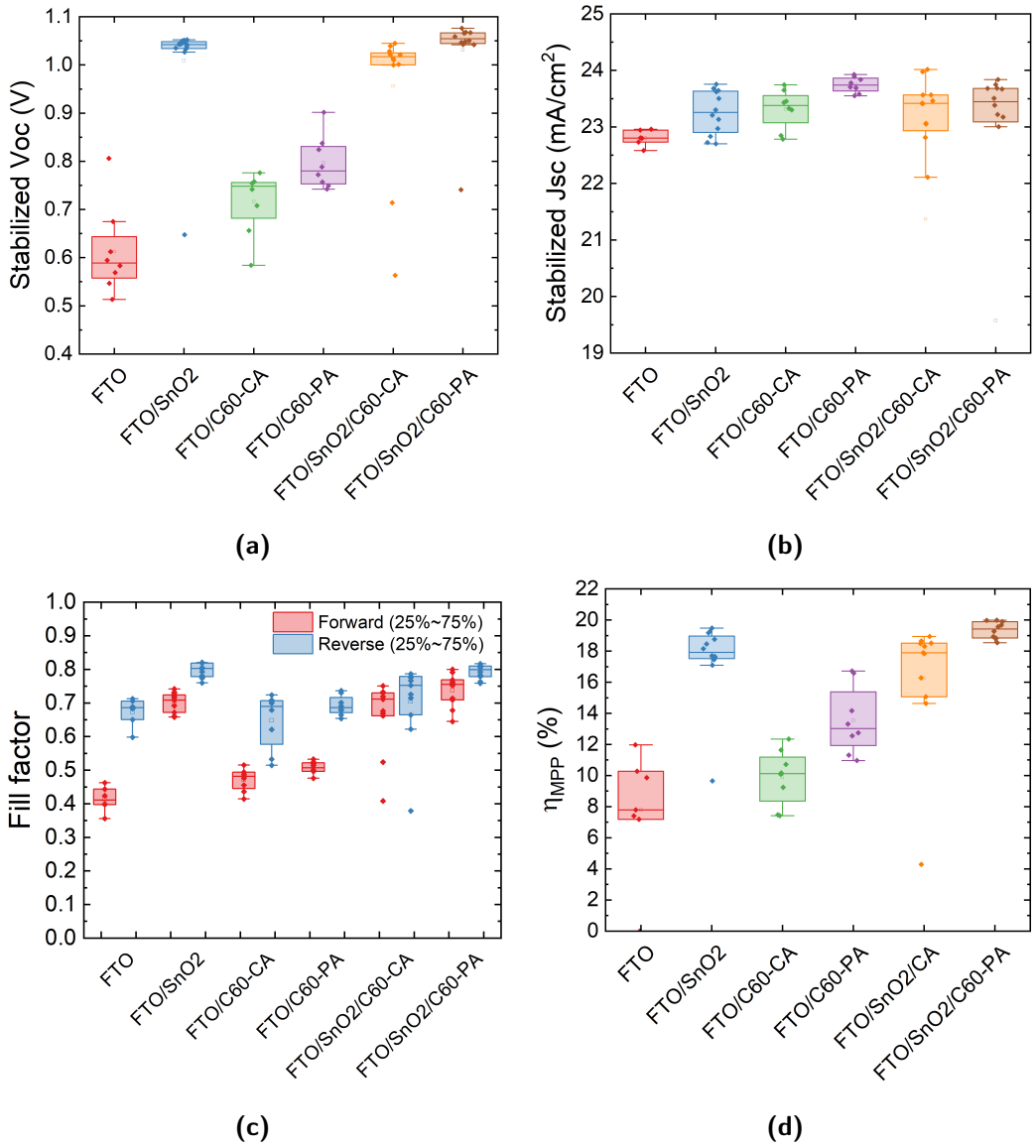

Figure 6.13: (a) Box plot of stabilized V_{oc} (b) J_{sc} (c) forward and reverse fill factor (d) maximum power point tracked efficiency (η_{MPP}) of bilayer films of perovskite on different modified FTO substrates.

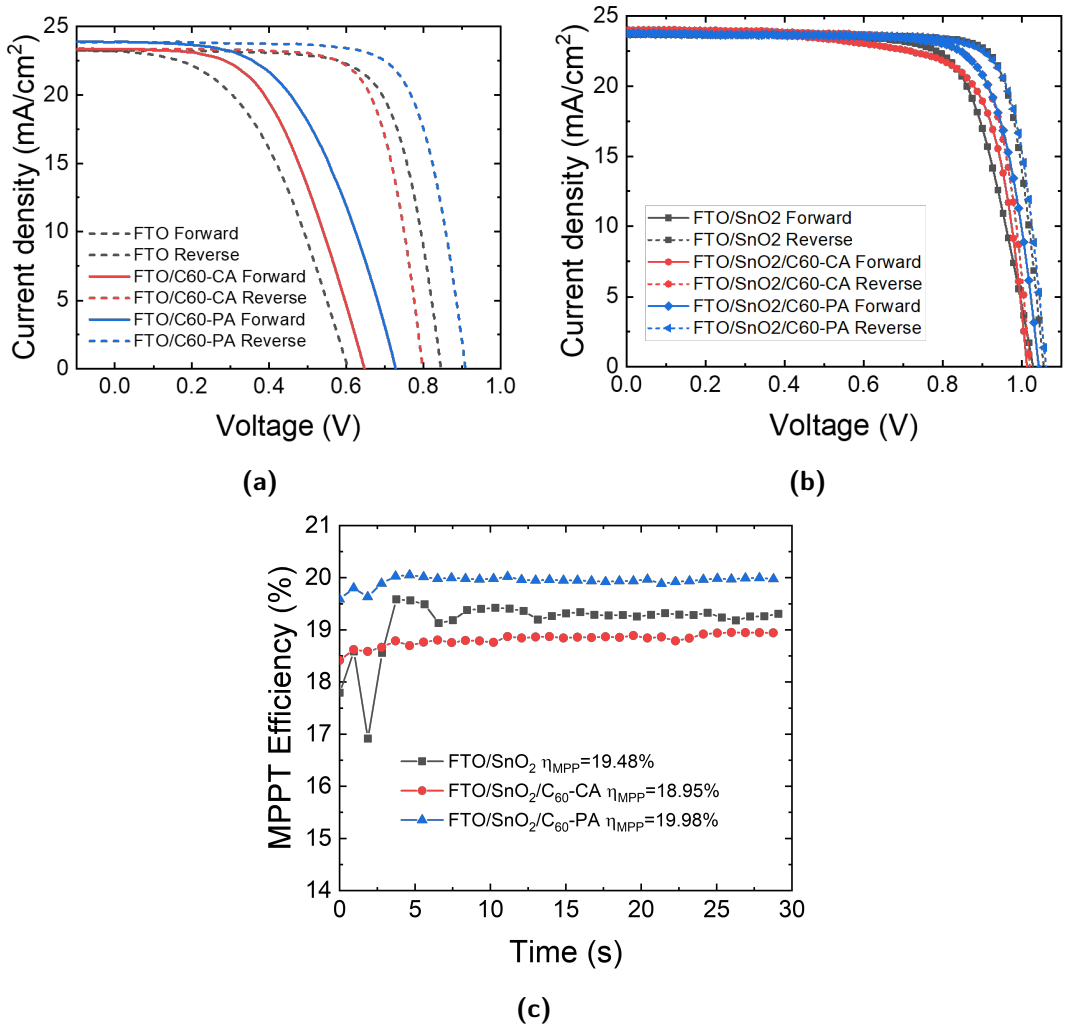

Figure 6.14: Forward and reverse J-V scan plots of different SAMs as the interlayer (a) without SnO_2 and (b) with SnO_2. (c) MPP tracking of C_{60}-PA, C_{60}-CA, SnO_2 champion devices.

It can be seen more clearly from SnO_2-free devices in Figure 6.14a that C_{60}-PA assists in current extraction and reduces non-radiative recombination since both J_{sc} and V_{oc} improved with C_{60}-PA only as an ETL. The difference in statistical mean between the V_{oc} of devices with C_{60}-PA and without it is 22.0 mV.

6.5 n-i-p Perovskite Solar Cells Stability

Recently, You et al. [204] suggested that when this C_{60}-PA is mixed together in the perovskite precursor and crystallized in the bulk, it can prevent halide segregation by passivating the grain boundaries through -$PO(OH)_2$ interacting with the perovskite and fullerene interacting with the halide. Furthermore, the moisture stability of the perovskite is also improved by the hydrophobic C_{60}-PA modification. The perovskite was able to resist degradation to δ-$FAPbI_3$ and PbI_2 under high (70%) relative humidity.

To test if our C_{60}-PA as a SAM interlayer could improve the SnO_2/perovskite interface stability, we fabricated some devices and first aged them in the 85°C dark under a nitrogen atmosphere for over 2,800 hours and then encapsulated them and brought them into the light, aged under 85°C AM 1.5 light for another 1,080 hours. The total aging time was 3,900 hours. (Figure 6.15). This stability test was done to compare the effects that light has on devices under an elevated temperature because we (our group) often get good device stability under an 85°C dark nitrogen environment, but when light is added as an extra stress factor, the devices degrade more rapidly.

Although the device stack used before had high η_{MPP}, doped Spiro-OMeTAD is considered unstable [208, 209] and Au electrodes can migrate into the device [86]. Hereby, the device stack was modified with more stable materials and passivation to test the long-term stability of the C_{60}-PA. The specific architecture used was: FTO/SnO_2/C_{60}-PA/Al_2O_3/$FA_{0.83}Cs_{0.17}Pb(I_{0.9}Br_{0.1})_3$ with $BMPBF_4$ additive/ n-octylammonium-Br/PTAA/Cr/Au in which the ETL is SnO_2 with or without Al_2O_3. 1-butyl-1-methylpiperidinium tetrafluoroborate ($BMPBF_4$) is an ionic liquid additive that stabilizes the perovskite [178]. Al_2O_3 was added to some devices to investigate if it can improve the perovskite adhesion on the substrate [210]. The results in Figure 6.15 show that the SnO_2 layer with C_{60}-PA SAM modification and/ or Al_2O_3 modification degrade faster than without them. Surprisingly, the maximum power point

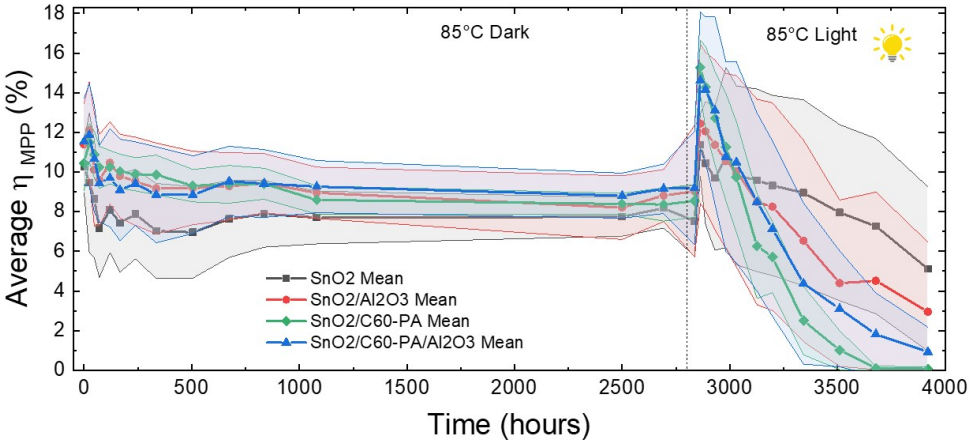

(a)

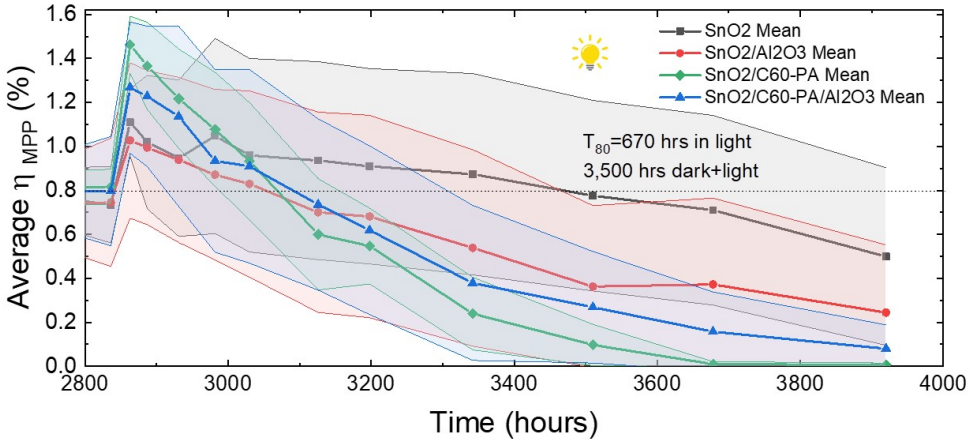

(b)

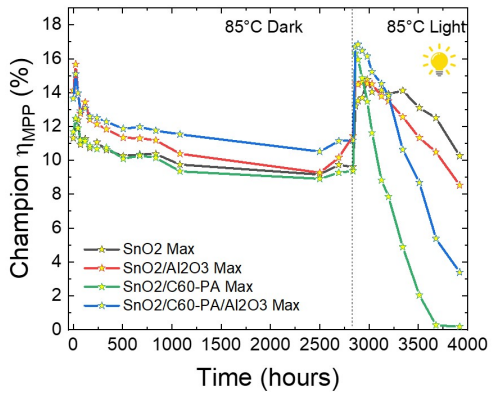

(c)

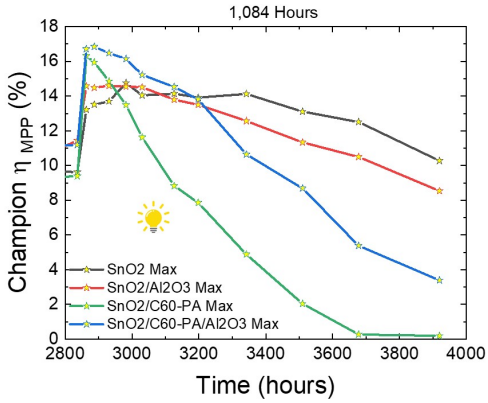

(d)

Figure 6.15: (a) Average η_{MPP} of devices with different ETL modification, first aged under an 85° C dark, nitrogen environment for 2,800 hrs and then taken into 85° C AM 1.5 for 1,084 hours. (b) Average η_{MPP} of devices normalized by the initial efficiency and zoomed into the last 1,084 hrs under the light. In (a) and (b), the error ranges denote the standard deviations. (c) Champion device η_{MPP} for each condition. (d) Champion device η_{MPP} zoomed into the last 1,084 hrs under the light.

tracked efficiencies of all devices were low (with this new stack) but quite stable under the dark for this structure, but once the devices were moved to under the light, their η_{MPP} jumped up by 3.8% for the SnO_2 devices and 6.7% for the SnO_2/C_{60}-PA on average. On closer inspection of the J-V curves evolution (Figure 6.16) reveals that under dark aging, the fill factor decreases over time and s-kink forms, but once the devices were introduced to the light, the fill factor increases again to higher than the pristine devices, and the s-kinks were essentially gone for the control devices. We postulate that the charge-extraction barrier that built up under the dark is removed by ion migration under light soaking. Moreover, the V_{oc} of the SnO_2 control device continues to increase. This was quite well reported as an oxidative passivation phenomenon under light [211]. In fact, the η_{MPP} of the C_{60}-PA devices initially increased more than it did for the control devices, but subsequently also dropped more dramatically.

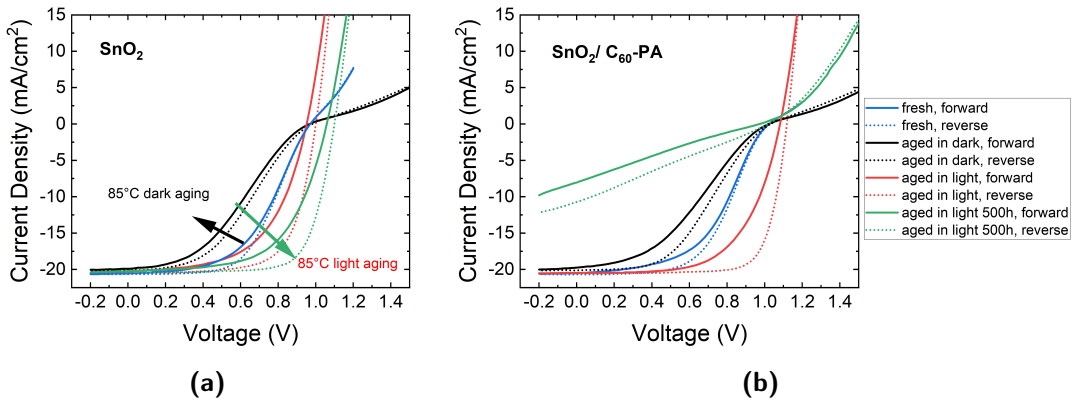

Figure 6.16: (a) J-V curve evolution of SnO_2 devices first aged under 85°C dark and then 85°C light. (b)J-V curve evolution of SnO_2/C_{60}-PA devices first aged under 85°C dark and then 85°C light.

In comparison, with a longer 85°C light aging time, the SnO_2/C_{60}-PA devices reduce in current density, indicating that there is a major difference in their interfacial degradation rate. According to the images taken at the end of the entire 3,900 hrs aging test (Figure 6.17), the perovskite on SnO_2 (control sample) stayed darker compared to the perovskites on any other modified SnO_2. These results follow the trend of our stability test results on the "half-stacks". Perovskite degrading at the

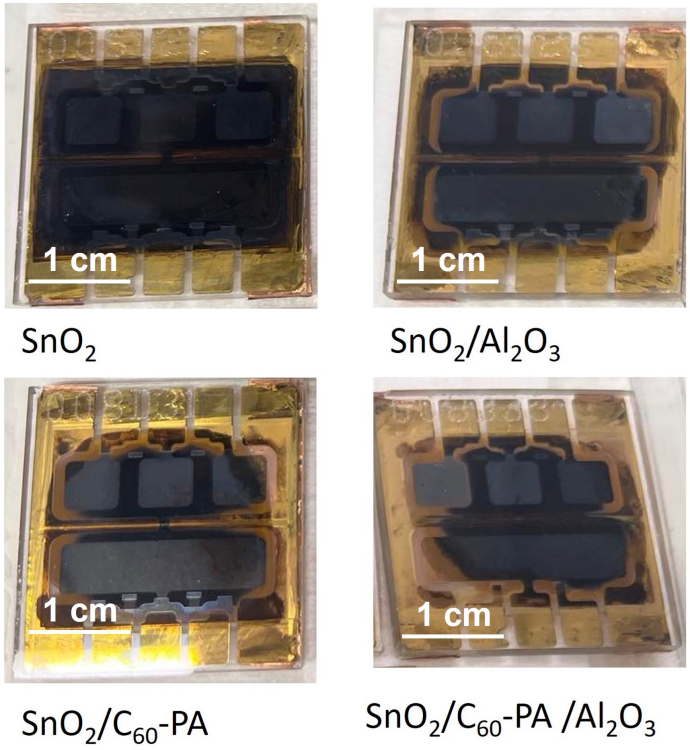

Figure 6.17: A picture of the devices after the entire 3,900 hrs aging process. The full substrate area is 30 mm×30 mm. The small devices are 0.25 cm^2 in size and the large device is 1 cm^2 in size.

interface (possibly due to delamination) with C_{60}-PA can explain their THz mobility drop over time.

Finally, to understand whether it was the C_{60}-PA/perovskite interface that was delaminating (as it appears in Figure 6.17), a "peeling test" was done on these degraded devices. The devices were cleaved from the substrate FTO side and cracked. The way in which the coverslip peeled off is indicative of the adhesion of each device layer to one another. As can be seen from Figure 6.18, while for both the SnO_2/C_{60}-PA device and the SnO_2/C_{60}-PA/Al_2O_3 device, the perovskite peeled off from the substrate, the SnO_2 device and SnO_2/Al_2O_3 device only peeled off from the metal contacts, indicating strong adhesion of the device stack to the substrate. Hence, we conclude that the C_{60}-PA interlayer weakens the mechanical adhesion of the SnO_2/perovskite interface, causing the device to degrade. The J-V curve evolution in Figure 6.16b is consistent with perovskite delaminating from the C_{60}-PA because compared to the control device (Figure 6.16a), the C_{60}-PA device loses current density and FF over

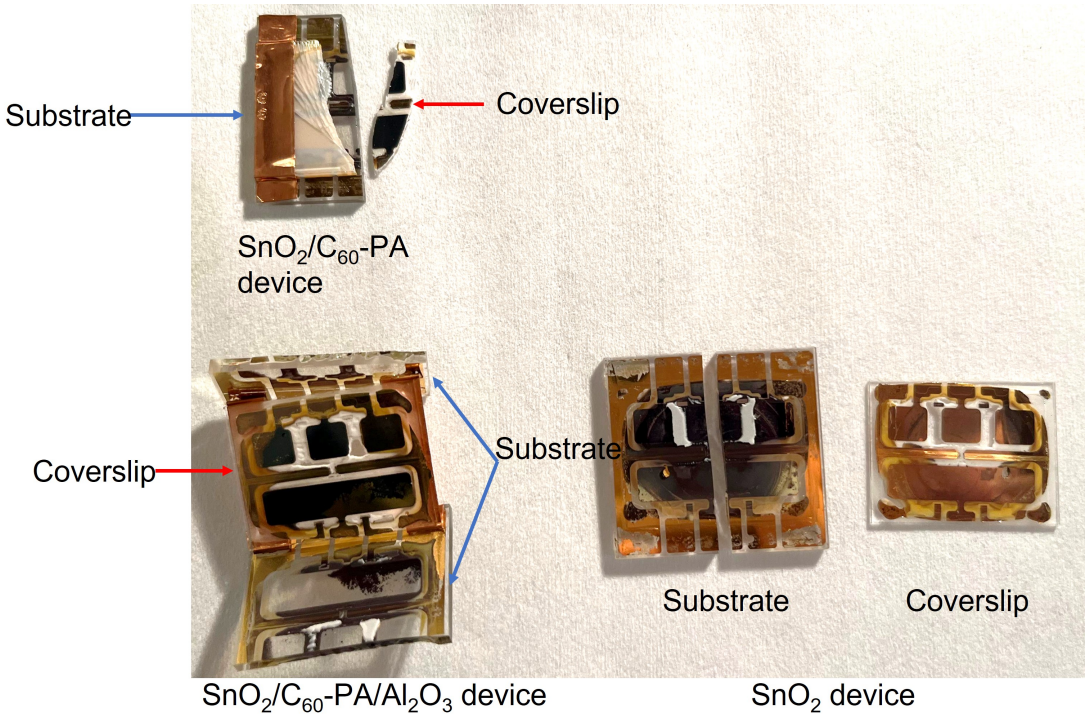

Figure 6.18: Photo of devices cleaved at the end of the stability test.

time while V_{oc} stays the same, which can be a result of losing contact area of the substrate to the rest of the device stack.

6.6 Conclusion

A new phosphonic acid SAM, C_{60}-PA, was investigated as a passivation and charge-extraction interlayer. C_{60}-PA was compared to a similar, commercially available, C_{60}-CA SAM. We found by adding the C_{60}-PA SAM on SnO_2, the PLQY of the perovskite film on top of the ETL increased, contributing to increased QFLS and V_{oc}. Moreover, the presence of this SAM seems to enhance electron extraction at the interface. The improvement was not found mostly due to improved crystallinity, grain size, or grain morphology of the perovskite bulk, but it is attributed to the passivation effects of C_{60}-PA on the SnO_2. While the performance of the solar cells improved by adding this C_{60}-PA SAM layer, it does not seem to make the interface more stable, rather it was found that it likely causes delamination. Further research needs to be done on synthesizing SAMs that are bi-functionally linking both the perovskite and SnO_2 sides to reduce delamination. In general, more work needs to be done to improve the stability of n-i-p solar cells.

CHAPTER 7

Conclusion

7.1 Summary and Future Work

The research in this thesis showed advancements towards enhancing the regular n-i-p device stability by changing the charge extraction layers, modifying perovskite interfaces, and improving perovskite bulk stability with additives.

Chapter 4 demonstrated how the commonly used hole-transporting material (HTM), Spiro-OMeTAD, is unstable and costly. A pair of new carbazole-based enamine hole-transporting materials were introduced to overcome these issues. Cost-wise, these materials are around ten times cheaper than Spiro-OMeTAD to manufacture. Stability-wise, these new HTMs have higher glass transition temperatures than Spiro-OMeTAD, and no hygroscopic dopants are needed. The devices made with these carbazole-based enamine HTMs maintained 83% of their peak efficiencies after 1,000 hours of 85°C thermal aging. While this work demonstrated the good thermal stability of these new HTMs, the light stability still needs improvement. However, the fact these carbazole-based enamine devices degrade at a similar rate to Spiro-OMeTAD

devices under light could mean that our device stack was not stable enough and their degradation was not limited by the HTMs but by other layers. Future work would include putting these new HTMs into a more stable device stack and testing them under the 85°C AM 1.5 light.

Chapter 5 investigated how the perovskite bulk can be passivated by means of amine additives. It was found that benzylamine (BnAm) can not only improve the optoelectronic properties of the perovskite through surface and grain boundary passivation, but also enhance the long-term thermal, light, and moisture stability. This chapter then investigated the precise role that BnAm plays in the perovskite bulk. It was found that BnAm reacts with the formamidinium (FA^+) cation to form $BnFA^+$, which subsequently forms a quasi-2D phase, passivating the perovskite. An amine-FA^+ reaction was identified and distinguished from the reaction that takes place when BnAX salts or methylammonium are added. The effects of amine additives in perovskite require closer scrutiny, as the net result is not straightforward. To investigate the full stability potential of BnAm in a way that avoided the stability limitations of n-i-p transport layers, the BnAm-modified perovskite was incorporated into a p-i-n device stack. As a result of the perovskite passivation, a remarkable T_{80} of 2,460 hours was achieved for the 1.68 eV wide-bandgap perovskite under a combined 65°C and AM 1.5 light stability test. This makes BnAm an excellent candidate to be incorporated into silicon/perovskite tandem solar cells for increasing the lifetime of the overall solar cell. More work is required to identify the 2D phase formed with $BnFA^+$ as the cation. In general, the role of additives in perovskite bulk passivation needs to be better understood. In particular, the reaction of amine additives with perovskite has long been overlooked. Understanding the mechanism of amine passivation can help us select and design suitable passivation for specific perovskite compositions.

Chapter 6 turned to modifying the electron-transporting layer, SnO_2, and identified the remaining instability issue with n-i-p solar cells. Following work on p-type phosphonic acid self-assembling monolayers (SAMs) [212, 213, 214], an n-type fullerene-based phosphonic acid SAM, C_{60}-PA, was tested as a SnO_2 modification

layer. The bilayer stack which had been treated with the C_{60}-PA had improved photoluminescence quantum yield, which translated to increased open-circuit voltage and performance of the full device. Following these positive device results, the stability of a C_{60}-PA interlayer in devices was tested. A 2,800-hour 85°C dark-aging test was conducted, followed by a 1,080-hour 85°C AM 1.5 light stability test. However, it was found that the fullerene SAM with only one functional group attached to the substrate suffered from delamination, exacerbating the instability issue. Nevertheless, the device configuration employed in this study showed impressive stability: there was hardly any loss in performance under 2,800 hours of 85°C dark aging. Under 85°C light, the average SnO_2 device T_{80} lifetime was 670 hours, which is comparable to the stability of p-i-n devices [178]. Finally, the instability of the C_{60}-PA interlayer was shown to be due to worse adhesion of the perovskite on the substrate. This result also suggests a potential problem for p-i-n solar cells, whose most widely-used and best-performing electron-transporting layer is fullerene-based (either C_{60} or PCBM).

Further work is required to design and synthesize self-assembling monolayers with bi-functional binding groups which can attach to both the substrates and the perovskite for better adhesion to improve the electron-tansporting layer/perovskite interfacial stability. Another option would be to add a second "zwitterionic" phosphonic acid passivation with two functional groups of a molecular length similar to C_{60}-PA. The zwitterion can either be mixed into the C_{60}-PA solution and spin-coated onto the substrate or be added on top of the C_{60}-PA in a 2-step deposition. A second bi-functional SAM can help increase the wettability of the perovskite precursor solution on the substrate (as has already been demonstrated for p-i-n solar cells [215]), and potentially strengthen the adhesion of the perovskite layer on the substrate.

7.2 Future Outlook

Since their introduction over a decade ago, perovskite solar cells have gradually become more competitive with other photovoltaic technologies. This is due to better

knowledge of the physics and chemistry of this material, and improvements in processing methods, materials, and architecture. At the time of writing, the US National Renewable Energy lab reports a record 32.5% efficiency silicon/perovskite tandem solar cell (by Helmholtz-Zentrum Berlin) and a 25.7% single-junction perovskite solar cell (by Ulsan National Institute of Science and Technology) [16]. Perovskite solar cell companies such as UtmoLight, Renshine Solar, and OxfordPV are creating megawatt solar panel production lines. However, the stability of perovskite solar cells remains a challenge if they are to compete with existing silicon PVs' average lifetime of over 25 years. Various ways to overcome this challenge have been investigated in this thesis. Building on this work, cheaper and more stable charge-transporting materials need to be designed and tested. The role of additives used for perovskite bulk passivation needs to be better understood. Most importantly, the degradation mechanism of perovskite solar cells need to be studied further. Understanding how a device fails under certain aging conditions should guide us in fabricating more stable perovskite solar cells which can hopefully be employed soon in renewable energy generation.

APPENDIX A

NMR Spectra of Carbazole-Based Enamine HTMs

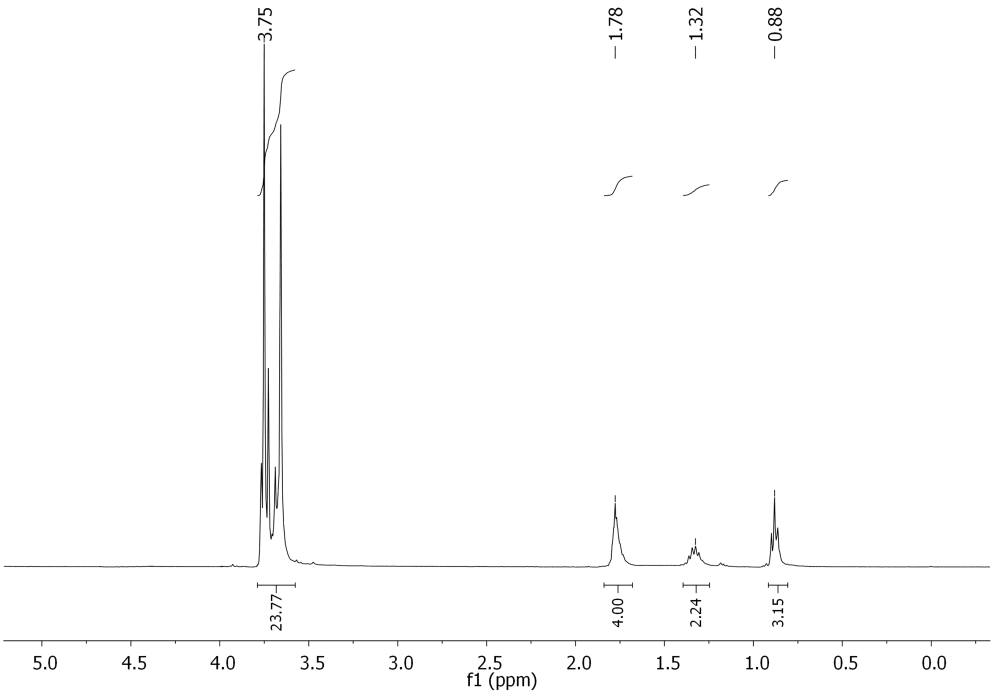

Figure A.1: N^3, N^3, N^6, N^6, 9-tetrakis[2,2-bis(-methoxyphenyl)ethenyl]-9-butyl-9H-carbazole-3,6-diamine (MeO4PEBCz). ^{1}H NMR (400 MHz, $CDCl_3$, δ, ppm). ^{1}H NMR spectra were taken and analyzed by Dr. Maryte Daskeviciene and Dr. Giedre Bubniene, Kaunas University of Technology, Lithuania.

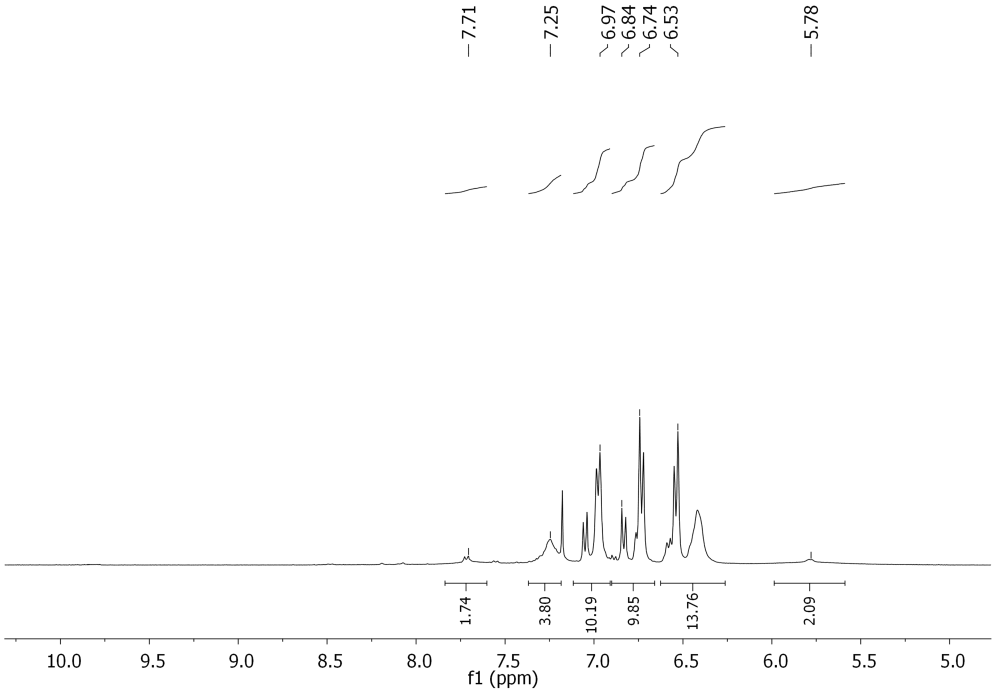

Figure A.2: (Continued from A.1)

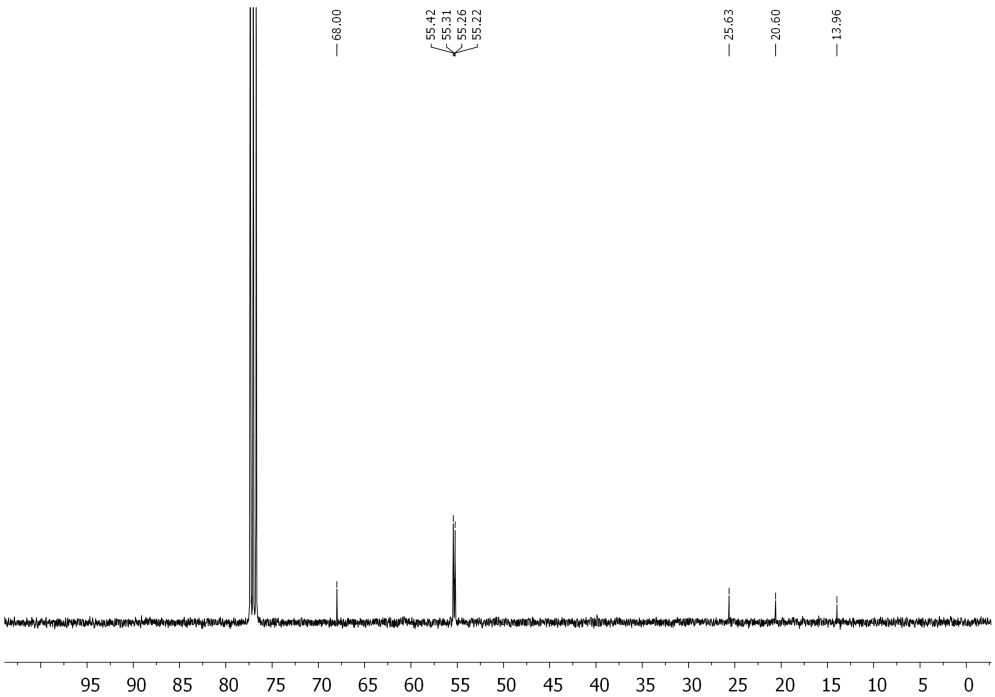

Figure A.3: N^3, N^3, N^6, N^6, 9-tetrakis[2,2-bis(-methoxyphenyl)ethenyl]-9-butyl-9H-carbazole-3,6-diamine (MeO4PEBCz). ^{13}C NMR (101 MHz, $CDCl_3$, δ, ppm). ^{13}C NMR spectra were taken and analyzed by Dr. Maryte Daskeviciene and Dr. Giedre Bubniene, Kaunas University of Technology, Lithuania.

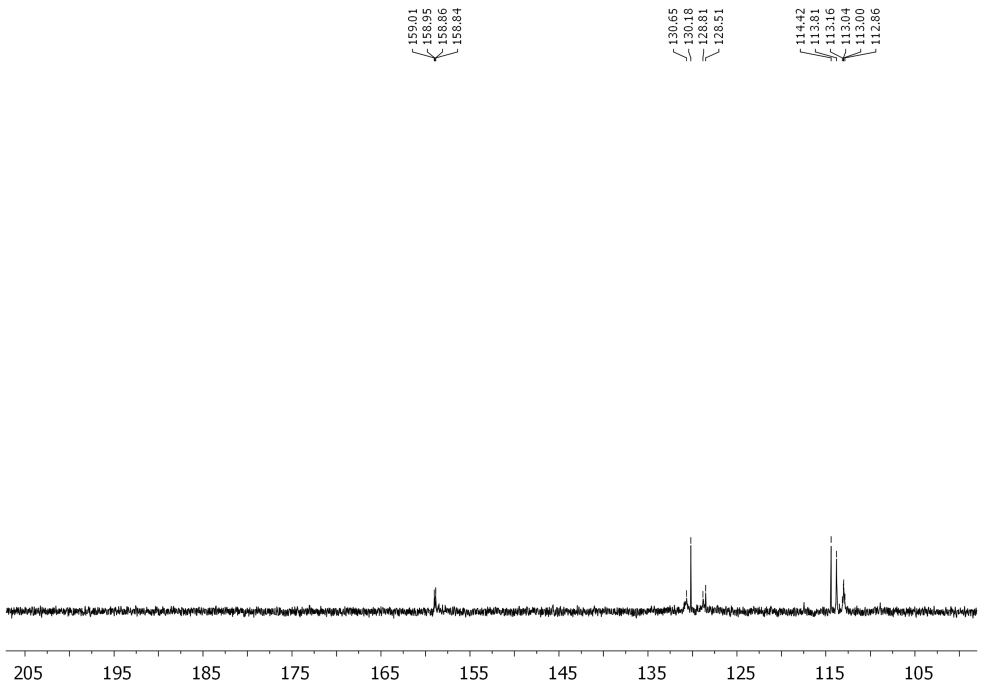

Figure A.4: (Continued from A.3)

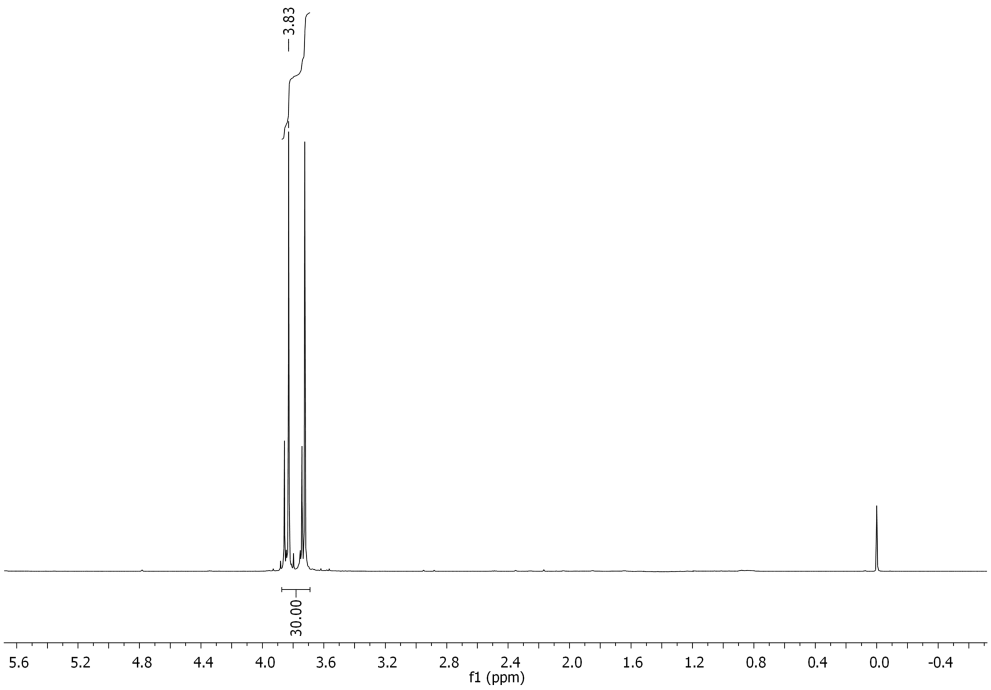

Figure A.5: N^3, N^6, N^6, 9-pentakis[2,2-bis(-methoxyphenyl)ethenyl]-9H-carbazole-3,6-diamine (MeO5PECz). ^{1}H NMR (700 MHz, $CDCl_3$, δ, ppm). ^{1}H NMR spectra were taken and analyzed by Dr. Maryte Daskeviciene and Dr. Giedre Bubniene, Kaunas University of Technology, Lithuania.

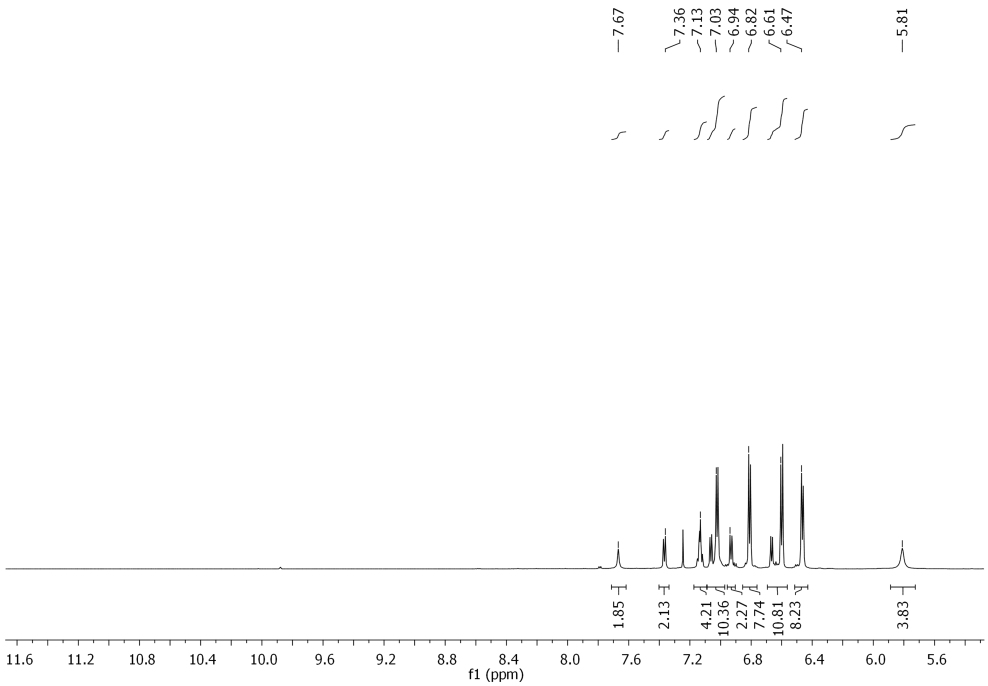

Figure A.6: (Continued from A.5)

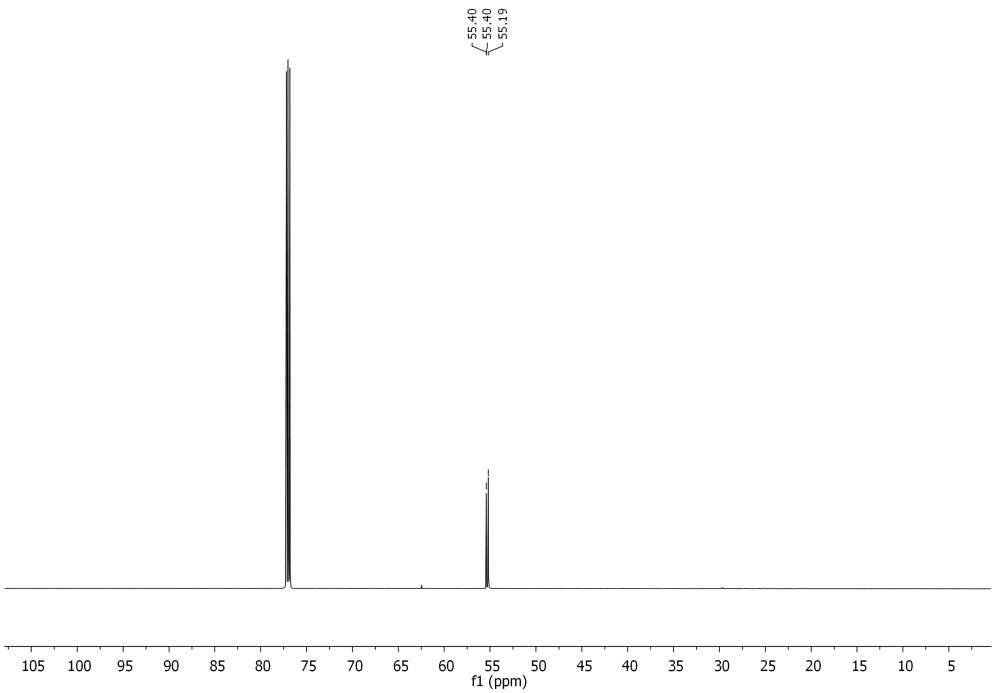

Figure A.7: N^3, N^6, N^6, 9-pentakis[2,2-bis(-methoxyphenyl)ethenyl]-9H-carbazole-3,6-diamine (MeO5PECz). ^{13}C NMR (176 MHz, $CDCl_3$, δ, ppm). ^{13}C NMR spectra were taken and analyzed by Dr. Maryte Daskeviciene and Dr. Giedre Bubniene, Kaunas University of Technology, Lithuania.

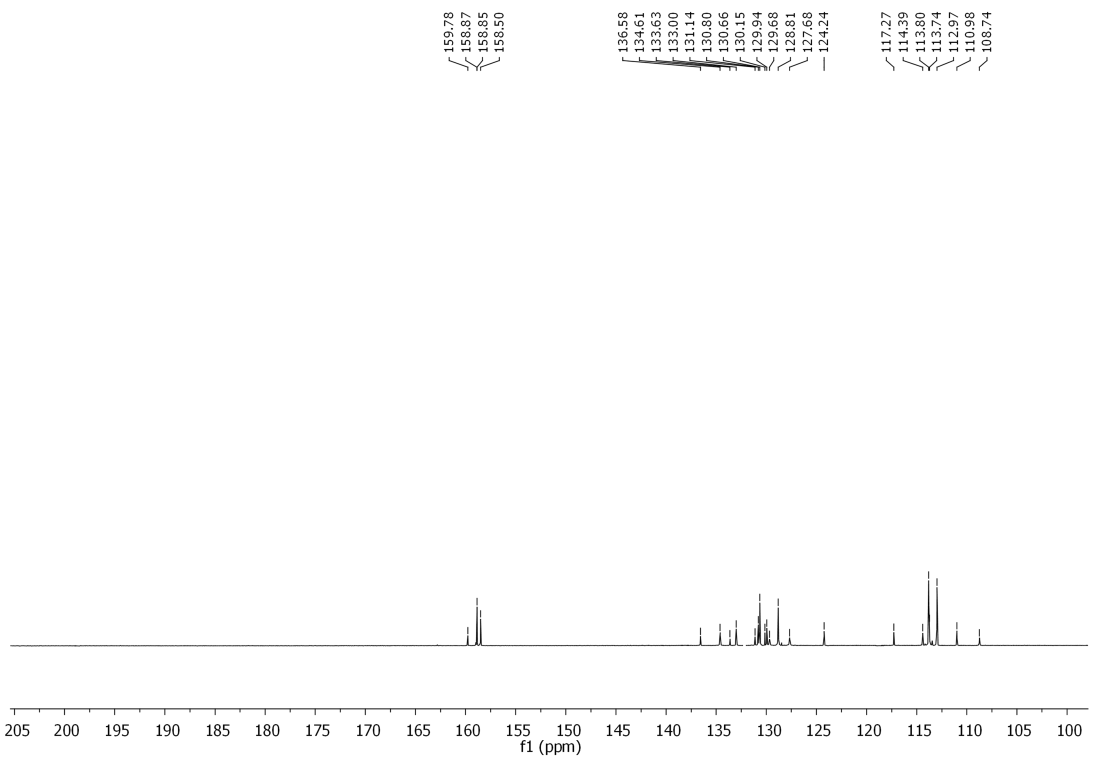

Figure A.8: (Continued from A.7)

APPENDIX B

Cost Estimation

This cost estimation is done by Dr. Maryte Daskeviciene and Dr. Giedre Bubniene from Kaunas University of Technology, Lithuania.

Diamine carbazole precursors could be obtained commercially or synthesized via a two or three-step procedure (Figure B.1) according to the procedures reported in the literature [216, 217, 218]. Due to low volumes of production and niche application of commercial diamine products its price is rather high, therefore, at the moment, for larger-scale synthesis, it makes more economic sense to synthesize the precursors in-house. Therefore, we have included the cost of precursor synthesis in the cost estimation calculations.

Materials intended for use on a large scale must be not only efficient but also cost-effective. For that reason, the estimation of the synthesis costs for both carbazole derivatives has been done based on the procedure established by Osedach et al. [216]. It was calculated that the synthesis cost of MeO5PECz is $ 7.83 per gram while for MeO4PEBCz it reaches 10.33 $/g. It would cost 10 to 12 times less to produce these HTMs than widely used standard spiro-OMeTAD, which costs $ 92 per gram

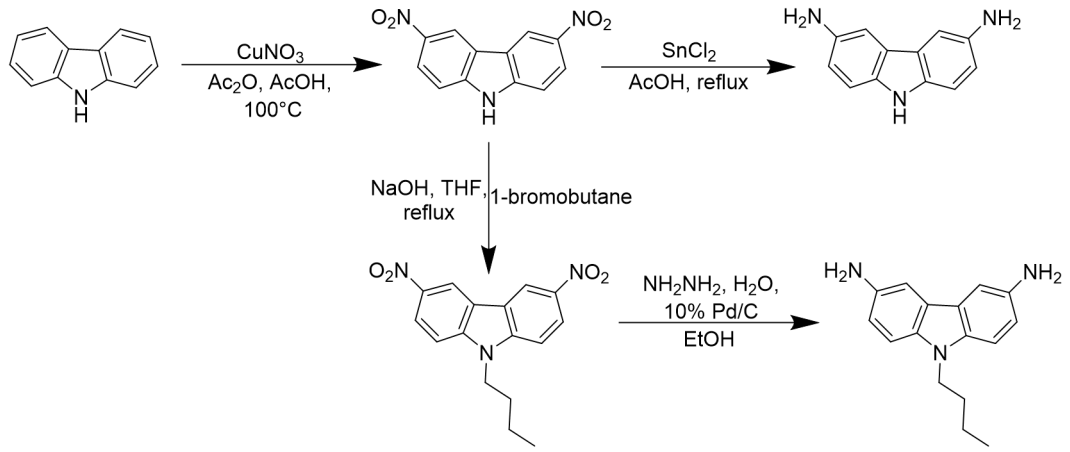

Figure B.1: Synthesis procedure of carbazole precursors.

to synthesize [217]. Synthesis of MeO5PECz and MeO4PEBCz does not require expensive column chromatography or sublimation, the purification is done by simple crystallization; furthermore, the palladium-catalyzed cross-coupling is not needed, avoiding traces of catalyst residue in the final step, which might act as photoquenchers or charge traps during device operation [218, 219].

Table B.1: Materials, quantities, and cost for the synthesis of MeO5PECz. 7.13€=7.83$

Chemicals	Weight reagent (g/g)	Weight solvent (g/g)	Weight Workup (g/g)	Price of chemicals (€/kg)	Cost of chemical (€/g product)	Cost per step (€/g)
Carbazole	0.28			200.00	0.05	
$Cu(NO_3)_2$	0.49			23.12	0.01	
Acetic acid		2		40.12	0.08	
Acetic anhydride		2.5		12.00	0.03	
Ethanol			30	6.08	0.20	
KOH			2.5	12.70	0.03	
HCl			10	4.31	0.04	
3,6-dinitro-9H-carbazole	0.77	4.5	42.5			0.44
$SnCl_2$	2.63			118.10	0.31	
Acetic acid		2.5		40.12	0.10	
HCl		12		4.31	0.05	
NaOH			20	4.28	0.09	
3,6-diamino-9H-carbazole	2.63	14.5	20			0.55
2,2-bis(4-methoxyphenyl)acetaldehyde	2.03			2300.00	4.67	
CSA	0.3			260.00	0.08	
THF		15		8.88	0.13	
Ethanol			200	6.08	1.22	
Acetone			22	1.52	0.04	
Total	5.73	34	284.5			7.13

Appendix B. Cost Estimation

Table B.2: Materials, quantities, and cost for the synthesis of MeO4PEBCz. 9.41€=10.33$

Chemicals	Weight reagent (g/g)	Weight solvent (g/g)	Weight Workup (g/g)	Price of chemicals (€/kg)	Cost of chemical (€/g product)	Cost per step (€/g)
3,6-dinitro-9H-carbazole	0.85			1222.22	1.04	
1-bromobutane	0.906			22.08	0.02	
THF		125	15	8.88	1.24	
NaOH	0.27			4.28	0.01	
9-butyl-3,6-dinitrocarbazole	2.026	125	15			2.31
Pd/C	0.05			5350.00	0.27	
$N_2H_4 \cdot xH_2O$	1			22.00	0.02	
Ethanol		17	4	6.08	0.13	
9-alkyl-3,6-diaminocarbazole	1.05	17	4			0.42
2,2-bis(4-methoxyphenyl)acetaldehyde	2.2			2300.00	5.06	
CSA	0.4			260.00	0.10	
Toluene		15		2.46	0.04	
Ethyl acetate			125	2.85	0.35	
Na_2SO_4			20	6.08	0.12	
Ethanol			100	6.08	0.61	
THF			45	8.88	0.4	
Total	5.676	157	309			9.41

Bibliography

[1] B. Freese, *Coal: A human history*. Basic Books, 2016. 1

[2] R. L. Galloway, *Annals of Coal Mining and the Coal Trade: The Invention of the Steam Engine and the Origin of the Railway*. Colliery guardian Company, limited, 1898. 1

[3] S. Pirani, *Burning up: A global history of fossil fuel consumption*. Pluto Press, 2018. 1

[4] B. Kopey, "Development of drilling technics from ancient ages to modern times," in *12th IFToMM World Congress, Besançon, France*, 2007. 1

[5] H. Devold, *Oil and gas production handbook: an introduction to oil and gas production*. Lulu. com, 2013. 1

[6] K. Rosentrater and R. Balamuralikrishna, "Essential highlights of the history of fluid mechanics," in *2005 Annual Conference*, pp. 10–579, 2005. 1

[7] L. Feng, Y. Hu, C. A. Hall, J. Wang, L. Feng, Y. Hu, C. A. Hall, and J. Wang, "The history of chinese oil industry development," *The Chinese Oil Industry: History and Future*, pp. 1–15, 2013. 1

[8] H. Ritchie, M. Roser, and P. Rosado, "Energy," *Our World in Data*, 2022. `https://ourworldindata.org/energy` (accessed mar. 18, 2023). 1, 2

[9] N. Wade, "CO_2 in climate: gloomsday predictions have no fault," *Science*, vol. 206, no. 4421, pp. 912–913, 1979. 2

[10] P. Jackson, "From stockholm to kyoto: A brief history of climate change," jun 2007. United Nations, `https://www.un.org/en/chronicle/article/stockholm-kyoto-brief-history-climate-change` (accessed jun. 30, 2023). 2

[11] J. Houghton, G. Jenkins, and J. Ephraums, "Climate change: The IPCC 1990 and 1992 assessments," 1990. 2

[12] "The cat thermometer," nov 2022. `https://climateactiontracker.org/global/cat-thermometer/` (accessed mar. 26, 2023). 3

[13] P. Bojek, "Solar pv – analysis," sep 2022. `https://www.iea.org/reports/solar-pv` (accessed jun. 29, 2023). 4, 5

[14] "Solar cell market (by material: Crystalline, thin film; by product: Bsf, perc/perl/pert/topcon, hjt, ibc & mwt, others; by technology: Monocrystalline, polycrystalline, cadmium telluride, amorphous siliconcopper indium gallium diselenide; by installation type: Residential, commercial, utility) - global industry analysis, size, share, growth, trends, regional outlook, and forecast 2022-2030," oct 2022. `https://www.precedenceresearch.com/solar-cell-market` (accessed jun. 29, 2023). 4

[15] D. Heinemann, W. Jürgens, R. Knecht, and J. Parisi, "30 years at the service of renewable energies," *Das forschungsmagazin der universität oldenburg Einblicke*, vol. 54, pp. 9–10, 2010. 4

[16] "Best research-cell efficiency chart," mar 2023. `https://www.nrel.gov/pv/cell-efficiency.html` (accessed mar. 26, 2023). 4, 5, 22, 32, 89, 142

[17] N. S. Baghel and N. Chander, "Performance comparison of mono and polycrystalline silicon solar photovoltaic modules under tropical wet and dry climatic conditions in east-central india," *Clean Energy*, vol. 6, no. 1, pp. 165–177, 2022. 4

[18] V. M. Fthenakis and P. Moskowitz, "Thin-film photovoltaic cells: Health and environmental issues in their manufacture use and disposal," *Progress in Photovoltaics: Research and Applications*, vol. 3, no. 5, pp. 295–306, 1995. 5

[19] Q. Liu, Y. Jiang, K. Jin, J. Qin, J. Xu, W. Li, J. Xiong, J. Liu, Z. Xiao, K. Sun, *et al.*, "18% efficiency organic solar cells," *Science Bulletin*, vol. 65, no. 4, pp. 272–275, 2020. 5

[20] X. Du, T. Heumueller, W. Gruber, A. Classen, T. Unruh, N. Li, and C. J. Brabec, "Efficient polymer solar cells based on non-fullerene acceptors with potential device lifetime approaching 10 years," *Joule*, vol. 3, no. 1, pp. 215–226, 2019. 6

[21] Z. Peng, Q. Wei, H. Chen, Y. Liu, F. Wang, X. Jiang, W. Liu, W. Zhou, S. Ling, and Z. Ning, "$Cs_{0.15}FA_{0.85}PbI_3/Cs_xFA_{1-x}PbI_3$ core/shell heterostructure for highly stable and efficient perovskite solar cells," *Cell Reports Physical Science*, vol. 1, no. 10, 2020. 6

[22] G. Granata, F. Pagnanelli, E. Moscardini, T. Havlik, and L. Toro, "Recycling of photovoltaic panels by physical operations," *Solar Energy Materials and Solar Cells*, vol. 123, pp. 239–248, 2014. 6

[23] C. B. Honsberg and S. G. Bowden, "PV Education," 2019. https://www.pveducation.org/ (accessed mar. 28, 2023). 7

[24] P. Altermatt, "The global standard spectrum (AM1.5g)," jun 2011. https://www2.pvlighthouse.com.au/resources/courses/altermatt/The%20Solar%20Spectrum/The%20global%20standard%20spectrum%20%28AM1-5g%29.aspx (accessed jun. 28, 2023). 8

[25] J. Blakemore, "Semiconducting and other major properties of gallium arsenide," *Journal of Applied Physics*, vol. 53, no. 10, pp. R123–R181, 1982. 9

[26] S. Maestre, "What's fermi level and why is it important in a semiconductor?," jul 2021. https://www.circuitbread.com/ee-faq/whats-fermi-level-and-why-is-it-important-in-a-semiconductor (accessed jun. 28, 2023). 10

[27] P. P. Altermatt, A. Schenk, F. Geelhaar, and G. Heiser, "Reassessment of the intrinsic carrier density in crystalline silicon in view of band-gap narrowing," *Journal of Applied Physics*, vol. 93, no. 3, pp. 1598–1604, 2003. 10

[28] J. A. Nelson, *The physics of solar cells*. World Scientific Publishing Company, 2003. 12

[29] H. Brooks, "Theory of the electrical properties of germanium and silicon," in *Advances in electronics and electron physics*, vol. 7, pp. 85–182, Elsevier, 1955. 14

[30] C. Herring, "Transport properties of a many-valley semiconductor," *The Bell System Technical Journal*, vol. 34, no. 2, pp. 237–290, 1955. 14

[31] K. Paul and P. Giri, "Plasmonic metal and semiconductor nanoparticle decorated TiO_2-based photocatalysts for solar light driven photocatalysis," in *Encyclopedia of Interfacial Chemistry* (K. Wandelt, ed.), pp. 786–794, Oxford: Elsevier, 2018. 18

[32] W. Shockley and H. J. Queisser, "Detailed balance limit of efficiency of p-n junction solar cells," *Journal of applied physics*, vol. 32, no. 3, pp. 510–519, 1961. 20

[33] G. E. Eperon, M. T. Hörantner, and H. J. Snaith, "Metal halide perovskite tandem and multiple-junction photovoltaics," *Nature Reviews Chemistry*, vol. 1, no. 12, p. 0095, 2017. 22

[34] G. E. Eperon, T. Leijtens, K. A. Bush, R. Prasanna, T. Green, J. T.-W. Wang, D. P. McMeekin, G. Volonakis, R. L. Milot, R. May, *et al.*, "Perovskite-perovskite tandem photovoltaics with optimized band gaps," *Science*, vol. 354, no. 6314, pp. 861–865, 2016. 22

[35] A. Kojima, K. Teshima, Y. Shirai, and T. Miyasaka, "Organometal halide perovskites as visible-light sensitizers for photovoltaic cells," *Journal of the american chemical society*, vol. 131, no. 17, pp. 6050–6051, 2009. 22

[36] A. S. Marques, R. M. Faria, J. N. Freitas, and A. F. Nogueira, "Low-temperature blade-coated perovskite solar cells," *Industrial & Engineering Chemistry Research*, vol. 60, no. 19, pp. 7145–7154, 2021. 23

[37] X. Zhang, L. Shen, P. Baral, S. Vijayaraghavan, F. Yan, X. Gong, and H. Wang, "Blade-coated inverted perovskite solar cells in an ambient environment," *Solar energy materials and solar cells*, vol. 246, p. 111894, 2022. 23

[38] K. Xu, A. Al-Ashouri, Z.-W. Peng, E. Köhnen, H. Hempel, F. Akhundova, J. A. Marquez, P. Tockhorn, O. Shargaieva, F. Ruske, *et al.*, "Slot-die coated triple-halide perovskites for efficient and scalable perovskite/silicon tandem solar cells," *ACS Energy Letters*, vol. 7, no. 10, pp. 3600–3611, 2022. 23

[39] J. B. Whitaker, D. H. Kim, B. W. Larson, F. Zhang, J. J. Berry, M. F. Van Hest, and K. Zhu, "Scalable slot-die coating of high performance perovskite solar cells," *Sustainable Energy & Fuels*, vol. 2, no. 11, pp. 2442–2449, 2018. 23

[40] H. Li, J. Zhou, L. Tan, M. Li, C. Jiang, S. Wang, X. Zhao, Y. Liu, Y. Zhang, Y. Ye, *et al.*, "Sequential vacuum-evaporated perovskite solar cells with more than 24% efficiency," *Science Advances*, vol. 8, no. 28, p. eabo7422, 2022. 23

[41] Y.-H. Chiang, M. Anaya, and S. D. Stranks, "Multisource vacuum deposition of methylammonium-free perovskite solar cells," *ACS Energy Letters*, vol. 5, no. 8, pp. 2498–2504, 2020. 23

[42] G. Grancini, C. Roldán-Carmona, I. Zimmermann, E. Mosconi, X. Lee, D. Martineau, S. Narbey, F. Oswald, F. De Angelis, M. Graetzel, *et al.*, "One-Year stable perovskite solar cells by 2D/3D interface engineering," *Nature communications*, vol. 8, no. 1, p. 15684, 2017. 23

[43] S. D. Stranks, G. E. Eperon, G. Grancini, C. Menelaou, M. J. Alcocer, T. Leijtens, L. M. Herz, A. Petrozza, and H. J. Snaith, "Electron-hole diffusion lengths exceeding 1 micrometer in an organometal trihalide perovskite absorber," *Science*, vol. 342, pp. 341–344, oct 2013. 23, 27

[44] T. Miyasaka, "Perovskite photovoltaics: Rare functions of organo lead halide in solar cells and optoelectronic devices," *Chemistry Letters*, vol. 44, no. 6, pp. 720–729, 2015. 25, 28

[45] M. M. Lee, J. Teuscher, T. Miyasaka, T. N. Murakami, and H. J. Snaith, "Efficient hybrid solar cells based on meso-superstructured organometal halide perovskites," *Science*, vol. 338, pp. 643–647, nov 2012. 25

[46] A. K. Jena, A. Kulkarni, and T. Miyasaka, "Halide perovskite photovoltaics: Background, status, and future prospects," *Chemical Reviews*, vol. 119, pp. 3036–3103, mar 2019. 25, 26, 27

[47] E. M. Sanehira, B. J. Tremolet de Villers, P. Schulz, M. O. Reese, S. Ferrere, K. Zhu, L. Y. Lin, J. J. Berry, and J. M. Luther, "Influence of electrode interfaces on the stability of perovskite solar cells: reduced degradation using

MoOx/Al for hole collection," *ACS Energy Letters*, vol. 1, no. 1, pp. 38–45, 2016. 25, 86

[48] G.-J. A. Wetzelaer and P. W. Blom, "Electron and hole transport in solution-processed fullerenes," *Journal of Materials Chemistry C*, vol. 9, no. 45, pp. 16068–16077, 2021. 26

[49] P. Caprioglio, M. Stolterfoht, C. M. Wolff, T. Unold, B. Rech, S. Albrecht, and D. Neher, "On the relation between the open-circuit voltage and quasi-fermi level splitting in efficient perovskite solar cells," *Advanced Energy Materials*, vol. 9, no. 33, p. 1901631, 2019. 26, 56, 80

[50] M. Stolterfoht, P. Caprioglio, C. M. Wolff, J. A. Márquez, J. Nordmann, S. Zhang, D. Rothhardt, U. Hörmann, Y. Amir, A. Redinger, L. Kegelmann, F. Zu, S. Albrecht, N. Koch, T. Kirchartz, M. Saliba, T. Unold, and D. Neher, "The impact of energy alignment and interfacial recombination on the internal and external open-circuit voltage of perovskite solar cells," *Energy & Environmental Science*, vol. 12, pp. 2778–2788, sep 2019. 26, 80, 117

[51] S. Sun, T. Salim, N. Mathews, M. Duchamp, C. Boothroyd, G. Xing, T. C. Sum, and Y. M. Lam, "The origin of high efficiency in low-temperature solution-processable bilayer organometal halide hybrid solar cells," *Energy & Environmental Science*, vol. 7, no. 1, pp. 399–407, 2014. 27

[52] G. Xing, N. Mathews, S. Sun, S. S. Lim, Y. M. Lam, M. Gratzel, S. Mhaisalkar, and T. C. Sum, "Long-range balanced electron-and hole-transport lengths in organic-inorganic $CH_3NH_3PbI_3$," *Science*, vol. 342, pp. 344–347, oct 2013. 27

[53] W.-J. Yin, T. Shi, and Y. Yan, "Superior photovoltaic properties of lead halide perovskites: Insights from first-principles theory," *The Journal of Physical Chemistry C*, vol. 119, pp. 5253–5264, mar 2015. 27, 28, 29, 30, 31, 85

[54] N. Phung, A. Al-Ashouri, S. Meloni, A. Mattoni, S. Albrecht, E. L. Unger, A. Merdasa, and A. Abate, "The role of grain boundaries on ionic defect migration in metal halide perovskites," *Advanced Energy Materials*, vol. 10, no. 20, p. 1903735, 2020. 30

[55] F. Brivio, K. T. Butler, A. Walsh, and M. van Schilfgaarde, "Relativistic quasiparticle self-consistent electronic structure of hybrid halide perovskite photovoltaic absorbers," *Physical Review B*, vol. 89, p. 155204, apr 2014. 31

[56] A. Rajagopal, Z. Yang, S. B. Jo, I. L. Braly, P.-W. Liang, H. W. Hillhouse, and A. K.-Y. Jen, "Highly efficient perovskite–perovskite tandem solar cells reaching 80% of the theoretical limit in photovoltage," *Advanced materials*, vol. 29, no. 34, p. 1702140, 2017. 31

[57] J. Cheng, I. Choi, W. Kim, H. Li, B. Koo, and M. J. Ko, "Wide-band-gap (2.0 eV) perovskite solar cells with a V_{OC} of 1.325 V fabricated by a green-solvent strategy," *ACS Applied Materials & Interfaces*, 2023. 31

[58] R. Prasanna, A. Gold-Parker, T. Leijtens, B. Conings, A. Babayigit, H.-G. Boyen, M. F. Toney, and M. D. McGehee, "Band gap tuning via lattice contraction and octahedral tilting in perovskite materials for photovoltaics," *Journal of the American Chemical Society*, vol. 139, pp. 11117–11124, aug 2017. 31

[59] F. Hao, C. C. Stoumpos, R. P. H. Chang, and M. G. Kanatzidis, "Anomalous band gap behavior in mixed sn and pb perovskites enables broadening of absorption spectrum in solar cells," *Journal of the American Chemical Society*, vol. 136, pp. 8094–8099, jun 2014. 32, 33

[60] A. Goyal, S. McKechnie, D. Pashov, W. Tumas, M. van Schilfgaarde, and V. Stevanović, "Origin of pronounced nonlinear band gap behavior in lead–tin hybrid perovskite alloys," *Chemistry of Materials*, vol. 30, pp. 3920–3928, Jun 2018. 32, 33

[61] S. Rühle, "Tabulated values of the shockley–queisser limit for single junction solar cells," *Solar Energy*, vol. 130, pp. 139–147, 2016. 32

[62] H. Chen, A. Maxwell, C. Li, S. Teale, B. Chen, T. Zhu, E. Ugur, G. Harrison, L. Grater, J. Wang, Z. Wang, L. Zeng, S. M. Park, L. Chen, P. Serles, R. A. Awni, B. Subedi, X. Zheng, C. Xiao, N. J. Podraza, T. Filleter, C. Liu, Y. Yang, J. M. Luther, S. De Wolf, M. G. Kanatzidis, Y. Yan, and E. H. Sargent, "Regulating surface potential maximizes voltage in all-perovskite tandems," *Nature 2022 613:7945*, vol. 613, pp. 676–681, nov 2022. 32

[63] T. Leijtens, G. E. Eperon, S. Pathak, A. Abate, M. M. Lee, and H. J. Snaith, "Overcoming ultraviolet light instability of sensitized TiO2 with meso-superstructured organometal tri-halide perovskite solar cells," *Nature Communications 2013 4:1*, vol. 4, pp. 1–8, dec 2013. 34

[64] C. Qiu, Y. Wu, J. Song, W. Wang, and Z. Li, "Efficient planar perovskite solar cells with ZnO electron transport layer," *Coatings*, vol. 12, p. 1981, dec 2022. 34

[65] S. S. Shin, S. J. Lee, and S. I. Seok, "Metal oxide charge transport layers for efficient and stable perovskite solar cells," *Advanced Functional Materials*, vol. 29, p. 1900455, nov 2019. 34

[66] J. Yang, B. D. Siempelkamp, E. Mosconi, F. De Angelis, and T. L. Kelly, "Origin of the thermal instability in $CH_3NH_3PbI_3$ thin films deposited on ZnO," *Chemistry of Materials*, vol. 27, pp. 4229–4236, jun 2015. 34

[67] T. Leijtens, I. K. Ding, T. Giovenzana, J. T. Bloking, M. D. McGehee, and A. Sellinger, "Hole transport materials with low glass transition temperatures and high solubility for application in solid-state dye-sensitized solar cells," *ACS Nano*, vol. 6, pp. 1455–1462, feb 2012. 34

[68] S. Kim, S. Bae, S.-W. Lee, K. Cho, K. D. Lee, H. Kim, S. Park, G. Kwon, S.-W. Ahn, H.-M. Lee, *et al.*, "Relationship between ion migration and interfacial degradation of $CH_3NH_3PbI_3$ perovskite solar cells under thermal conditions," *Scientific reports*, vol. 7, no. 1, p. 1200, 2017. 34

[69] R. A. Kerner, S. Heo, K. Roh, K. MacMillan, B. W. Larson, and B. P. Rand, "Organic hole transport material ionization potential dictates diffusion kinetics of iodine species in halide perovskite devices," *ACS Energy Letters*, vol. 6, pp. 501–508, feb 2021. 34

[70] J. Wang, J. Zhang, Y. Yang, Y. Dong, W. Wang, B. Hu, J. Li, W. Cao, K. Lin, D. Xia, *et al.*, "Li-TFSI endohedral metal-organic frameworks in stable perovskite solar cells for anti-deliquescent and restricting ion migration," *Chemical Engineering Journal*, vol. 429, p. 132481, 2022. 34

[71] Z. Li, C. Xiao, Y. Yang, S. P. Harvey, D. H. Kim, J. A. Christians, M. Yang, P. Schulz, S. U. Nanayakkara, C.-S. Jiang, *et al.*, "Extrinsic ion migration in perovskite solar cells," *Energy & Environmental Science*, vol. 10, no. 5, pp. 1234–1242, 2017. 34

[72] F. Lamberti, T. Gatti, E. Cescon, R. Sorrentino, A. Rizzo, E. Menna, G. Meneghesso, M. Meneghetti, A. Petrozza, and L. Franco, "Evidence of spiro-OMeTAD de-doping by tert-butylpyridine additive in hole-transporting layers for perovskite solar cells," *Chem*, vol. 5, no. 7, pp. 1806–1817, 2019. 34

[73] G. Ren, W. Han, Q. Zhang, Z. Li, Y. Deng, C. Liu, and W. Guo, "Overcoming perovskite corrosion and de-doping through chemical binding of halogen bonds toward efficient and stable perovskite solar cells," *Nano-Micro Letters*, vol. 14, no. 1, p. 175, 2022. 34

[74] S. Wang, Z. Huang, X. Wang, Y. Li, M. Günther, S. Valenzuela, P. Parikh, A. Cabreros, W. Xiong, and Y. S. Meng, "Unveiling the role of tBP–LiTFSI complexes in perovskite solar cells," *Journal of the American Chemical Society*, vol. 140, no. 48, pp. 16720–16730, 2018. 34

[75] J. Zhao, Y. Deng, H. Wei, X. Zheng, Z. Yu, Y. Shao, J. E. Shield, and J. Huang, "Strained hybrid perovskite thin films and their impact on the intrinsic stability of perovskite solar cells," *Science Advances*, vol. 3, p. eaao5616, feb 2023. 35

[76] H. Wang, C. Zhu, L. Liu, S. Ma, P. Liu, J. Wu, C. Shi, Q. Du, Y. Hao, S. Xiang, *et al.*, "Interfacial residual stress relaxation in perovskite solar cells with improved stability," *Advanced Materials*, vol. 31, no. 48, p. 1904408, 2019. 35

[77] C. Zhu, X. Niu, Y. Fu, N. Li, C. Hu, Y. Chen, X. He, G. Na, P. Liu, H. Zai, *et al.*, "Strain engineering in perovskite solar cells and its impacts on carrier dynamics," *Nature communications*, vol. 10, no. 1, p. 815, 2019. 35

[78] G. Yuan, W. Xie, Q. Song, S. Ma, Y. Ma, C. Shi, M. Xiao, F. Pei, X. Niu, Y. Zhang, *et al.*, "Inhibited crack development by compressive strain in perovskite solar cells with improved mechanical stability," *Advanced Materials*, p. 2211257, 2023. 35

[79] R. Cheacharoen, N. Rolston, D. Harwood, K. A. Bush, R. H. Dauskardt, and M. D. McGehee, "Design and understanding of encapsulated perovskite solar cells to withstand temperature cycling," *Energy & Environmental Science*, vol. 11, no. 1, pp. 144–150, 2018. 35

[80] D.-J. Xue, Y. Hou, S.-C. Liu, M. Wei, B. Chen, Z. Huang, Z. Li, B. Sun, A. H. Proppe, Y. Dong, M. I. Saidaminov, S. O. Kelley, J.-S. Hu, and E. H. Sargent, "Regulating strain in perovskite thin films through charge-transport layers," *Nature Communications*, vol. 11, no. 1, p. 1514, 2020. 35

[81] J. Zhao, Y. Deng, H. Wei, X. Zheng, Z. Yu, Y. Shao, J. E. Shield, and J. Huang, "Strained hybrid perovskite thin films and their impact on the intrinsic stability of perovskite solar cells," *Science advances*, vol. 3, no. 11, p. eaao5616, 2017. 35

[82] N. Rolston, K. A. Bush, A. D. Printz, A. Gold-Parker, Y. Ding, M. F. Toney, M. D. McGehee, and R. H. Dauskardt, "Engineering stress in perovskite solar cells to improve stability," *Advanced Energy Materials*, vol. 8, no. 29, p. 1802139, 2018. 35

[83] Z. Huang, L. Li, T. Wu, T. Xue, W. Sun, Q. Pan, H. Wang, H. Xie, J. Chi, T. Han, *et al.*, "Wearable perovskite solar cells by aligned liquid crystal elastomers," *Nature Communications*, vol. 14, no. 1, p. 1204, 2023. 35

[84] Q. Dong, C. Zhu, M. Chen, C. Jiang, J. Guo, Y. Feng, Z. Dai, S. K. Yadavalli, M. Hu, X. Cao, *et al.*, "Interpenetrating interfaces for efficient perovskite solar cells with high operational stability and mechanical robustness," *Nature Communications*, vol. 12, no. 1, p. 973, 2021. 35

[85] Z. Dai, S. K. Yadavalli, M. Chen, A. Abbaspourtamijani, Y. Qi, and N. P. Padture, "Interfacial toughening with self-assembled monolayers enhances perovskite solar cell reliability," *Science*, vol. 372, no. 6542, pp. 618–622, 2021. 35

[86] K. Domanski, J. P. Correa-Baena, N. Mine, M. K. Nazeeruddin, A. Abate, M. Saliba, W. Tress, A. Hagfeldt, and M. Grätzel, "Not all that glitters is gold: Metal-migration-induced degradation in perovskite solar cells," *ACS Nano*, vol. 10, pp. 6306–6314, jun 2016. 36, 132

[87] A. Davis, T. Tran, and D. R. Young, "Solution chemistry of iodide leaching of gold," *Hydrometallurgy*, vol. 32, no. 2, pp. 143–159, 1993. 36

[88] T. A. Green, "Gold etching for microfabrication," *Gold Bulletin*, vol. 47, no. 3, pp. 205–216, 2014. 36

[89] S. Svanström, T. J. Jacobsson, G. Boschloo, E. M. J. Johansson, H. Rensmo, and U. B. Cappel, "Degradation mechanism of silver metal deposited on lead halide perovskites," *ACS Applied Materials & Interfaces*, vol. 12, pp. 7212–7221, feb 2020. 36

[90] J. T. DuBose, P. S. Mathew, J. Cho, M. Kuno, and P. V. Kamat, "Modulation of photoinduced iodine expulsion in mixed halide perovskites with electrochemical bias," *The Journal of Physical Chemistry Letters*, vol. 12, no. 10, pp. 2615–2621, 2021. 36

[91] S. Cacovich, L. Cinà, F. Matteocci, G. Divitini, P. A. Midgley, A. Di Carlo, and C. Ducati, "Gold and iodine diffusion in large area perovskite solar cells under illumination," *Nanoscale*, vol. 9, no. 14, pp. 4700–4706, 2017. 36

[92] C. Besleaga, L. E. Abramiuc, V. Stancu, A. G. Tomulescu, M. Sima, L. Trinca, N. Plugaru, L. Pintilie, G. A. Nemnes, M. Iliescu, *et al.*, "Iodine migration and degradation of perovskite solar cells enhanced by metallic electrodes," *The journal of physical chemistry letters*, vol. 7, no. 24, pp. 5168–5175, 2016. 36

[93] C. Li, S. Tscheuschner, F. Paulus, P. E. Hopkinson, J. Kießling, A. Köhler, Y. Vaynzof, and S. Huettner, "Iodine migration and its effect on hysteresis in perovskite solar cells," *Advanced Materials*, vol. 28, no. 12, pp. 2446–2454, 2016. 36

[94] D. Lin, T. Shi, H. Xie, F. Wan, X. Ren, K. Liu, Y. Zhao, L. Ke, Y. Lin, Y. Gao, *et al.*, "Ion migration accelerated reaction between oxygen and metal halide perovskites in light and its suppression by cesium incorporation," *Advanced Energy Materials*, vol. 11, no. 8, p. 2002552, 2021. 36

[95] Y.-C. Zhao, W.-K. Zhou, X. Zhou, K.-H. Liu, D.-P. Yu, and Q. Zhao, "Quantification of light-enhanced ionic transport in lead iodide perovskite thin films and its solar cell applications," *Light: Science & Applications*, vol. 6, no. 5, pp. e16243–e16243, 2017. 36

[96] X. Zheng, Y. Hou, C. Bao, J. Yin, F. Yuan, Z. Huang, K. Song, J. Liu, J. Troughton, N. Gasparini, C. Zhou, Y. Lin, D.-J. Xue, B. Chen, A. K. Johnston, N. Wei, M. N. Hedhili, M. Wei, A. Y. Alsalloum, P. Maity, B. Turedi, C. Yang, D. Baran, T. D. Anthopoulos, Y. Han, Z.-H. Lu, O. F. Mohammed, F. Gao, E. H. Sargent, and O. M. Bakr, "Managing grains and interfaces via ligand anchoring enables 22.3%-efficiency inverted perovskite solar cells," *Nature Energy*, vol. 5, pp. 131–140, feb 2020. 37, 90

[97] F. Wang, W. Geng, Y. Zhou, H.-H. Fang, C.-J. Tong, M. A. Loi, L.-M. Liu, and N. Zhao, "Phenylalkylamine passivation of organolead halide perovskites enabling high-efficiency and air-stable photovoltaic cells," *Advanced materials*, vol. 28, no. 45, pp. 9986–9992, 2016. 37

[98] H. Ran, L. Cao, Y. Zhao, M. Chen, P. Qi, H. Wu, Y. Lu, Y. Zhang, S. Wang, and Y. Tang, "Constructing 2d passivation layer on perovskites based on 3-chlorobenzylamine enables efficient and stable perovskite solar cells," *Journal of Alloys and Compounds*, vol. 926, p. 166891, 2022. 37

[99] W. Feng, C. Zhang, J.-X. Zhong, L. Ding, and W.-Q. Wu, "Correlating alkyl chain length with defect passivation efficacy in perovskite solar cells," *Chemical Communications*, vol. 56, no. 37, pp. 5006–5009, 2020. 37

[100] V. Valenzano, A. Cesari, F. Balzano, A. Milella, F. Fracassi, A. Listorti, G. Gigli, A. Rizzo, G. Uccello-Barretta, and S. Colella, "Methylammonium-formamidinium reactivity in aged organometal halide perovskite inks," *Cell Reports Physical Science*, vol. 2, no. 5, p. 100432, 2021. 37

[101] X. Wang, Y. Fan, L. Wang, C. Chen, Z. Li, R. Liu, H. Meng, Z. Shao, X. Du, H. Zhang, G. Cui, and S. Pang, "Perovskite solution aging: What happened and how to inhibit?," *Chem*, vol. 6, no. 6, pp. 1369–1378, 2020. 37, 71

[102] Q. Jiang, J. Tong, Y. Xian, R. A. Kerner, S. P. Dunfield, C. Xiao, R. A. Scheidt, D. Kuciauskas, X. Wang, M. P. Hautzinger, R. Tirawat, M. C. Beard, D. P. Fenning, J. J. Berry, B. W. Larson, Y. Yan, and K. Zhu, "Surface reaction for efficient and stable inverted perovskite solar cells," *Nature 2022*, pp. 1–2, sep 2022. 37

[103] R. A. Kerner, T. H. Schloemer, P. Schulz, J. J. Berry, J. Schwartz, A. Sellinger, and B. P. Rand, "Amine additive reactions induced by the soft Lewis acidity of Pb^{2+} in halide perovskites. Part I: evidence for Pb–alkylamide formation," *Journal of Materials Chemistry C*, vol. 7, pp. 5251–5259, may 2019. 37, 90

[104] S. Zhou, M. Daskeviciene, M. Steponaitis, G. Bubniene, V. Jankauskas, K. Schutt, P. Holzhey, A. R. Marshall, P. Caprioglio, G. Christoforo, J. M. Ball, T. Malinauskas, V. Getautis, and H. J. Snaith, "Low-cost dopant-free carbazole enamine hole-transporting materials for thermally stable perovskite solar cells," *Solar RRL*, vol. 6, p. 2100984, jan 2022. 41, 63

[105] S. K. Hau, Y.-J. Cheng, H.-L. Yip, Y. Zhang, H. Ma, and A. K.-Y. Jen, "Effect of chemical modification of fullerene-based self-assembled monolayers on the performance of inverted polymer solar cells," *ACS Applied Materials & Interfaces*, vol. 2, pp. 1892–1902, jul 2010. 42

[106] J. C. de Mello, H. F. Wittmann, and R. H. Friend, "An improved experimental determination of external photoluminescence quantum efficiency," *Advanced Materials*, vol. 9, pp. 230–232, mar 1997. 50

[107] T. Kirchartz, J. A. Márquez, M. Stolterfoht, and T. Unold, "Photoluminescence-based characterization of halide perovskites for photovoltaics," *Advanced Energy Materials*, vol. 10, p. 1904134, jul 2020. 50

[108] P. Tiwana, P. Parkinson, M. B. Johnston, H. J. Snaith, and L. M. Herz, "Ultrafast terahertz conductivity dynamics in mesoporous TiO_2: influence of dye sensitization and surface treatment in solid-state dye-sensitized solar cells," *The Journal of Physical Chemistry C*, vol. 114, no. 2, pp. 1365–1371, 2010. 53

[109] C. Wehrenfennig, M. Liu, H. J. Snaith, M. B. Johnston, and L. M. Herz, "Charge-carrier dynamics in vapour-deposited films of the organolead halide perovskite $CH_3NH_3PbI_{3-x}Cl_x$," *Energy & Environmental Science*, vol. 7, no. 7, pp. 2269–2275, 2014. 53

[110] U. Rau, "Reciprocity relation between photovoltaic quantum efficiency and electroluminescent emission of solar cells," *Physical Review B*, vol. 76, p. 085303, aug 2007. 56, 77

[111] S. N. Habisreutinger, B. Wenger, H. J. Snaith, and R. J. Nicholas, "Dopant-free planar n–i–p perovskite solar cells with steady-state efficiencies exceeding 18%," *ACS Energy Letters*, vol. 2, pp. 622–628, mar 2017. 57

[112] J. J. Yoo, G. Seo, M. R. Chua, T. G. Park, Y. Lu, F. Rotermund, Y.-K. Kim, C. S. Moon, N. J. Jeon, J.-P. Correa-Baena, V. Bulović, S. S. Shin, M. G. Bawendi, and J. Seo, "Efficient perovskite solar cells via improved carrier management," *Nature*, vol. 590, pp. 587–593, feb 2021. 60, 117

[113] H. Min, M. Kim, S.-U. Lee, H. Kim, G. Kim, K. Choi, J. H. Lee, and S. I. Seok, "Efficient, stable solar cells by using inherent bandgap of α-phase formamidinium lead iodide," *Science*, vol. 366, pp. 749–753, nov 2019. 60

[114] G. Kim, H. Min, K. S. Lee, D. Y. Lee, S. M. Yoon, and S. I. Seok, "Impact of strain relaxation on performance of α-formamidinium lead iodide perovskite solar cells," *Science*, vol. 370, pp. 108–112, oct 2020. 60

[115] U. Bach, D. Lupo, P. Comte, J. E. Moser, F. Weissörtel, J. Salbeck, H. Spreitzer, and M. Grätzel, "Solid-state dye-sensitized mesoporous TiO 2 solar cells with high photon-to-electron conversion efficiencies," *Nature 1998 395:6702*, vol. 395, pp. 583–585, oct 1998. 60

[116] T. Leijtens, G. E. Eperon, N. K. Noel, S. N. Habisreutinger, A. Petrozza, and H. J. Snaith, "Stability of metal halide perovskite solar cells," *Advanced Energy Materials*, vol. 5, p. 1500963, oct 2015. 60

[117] W. Nie, J.-C. Blancon, A. J. Neukirch, K. Appavoo, H. Tsai, M. Chhowalla, M. A. Alam, M. Y. Sfeir, C. Katan, J. Even, *et al.*, "Light-activated photocurrent degradation and self-healing in perovskite solar cells," *Nature communications*, vol. 7, no. 1, p. 11574, 2016. 60

[118] G. Divitini, S. Cacovich, F. Matteocci, L. Cinà, A. Di Carlo, and C. Ducati, "In situ observation of heat-induced degradation of perovskite solar cells," *Nature Energy*, vol. 1, no. 2, pp. 1–6, 2016. 60

[119] M. Salado, L. Contreras-Bernal, L. Caliò, A. Todinova, C. López-Santos, S. Ahmad, A. Borras, J. Idígoras, and J. A. Anta, "Impact of moisture on efficiency-determining electronic processes in perovskite solar cells," *Journal of Materials Chemistry A*, vol. 5, no. 22, pp. 10917–10927, 2017. 60

[120] A. Solanki, P. Yadav, S.-H. Turren-Cruz, S. S. Lim, M. Saliba, and T. C. Sum, "Cation influence on carrier dynamics in perovskite solar cells," *Nano Energy*, vol. 58, pp. 604–611, 2019. 60

[121] G. E. Eperon, S. N. Habisreutinger, T. Leijtens, B. J. Bruijnaers, J. J. Van Franeker, D. W. Dequilettes, S. Pathak, R. J. Sutton, G. Grancini, D. S. Ginger, R. A. Janssen, A. Petrozza, and H. J. Snaith, "The importance of moisture in hybrid lead halide perovskite thin film fabrication," *ACS Nano*, vol. 9, pp. 9380–9393, sep 2015. 60

[122] D. Wang, M. Wright, N. K. Elumalai, and A. Uddin, "Stability of perovskite solar cells," *Solar Energy Materials and Solar Cells*, vol. 147, pp. 255–275, apr 2016. 60

[123] A. M. A. Leguy, Y. Hu, M. Campoy-Quiles, M. I. Alonso, O. J. Weber, P. Azarhoosh, M. van Schilfgaarde, M. T. Weller, T. Bein, J. Nelson, P. Docampo, and P. R. F. Barnes, "Reversible hydration of $CH_3NH_3PbI_3$ in films, single crystals, and solar cells," *Chemistry of Materials*, vol. 27, pp. 3397–3407, may 2015. 60

[124] H. Kim, K.-G. Lim, and T.-W. Lee, "Planar heterojunction organometal halide perovskite solar cells: roles of interfacial layers," *Energy Environ. Sci.*, vol. 9, pp. 12–30, 2016. 60

[125] W. Zhang, F. Zhang, B. Xu, Y. Li, L. Wang, B. Zhang, Y. Guo, J. M. Gardner, L. Sun, and L. Kloo, "Organic salts as p-type dopants for efficient LiTFSI-free perovskite solar cells," *ACS applied materials & interfaces*, vol. 12, no. 30, pp. 33751–33758, 2020. 60, 61

[126] T. Du, W. Xu, M. Daboczi, J. Kim, S. Xu, C. T. Lin, H. Kang, K. Lee, M. J. Heeney, J. S. Kim, J. R. Durrant, and M. A. McLachlan, "p-Doping of organic hole transport layers in p-i-n perovskite solar cells: Correlating open-circuit voltage and photoluminescence quenching," *Journal of Materials Chemistry A*, vol. 7, pp. 18971–18979, aug 2019. 60, 71, 82

[127] J. Burschka, A. Dualeh, F. Kessler, E. Baranoff, N. L. Cevey-Ha, C. Yi, M. K. Nazeeruddin, and M. Grätzel, "Tris(2-(1 H -pyrazol-1-yl)pyridine)cobalt(III) as p-type dopant for organic semiconductors and its application in highly efficient solid-state dye-sensitized solar cells," *Journal of the American Chemical Society*, vol. 133, pp. 18042–18045, nov 2011. 60

[128] M. D. Irwin, D. B. Buchholz, A. W. Hains, R. P. Chang, and T. J. Marks, "p-Type semiconducting nickel oxide as an efficiency-enhancing anode interfacial layer in polymer bulk-heterojunction solar cells," *Proceedings of the National Academy of Sciences of the United States of America*, vol. 105, pp. 2783–2787, feb 2008. 60

[129] J. H. Noh, N. J. Jeon, Y. C. Choi, M. K. Nazeeruddin, M. Grätzel, and S. I. Seok, "Nanostructured $TiO_2/CH_3NH_3PbI_3$ heterojunction solar cells employing spiro-OMeTAD/Co-complex as hole-transporting material," *Journal of Materials Chemistry A*, vol. 1, pp. 11842–11847, sep 2013. 61

[130] A. Abate, T. Leijtens, S. Pathak, J. Teuscher, R. Avolio, M. E. Errico, J. Kirkpatrik, J. M. Ball, P. Docampo, I. McPherson, and H. J. Snaith, "Lithium salts as "redox active" p-type dopants for organic semiconductors and their impact in solid-state dye-sensitized solar cells," *Physical Chemistry Chemical Physics*, vol. 15, pp. 2572–2579, jan 2013. 61, 65

[131] J.-Y. Seo, H.-S. Kim, S. Akin, M. Stojanovic, E. Simon, M. Fleischer, A. Hagfeldt, S. M. Zakeeruddin, and M. Grätzel, "Novel p-dopant toward highly efficient and stable perovskite solar cells," *Energy & Environmental Science*, vol. 11, pp. 2985–2992, oct 2018. 61

[132] N. Sakai, R. Warren, F. Zhang, S. Nayak, J. Liu, S. V. Kesava, Y.-H. Lin, H. S. Biswal, X. Lin, C. Grovenor, T. Malinauskas, A. Basu, T. D. Anthopoulos, V. Getautis, A. Kahn, M. Riede, P. K. Nayak, and H. J. Snaith, "Adduct-based

p-doping of organic semiconductors," *Nature Materials*, vol. 20, pp. 1248–1254, apr 2021. 61

[133] T. H. Schloemer, J. A. Christians, J. M. Luther, and A. Sellinger, "Doping strategies for small molecule organic hole-transport materials: impacts on perovskite solar cell performance and stability," *Chemical Science*, vol. 10, no. 7, pp. 1904–1935, 2019. 61

[134] Z. Song, J. Liu, G. Wang, W. Zuo, C. Liao, and J. Mei, "Understanding the photovoltaic performance of perovskite-spirobifluorene solar cells," *ChemPhysChem*, vol. 18, pp. 3030–3038, nov 2017. 61

[135] Y. Cho, H. D. Kim, J. Zheng, J. Bing, Y. Li, M. Zhang, M. A. Green, A. Wakamiya, S. Huang, H. Ohkita, and A. W. Ho-Baillie, "Elucidating mechanisms behind ambient storage-induced efficiency improvements in perovskite solar cells," *ACS Energy Letters*, vol. 6, pp. 925–933, mar 2021. 61

[136] Z. Li, C. Xiao, Y. Yang, S. P. Harvey, D. H. Kim, J. A. Christians, M. Yang, P. Schulz, S. U. Nanayakkara, C.-S. Jiang, J. M. Luther, J. J. Berry, M. C. Beard, M. M. Al-Jassim, and K. Zhu, "Extrinsic ion migration in perovskite solar cells," *Energy & Environmental Science*, vol. 10, pp. 1234–1242, may 2017. 61, 80

[137] S. Wang, W. Yuan, and Y. S. Meng, "Spectrum-dependent spiro-ometad oxidization mechanism in perovskite solar cells," *ACS Applied Materials and Interfaces*, vol. 7, pp. 24791–24798, nov 2015. 61

[138] H.-S. Kim, J.-Y. Seo, and N.-G. Park, "Material and device stability in perovskite solar cells," *ChemSusChem*, vol. 9, pp. 2528–2540, sep 2016. 61

[139] A. K. Jena, Y. Numata, M. Ikegami, and T. Miyasaka, "Role of spiro-OMeTAD in performance deterioration of perovskite solar cells at high temperature and

reuse of the perovskite films to avoid Pb-waste," *Journal of Materials Chemistry A*, vol. 6, pp. 2219–2230, jan 2018. 61, 84

[140] A. K. Jena, M. Ikegami, and T. Miyasaka, "Severe morphological deformation of spiro-OMeTAD in $(CH_3NH_3)PbI_3$ solar cells at high temperature," *ACS Energy Letters*, vol. 2, no. 8, pp. 1760–1761, 2017. 61, 84

[141] Y. Ko, Y. Kim, C. Lee, Y. Kim, and Y. Jun, "Investigation of hole-transporting poly(triarylamine) on aggregation and charge transport for hysteresisless scalable planar perovskite solar cells," *ACS Applied Materials and Interfaces*, vol. 10, pp. 11633–11641, apr 2018. 61

[142] K. Rakstys, C. Igci, and M. K. Nazeeruddin, "Efficiency vs. stability: dopant-free hole transporting materials towards stabilized perovskite solar cells," *Chemical Science*, vol. 10, no. 28, pp. 6748–6769, 2019. 61, 62

[143] D. Bharath, M. Sasikumar, N. R. Chereddy, J. R. Vaidya, and S. Pola, "Synthesis of new 2-((5-(4-alkyl-4H-dithieno[3,2-b:2",3"-d]pyrrol-2-yl)thiophen-2-yl)methylene)malononitrile: Dopant free hole transporting materials for perovskite solar cells with high power conversion efficiency," *Solar Energy*, vol. 174, pp. 130–138, nov 2018. 62

[144] A. Al-Ashouri, A. Magomedov, M. Roß, M. Jošt, M. Talaikis, G. Chistiakova, T. Bertram, J. A. Márquez, E. Köhnen, E. Kasparavičius, *et al.*, "Conformal monolayer contacts with lossless interfaces for perovskite single junction and monolithic tandem solar cells," *Energy & Environmental Science*, vol. 12, no. 11, pp. 3356–3369, 2019. 62

[145] R. Azmi, S. Y. Nam, S. Sinaga, Z. A. Akbar, C.-L. Lee, S. C. Yoon, I. H. Jung, and S.-Y. Jang, "High-performance dopant-free conjugated small molecule-based hole-transport materials for perovskite solar cells," *Nano Energy*, vol. 44, pp. 191–198, feb 2018. 62

[146] N. L. Chang, J. Zheng, Y. Wu, H. Shen, F. Qi, K. Catchpole, A. Ho-Baillie, and R. J. Egan, "A bottom-up cost analysis of silicon–perovskite tandem photovoltaics," *Progress in Photovoltaics: Research and Applications*, vol. 29, no. 3, pp. 401–413, 2021. 62, 63

[147] L. Nakka, Y. Cheng, A. G. Aberle, and F. Lin, "Analytical review of Spiro-OMeTAD hole transport materials: paths toward stable and efficient perovskite solar cells," *Advanced Energy and Sustainability Research*, vol. 3, p. 2200045, aug 2022. 64

[148] K. Kawabata, M. Saito, N. Takemura, I. Osaka, and K. Takimiya, "Effects of branching position of alkyl side chains on ordering structure and charge transport property in thienothiophenedione- and quinacridone-based semiconducting polymers," *Polymer Journal*, vol. 49, pp. 169–176, jan 2017. 66

[149] B. Fu, J. Baltazar, A. R. Sankar, P.-H. Chu, S. Zhang, D. M. Collard, and E. Reichmanis, "Enhancing field-effect mobility of conjugated polymers through rational design of branched side chains," *Advanced Functional Materials*, vol. 24, pp. 3734–3744, jun 2014. 66

[150] A.-R. Han, G. K. Dutta, J. Lee, H. R. Lee, S. M. Lee, H. Ahn, T. J. Shin, J. H. Oh, and C. Yang, "ϵ-branched flexible side chain substituted diketopyrrolopyrrole-containing polymers designed for high hole and electron mobilities," *Advanced Functional Materials*, vol. 25, pp. 247–254, jan 2015. 66

[151] J. Mei, H.-C. Wu, Y. Diao, A. Appleton, H. Wang, Y. Zhou, W.-Y. Lee, T. Kurosawa, W.-C. Chen, and Z. Bao, "Effect of spacer length of siloxane-terminated side chains on charge transport in isoindigo-based polymer semiconductor thin films," *Advanced Functional Materials*, vol. 25, pp. 3455–3462, jun 2015. 66

[152] I. Kang, H. J. Yun, D. S. Chung, S. K. Kwon, and Y. H. Kim, "Record high hole mobility in polymer semiconductors via side-chain engineering," *Journal of the American Chemical Society*, vol. 135, pp. 14896–14899, oct 2013. 66

[153] J. Mei, D. H. Kim, A. L. Ayzner, M. F. Toney, and Z. Bao, "Siloxane-terminated solubilizing side chains: Bringing conjugated polymer backbones closer and boosting hole mobilities in thin-film transistors," *Journal of the American Chemical Society*, vol. 133, pp. 20130–20133, dec 2011. 66

[154] M. Saliba, J.-P. Correa-Baena, C. M. Wolff, M. Stolterfoht, N. Phung, S. Albrecht, D. Neher, and A. Abate, "How to make over 20% efficient perovskite solar cells in regular (n–i–p) and inverted (p–i–n) architectures," *Chemistry of Materials*, vol. 30, no. 13, pp. 4193–4201, 2018. 66

[155] J.-Y. Seo, S. Akin, M. Zalibera, M. A. R. Preciado, H.-S. Kim, S. M. Zakeeruddin, J. V. Milić, and M. Grätzel, "Dopant engineering for spiro-ometad hole-transporting materials towards efficient perovskite solar cells," *Advanced Functional Materials*, p. 2102124, aug 2021. 66

[156] M. A. García and J. Balenzategui, "Estimation of photovoltaic module yearly temperature and performance based on nominal operation cell temperature calculations," *Renewable Energy*, vol. 29, no. 12, pp. 1997–2010, 2004. 67

[157] R. Lygaitis, V. Getautis, and J. V. Grazulevicius, "Hole-transporting hydrazones," *Chemical Society Reviews*, vol. 37, no. 4, pp. 770–788, 2008. 68

[158] X. Zhao, H.-S. Kim, J.-Y. Seo, and N.-G. Park, "Effect of selective contacts on the thermal stability of perovskite solar cells," *ACS applied materials & interfaces*, vol. 9, no. 8, pp. 7148–7153, 2017. 69, 84

[159] M. Salado, J. Idigoras, L. Calio, S. Kazim, M. K. Nazeeruddin, J. A. Anta, and S. Ahmad, "Interface play between perovskite and hole selective layer on the

performance and stability of perovskite solar cells," *ACS Applied Materials & Interfaces*, vol. 8, pp. 34414–34421, dec 2016. 70, 71

[160] J. Cao, S. Mo, X. Jing, J. Yin, J. Li, and N. Zheng, "Trace surface-clean palladium nanosheets as a conductivity enhancer in hole-transporting layers to improve the overall performances of perovskite solar cells," *Nanoscale*, vol. 8, pp. 3274–3277, feb 2016. 71

[161] S. Sidhik, D. Esparza, A. Martínez-Benítez, T. Lopez-Luke, R. Carriles, I. Mora-Sero, and E. de la Rosa, "Enhanced photovoltaic performance of mesoscopic perovskite solar cells by controlling the interaction between $CH_3NH_3PbI_3$ films and $CsPbX_3$ perovskite nanoparticles," *The Journal of Physical Chemistry C*, vol. 121, pp. 4239–4245, mar 2017. 71

[162] V. M. Le Corre, M. Stolterfoht, L. Perdigón Toro, M. Feuerstein, C. Wolff, L. Gil-Escrig, H. J. Bolink, D. Neher, and L. J. A. Koster, "Charge transport layers limiting the efficiency of perovskite solar cells: How to optimize conductivity, doping, and thickness," *ACS Applied Energy Materials*, vol. 2, pp. 6280–6287, sep 2019. 71

[163] W. Li, H. Dong, L. Wang, N. Li, X. Guo, J. Li, and Y. Qiu, "Montmorillonite as bifunctional buffer layer material for hybrid perovskite solar cells with protection from corrosion and retarding recombination," *Journal of Materials Chemistry A*, vol. 2, pp. 13587–13592, sep 2014. 71

[164] S. Wang, Z. Huang, X. Wang, Y. Li, M. Günther, S. Valenzuela, P. Parikh, A. Cabreros, W. Xiong, and Y. S. Meng, "Unveiling the role of tBP-LiTFSI complexes in perovskite solar cells," *Journal of the American Chemical Society*, vol. 140, pp. 16720–16730, dec 2018. 71

[165] S. Wang, M. Sina, P. Parikh, T. Uekert, B. Shahbazian, A. Devaraj, and Y. S. Meng, "Role of 4-tert-butylpyridine as a hole transport layer morphological controller in perovskite solar cells," *Nano Letters*, vol. 16, pp. 5594–5600, sep 2016. 71, 84

[166] S. N. Habisreutinger, N. K. Noel, H. J. Snaith, and R. J. Nicholas, "Investigating the role of 4-tert butylpyridine in perovskite solar cells," *Advanced Energy Materials*, vol. 7, no. 1, p. 1601079, 2017. 71

[167] P. Song, L. Shen, L. Zheng, K. Liu, W. Tian, J. Chen, Y. Luo, C. Tian, L. Xie, and Z. Wei, "Double-layered SnO_2/NH_4Cl-SnO_2 for efficient planar perovskite solar cells with improved operational stability," *Nano Select*, vol. 2, pp. 1779–1787, sep 2021. 76

[168] D. Yang, R. Yang, K. Wang, C. Wu, X. Zhu, J. Feng, X. Ren, G. Fang, S. Priya, and S. F. Liu, "High efficiency planar-type perovskite solar cells with negligible hysteresis using EDTA-complexed SnO2," *Nature Communications 2018 9:1*, vol. 9, pp. 1–11, aug 2018. 76, 117

[169] T. Bu, J. Li, F. Zheng, W. Chen, X. Wen, Z. Ku, Y. Peng, J. Zhong, Y. B. Cheng, and F. Huang, "Universal passivation strategy to slot-die printed SnO2 for hysteresis-free efficient flexible perovskite solar module," *Nature Communications 2018 9:1*, vol. 9, pp. 1–10, nov 2018. 76

[170] M. Kim, I.-w. Choi, S. J. Choi, J. W. Song, S.-I. Mo, J.-H. An, Y. Jo, S. Ahn, S. K. Ahn, G.-H. Kim, and D. S. Kim, "Enhanced electrical properties of Li-salts doped mesoporous TiO_2 in perovskite solar cells," *Joule*, vol. 5, pp. 659–672, mar 2021. 80

[171] G. Tumen-Ulzii, C. Qin, T. Matsushima, M. R. Leyden, U. Balijipalli, D. Klotz, and C. Adachi, "Understanding the degradation of spiro-ometad-based perovskite solar cells at high temperature," *Solar RRL*, vol. 4, p. 2000305, oct 2020. 84, 117

[172] A. Magomedov, E. Kasparavičius, K. Rakstys, S. Paek, N. Gasilova, K. Genevičius, G. Juška, T. Malinauskas, M. K. Nazeeruddin, and V. Getautis, "Pyridination of hole transporting material in perovskite solar cells questions the long-term stability," *Journal of Materials Chemistry C*, vol. 6, pp. 8874–8878, aug 2018. 84

[173] F. Lamberti, T. Gatti, E. Cescon, R. Sorrentino, A. Rizzo, E. Menna, G. Meneghesso, M. Meneghetti, A. Petrozza, and L. Franco, "Evidence of spiro-ometad de-doping by tert-butylpyridine additive in hole-transporting layers for perovskite solar cells," *Chem*, vol. 5, pp. 1806–1817, jul 2019. 84

[174] E. Kasparavicius, A. Magomedov, T. Malinauskas, and V. Getautis, "Long-term stability of the oxidized hole-transporting materials used in perovskite solar cells," *Chemistry - A European Journal*, vol. 24, pp. 9910–9918, jul 2018. 84

[175] T. Malinauskas, D. Tomkute-Luksiene, R. Sens, M. Daskeviciene, R. Send, H. Wonneberger, V. Jankauskas, I. Bruder, and V. Getautis, "Enhancing thermal stability and lifetime of solid-state dye-sensitized solar cells via molecular engineering of the hole-transporting material spiro-OMeTAD," *ACS Applied Materials and Interfaces*, vol. 7, pp. 11107–11116, jun 2015. 84

[176] J. A. Christians, P. Schulz, J. S. Tinkham, T. H. Schloemer, S. P. Harvey, B. J. Tremolet de Villers, A. Sellinger, J. J. Berry, and J. M. Luther, "Tailored interfaces of unencapsulated perovskite solar cells for >1,000 hour operational stability," *Nature Energy*, vol. 3, no. 1, pp. 68–74, 2018. 85

[177] S. Bai, P. Da, C. Li, Z. Wang, Z. Yuan, F. Fu, M. Kawecki, X. Liu, N. Sakai, J. T.-W. Wang, S. Huettner, S. Buecheler, M. Fahlman, F. Gao, and H. J. Snaith, "Planar perovskite solar cells with long-term stability using ionic liquid additives," *Nature 2019 571:7764*, vol. 571, pp. 245–250, jul 2019. 85

[178] Y.-H. Lin, N. Sakai, P. Da, J. Wu, H. C. Sansom, A. J. Ramadan, S. Mahesh, J. Liu, R. D. Oliver, J. Lim, *et al.*, "A piperidinium salt stabilizes efficient metal-halide perovskite solar cells," *Science*, vol. 369, no. 6499, pp. 96–102, 2020. 85, 132, 141

[179] M. M. Tavakoli, M. Saliba, P. Yadav, P. Holzhey, A. Hagfeldt, S. M. Zakeeruddin, and M. Grätzel, "Synergistic crystal and interface engineering for efficient and stable perovskite photovoltaics," *Advanced Energy Materials*, vol. 9, no. 1, p. 1802646, 2019. 85

[180] E. Akman and S. Akin, "Poly(N,N'-bis-4-butylphenyl-N,N'-bisphenyl)benzidine-based interfacial passivation strategy promoting efficiency and operational stability of perovskite solar cells in regular architecture," *Advanced Materials*, vol. 33, p. 2006087, jan 2021. 85

[181] M. T. Hörantner and H. J. Snaith, "Predicting and optimising the energy yield of perovskite-on-silicon tandem solar cells under real world conditions," *Energy & Environmental Science*, vol. 10, no. 9, pp. 1983–1993, 2017. 89

[182] S. Macpherson, T. A. Doherty, A. J. Winchester, S. Kosar, D. N. Johnstone, Y. H. Chiang, K. Galkowski, M. Anaya, K. Frohna, A. N. Iqbal, S. Nagane, B. Roose, Z. Andaji-Garmaroudi, K. W. Orr, J. E. Parker, P. A. Midgley, K. M. Dani, and S. D. Stranks, "Local nanoscale phase impurities are degradation sites in halide perovskites," *Nature*, vol. 607, pp. 294–300, may 2022. 89

[183] L. E. Mundt, F. Zhang, A. F. Palmstrom, J. Xu, R. Tirawat, L. L. Kelly, K. H. Stone, K. Zhu, J. J. Berry, M. F. Toney, and L. T. Schelhas, "Mixing matters: Nanoscale heterogeneity and stability in metal halide perovskite solar cells," *ACS Energy Letters*, vol. 7, pp. 471–480, jan 2022. 89

[184] K. Datta, B. T. van Gorkom, Z. Chen, M. J. Dyson, T. P. A. van der Pol, S. C. J. Meskers, S. Tao, P. A. Bobbert, M. M. Wienk, and R. A. J. Janssen, "Effect of light-induced halide segregation on the performance of mixed-halide perovskite solar cells," *ACS Applied Energy Materials*, vol. 4, pp. 6650–6658, jul 2021. 90

[185] E. S. Parrott, R. L. Milot, T. Stergiopoulos, H. J. Snaith, M. B. Johnston, and L. M. Herz, "Effect of structural phase transition on charge-carrier lifetimes and defects in $CH_3NH_3SnI_3$ perovskite," *The Journal of Physical Chemistry Letters*, vol. 7, pp. 1321–1326, apr 2016. 90

[186] W. Feng, C. Zhang, J. X. Zhong, L. Ding, and W. Q. Wu, "Correlating alkyl chain length with defect passivation efficacy in perovskite solar cells," *Chemical Communications*, vol. 56, pp. 5006–5009, may 2020. 90

[187] A. J. Ramadan, N. K. Noel, S. Fearn, N. Young, M. Walker, L. A. Rochford, and H. J. Snaith, "Unravelling the improved electronic and structural properties of methylammonium lead iodide deposited from acetonitrile," *Chemistry of Materials*, vol. 30, pp. 7737–7743, nov 2018. 90

[188] M. Taddei, J. A. Smith, B. M. Gallant, S. Zhou, R. J. E. Westbrook, Y. Shi, J. Wang, J. N. Drysdale, D. P. McCarthy, S. Barlow, S. R. Marder, H. J. Snaith, and D. S. Ginger, "Ethylenediamine addition improves performance and suppresses phase instabilities in mixed-halide perovskites," *ACS Energy Letters*, pp. 4265–4273, nov 2022. 90, 125

[189] Z. Li, X. Wang, Z. Wang, Z. Shao, L. Hao, Y. Rao, C. Chen, D. Liu, Q. Zhao, X. Sun, C. Gao, B. Zhang, X. Wang, L. Wang, G. Cui, and S. Pang, "Ammonia for post-healing of formamidinium-based Perovskite films," *Nature Communications*, vol. 13, no. 1, p. 4417, 2022. 91, 117

[190] Y. Fang, H. Wei, Q. Dong, and J. Huang, "Quantification of re-absorption and re-emission processes to determine photon recycling efficiency in perovskite single crystals," *Nature Communications*, vol. 8, no. 1, p. 14417, 2017. 101

[191] C. M. Wolff, P. Caprioglio, M. Stolterfoht, and D. Neher, "Nonradiative recombination in perovskite solar cells: the role of interfaces," *Advanced Materials*, vol. 31, no. 52, p. 1902762, 2019. 117

[192] E. H. Jung, B. Chen, K. Bertens, M. Vafaie, S. Teale, A. Proppe, Y. Hou, T. Zhu, C. Zheng, and E. H. Sargent, "Bifunctional surface engineering on SnO2reduces energy loss in perovskite solar cells," *ACS Energy Letters*, vol. 5, pp. 2796–2801, sep 2020. 117

[193] K. G. Godinho, A. Walsh, and G. W. Watson, "Energetic and electronic structure analysis of intrinsic defects in SnO2," *Journal of Physical Chemistry C*, vol. 113, pp. 439–448, jan 2009. 117

[194] Y. Luan, X. Yi, P. Mao, Y. Wei, J. Zhuang, N. Chen, T. Lin, C. Li, and J. Wang, "High-performance planar perovskite solar cells with negligible hysteresis Using 2,2,2-Trifluoroethanol-incorporated SnO_2," *iScience*, vol. 16, pp. 433–441, 2019. 117

[195] K. Liu, C. Tian, Y. Liang, Y. Luo, L. Xie, and Z. Wei, "Progress toward understanding the fullerene-related chemical interactions in perovskite solar cells," *Nano Research*, vol. 15, no. 8, pp. 7139–7153, 2022. 118

[196] K. Liu, S. Chen, J. Wu, H. Zhang, M. Qin, X. Lu, Y. Tu, Q. Meng, and X. Zhan, "Fullerene derivative anchored SnO_2 for high-performance perovskite solar cells," *Energy & Environmental Science*, vol. 11, no. 12, pp. 3463–3471, 2018. 118

[197] J. Wang, K. Datta, C. H. Weijtens, M. M. Wienk, and R. A. Janssen, "Insights into fullerene passivation of SnO_2 electron transport layers in perovskite solar cells," *Advanced Functional Materials*, vol. 29, no. 46, p. 1905883, 2019. 118

[198] W. Ke, D. Zhao, C. Xiao, C. Wang, A. J. Cimaroli, C. R. Grice, M. Yang, Z. Li, C.-S. Jiang, M. Al-Jassim, K. Zhu, M. G. Kanatzidis, G. Fang, and Y. Yan, "Cooperative tin oxide fullerene electron selective layers for high-performance planar perovskite solar cells," *Journal of Materials Chemistry A*, vol. 4, no. 37, pp. 14276–14283, 2016. 118

[199] T. Cao, K. Chen, Q. Chen, Y. Zhou, N. Chen, and Y. Li, "Fullerene derivative-modified SnO_2 electron transport layer for highly efficient perovskite solar cells with efficiency over 21%," *ACS Applied Materials and Interfaces*, vol. 11, pp. 33825–33834, sep 2019. 118

[200] E. Jiang, Y. Ai, J. Yan, N. Li, L. Lin, Z. Wang, C. Shou, B. Yan, Y. Zeng, J. Sheng, and J. Ye, "Phosphate-passivated SnO_2 electron transport layer for high-performance perovskite solar cells," *ACS Applied Materials & Interfaces*, vol. 11, pp. 36727–36734, oct 2019. 118

[201] A. Mingorance, H. Xie, H. Kim, Z. Wang, M. Balsells, A. Morales-Melgares, N. Domingo, W. Tress, J. Fraxedas, and N. Vlachopoulos, "Interfacial engineering of metal oxides for highly stable halide perovskite solar cells," *Advanced Materials Interfaces*, vol. 5, no. 22, p. 1800367, 2018. 118

[202] D. Xue, T. Wakahara, K. Marumoto, and K. Tsukagoshi, "High charge transfer from C_{60} pyrrolidine tris-acid to SnO_2 electron transport layer directly observed by ESR spectroscopy," *ACS Applied Energy Materials*, feb 2023. 118

[203] S. K. Huang, Y. C. Wang, W. C. Ke, Y. T. Kao, N. Z. She, J. X. Li, C. W. Luo, A. Yabushita, D. Y. Wang, Y. J. Chang, K. Tsukagoshi, and C. W. Chen, "Unravelling the origin of the photocarrier dynamics of fullerene-derivative passivation of SnO_2 electron transporters in perovskite solar cells," *Journal of Materials Chemistry A*, vol. 8, pp. 23607–23616, nov 2020. 118

[204] S. You, H. Zeng, Y. Liu, B. Han, M. Li, L. Li, X. Zheng, R. Guo, L. Luo, Z. Li, C. Zhang, R. Liu, Y. Zhao, S. Zhang, Q. Peng, T. Wang, Q. Chen, F. T. Eickemeyer, B. Carlsen, S. M. Zakeeruddin, L. Mai, Y. Rong, M. Grätzel, and X. Li, "Radical polymeric p-doping and grain modulation for stable, efficient perovskite solar modules," *Science*, vol. 379, pp. 288–294, jan 2023. 118, 132

[205] N. Adden, L. J. Gamble, D. G. Castner, A. Hoffmann, G. Gross, and H. Menzel, "Phosphonic acid monolayers for binding of bioactive molecules to titanium surfaces," *Langmuir*, vol. 22, pp. 8197–8204, sep 2006. 121

[206] H. Idriss, "On the wrong assignment of the xps o1s signal at 531–532 ev attributed to oxygen vacancies in photo-and electro-catalysts for water splitting and other materials applications," *Surface Science*, vol. 712, p. 121894, 2021. 121

[207] S. Jariwala, S. Burke, S. Dunfield, R. C. Shallcross, M. Taddei, J. Wang, G. E. Eperon, N. R. Armstrong, J. J. Berry, and D. S. Ginger, "Reducing surface recombination velocity of methylammonium-free mixed-cation mixed-halide perovskites via surface passivation," *Chemistry of Materials*, vol. 33, no. 13, pp. 5035–5044, 2021. 125

[208] Q. Luo, Y. Zhang, C. Liu, J. Li, N. Wang, and H. Lin, "Iodide-reduced graphene oxide with dopant-free spiro-OMeTAD for ambient stable and high-efficiency perovskite solar cells," *Journal of Materials Chemistry A*, vol. 3, no. 31, pp. 15996–16004, 2015. 132

[209] R. S. Sanchez and E. Mas-Marza, "Light-induced effects on Spiro-OMeTAD films and hybrid lead halide perovskite solar cells," *Solar Energy Materials and Solar Cells*, vol. 158, pp. 189–194, 2016. 132

[210] M. Schultes, N. Giesbrecht, J. Küffner, E. Ahlswede, P. Docampo, T. Bein, and M. Powalla, "Universal nanoparticle wetting agent for upscaling perovskite solar cells," *ACS applied materials & interfaces*, vol. 11, no. 13, pp. 12948–12957, 2019. 132

[211] J. S. Godding, A. J. Ramadan, Y.-H. Lin, K. Schutt, H. J. Snaith, and B. Wenger, "Oxidative passivation of metal halide perovskites," *Joule*, vol. 3, no. 11, pp. 2716–2731, 2019. 134

[212] A. Al-Ashouri, E. Köhnen, B. Li, A. Magomedov, H. Hempel, P. Caprioglio, J. A. Márquez, A. B. Morales Vilches, E. Kasparavicius, J. A. Smith, *et al.*, "Monolithic perovskite/silicon tandem solar cell with> 29% efficiency by enhanced hole extraction," *Science*, vol. 370, no. 6522, pp. 1300–1309, 2020. 140

[213] A. Al-Ashouri, A. Magomedov, M. Roß, M. Jošt, M. Talaikis, G. Chistiakova, T. Bertram, J. A. Márquez, E. Köhnen, E. Kasparavičius, *et al.*, "Conformal monolayer contacts with lossless interfaces for perovskite single junction and monolithic tandem solar cells," *Energy & Environmental Science*, vol. 12, no. 11, pp. 3356–3369, 2019. 140

[214] K. Brinkmann, T. Becker, F. Zimmermann, C. Kreusel, T. Gahlmann, M. Theisen, T. Haeger, S. Olthof, C. Tückmantel, M. Günster, *et al.*, "Perovskite–organic tandem solar cells with indium oxide interconnect," *Nature*, vol. 604, no. 7905, pp. 280–286, 2022. 140

[215] A. Al-Ashouri, M. Marcinskas, E. Kasparavičius, T. Malinauskas, A. Palmstrom, V. Getautis, S. Albrecht, M. D. McGehee, and A. Magomedov, "Wettability improvement of a carbazole-based hole-selective monolayer for reproducible perovskite solar cells," *ACS Energy Letters*, vol. 8, pp. 898–900, 2023. 141

[216] T. P. Osedach, T. L. Andrew, and V. Bulović, "Effect of synthetic accessibility on the commercial viability of organic photovoltaics," *Energy & Environmental Science*, vol. 6, no. 3, pp. 711–718, 2013. 149

[217] M. Petrus, T. Bein, T. Dingemans, and P. Docampo, "A low cost azomethine-based hole transporting material for perovskite photovoltaics," *Journal of Materials Chemistry A*, vol. 3, no. 23, pp. 12159–12162, 2015. 149, 150

[218] M. Degbia, M. B. Manaa, B. Schmaltz, N. Berton, J. Bouclé, R. Antony, and F. T. Van, "Carbazole-based hole transporting material for solid state dye-sensitized solar cells: Influence of the purification methods," *Materials Science in Semiconductor Processing*, vol. 43, pp. 90–95, 2016. 149, 150

[219] O. Usluer, M. Abbas, G. Wantz, L. Vignau, L. Hirsch, E. Grana, C. Brochon, E. Cloutet, and G. Hadziioannou, "Metal residues in semiconducting polymers: impact on the performance of organic electronic devices," *ACS Macro Letters*, vol. 3, no. 11, pp. 1134–1138, 2014. 150